

# Exploring the Behaviour and Catalytic Properties of Cyclen Derived DO3A Triamide Derivatives

Louis Lamont

Keble College, University of Oxford



A thesis submitted for the degree of

*Doctor of Philosophy* in Inorganic Chemistry

**Trinity Term 2023**

***Abstract***

**Exploring the Behaviour and Catalytic Properties of Cyclen  
Derived DO3A Triamide derivatives**

Catalysts have played, and will continue to serve, a vital role in an increasing range of processes. While the role of lanthanides in catalysis is well known, the development of homogenous water-soluble lanthanide-containing catalysts is relatively understudied and includes various desirable properties.

Chapter-1 introduces lanthanide chemistry, covering their coordinative abilities, photophysics, definitions of stability and local magnetic fields. Including a description of their current catalytic uses.

Chapter-2 focuses on the study of Ln.p.DO3A (Ln = Eu, Tb) complexes as a prototype system. These systems are shown to catalyse the fluorination of halocarboxylic acid substrates, via a proposed ternary complex.

Chapter-3 details the synthesis of DO3AM derivatives, conceived to favour binding of fluoride and carboxylic acids. A number of synthetic routes to these systems were explored, and it was found that amide coupling of DO3A free acids offered the best combination of yield and synthetic flexibility.

Chapter-4 focuses on luminescence measurements of the eight DO3AM-derived complexes synthesised in chapter-3, and on the binding of fluoride and carboxylate guests. The affinity of these complexes for anionic guests was found to be dependent on the nature of the amide side chains, which provide structural rigidity and influence solubility. Quantification of binding with anionic guests using DynaFit<sup>®</sup> and measurement of luminescence lifetimes was used to select three

complexes which resist self-aggregation and display significant affinity for carboxylates and fluoride.

Chapter-5 explores the use of these three candidate complexes in the fluorination of halocarboxylic acid substrates with fluoride ions.  $^{19}\text{F}$  NMR spectroscopy was used to follow the course of fluorination. All the candidate complexes were shown to accelerate the rate of reaction relative to the control. These results indicate that practical fluorination using these methods is a realistic possibility.

Chapter-6 summarises and draws conclusions from the work covered in this thesis, with comments on potential future work.

Chapter-7 describes the experimental procedures followed in accomplishing the results reported in chapters 2-5.

The appendix includes some spectroscopic data not included in chapters 2-5.

## **Acknowledgements**

8 years. 8 long years. I didn't think proving I had some ability at chemistry would take me this long but apparently it has. Starting at Oriel October 2015 I didn't think that I would still be knocking about come 2023 but here we are.

Working in Steve's group these past 5 years has been a pleasure, from my masters to my DPhil he has been a source of unwavering support and savant knowledge on all things, somehow not just chemistry. I could not have wished for a better supervisor to guide me through a single degree let alone two.

The Faulkner group has been a mainstay of the past 5 years, and as the people in it changed and I moved from young whipper snapper to old has been. It's reassuring to know that the same support, guidance and knowledge will always be there and that help will always be provided. Special mentions must go to a few people though. De-borah Sne-ddon, although annoyingly other people found out she was smart and she got a job as a lecturer in the last few months of this being written, no one played a bigger role in providing motivation and organisation to the group itself and to me personally. I've never met someone so able and always willing to help others before herself and a lot of this thesis would sound a lot worse if it wasn't for her. Carlson my fellow anion binder and the trailblazer for so many of the techniques used in the group, another proofreader who's work in this thesis is second to none, without a doubt one of the finest additions the Faulkner group has ever had and one of the most diligent scientists I've ever met. Dani the source of synthetic wisdom every lab wants and who we were lucky enough to get, always ready with column conditions whenever anyone needed them. Grace for being the lab mum we didn't deserve but the best one we could ever ask for, the PeMac system has never been so quiet since you left, but we just about learned to look after ourselves a bit before you graduated. Laura and Marie, I couldn't have asked for two better friends to go through this experience with, always willing to talk things through and form our own DPhil support group, a huge aspect I'm going to miss leaving the lab. Cam, Charlotte and recent addition Johnny, just DPhils trying to make their way in the lab but still helping, mainly with the crossword but that's still something worth acknowledging. To all the other members of the Faulkner group and especially the Part IIs, there are so many people who made this group into the welcoming environment it is that I can't name them all. I guess one springs to mind and that's Emma or chief support officer as she's known, no one has ever said 'you're almost done' or 'you're doing so well' as much as she has and made me feel better every time, her support has made this last year much better than I imagined it would be. This last thanks goes to all the friends, teammates, acquaintances and anyone else under the sun I encountered while at Oxford all these years. It hasn't always been easy, but I know for certain that I can't call this experience hard or not enjoyable, I've had a wonderful time and could definitely be accused of having too much fun.

The main people responsible for all of this are my parents, while having no clue what I do at university they have continued to support me in all things, and wanted only what any parent wants for their kid. For them to be happy. I can safely say that they have accomplished this mission and much much more.

In summary I would say, I've made a lot of friends, done a lot of stuff and had a wonderful time with all of it. This chapter of life is closing and its now time for the next, hopefully if you're reading this you have fun with the next seven.

## Contents

<b>Abstract</b> .....	<b>i</b>
<b>Acknowledgements</b> .....	<b>iii</b>
<b>Contents</b> .....	<b>iv</b>
<b>Abbreviations</b> .....	<b>vii</b>
<b>Chapter-1: Introduction</b> .....	<b>1</b>
<b>1.1 General lanthanide chemistry</b> .....	<b>1</b>
<b>1.2 Coordination chemistry of lanthanide complexes</b> .....	<b>2</b>
<b>1.2.1 Macrocyclic chemistry of lanthanides</b> .....	<b>4</b>
<b>1.2.2 Isomerism in Lanthanide complexes</b> .....	<b>7</b>
<b>1.3 Thermodynamic vs kinetic stability</b> .....	<b>10</b>
<b>1.3.1 Thermodynamic stability</b> .....	<b>10</b>
<b>1.3.2 Kinetic stability</b> .....	<b>12</b>
<b>1.4 Photophysics of lanthanides</b> .....	<b>14</b>
<b>1.4.1 Selection rules</b> .....	<b>16</b>
<b>1.4.2 Indirect and Direct excitation</b> .....	<b>17</b>
<b>1.4.3 Quenching</b> .....	<b>18</b>
<b>1.5 Paramagnetic NMR spectroscopy</b> .....	<b>20</b>
<b>1.5.1 Fermi contact shift</b> .....	<b>22</b>
<b>1.5.2 Pseudocontact shift</b> .....	<b>22</b>
<b>1.6 Magnetic anisotropy</b> .....	<b>23</b>
<b>1.7 Catalysis at lanthanide centres</b> .....	<b>26</b>
<b>1.8 Aim and Scope</b> .....	<b>31</b>
<b>1.9 References</b> .....	<b>33</b>
<b>Chapter-2: Exploring the catalytic behaviour of p.DO3A complexes</b> .....	<b>40</b>
<b>2.1 Aim and scope</b> .....	<b>40</b>
<b>2.2 Ln.p.DO3A a prototype system</b> .....	<b>40</b>
<b>2.3 Previous applications and uses of p.DO3A</b> .....	<b>42</b>
<b>2.4 Synthesis of p.DO3A</b> .....	<b>43</b>
<b>2.5 Luminescence studies of Ln.p.DO3A complexes</b> .....	<b>46</b>
<b>2.5.1 Eu.p.DO3A</b> .....	<b>46</b>
<b>2.5.2 Tb.p.DO3A</b> .....	<b>56</b>
<b>2.6 Catalytic studies</b> .....	<b>61</b>

2.6.1	NMR spectroscopy studies of fluorination.....	62
2.6.2	Conclusions on catalytic studies.....	70
2.7	Summary and conclusions.....	71
2.8	References.....	73
<b>Chapter 3: Synthesis of DO3AM derivatives.....</b>		<b>76</b>
3.1	DO3AM and DOTAM complexes.....	76
3.1.1	Applications and uses of DO3AM and DOTAM.....	77
3.2	Aim and scope.....	79
3.3	Design strategy for p.DO3AM ligands.....	81
3.3.1	Selection of pendant arms.....	83
3.3.2	Initial synthetic pathway.....	88
3.3.3	Synthetic adaptation and optimisation.....	89
3.3.4	Acid-amide coupling.....	94
3.3.5	Final steps and complexation.....	97
3.3.6	Characterisation.....	100
3.4	Summary and conclusions.....	101
3.5	References.....	102
<b>Chapter-4: Photophysical studies on DO3AM derivatives.....</b>		<b>104</b>
4.1	Aim and Scope.....	104
4.2	Introduction to luminescence studies methodology.....	106
4.3	Eu.p.DO3AM.Phen.....	106
4.3.1	Eu.p.DO3AM.Phen.O'Bu.....	107
4.3.2	Eu.p.DO3AM.Phen.OMe.....	113
4.3.3	Eu.p.DO3AM.Phen.OH.....	119
4.3.4	System summary.....	123
4.4	Eu.p.DO3AM.Pro.....	124
4.4.1	Eu.p.DO3AM.Pro.O'Bu.....	125
4.4.2	Eu.p.DO3AM.Pro.OMe.....	129
4.4.3	Eu.p.DO3AM.Pro.OH.....	135
4.4.4	System summary.....	144
4.5	Eu.p.DO3AM.Lys.....	144
4.5.1	Eu.p.DO3AM.Lys.O'Bu.CBz.....	145
4.5.2	Eu.p.DO3AM.Lys.OMe.....	150
4.5.3	System summary.....	158
4.6	Conclusions.....	159

4.7	References .....	162
<b>Chapter-5: Catalytic studies on DO3AM derivatives .....</b>		<b>163</b>
5.1	Aim and Scope .....	163
5.2	Proposed catalytic route .....	164
5.3	Catalysis investigation by Multinuclear NMR spectroscopy .....	165
5.3.1	NMR spectroscopy catalysis lanthanide catalyst choice .....	167
5.4	Catalytic NMR spectroscopy methodology .....	168
5.5	Eu.p.DO3AM.Pro.OMe catalytic studies .....	169
5.6	Eu.p.DO3AM.Phen.OMe catalytic studies .....	173
5.7	Eu.p.DO3AM.Lys.OMe catalytic studies .....	177
5.8	Discussion .....	181
5.9	Conclusions .....	183
5.10	References .....	185
<b>Chapter-6: Conclusions and Future Work .....</b>		<b>186</b>
<b>Chapter-7: Experimental procedures .....</b>		<b>189</b>
7.1	Reagents and solvents .....	189
7.2	Vacuum processing, Dialysis, Centrifugation, Filtration, TLC and Column chromatography .....	190
7.3	Preparation of buffers in water .....	191
7.4	Physical Methods .....	192
7.4.1	NMR spectra .....	192
7.4.2	Mass Spectrometry .....	193
7.4.3	Luminescence spectra .....	194
7.5	Software details .....	198
7.5.1	DynaFit® .....	199
7.6	Synthesis of ligands and complexes .....	203
7.7	References .....	244
<b>Appendix .....</b>		<b>246</b>

**Abbreviations**

A	inner-sphere contribution
a.u.	arbitrary units
ACS	American Chemical Society
B	outer-sphere contribution
Boc	<i>tert</i> -butyloxycarbonyl
br	broad
CA	Contrast Agent
Calc.	calculated
CBz	Carboxybenzyl
CEST	Chemical Exchange Saturation Transfer
C <sub>J</sub>	Bleaney Constant
conc.	concentration
cycl.	cyclen ring
cyclen	1,4,7,10-tetraazacyclododecane
d	doublet
D <sub>2</sub>	Deuterium gas
DCM	Dichloromethane
DCTB	trans-2-[3-(4- <i>tert</i> -Butylphenyl)-2-methyl-2-propenylidene]malononitrile
dd	double doublet
ddd	double double doublet
dddd	double double double doublet
DIPEA	N,N-Diisopropylethylamine
DMF	N,N-Dimethylformamide
DMSO	N,N-Dimethyl sulfoxide
DO3A	2,2',2''-(1,4,7,10-tetraazacyclododecane-1,4,7-triyl)triacetic acid
DO3AM	2,2',2''-(1,4,7,10-tetraazacyclododecane-1,4,7-triyl)triacetamide
DOTA	2,2',2'',2'''-(1,4,7,10-tetraazacyclododecane-1,4,7,10-tetrayl)tetraacetic acid
DOTAM	2,2',2'',2'''-(1,4,7,10-tetraazacyclododecane-1,4,7,10-tetrayl)tetraacetamide
DOTAREM <sup>®</sup>	2-[4,7-bis(carboxylatomethyl)-10-(carboxymethyl)-1,4,7,10-tetraazacyclododec-1-yl]acetate; gadolinium(3+); (2 <i>R</i> ,3 <i>R</i> ,4 <i>R</i> ,5 <i>S</i> )-6-(methylamino)hexane-1,2,3,4,5-pentol
DOTMAM	1,4,7,10-tetrakis(methylcarbamoylmethyl)-1,4,7,10-tetraazacyclododecane
dt	double triplet
DTMA	1,4,7,10-tetrakis[(N-methylcarbamoyl)methyl]-1,4,7,10-tetraazacyclododecane
ED	Electric Dipole
eq	equivalents
ESI	Electrospray ionisation

ET	Energy Transfer
eT	electron transfer
EtOAc	Ethyl Acetate
FDA	Federal Drug administration
FLP	Frustrated Lewis Pair
<i>g</i>	Landé factor
h	hours
H <sub>2</sub>	Hydrogen gas
HATU	Hexafluorophosphate Azabenzotriazole Tetramethyl Uronium
HCl	Hydrochloric acid
HEPES	4-(2-Hydroxyethyl)piperazine-1-ethane-sulfonic acid
HOBt	Hydroxybenzotriazole
HPLC	High-performance liquid chromatography
HRMS	High-resolution mass spectrometry
Hz	Hertz
Hz	Hertz
IPA	propan-2-ol
<i>ISC</i>	intersystem crossing
IUPAC	International Union of Pure and Applied Chemistry
<i>J</i>	Coupling constant
<i>K</i> <sub>1</sub>	first binding event (constant)
<i>K</i> <sub>2</sub>	second binding event (constant)
KF	Potassium Fluoride
<i>K</i> <sub>LnL</sub>	binding strength of lanthanide to ligand
<i>K</i> <sub>ML</sub>	binding strength of metal to ligand
LIS	Lanthanide Induced Shift
Ln	Lanthanide
LRMS	Low-Resolution Mass Spectrometry
Lys	L-Lysine
m	multiplet
<i>m/z</i>	mass to charge ratio
M <sup>-1</sup>	per mole
MALDI	Matrix Assisted Laser Desorption/Ionization
MD	Magnetic Dipole
Me <sub>4</sub> TACD	1,4,7,10-tetramethyl-1,4,7,10-tetraazacyclododecane
MeCN	acetonitrile
MeOD	Deuterated Methanol
MeOH	Methanol
MgSO <sub>4</sub>	Magnesium Sulphate
MHz	megahertz
min	minutes
mL	millilitre

mM	millimolar
mol dm <sup>-3</sup>	moles per decimetre cubed
MRI	Magnetic Resonance Imaging
MS	Mass Spectrometry
ms	millisecond
NaHCO <sub>3</sub>	Sodium bicarbonate
NaOAc	Sodium Acetate
NaOH	Sodium Hydroxide
NIR	Near Infra-Red
nm	nanometer
NMR	Nuclear Magnetic Resonance
NOE	Nuclear Overhauser Effect
NSF	Nephrogenic Systemic Fibrosis
OMe	methoxy
O <sup>t</sup> Bu	<i>tert</i> -butoxy
OTf	trifluoromethane sulfonate
p.DO3A	2,2',2''-(10-(prop-2-yn-1-yl)-1,4,7,10-tetraazacyclododecane-1,4,7-triyl)triacetic acid
p.DO3AM.Lys.CBz.O <sup>t</sup> Bu	tri- <i>tert</i> -butyl 2,2',2''-((2,2',2''-(10-(prop-2-yn-1-yl)-1,4,7,10-tetraazacyclododecane-1,4,7-triyl)tris(acetyl))tris(azanediyl))(2S,2'S,2''S)-tris(6-(((benzyloxy)carbonyl)amino)hexanoate)
p.DO3AM.Lys.OH	(2S,2'S,2''S)-2,2',2''-((2,2',2''-(10-(prop-2-yn-1-yl)-1,4,7,10-tetraazacyclododecane-1,4,7-triyl)tris(acetyl))tris(azanediyl))tris(6-aminohexanoic acid)
p.DO3AM.Lys.OMe	trimethyl 2,2',2''-((2,2',2''-(10-(prop-2-yn-1-yl)-1,4,7,10-tetraazacyclododecane-1,4,7-triyl)tris(acetyl))tris(azanediyl))(2S,2'S,2''S)-tris(6-aminohexanoate)
p.DO3AM.Lys.O <sup>t</sup> Bu.OMe	trimethyl 2,2',2''-((2,2',2''-(10-(prop-2-yn-1-yl)-1,4,7,10-tetraazacyclododecane-1,4,7-triyl)tris(acetyl))tris(azanediyl))(2S,2'S,2''S)-tris(6-((( <i>tert</i> -butoxycarbonyl)amino)hexanoate)
p.DO3AM.Lys.O <sup>t</sup> Bu.O <sup>t</sup> Bu	tri- <i>tert</i> -butyl 2,2',2''-((2,2',2''-(10-(prop-2-yn-1-yl)-1,4,7,10-tetraazacyclododecane-1,4,7-triyl)tris(acetyl))tris(azanediyl))(2S,2'S,2''S)-tris(6-((( <i>tert</i> -butoxycarbonyl)amino)hexanoate)
p.DO3AM.Phen.OH	2,2',2''-((2,2',2''-(10-(prop-2-yn-1-yl)-1,4,7,10-tetraazacyclododecane-1,4,7-triyl)tris(acetyl))tris(azanediyl))tris(3-phenylpropanoic acid)
p.DO3AM.Phen.OMe	trimethyl 2,2',2''-((2,2',2''-(10-(prop-2-yn-1-yl)-1,4,7,10-tetraazacyclododecane-1,4,7-triyl)tris(acetyl))tris(azanediyl))tris(3-phenylpropanoate)
p.DO3AM.Phen.O <sup>t</sup> Bu	tri- <i>tert</i> -butyl 2,2',2''-((2,2',2''-(10-(prop-2-yn-1-yl)-1,4,7,10-tetraazacyclododecane-1,4,7-triyl)tris(acetyl))tris(azanediyl))tris(3-phenylpropanoate)

p.DO3AM.Pro.OH	(2'S,2''S)-(2,2',2''-(10-(prop-2-yn-1-yl)-1,4,7,10-tetraazacyclododecane-1,4,7-triyl)tris(acetyl))tri-L-proline
p.DO3AM.Pro.OMe	trimethyl (2,2',2''-(10-(prop-2-yn-1-yl)-1,4,7,10-tetraazacyclododecane-1,4,7-triyl)tris(acetyl))(2'S,2''S)-tri-L-prolinate
p.DO3AM.Pro.O'Bu	tri-tert-butyl (2,2',2''-(10-(prop-2-yn-1-yl)-1,4,7,10-tetraazacyclododecane-1,4,7-triyl)tris(acetyl))(2'S,2''S)-tri-L-prolinate
ParaCEST	Paramagnetic Chemical Exchange Saturation Transfer
Pd/C	Palladium on carbon
PeT	Photoelectron transfer
PET	Positron Emission Tomography
Phen	L-Phenylalanine
ppm	parts per million
Pro	L-Proline
PTFE	Polytetrafluoroethylene
$q$	number of water molecules in the inner-coordination sphere
$R_f$	Retention factor
RSC	Royal Society of Chemistry
RT	Room Temperature
s	singlet
S <sub>0</sub>	ground state singlet level
S <sub>1</sub>	excited state singlet level
SAP	Square Anti-Prismatic
S <sub>N</sub> 2	Substitution Nucleophilic Bimolecular
t	triplet
T	Temperature
T <sub>1</sub>	triplet level
TBA <sup>+</sup>	tetra-n-butyl ammonium ion
TBAF	Tetra-n-butylammonium fluoride
TBTU	2-(1H-Benzotriazole-1-yl)-1,1,3,3-tetramethylaminium tetrafluoroborate
TFA	Trifluoroacetic acid
TLC	Thin layer chromatography
TOF	Time of Flight
Tris	<i>tris</i> (hydroxymethyl)aminomethane hydrochloride
TSAP	Twisted Square AntiPrismatic
UPLC	Ultra Performance Liquid Chromatography
UV	UltraViolet
v/v	volume by volume
Vis	Visible
Z <sub>eff</sub>	effective nuclear charge
δ <sub>F</sub>	Fermi contact shift contribution

$\delta_{\text{LIS}}$	Lanthanide induced shift contribution
$\delta_{\text{pc}}$	pseudocontact shift contribution
$\lambda$	wavelength
$\lambda_{\text{em}}$	emission wavelength
$\lambda_{\text{ex}}$	excitation wavelength
$\mu_{\text{B}}$	Bohr magneton
$\tau$	lifetime



## Chapter-1: Introduction

### 1.1 General lanthanide chemistry

Lanthanide (Ln) chemistry is a field of study that rose to prominence in the 1970s, and while initial study was slow, research into them has increased greatly moving into the 21<sup>st</sup> century.<sup>1,2</sup> Initially there was difficulty associated with isolating them in their pure form, this prevented the exploration of their chemistry, but with the advent of modern separation techniques exploration into individual lanthanides became possible.<sup>3-5</sup> The use of more sophisticated chelators in solvent extraction systems has made separation more facile, while also generating a lot of interest and research into more effective chelators.<sup>6-8</sup> This separation is so difficult due to their similar ionic radii (**Figure-1.1**) and prevalence for the +3 oxidation state, giving them similar effective nuclear charges ( $Z_{\text{eff}}$ ) and hence very similar chemical reactivity in biological systems.<sup>9-11</sup>

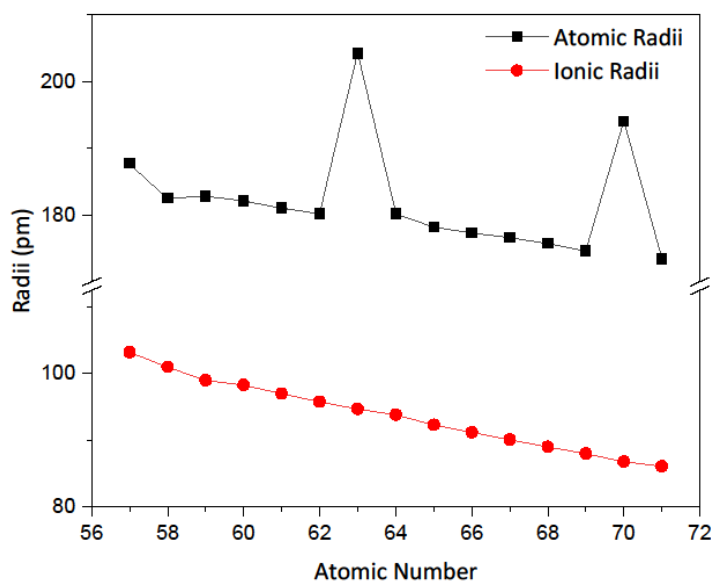


**Figure-1.1.** Graph illustrating the change in Atomic (Black) and Ionic (Ln(III)) (Red) radii of the lanthanides (lanthanum-lutetium) with increasing atomic number.

The similarity of the lanthanide series, in terms of oxidation state and reactivity is derived from the  $4f$  valence orbitals. This partial occupation of the  $4f$  orbitals has led to lanthanides also being referred to as ‘the  $4f$  elements’. The  $4f$  orbitals, in comparison to the  $5s$ ,  $5p$  and  $6s$  subshells, have a small radial extent leading the valence electrons to be deemed ‘core-like’.<sup>12</sup> This ‘core-like’ electron distribution is down to the phenomenon known as the ‘lanthanide contraction’. This effect describes the effect of the poor electron shielding of the  $4f$  orbitals, leading to the observation that the  $4d$  and  $5d$  transition metals have comparatively similar atomic radii.<sup>13</sup> This poor shielding effect means the addition of electrons into the  $4f$  orbitals does not have a profound effect on the reactivity, but instead leads to a decreasing ionic radius.<sup>14</sup> This decreased ionic radius means that the radial extent of the  $4f$  orbitals will not enable effective overlap between the  $4f$  and ligand orbitals. This results in ligand-field effects on the order of  $500\text{cm}^{-1}$  ( $6\text{ kJ mol}^{-1}$ ), much lower than the associated ligand fields for d-metal complexes. This leads to complex formation governed by steric factors rather than electronic factors.<sup>15–18</sup> While these relatively small splitting values lead to a less well defined coordination sphere in comparison to transition metal complexes, they are not negligible and cause conformational preferences in solution.<sup>19</sup> The ratio of such conformations in solution can be altered by designing ligands to yield specific coordination spheres for targeted purposes. Modification of groups on the ligands in question can give desirable effects such as solubility, rigidity and specific complex geometry.<sup>20</sup>

## 1.2 Coordination chemistry of lanthanide complexes

The coordination chemistry of the f-elements differs greatly from all other metal complexes, most notably from transition metal complexes. The low crystal field

splitting in lanthanide complexes leads to sterics being the main driving force in determining a complexes geometry. This differs greatly from the strong electronic driving force in transition metal complexes, which leads to highly organised complex geometries with high barriers to conformational interconversion. Therefore, while transition metal complex geometry would favour structures with 4-6 coordinate geometries, lanthanide complex coordination numbers can vary from 3 to 12, dependant on the steric constraints of the ligand (**Figure-1.2**).<sup>21,22</sup> This makes the conformations of lanthanide complexes difficult to predict, due to small energetic differences between conformations making interconversion very facile.

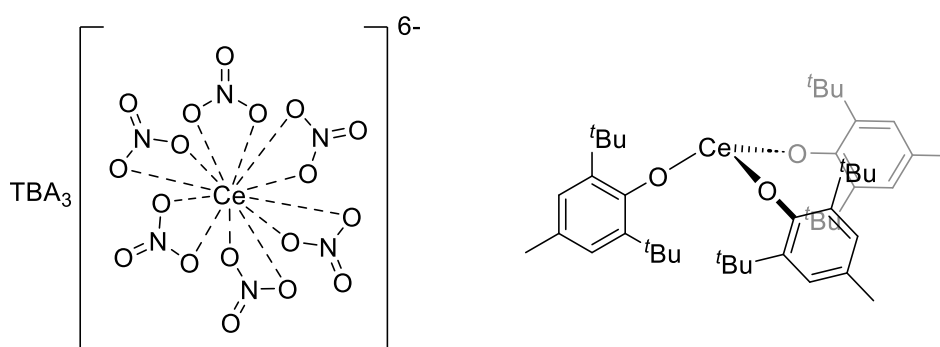


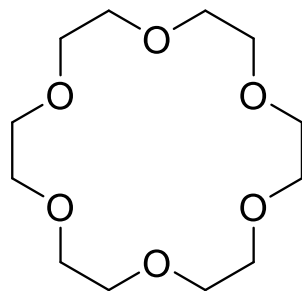
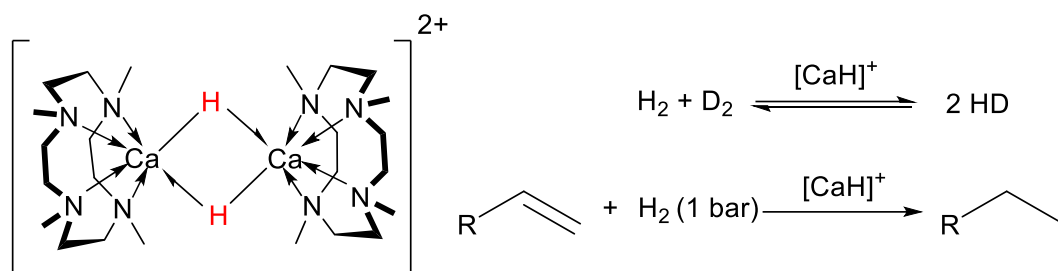
**Figure-1.2.** Structures of tetrabutylammonium hexanitrate cerium(III) (*left*) and  $[\text{Ce}(\text{OAr})_3]$  ( $\text{Ar} = 1,6\text{-}(\text{tBu})_2\text{-4-MeC}_6\text{H}_2$ ) (*right*).

As aforementioned, due to the lack of orbital overlap the interaction between the ligand and the metal is predominantly electrostatic in nature, meaning there is no overall directionality in their bonding.<sup>15,23</sup> This combination of factors along with the decreasing size of lanthanide ions from across the period, means that the earlier lanthanides favour higher coordination numbers (9-coordinate) and the later prefer lower coordination numbers (8-coordinate).<sup>2,15,24,25</sup> Overall, the lanthanides that are relatively smaller in size with a high charge density, facilitate the formation of complexes with a high coordination number. Forming many metal-ligand bonds

which is the main thermodynamic driving force. They preferentially bind with hard Lewis bases due to their own hard Lewis acidic nature.<sup>26</sup> The coordination chemistry is therefore difficult to predict in comparison to other groups in the Periodic Table, leading to an initial lack of interest, but the increasing knowledge and development of new chelators and macrocyclic ligands has caused a great amount of interest in this area.<sup>27</sup>

### 1.2.1 Macrocyclic chemistry of lanthanides

To render these complexes kinetically inert to ligand substitution, specific ligands must be used to achieve this and other desirable properties. Macrocycles offer the entropic benefits of the chelate effect and a strong degree of pre-organisation, enabling favourable binding to cations of a certain size. This pre-organisation can create cavities causing favourable binding of specific lanthanides. The preference for matching the size of the cavity with the metal ion is exemplified by the selectivity of crown ethers with group 1 metals, and by the release of steric strain upon complexation. **(Figure-1.3).**<sup>28-30</sup>



	Na <sup>+</sup>	K <sup>+</sup>	Rb <sup>+</sup>	Cs <sup>+</sup>
logK	4.42	>5.5	5.35	4.37

**Figure-1.3.** *Top:* Chemical structure of  $[Ca_2H_2(Me_4TACD)_2]^{2+}$  and its application in catalysing the HD exchange between  $H_2$  and  $D_2$  and the hydrogenation of unactivated 1-alkenes. *Bottom:* Chemical structure of 18-crown-6 with stability constants (log K) in methanol (MeOH), showing greater stability hence preference for  $K^+$  ions.

The widely studied ligand in the field of lanthanide complex chemistry is DOTA.

In combination with Gd(III), it is used as an FDA approved MRI contrast agent,

with this utility leading to further exploration of the DOTA ligand and its

derivatives (**Figure-1.4**).<sup>31,32</sup>

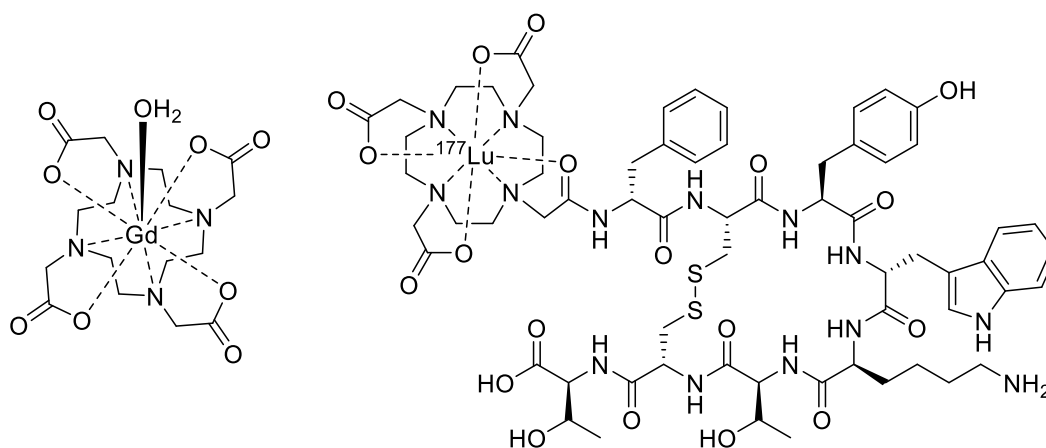


**Figure-1.4.** Chemical structures of FDA approved and commercially available MRI contrast agent DOTAREM<sup>®</sup> (*left*) and radiopharmaceutical for peptide receptor radionuclide therapy Lutathera<sup>®</sup> (*right*).<sup>31,32</sup>

This organic motif has become very valued. The nitrogen atoms on the central cyclen ring provide an ease of functionalisation, enabling extensive modification of the ligand which allows incorporation of desirable features.<sup>33–36</sup> Modifications range from sterically demanding groups to increase the energetic barrier to demetallation, to the inclusion of strongly absorbing chromophores to enable sensitisation of Ln(III) ions.<sup>37,38</sup> Polyazacarboxylate macrocyclic ligands are thus researched heavily, with their complex variants playing an increasing role in several biomedical imaging modalities.<sup>20,39–42</sup>

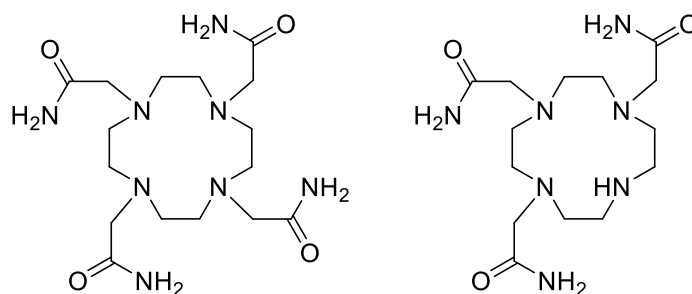


**Figure-1.5.** Structures of DOTAM (*left*) and DO3AM (*right*)

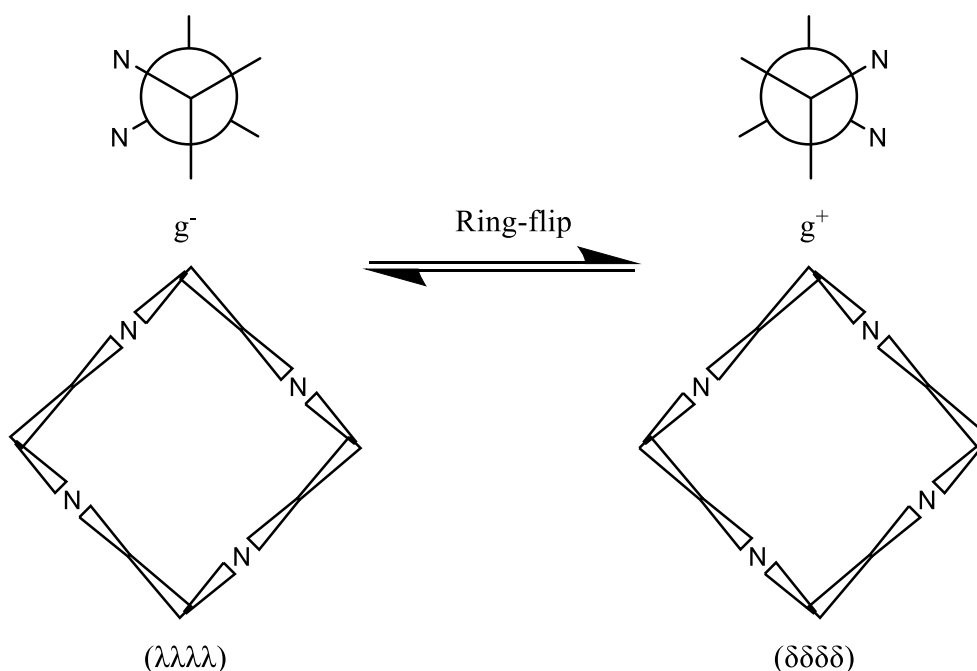
While DOTAM has seen comparatively less interest in the imaging field, the inclusion of an amide linker increases the potential for functionalisation.<sup>43,44</sup>

DOTAM is used for theranostics and drug delivery as a ligand but not as a metal complex.<sup>45,46</sup> The potential for functionalisation has seen DOTAM based Ln(III) complexes grow in popularity.<sup>45,47-49</sup> While DOTA based complexes have an overall negative charge, Ln(III) DOTAM complexes are positively charged. This positive charge has seen their investigation in numerous fields of biological chemistry including reaction catalysis and biological imaging.<sup>46,49</sup> [Ln(DOTAM)]<sup>3+</sup> complexes display similar properties to analogous [Ln(DOTA)]<sup>-</sup> complexes, however some of their physical properties differ in magnitude. The use of amides instead of acetate groups as ligands, leads to a decrease in the thermodynamic stability of these complexes, with log  $K_{ML}$  values 10-15 orders of magnitude lower than the corresponding DOTA complexes.<sup>50</sup> In opposition to this, DOTAM based complexes display a high kinetic inertness, having longer lifetimes for inner sphere water molecules than [Ln(DOTA)(H<sub>2</sub>O)]<sup>-</sup> (Eu[DOTAM]<sup>3+</sup>=1.79 ms<sup>-1</sup>), while also having lower rate constants for demetallation in Cu<sup>2+</sup> and proton assisted dissociation.<sup>50</sup> This could be due to the preformed cavity in DOTAM having a high affinity for lanthanide ions, as the hard acetate binding groups of DOTA should play an important role based on the electrostatic interactions between ligand and metal.<sup>51</sup>

### 1.2.2 Isomerism in Lanthanide complexes

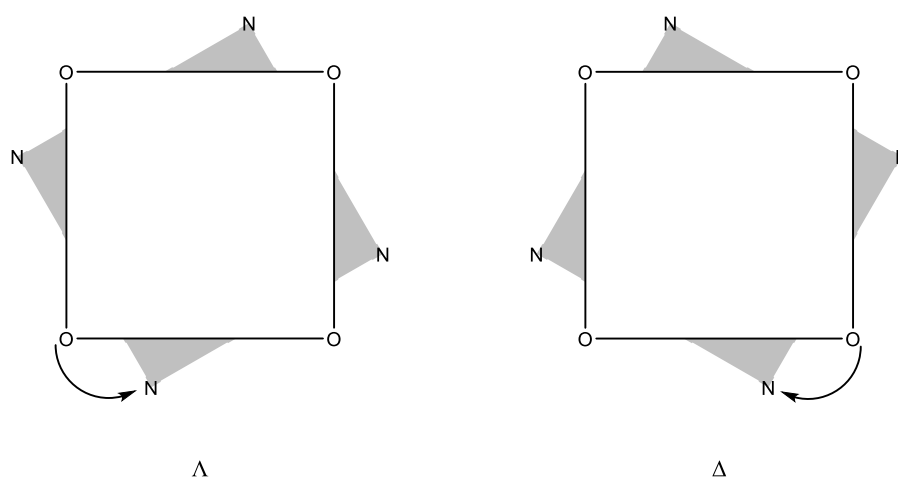
Isomerism in DOTA, DOTAM and similar cyclen based complexes has been investigated extensively.<sup>52-55</sup> This is partly due to the potential applications requiring particular conformations, such as DOTAREM<sup>®</sup> (**Figure-1.4**) requiring fast water exchange to facilitate rapid water exchange, thus favouring the Twisted-Square-Anti-Prism (TSAP) form.<sup>31,56</sup> With this TSAP form in exchange with the

Square-Anti-Prism (SAP) form, ligands must be designed to have a specific conformational preference.<sup>57,58</sup> Cyclen based complexes exist in two different forms (two pairs of enantiomers) (**Scheme-1.1**).



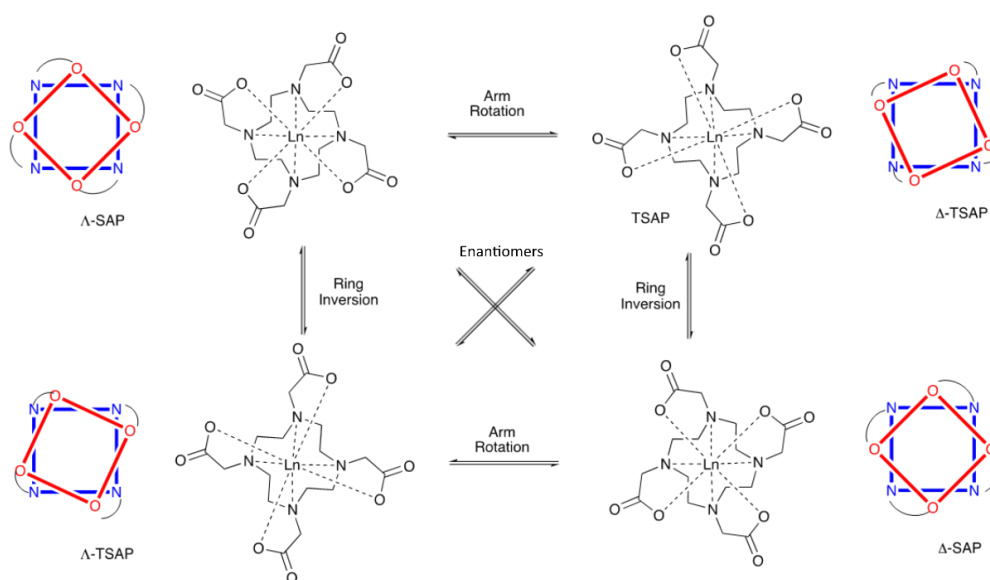
**Scheme-1.1.**  $g^-/g^+$  ring conformations<sup>57</sup>

All cyclen based ligands have good conformational freedom when in solution. Upon complexation to a Ln(III) ion, only the [3.3.3.3] conformation is possible.<sup>55</sup> [3.3.3.3] denotes the four straight segments of three bonds. The geometry of the N-C-C-N moieties renders only two possible enantiomers.<sup>54</sup> Switching between these two enantiomers requires an inversion of the ring, commonly called a 'ring-flip'. The pendant arms bearing the donor groups in both tetra and tri-substituted cyclen, must also all lean the same way due to steric repulsion between the neighbouring arms. The concerted arrangement describes either a positive (clockwise) or negative (anti-clockwise) N-C-C-O dihedral angle, giving rise to  $\Delta$  and  $\Lambda$  forms of each enantiomer (**Scheme-1.2**).<sup>52,57,58</sup>



**Scheme-1.2.**  $\Delta$  and  $\Lambda$  metal coordination modes.

These two conformational chirality elements ( $\Delta/\Lambda$  and  $(\lambda\lambda\lambda\lambda)/(\delta\delta\delta\delta)$ ) covering the macrocycle and side-arms combined provide four stereoisomers. This comprises two pair of enantiomers and the remaining relationships being diastereomeric (**Scheme-1.3**).

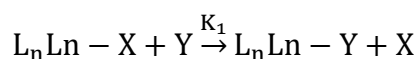


**Scheme-1.3.** Illustrations of the possible diastereoisomers in DOTA, detailing the orientation of the macrocycle and pendant arms, along with the interconversion between isomers.

Conformational preference of DOTA-like complexes is also affected by the identity of the Ln(III) used, with earlier lanthanides (La(III)-Pm(III)) favouring TSAP, and later lanthanides (Sm(III)-Lu(III)) favouring the SAP geometry.<sup>59</sup> Exchanging DOTA for DO3A decreases the energetic barrier to arm rotation, meaning that on the NMR timescale this interconversion is faster, thus broadening peaks within the NMR spectrum (Eu(III) chemical shifts; TSAP  $\approx$  30-40 ppm, SAP  $\approx$  15-20 ppm).<sup>60,61</sup>

### 1.3 Thermodynamic vs kinetic stability

When referring to the stability of complexes, traditionally the thermodynamic stability is enough to justify whether a complex is stable for the associated use e.g. *in vivo* applications. For use in solution, this definition is inappropriate: transition metal complexes exhibit very high thermodynamic stabilities as do lanthanide complexes.<sup>62</sup> While hexa-aquo transition metal complexes show variation in their kinetic lability, hydrated lanthanide complexes all have very high ligand exchange rates.<sup>63</sup> A new definition for stability must be employed to quantify this. Ligand lability as detailed in **Equation-1.1** can be used to describe the inner solvation sphere. This is important for lanthanide complex applications, making tailoring of the rate of exchange a priority.<sup>64</sup>



**Equation-1.1.** equilibria detailing the exchange of ligand *X* with ligand *Y* at a complexed lanthanide centre ( $L_nLn$ ), with equilibrium defined by equilibrium constant  $K_1$ .

#### 1.3.1 Thermodynamic stability

The thermodynamic stability of these complexes is of importance but does not describe the full picture of the complex in question. Thermodynamic stability is

defined as the stability constant in a complex equilibrium formation ( $\log K_{ML}$ ), with the value detailing a ligands affinity for the metal ion in question (**Equation-1.2**).<sup>65</sup>



**Equation-1.2.** Complex formation between a Ln(III) ion and a ligand ( $L$ ), with  $K_{LnL}$  detailing the affinity of Ln(III) for a given ligand.

$K_{LnL}$  alone does not provide the full picture, the value of  $K_{LnL}$  mentions the relative activities of complex  $LnL$  against free  $Ln$  and  $L$ . A high value of  $K_{ML}$  indicates that  $L$  binds more strongly than the previous ligand, enabling comparison of the binding strength of different ligands. Quantification of the thermodynamic selectivity between metal ions is also possible, this being the difference between the  $\log K_{ML}$  values (**Equation-1.3**).<sup>66</sup>

$$\Delta \log K_{Ln/M} = \Delta \log K_{LnL} - \Delta \log K_{ML}$$

**Equation-1.3.** Logarithmic operation defining thermodynamic selectivity for Ln(III) ion in comparison to another metal ion (M). Positive value indicating preference for Ln(III), negative indicating a preference for M.

With the sequential difference between lanthanides being small, this is of particular interest. With these methods of quantification, the labels ‘stable’ and ‘unstable’ refer to the energy change that occurs in complex formation, specifically the Gibbs free energy change (**Equation-1.4**).

$$\Delta G = \Delta H - T\Delta S = -RT \ln K$$

**Equation-1.4.** Gibbs free energy change ( $\Delta G$ ) as a function of the entropy change ( $\Delta S$ ) and enthalpy change ( $\Delta H$ ) or of the equilibrium constant ( $K$ ).

A negative value of  $\Delta G$  would indicate a stable complex and a positive value an unstable complex. However, this does not provide any kinetic information about

this reaction. Another definition is needed if ligand exchange is to be correctly explored and interpreted.<sup>67,68</sup>

However, despite the appeal of using affinity constants to assess the stability of a complex, it needs to be borne in mind that these numbers reflect thermodynamic equilibria. As such, the central tenet of establishing a binding constant is that an equilibrium can be established between free and bound metal ions. In many cases where polydentate macrocyclic ligands are used, this is emphatically not true over a normal experimental timescale. Furthermore, in cases where equilibrium is established, the low solubility of many lanthanide salts can mean that kinetic traps exist *in vivo* that can remove metals from the mixture. In a clinical context this lability can constitute a real problem, leading to serious side effects and nephrogenic systemic fibrosis (NSF), as demonstrated for Gd(III) MRI contrast agents in renally impaired patients.<sup>69</sup> Both extremes illustrate the importance of considering kinetic rather than thermodynamic stability, as will be discussed next.

### 1.3.2 Kinetic stability

While thermodynamic stability details the feasibility of a reaction and the stability of the resulting complex, kinetic stability details the complexes' ability to undergo ligand substitution, specifically the speed at which it occurs.<sup>20</sup> The terms 'labile' and 'inert' are used to describe ligand exchange reactions that occur quickly and slowly respectively. In labile complexes the rate of ligand substitution is high.<sup>70</sup> While in inert complexes, even if they are thermodynamically unstable, the rate of reaction is so low that substitution will not occur unless excessive time or forcing conditions are used (**Table-1.1**).<sup>20</sup>

**Table-1.1.** Comparison of the thermodynamic and kinetic parameters describing the stability of [Eu.DOTA]<sup>-</sup> and [Eu.DOTAM]<sup>3+</sup> (**Figure-1.6**). Where  $K$  is the association constant in,  $k_0$  is the rate of spontaneous dissociation,  $k_1$  rate of dissociation of mono protonated species, and  $k_1[\text{H}^+]$  is the rate of protonation at varying pH.

Complex	$K$ ( $\text{M}^{-1}$ )	$k_0$ , $\text{s}^{-1}$	$k_1$ , $\text{s}^{-1}\text{M}^{-1}$	$k_1[\text{H}^+]$ at pH = 7	$k_1[\text{H}^+]$ at pH = 1
[Eu.DOTA] <sup>-*</sup>	$10^{23.6}$	$<5 \times 10^{-8}$	$5 \times 10^{-6}$	$5 \times 10^{-13}$	$5 \times 10^{-7}$
[Eu.DOTAM] <sup>3+<sup>#</sup></sup>	$10^{13.7}$	$1.5 \times 10^{-7}$	$5.6 \times 10^{-7}$	$5.6 \times 10^{-14}$	$5.6 \times 10^{-8}$

\*Values taken from the averages of references.<sup>71-73</sup>  
<sup>#</sup>Values taken from reference.<sup>74</sup>

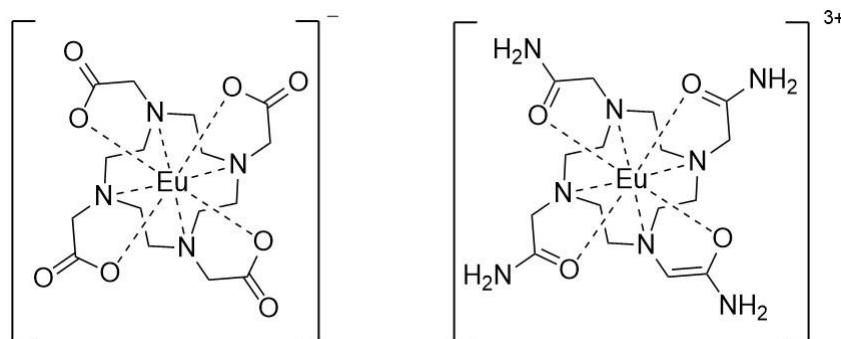


**Figure-1.6.** Chemical structures of [Eu.DOTA]<sup>-</sup> (*left*) and [Eu.DOTAM]<sup>3+</sup> (*right*).

Thermodynamic and kinetic stability are related to one another, but it is still necessary to describe them using separate terms. These stabilities can run parallel to one another, but they often differ (**Table-1.2**).<sup>75</sup>

**Table-1.2.** Detailing the basic details between thermodynamic and kinetic stability.<sup>50,76</sup>

	Thermodynamic	Kinetic
<b>Definition</b>	The tendency to exist under equilibrium conditions.	The speciation of complexes in solution.
<b>Quantifiable values</b>	Equilibrium constants	Rate of dissociation
<b>Classification</b>	Stable/Unstable	Labile/Inert

What this table shows is that there is great variability in both definitions of stability.

Therefore, in a set of elements with high kinetic lability in their hydrated form in

solution, such as that of the lanthanides, enforcing kinetic stability is of paramount importance if they are to be functionalised effectively.

#### 1.4 Photophysics of lanthanides

The lanthanides in their +3 oxidation state with unpaired electrons (all lanthanides covered in this thesis are +3) each exhibit their own characteristic absorption and emission spectra, arising from the specific electronic transitions within their manifold of  $^{2S+1}L_J$  states.<sup>77,78</sup> Lanthanides may ‘luminesce’ in two distinct ways; fluorescence ( $\Delta S = 0$ , lifetime order of  $10^{-7}$  s) and phosphorescence ( $\Delta S \neq 0$ , lifetimes range between  $10^{-6}$  and 1 s).<sup>79</sup> In combination these two processes detail lanthanide luminescence, with the vast majority of these transitions involving a change in spin.<sup>80</sup>

Due to the large number of microstates resulting from the  $^{2S+1}L_J$  manifold, absorption and emission spectra show more peaks in comparison to d-block metals.<sup>81</sup> With the associated difference in wavelengths being related to the energetic gaps between these electronic microstates, unique to each lanthanide (**Figure-1.7**).<sup>82,83</sup>

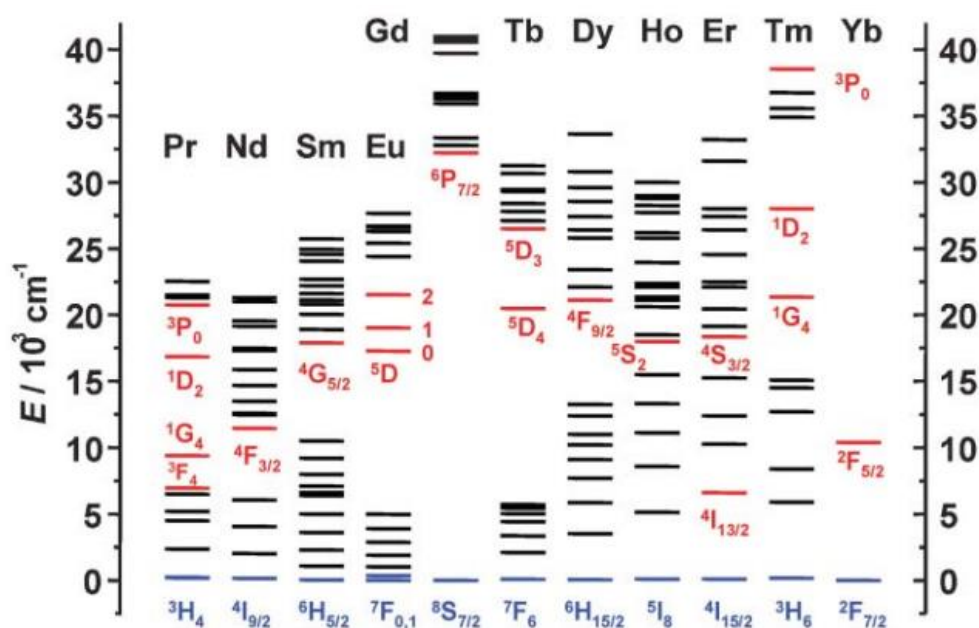


**Figure-1.7.** Partial energy level diagrams for the lanthanide aquo ions, with main luminescent levels (red) and fundamental levels (blue), taken from reference.<sup>84</sup>

Some of the transitions within Ln(III) ions are deemed hypersensitive transitions.<sup>85</sup>

The form/shape and intensity of these transitions is highly dependent on the local coordination environment, making interpretation of these peaks useful in determining changes at the Ln(III) centre.<sup>86,87</sup> These are sensitive to external factors such as pH, local site symmetry, temperature and chelators (along with dependence on the nature of the chelator in question).<sup>84,88</sup> While several explanations have been proposed for this the most successful, proposed by Mason *et al.*<sup>89</sup> details a dynamic coupling mechanism where the intensity of the hypersensitive transitions arises from the induced electric dipoles in the ligands by the transition quadrupole moment of the metal ion. Thus, meaning they obey the selection rules, covering ‘electric quadrupoles’.<sup>90</sup> Through this research these hypersensitive transitions have been exploited as a spectroscopic probe to detail the solution phase interactions of lanthanides with an assortment of ligands (Table-1.2).<sup>91</sup>

**Table-1.2.** Selected hypersensitive transitions of the Ln(III) ions observed in absorption and emission spectra.\*

Ln(III) ion	Transition	Approx. Wavelength (nm)
Sm	${}^4F_{1/2}, {}^4F_{3/2} \rightarrow {}^6H_{5/2}$	1560
	${}^4G_{5/2} \rightarrow {}^6H_{5/2}$	560
Eu	${}^5D_2 \rightarrow {}^7F_0$	465
	<b><math>{}^5D_1 \rightarrow {}^7F_1</math></b>	<b>535</b>
	<b><math>{}^5D_0 \rightarrow {}^7F_2</math></b>	<b>613</b>
Gd	${}^6P_{5/2}, {}^6P_{5/2} \rightarrow {}^8S_{7/2}$	308
Dy	${}^6F_{11/2} \rightarrow {}^6H_{15/2}$	1300
	${}^4G_{11/2}, {}^4I_{15/2} \rightarrow {}^6H_{15/2}$	427
Ho	${}^3H_6 \rightarrow {}^5I_8$	361
	${}^5G_6 \rightarrow {}^5I_8$	452

---

\* The highlighted transitions are extensively studied in this thesis

### 1.4.1 Selection rules

The  $f$ - $f$  transitions detailed above (**Table-1.2**) are governed by the Laporte selection rule which states that for an electronic transition to be allowed, the parity between the final and initial states must change.<sup>89,90</sup> Due to the partially forbidden nature of these transitions, arising from there being no change in parity, these transitions have low absorption coefficients and hence low intensity spectra in the visible region of the electromagnetic spectrum.<sup>92</sup> The long luminescence lifetimes of lanthanides arise from this also, with lower transition probabilities, resulting in long-lived excited states.<sup>93</sup> This makes the use of time-gated or time-resolved techniques particularly advantageous, allowing separation of the desired signal from background fluorescence, through the use of a delay time after an initial excitation pulse.<sup>94</sup>

## 1.4.2 Indirect and Direct excitation

To circumvent the low probability of direct excitation, indirect excitation through ‘antenna’ has been extensively used.<sup>95–97</sup> A chromophore is appended to the Ln(III) ion by ligation to the metal centre (**Figure-1.8**). Suitability of this chromophore is determined by the degree of overlap and energetic match with the lanthanide *f*-orbitals.<sup>96</sup> This occurs via the chromophore absorbing a photon and forming an excited singlet state, undergoing intersystem crossing to form a triplet, which then energy transfers to the lanthanide using a Förster or Dexter mechanism.<sup>98,99</sup> While direct chromophore singlet to lanthanide singlet energy transfer has been observed it is not the predominant pathway.

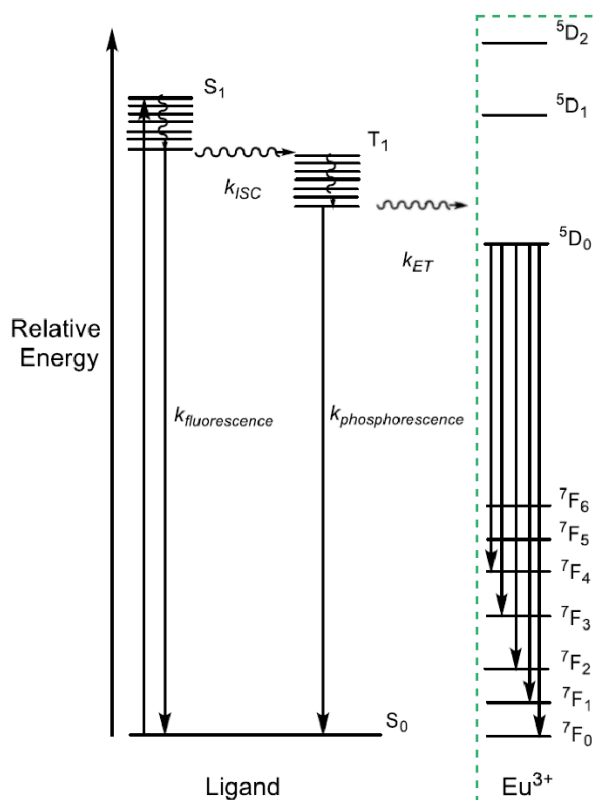


**Figure-1.8.** Simplified Jablonski diagram for a Eu(III) complex with an appended chromophore and associated transitions. Electronic transitions highlighted (green) investigated extensively in this thesis via direct excitation. *ISC*, intersystem crossing; *ET*, energy transfer.

These luminescing moieties often necessitate inclusion of aromatic groups or groups deemed undesirable for the purposes of this thesis, making indirect excitation only possible for one complex (detailed in chapter-2). Lack of a suitable chromophore necessitates a return to direct excitation of the Ln(III) ion, for all other luminescence measurements taken within this thesis. Therefore, due to a lack of signal strength due to the inefficiency of direct as opposed to indirect excitation, higher concentrations of Ln(III) complex must be used to create a strong signal. For the purpose of luminescence Eu(III) and Tb(III) are good candidates due to their high quantum yields and detectable visible range emissions.<sup>93,100</sup> Where the quantum yield ( $\Phi$ ) is the ratio of absorbed to emitted photons (between 0 and 1 for systems in which a single photon is emitted from the excited state).

### 1.4.3 Quenching

Quenching of lanthanide excited states can occur in multiple ways.<sup>101</sup> Most apparent is luminescence by emission of a photon. Vibrational quenching is a process which predominates when small molecule oscillators in the coordination sphere, typically O-H or N-H bonds, facilitate non-radiative energy loss thus quenching the excited state.<sup>102</sup> This is another reason to encapsulate Ln(III) ions in polydentate ligands, to hinder the approach of quenching species.<sup>103</sup> Observation of the deactivation processes can also provide relevant structural information. From these deactivation processes further information about the speciation of the complex under investigation in solution can be gained (**Equation-1.5**).<sup>104,105</sup>

$$k_{\text{obs}} \equiv k^{\text{r}} + \sum_{\text{n}} k_{\text{n}}^{\text{nr}} \equiv \sum_{\text{i}} k_{\text{i}}^{\text{vibr}} (\text{T}) + \sum_{\text{j}} k_{\text{j}}^{\text{pet}} (\text{T}) \sum_{\text{k}} k'_{\text{k}}^{\text{nr}}$$

**Equation-1.5.** Overall deactivation rate constant ( $k_{\text{obs}}$ , inversely proportional to the observed lifetime) represented as the sum of radiative ( $k_{\text{r}}$ ) and non-radiative ( $k_{\text{nr}}$ ) rate constants. Non-radiative rate constants being the sum of vibrational ( $k_{\text{i}}^{\text{vibr}}$ ), photoinduced-electron transfer ( $k_{\text{j}}^{\text{pet}}$ ) (PeT) and other minor processes ( $k'_{\text{k}}^{\text{nr}}$ ).

The hydration number ( $q$ ) describes the number of solvent molecules in the Ln(III) ions first coordination sphere, calculated using the modified Horrocks equation (**Equation-1.6**).<sup>106</sup>

$$q = A(k_{\text{OH}} - k_{\text{OD}} - B)$$

**Equation-1.6.** Modified Horrocks equation, where  $q$  is the hydration number, A is a proportionality constant detailing the sensitivity of each Ln to O-H vibronic quenching, B represents additional sources of quenching in the outer-sphere.

While originally only made to measure hydration numbers in water, it was further modified by Parker *et al.*<sup>102</sup> to include MeOH and deuterated methanol (MeOD). The equation assumes that O-D oscillators have a negligible contribution to vibrational relaxation. Therefore, this equation can be simplified to **Equation-1.7** and in combination with values for factors A and B (**Table-1.3**), can calculate the hydration number for a range of Ln(III) complexes.

**Table-1.3.** Parameters for determination of  $q$  for Eu(III) complexes,  $\eta_{\text{OH}}$  represents the number of O-H oscillators present and  $\eta_{\text{CONH}}$  represents the number of amide oscillators present.<sup>102</sup>

Lanthanide	Solvent	A (ms)*	B (ms)*
Eu(III)	water	1.2	$0.25 + 0.44\eta_{\text{OH}} + 0.075\eta_{\text{CONH}}$
	MeOH	2.4	$0.125 + 0.44\eta_{\text{OH}} + 0.075\eta_{\text{CONH}}$

\* A = inner-sphere contribution, B = outer sphere contribution. A and B are determined using a series of complexes of known  $q$  value from X-ray crystal structures

$$q = A \left( \frac{1}{\tau_{\text{H}_2\text{O}}^{\text{obs}}} - \frac{1}{\tau_{\text{D}_2\text{O}}^{\text{obs}}} - B \right)$$

**Equation-1.7.** Simplified Horrocks equation allowing calculation of hydration numbers from observed lifetime data.

This equation gives good results for complexes with fewer than three bound water molecules.<sup>107</sup>  $q$  is rarely an integer, due to  $A$  and  $B$  being averaged across all previous crystallographic data. Variations of the Ln-O distance are amplified due to the through-space dependency of quenching ( $r^{-6}$ ).<sup>104,105</sup> While the number of assumptions and inherent errors means this equation loses its utility in multimetallic systems, for the purposes of this thesis and wider research into mononuclear complexes it remains regularly used.<sup>107,108</sup>

## 1.5 Paramagnetic NMR spectroscopy

NMR spectroscopy is one of the most widely used spectroscopic techniques, providing highly accurate information on both local and neighbouring chemical environments with atomic resolution.<sup>109</sup> For extended structural information, the nuclear Overhauser effect (NOE) is one of the most useful techniques.<sup>110</sup> The ‘Overhauser effect’ also known as ‘dynamic nuclear polarisation’, is the observed change in the integrated intensity of an NMR spectroscopy resonance when the sample is irradiated with a specific radio-frequency corresponding to another NMR spectroscopy resonance.<sup>111</sup> The observed change in resonance corresponds to the distance from the specific nuclei being irradiated.<sup>112</sup> This observation of the dipolar interactions within a molecules local environment allows determination of internuclear distances. This effect becomes especially pronounced in molecules containing paramagnets.<sup>113</sup> Unpaired electron spins have considerably larger magnetic moments, roughly 658 times that of a proton nucleus.<sup>109</sup> The ease of

detection and ability to generate long-range structural information (100 Å) from the paramagnetic centre, made this the key method in structural determination of proteins and biomolecules.<sup>114</sup>

All Ln(III) ions, with the exception of La(III) and Lu(III), are paramagnetic due to the presence of unpaired electrons in their valence shell.<sup>115</sup> The interaction of the unpaired electrons with NMR active nuclei affects the spectra, the spectral change has been referred to as the Lanthanide Induced Shift (LIS). The interaction between these spins can cause large chemical shift changes ( $\delta$ ), substantial broadening of the resonances is also possible, making the interpretation of conventional  $^1\text{H}$  NMR impossible due to being impossible to resolve in comparison to the surrounding nuclei.<sup>116</sup> In comparison to paramagnetic transition metals, lanthanides always result in shifted NMR spectra. In transition metal complexes due to the extensive orbital overlap between metal and ligand, electron spin pairing leads to complexes with paramagnetic electron configurations being diamagnetic.<sup>117</sup> With Ln complexes, due to the minimal covalency involved in their complexes, this effect persists upon complexation. Making manipulation of the LIS a powerful tool in structural elucidation.<sup>43,118</sup> The chemical shift observed is a result of through-space or through-bond interactions, resulting in the equation describing the LIS being split into two parts. These two parts being the Fermi contact shift (through-bond) and the psudeocontact shift (through-space) (**Equation-1.8**).<sup>119,120</sup>

$$\delta_{\text{LIS}} = \delta_{\text{F}} + \delta_{\text{pc}}$$

**Equation-1.8.** The components the lanthanide induced shift ( $\delta_{\text{LIS}}$ ) as a combination of the Fermi-contact shift contribution ( $\delta_{\text{F}}$ ) and the pseudocontact shift contribution ( $\delta_{\text{pc}}$ ).

### 1.5.1 Fermi contact shift

The contact shift arises from the interaction and transmission of residual electron spin from lanthanide-based *f*-orbitals, through bonds, to the observed NMR active nucleus.<sup>121</sup> The magnitude of this shift depends on multiple factors such as the number and length of separating bonds, the identity of the observed nucleus and the spatial orientation of the bonds and nuclei.<sup>122</sup> In transition metal complexes this effect is very pronounced due to the high degree of covalency. The extensive overlap between orbitals means this transmission is the most effective and hence predominant mechanism. Due to the emphasis on orbital overlap within this interaction, in lanthanide complexes this interaction is assumed to be negligible due to the poor radial extent of the 4*f*-orbitals thus minimal covalency.

### 1.5.2 Pseudocontact shift

The predominant effect on the NMR of paramagnetic lanthanide complexes arises from the pseudocontact or ‘through-space’ interaction.<sup>119</sup> This effect arises from the interaction of the unpaired electron spins on the paramagnet and the nuclear spin of the observed nuclei. This dipolar interaction is observable over much larger distances, their independence from bonds and bond angles, renders easily interpretable information for spatial determination (**Equations-1.9,1.10**).<sup>123,124</sup>

$$\delta_{pc} = \frac{C_J \mu_B^2}{60(kT)^2} \left[ \frac{(3 \cos^2 \theta - 1) B_0^2}{r^3} + \frac{(\sin^2 \theta \cos 2\varphi) B_2^2}{r^3} \right]$$

**Equation-1.9.** Pseudocontact shift contribution ( $\delta_{pc}$ ) to the chemical shift is quantified by Bleaney, as a combination of the nuclear coordinates ( $\{r, \theta, \psi\}$  spherical polar coordinates),  $\mu_B$  the Bohr magneton, parameters are second order ligand field parameters (dependant on local symmetry and polarisability where  $n = 0, 2$ ) and the Bleaney constant ( $C_J$ ) quantified in (**Equation-1.10**).

$$C_J = g^2 J(J+1)(2J-1)(2J+3) \langle J | \alpha | J \rangle$$

**Equation-1.10.** Bleaney constant ( $C_J$ ) as a result of the Landé factor ( $g$ ), with  ${}^3J_{HH}$  terms marking the Bleaney constant as unique to each Ln ion.

The values gained from this equation can be used to interpret the magnetic field distribution around the central metal ion, quantifying both the sign and the magnitude at points around the ion. While this equation is useful for rough calculations, the assumptions inherent to the equation limit its use for in depth study.<sup>125</sup> The main assumption is that the ligand field splitting is less than  $kT$ , yet there are an increasing number of complexes with splitting greater than  $kT$ . This invalidates **Equation-1.9** as it relies upon a well isolated ground state, where the overall splitting of the ground multiplet  ${}^3J_{HH}$  state is smaller than  $kT$ . Even at room temperature, the value of  $kT$  is exceeded by the ligand field splitting in many complexes, with **Equation-1.9**'s predicted trends being invalidated by many isostructural lanthanide complex series.<sup>125</sup> While this theory provides a rough guide, its limitations make it unreliable for very similar complexes with high degrees of symmetry and completely inaccurate for asymmetrical complexes. This rough idea is somewhat useful, yet for more in depth analysis of the magnetic field distribution around the lanthanide ion, more sensitive techniques are needed.

## 1.6 Magnetic anisotropy

In Bleaney, Landé and van Vleck's approximations to address lanthanide paramagnetism, many of the above-mentioned limitations continue to make these theories inaccurate for application to Ln complexes.<sup>126,127</sup> These theories assume independence of notable ligand field splitting values, yet it has been proven extensively that not only are these non-negligible but the ligand field splitting can

be quite large ( $\sim 1500 \text{ cm}^{-1}$ ).<sup>128,129</sup> In most cases the ligand field splitting is still a small effect, yet it does still affect the distribution of  $m_J$  states around the lanthanide centre thus affecting the population of these states. Sievers *et al.*<sup>130</sup> initially, followed by Long *et al.*<sup>131</sup> generated pictorial representations of the lowest occupied  $m_J$  states for the lowest  $^3J_{HH}$  states of the Ln(III) free ions.

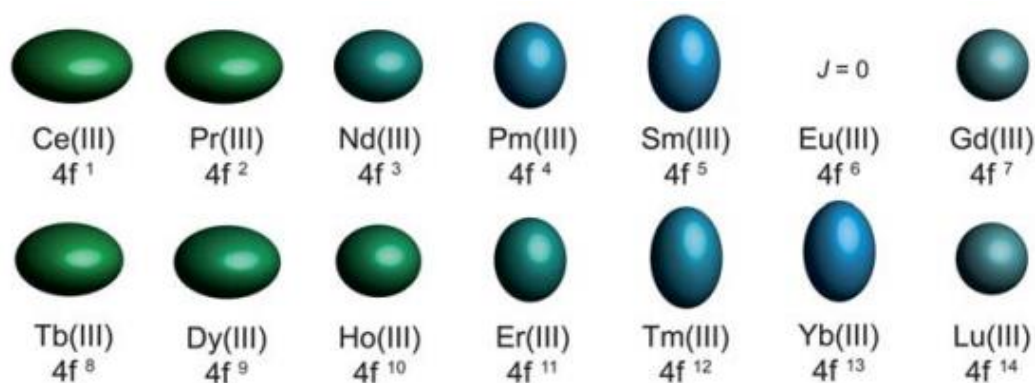


**Figure-1.9.** Pictorial representations of the lowest occupied  $m_J$  state for the lowest  $^3J_{HH}$  states of the free Ln(III) ions. Showing the prevalence for oblate (principal axis in the easy plane, *left*) in certain ions and prolate (aligned with the magnetic easy axis, *right*). Taken from reference.<sup>131</sup>

Additionally the thermal population of low-lying  $m_J$  states must be accounted for, with the ordering of these states affected by the ligand field, changes in local coordination environments can skew relative populations in each  $m_J$  state.<sup>132</sup> Many factors can affect the exact anisotropy of a complex, such as coordination environment, donor set, temperature.<sup>133</sup> Of great importance for this thesis is the anisotropic change on the binding of anionic guests, with this having the potential to cause great change in the distribution around the Ln(III) centre (**Figure-1.10**).

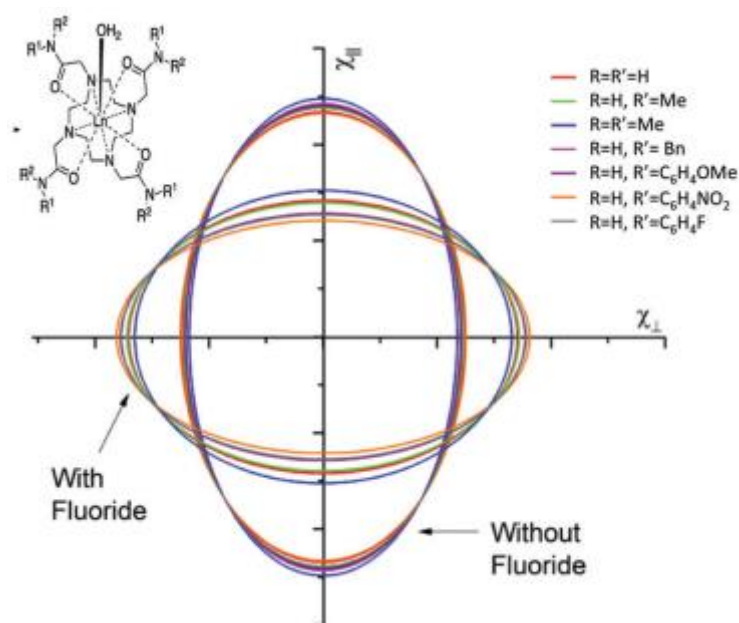


**Figure-1.10.** Representation of the variation in observed magnetic anisotropy for a series of Yb(III) complexes based on a DOTAM framework, in the presence and absence of fluoride. Taken from reference.<sup>134</sup>

Anion binding causing local magnetic fields to change, or in extremes ‘flip’, shows the importance local magnetic field have. Opening up new avenues for anion detection.<sup>135</sup> This also shows the importance of the aforementioned ligand field splitting in determining  $m_J$  states. Previously this was believed to be independent of the ligand, only depending on the Ln(III) identity, with these constants tabulated in the literature.<sup>136</sup> However, while this does work for some experimental observations, it does not fit with a growing number of observed Ln(III) complexes. With this being proven to not apply to isostructural Ln(III) complexes, showing the serious limitations inherent within this original theory.<sup>125</sup> This prompts further investigation into the field of anion recognition and selective binding, with probing the anisotropic distribution around a Ln(III) centre with various methodologies, widely regarded as one of the best methods for structural elucidation.

## 1.7 Catalysis at lanthanide centres

Lanthanides have seen great utility in the field of catalysis, with two prevalent uses being catalytic cracking and petroleum refining.<sup>137</sup> This has prompted further research into alternative methods of use where they range from being the majority to the minority component in the catalysts employed. The catalysts range from plain oxides to complex organometallics, with the more advanced catalysts being capable of stereoselectivity.

There are several reactions that can be catalysed by lanthanide oxides alone, primarily concerning the oxidative ability of Ce(IV). Cerium carboxylates have seen wide use as smoke suppressants, forming very small lanthanide oxide particles and catalysing the oxidation of soot and carbon monoxide to CO<sub>2</sub> in the combustion chamber (**Figure-1.11**).<sup>138</sup> Lanthanide oxides act to support the catalysts already used in these reactions, particularly to influence oxygenate production.

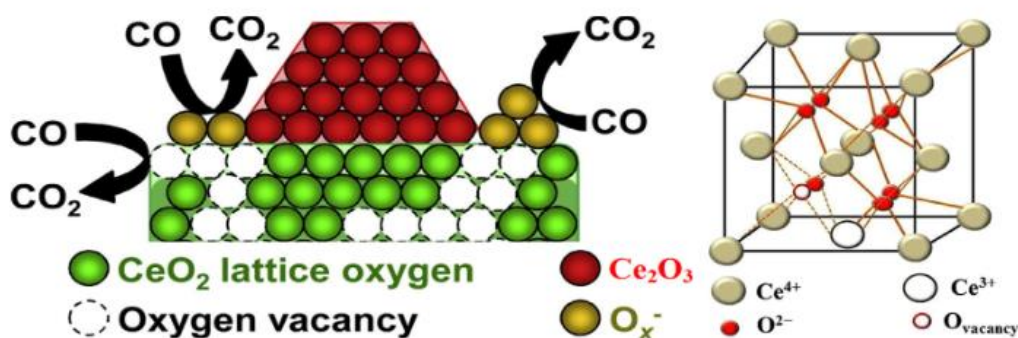


**Figure-1.11.** Conversion of CO into CO<sub>2</sub> by ceria oxide lattice oxygen, figure from reference.<sup>138</sup>

Other catalysts seek to make use of the unique size and ionic charge around Ln(III) ions. Their inclusion in perovskite-like structures stabilises these structures.<sup>139</sup> In catalysts such as zeolites or aluminosilicates, lanthanides are doped into these structures to stabilise them against the high temperature environments; stabilising

these structures prevents their thermal degradation and hence sintering of the catalysts (**Figure-1.12**). Most exhaust catalysts use ceramic monoliths which lanthanides form an essential part of. In alumina-based structures they serve to prevent degradation of high surface area gamma-alumina to low surface area alpha-alumina. While these compounds work well as catalysts within their area, they cannot be said to create any of their products selectively.

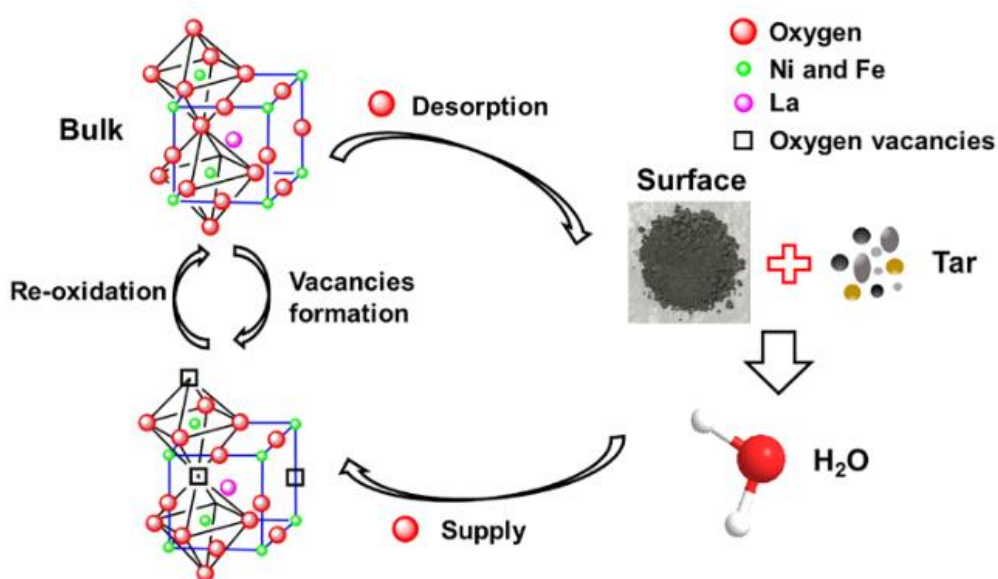


**Figure-1.12.** Hypothesised oxygen transition cycle during tar cracking over fresh  $\text{LaNi}_{1-x}\text{Fe}_x\text{O}_3$  catalyst, figure from reference.<sup>140</sup>

Lanthanides have also been a key part in non-oxide systems. Development of complexes that can catalyse specific reactions through the formation of temporary Ln-C or Ln-H bonds has seen much interest. This has resulted in the creation of highly active and homogeneous polymerisation catalysts along with other applications. The large size, coordination number and non-directionality in bonding is made use of, facilitating many different reaction geometries.<sup>141</sup> This can be achieved due to the low energy barrier to conformational interchange, allowing lanthanides to act as a template for catalytic reactions to take place upon. These

reactions vary greatly from coordination rearrangements, reductions and some catalysts being stereoselective (**Figure-1.13**). In comparison to other catalysts lanthanides have several desirable qualities, their hydrophilic behaviour enables the use of aqueous media as a solvent in these reactions. This negates the use of organic solvents which other Lewis acidic catalysts would require, making Ln based catalysts an attractive option as they are deemed more 'green'.<sup>142,143</sup>

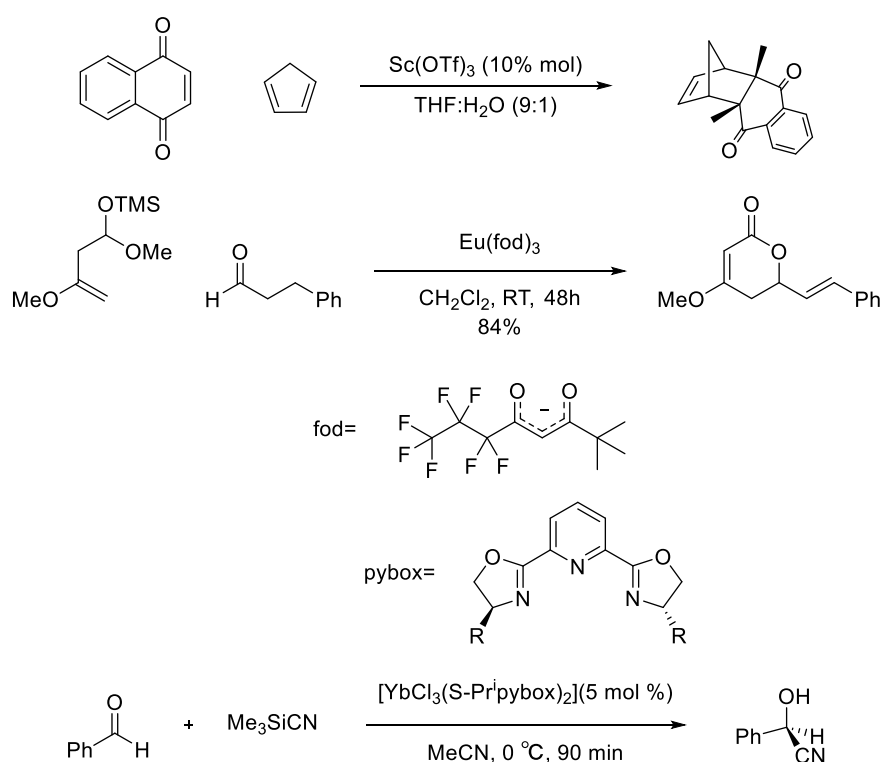


**Figure-1.13.** Figure depicting lanthanides in catalytic roles. *Top*: Reaction of naphthoquinone with cyclopentadiene in a stereoselective Diels-Alder reaction in aqueous media, recreated from reference.<sup>141</sup> *Middle*: Cycloaddition of 1,3-dimethoxy-1-trisilyloxybutadiene to cinnamaldehyde catalysed by Lewis acidic Eu(fod)<sub>3</sub> to create kawain, recreated from reference.<sup>144</sup> *Bottom*: Enantioselective silylcyanation of aldehydes catalysed by [YbCl<sub>3</sub>(S-Pr<sup>i</sup>-pybox)<sub>2</sub>], recreated from reference.<sup>145</sup>

The current generation of stereoselective catalysts achieve this selectivity by a rigid defined coordination sphere. This area is continuing to expand to other reactions, thus necessitating new motifs upon which these are based. Due to the facility of modification via the four nitrogen groups on the ring, cyclen based derivatives have always been of interest. The first notable example was by Dickins *et al*, who

demonstrated that a chiral lanthanide complex could impart an enantioselective preference upon the outcome of the Henry reactions that it catalysed (**Figure-1.14**).<sup>146</sup>

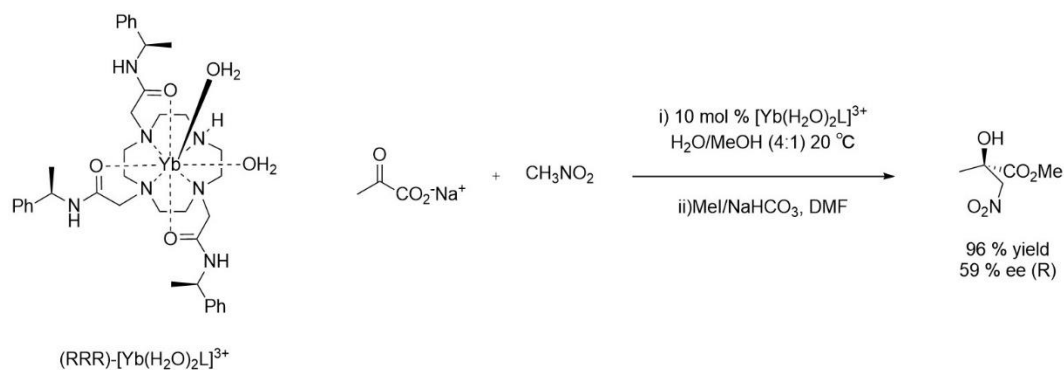


**Figure-1.14.** Henry reaction between simple pyruvate salts and nitromethane in aqueous media to give a single major product, recreated from reference.<sup>146</sup>

The ability to alter the spread of enantiomers in the reaction output is highly desirable and has prompted further research. One of the best examples of enantioselectivity by cyclen based macrocycles comes from research by Mei *et al.*<sup>147</sup> which involves the synthesis of new hexadentate systems, which create multiple binding modes. Modification of the arms of this hexadentate motif can change the stereochemical preferences of the products of this catalysed reaction (**Figure-1.15**).<sup>148</sup>

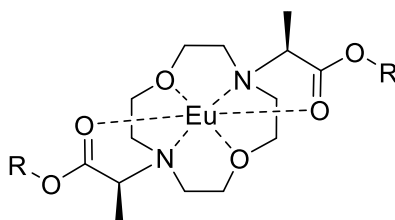


**Figure-1.15.** Chemical structure of polyaminopolycarboxylate-based ligand motif for stereoselective catalysis of aldol reactions, modification of R-group identity influences stereoselectivity, recreated from reference.<sup>148</sup>

Through further research Mei *et al*<sup>148</sup>. hypothesised a stereoselective transition state to rationalise their observations, showing a steric element that resulted in a facial preference for an aldol reaction to proceed (**Figure-1.16**).

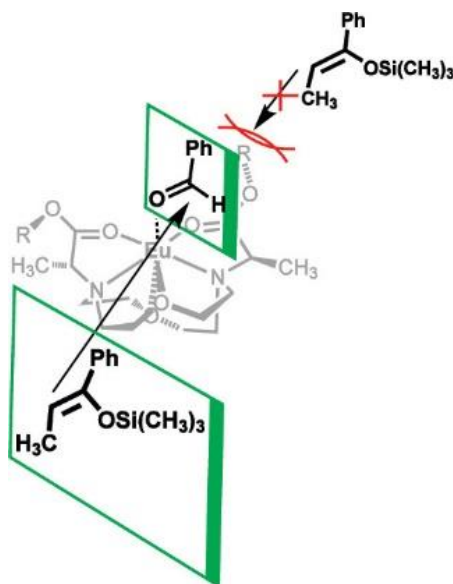


**Figure-1.16.** Proposed general transition state for the asymmetric Mukaiyama aldol reaction with polyaminopolycarboxylate-based europium complexes imparting a stereoselective preference. Reproduced from reference.<sup>148</sup>

Despite the degree of stereoselectivity varying, the field of lanthanide macrocyclic complexes in catalysis is a burgeoning one. With the ability to impart an enantiomeric preference on reaction output which is highly desirable in many chemical fields, this area will continue to see further research, including in this thesis.

The importance of the macrocycle in catalysis involving Ln(III) ions is evident in work done by Morrow *et al.*<sup>149</sup> which details the use of a specific complex in RNA cleavage (**Figure 1.17**).

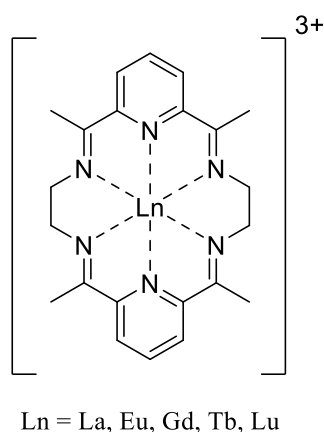


**Figure-1.17.** Chemical structure of Ln(III) containing complex for RNA cleavage.<sup>149</sup>

With this complex working to increase the rate of RNA cleavage, whereas other Ln(III) complexes containing EDTA, another hexadentate ligand, are completely inactive under similar conditions. Once again, this shows that macrocycles must be designed for specific purposes to render them catalytically active for specific reactions, with the main purpose being to prevent decomplexation of the Ln(III) ion once in solution.

## 1.8 Aim and Scope

The aim of this thesis is to create a series of coordinatively unsaturated heptadentate Ln.DO3A and Ln.DO3AM derivatives, in an effort to catalyse fluorination of halocarboxylic acid derivatives in a one-pot manner, with an eye towards increasing the ease of selective fluorination of biomolecules for PET imaging.

Chapter-2 explores the use of kinetically inert Ln.p.DO3A for use in catalysis. This Chapter details the synthesis of these complexes, followed by monitoring their interactions with guest anions (fluoride and acetate) by luminescence spectroscopy. After quantification of the respective binding strengths, the catalytic activity of

these complexes with regard to fluorination of a group of halocarboxylic acid derivatives is investigated. Coulombic laws of attraction suggest the importance of cationic hosts for the reaction of anionic guests in solution. The complexes detailed serve as prototype systems for the Ln.p.DO3AM derivatives synthesised later in the thesis.

Chapter-3 details the synthetic considerations and challenges in developing cationic Ln.p.DO3AM derivatives bearing amino-acid side-chains. In the hope that through novel ligand design, complexes with more desirable properties can be created through inclusion of amino acids appended to a central cyclen ring. A total of eight different Ln.p.DO3AM derivatives, categorised into three families based on amino acids used (proline, lysine, phenylalanine), are successfully synthesised and characterised.

Chapter-4 accounts for the speciation of the Ln.p.DO3AM complexes, synthesised in Chapter-3. This was achieved through observation of luminescence spectra upon the addition of anionic guests (fluoride and acetate). This is explored using steady-state luminescence, time-resolved phosphorescence and measurement of luminescence lifetimes. To probe the complexes in solution phase in protic (MeOH) and aqueous media.

Chapter-5 studies the catalytic behaviour of the Ln.p.DO3AM derivatives, upon addition to a suitable set of fluorination reactions with a range of halocarboxylic acid substrates.

## 1.9 References

- 1 V. Zepf, J. Simmons, A. Reller, C. Rennie, M. Ashfield and B. Achzet, *Materials Critical to the Energy Industry: An Introduction*, 2014.
- 2 J. C. G. Bünzli, in <sup>3</sup>J<sub>HH</sub> *Coord Chem*, 2014, **67**, 3706-3733
- 3 P. G. Jaison, P. Kumar, V. M. Telmore and S. K. Aggarwal, <sup>3</sup>J<sub>HH</sub> *Liq Chromatogr Relat Technol*, 2009, **32**, 2146–2163.
- 4 R. S. Dybczyński, K. Kulisa, M. Pyszynska and A. Bojanowska-Czajka, <sup>3</sup>J<sub>HH</sub> *Chromatogr A*, 2015, **1386**, 74–80.
- 5 P. Kumar, P. G. Jaison, V. M. Telmore, D. Alamelu, S. K. Aggarwal, B. Sadhu and M. Sundararajan, <sup>3</sup>J<sub>HH</sub> *Radioanal Nucl Chem*, 2016, **308**, 303–310.
- 6 A. G. Baldwin, A. S. Ivanov, N. J. Williams, R. J. Ellis, B. A. Moyer, V. S. Bryantsev and J. C. Shafer, *ACS Cent Sci*, 2018, **4**, 739–747.
- 7 Z. Baranyai, G. Tircsó and F. Rösch, , DOI:10.1002/ejic.201900706.
- 8 E. Terreno, M. Botta, F. Fedeli, B. Mondino, L. Milone and S. Aime, *Inorg Chem*, 2003, **42**, 4891–4897.
- 9 J. A. Cotruvo, *ACS Cent Sci*, 2019, **5**, 1496–1506.
- 10 E. R. Featherston and J. A. Cotruvo, *Biochimica et Biophysica Acta (BBA) - Molecular Cell Research*, 2021, **1868**, 118864.
- 11 S. A. Cotton and J. M. Harrowfield, in *Encyclopedia of Inorganic and Bioinorganic Chemistry*, John Wiley & Sons, Ltd, Chichester, UK, 2012.
- 12 S. Cotton, *Lanthanide and actinide chemistry*, 16th edn., 2006, vol. 44.
- 13 R. Eriş, M. V. Akdeniz and A. O. Mekhrabov, *Metallurgical and Materials Transactions A*, 2021, **52**, 2298–2313.
- 14 H. Lumpe, A. Pol, H. J. M. Op den Camp and L. J. Daumann, *Dalton Transactions*, 2018, **47**, 10463–10472.
- 15 S. A. Cotton and J. M. Harrowfield, in *Encyclopedia of Inorganic and Bioinorganic Chemistry*, John Wiley & Sons, Ltd, Chichester, UK, 2012.
- 16 N. Cecilia Martinez-Gomez, H. N. Vu and E. Skovran, *Inorg Chem*, 2016, **55**, 10083–10089.
- 17 P. P. Hallmen, G. Rauhut, H. Stoll, A. O. Mitrushchenkov and J. van Slageren, <sup>3</sup>J<sub>HH</sub> *Chem Theory Comput*, 2018, **14**, 3998–4009.
- 18 B. L. E Orgel, <sup>3</sup>J<sub>HH</sub> *Chem Soc*, 1952, 4756–4761.
- 19 A. L. du Preez and R. J. P. Williams, *J. Chem. Soc., Dalton Trans.*, 1986, 1425–1429.
- 20 T. J. Sørensen and S. Faulkner, *Acc Chem Res*, 2018, **51**, 2493–2501.

- 21 M. F. Haddow, R. J. Newland, B. E. Tegner and S. M. Mansell, *CrystEngComm*, 2019, **21**, 2884–2892.
- 22 M. K. Ghosh, S. K. Chandraker, S. Sikdar, C. Das and T. K. Ghorai, *Chemical Papers*, 2022, **76**, 3259–3273.
- 23 K. Mikami, M. Terada and T. Nakai, *Control of Chelation/Nonchelation Stereoselections in Lanthanide-catalysed Aldol Reactions*, 1993.
- 24 S. A. Cotton, *Comptes Rendus Chimie*, 2005, **8**, 129–145.
- 25 S. A. Cotton and P. R. Raithby, *Coord Chem Rev*, 2017, **340**, 220–231.
- 26 D. Ćcija, J. I. Urgel, A. P. Seitsonen, W. Auwärter and J. V. Barth, *Acc Chem Res*, 2018, **51**, 365–375.
- 27 X.-Z. Li, C.-B. Tian and Q.-F. Sun, *Chem Rev*, 2022, **122**, 6374–6458.
- 28 H.-J. Buschmann,  $^3J_{HH}$  *Solution Chem*, 1987, **16**, 181–190.
- 29 Y. Inokuchi, O. V. Boyarkin, R. Kusaka, T. Haino, T. Ebata and T. R. Rizzo,  $^3J_{HH}$  *Phys Chem A*, 2012, **116**, 4057–4068.
- 30 D. Schuhknecht, C. Lhotzky, T. P. Spaniol, L. Maron and J. Okuda, *Angewandte Chemie International Edition*, 2017, **56**, 12367–12371.
- 31 M. OUDKERK, P. E. SIJENS, E. J. R. VAN BEEK and T. J. A. KUIJPERS, *Invest Radiol*, 1995, **30**, 75–78.
- 32 U. Hennrich and K. Kopka, *Pharmaceuticals*, 2019, **12**, 114.
- 33 F. Chuburu, M. Le Baccon and H. Handel, *Tetrahedron*, 2001, **57**, 2385–2390.
- 34 H. Li, A. Vardanyan, C. Charnay, L. Raehm, G. A. Seisenbaeva, R. Pleixats and J. Durand, *ChemNanoMat*, 2020, **6**, 1625–1634.
- 35 S. Aoki, H. Kawatani, T. Goto, E. Kimura and M. Shiro, *J Am Chem Soc*, 2001, **123**, 1123–1132.
- 36 N. Cakić, S. Gündüz, R. Rengarasu and G. Angelovski, *Tetrahedron Lett*, 2015, **56**, 759–765.
- 37 G. Chen, N. J. Wardle, J. Sarris, N. P. Chatterton and S. W. A. Bligh, *Dalton Transactions*, 2013, **42**, 14115.
- 38 B. Drahoš and Z. Trávníček, *Molecules*, 2013, **18**, 13940–13956.
- 39 M. C. Heffern, L. M. Matosziuk and T. J. Meade, *Chem Rev*, 2014, **114**, 4496–4539.
- 40 J. Wahsner, E. M. Gale, A. Rodríguez-Rodríguez and P. Caravan, *Chem Rev*, 2019, **119**, 957–1057.
- 41 J.-C. G. Bünzli, *Coord Chem Rev*, 2015, **293–294**, 19–47.
- 42 S. J. Butler and D. Parker, *Chem. Soc. Rev.*, 2013, **42**, 1652–1666.

- 43 B. Graham, C. T. Loh, J. D. Swarbrick, P. Ung, J. Shin, H. Yagi, X. Jia, S. Chhabra, N. Barlow, G. Pintacuda, T. Huber and G. Otting, *Bioconjug Chem*, 2011, **22**, 2118–2125.
- 44 M. Suchý, A. X. Li, R. Bartha and R. H. E. Hudson, *Bioorg Med Chem*, 2008, **16**, 6156–6166.
- 45 C. Peukert, K. Rox, B. Karge, S.-K. Hotop and M. Brönstrup, *ACS Infect Dis*, 2023, **9**, 330–341.
- 46 H.-Y. Hu, N.-H. Lim, D. Ding-Pfennigdorff, J. Saas, K. Ulrich Wendt, O. Ritzeler, H. Nagase, O. Plettenburg, C. Schultz and M. Nazare, *Bioconjug Chem*, 2015, **26**, 383–388.
- 47 B. Brennecke, Q. Wang, W. Haap, U. Grether, H.-Y. Hu and M. Nazaré, *Bioconjug Chem*, 2021, **32**, 702–712.
- 48 M. Suchý, M. Milne, A. A. H. Elmehriki, N. McVicar, A. X. Li, R. Bartha and R. H. E. Hudson, *<sup>3</sup>J<sub>HH</sub> Med Chem*, 2015, **58**, 6516–6532.
- 49 K. Ferreira, H.-Y. Hu, V. Fetz, H. Prochnow, B. Rais, P. P. Müller and M. Brönstrup, *Angewandte Chemie International Edition*, 2017, **56**, 8272–8276.
- 50 G. Tircsó, E. Tircsóné Benyó, Z. Garda, J. Singh, R. Trokowski, E. Brücher, A. D. Sherry, É. Tóth and Z. Kovács, *<sup>3</sup>J<sub>HH</sub> Inorg Biochem*, 2020, **206**, 111042.
- 51 P. Urbanovský, J. Kotek, I. Cisařová and P. Hermann, *Dalton Transactions*, 2020, **49**, 1555–1569.
- 52 J. Vipond, M. Woods, P. Zhao, G. Tircsó, J. Ren, S. G. Bott, D. Ogrin, G. E. Kiefer, Z. Kovacs and A. D. Sherry, *Inorg Chem*, 2007, **46**, 2584–95.
- 53 Y. Lee, Z. Mou, A. C. L. Opina and O. Vasalatiy, *Eur<sup>3</sup>J<sub>HH</sub> Inorg Chem*, 2021, **2021**, 1428–1440.
- 54 C. Kumas, W. S. Fernando, P. Zhao, M. Regueiro-Figueroa, G. E. Kiefer, A. F. Martins, C. Platas-Iglesias and A. D. Sherry, *Inorg Chem*, 2016, **55**, 9297–9305.
- 55 A. C. L. Opina, M. Strickland, Y.-S. Lee, N. Tjandra, R. A. Byrd, R. E. Swenson and O. Vasalatiy, *Dalton Transactions*, 2016, **45**, 4673–4687.
- 56 L. Dai, C. M. Jones, W. T. K. Chan, T. A. Pham, X. Ling, E. M. Gale, N. J. Rotile, W. C.-S. Tai, C. J. Anderson, P. Caravan and G.-L. Law, *Nat Commun*, 2018, **9**, 857.
- 57 L. Dai, J. Zhang, Y. Chen, L. E. Mackenzie, R. Pal and G.-L. Law, *Inorg Chem*, 2019, **58**, 12506–12510.
- 58 G. Tircso, B. C. Webber, B. E. Kucera, V. G. Young and M. Woods, *Inorg Chem*, 2011, **50**, 7966–7979.
- 59 S. Aime, M. Botta, M. Fasano, M. P. M. Marques, C. F. G. C. Geraldès, D. Pubanz and A. E. Merbach, *Inorg Chem*, 1997, **36**, 2059–2068.
- 60 S. Aime, M. Botta and G. Ermondi, *Inorg Chem*, 1992, **31**, 4291–4299.

- 61 N. Cakić, T. Ž. Verbić, R. M. Jelić, C. Platas-Iglesias and G. Angelovski, *Dalton Transactions*, 2016, **45**, 6555–6565.
- 62 G. Tircsó, Z. Garda, F. K. Kálmán, Z. Baranyai, I. Pócsi, G. Balla and I. Tóth,<sup>3</sup>*J<sub>HH</sub> Inorg Biochem*, 2013, **127**, 53–61.
- 63 L. Helm and A. E. Merbach, *Coord Chem Rev*, 1999, **187**, 151–181.
- 64 C. H. Langford and T. R. Stengle, *Annu Rev Phys Chem*, 1968, **19**, 193–214.
- 65 S. Muthaiah, A. Bhatia and M. Kannan, in *Stability and Applications of Coordination Compounds*, IntechOpen, 2020.
- 66 P. W. Dimmock, P. Warwick and R. A. Robbins, *Analyst*, 1995, **120**, 2159.
- 67 G. R. Choppin, *Pure and Applied Chemistry*, 1971, **27**, 23–42.
- 68 D. Nomizu, Y. Tsuchida, M. Matsumiya and K. Tsunashima,<sup>3</sup>*J<sub>HH</sub> Mol Liq*, 2020, **318**, 114008.
- 69 A. D. Sherry, P. Caravan and R. E. Lenkinski,<sup>3</sup>*J<sub>HH</sub> Magn Reson Imaging*, 2009, **30**, 1240–8.
- 70 F. Cotton, G. Wilkinson, C. A. Murillo and M. Bochmann, *Advanced Inorganic Chemistry*, 6th edn., 1999.
- 71 W. P. Cacheris, S. K. Nickle and A. D. Sherry, *Inorg Chem*, 1987, **26**, 958–960.
- 72 É. Tóth and E. Brücher, *Inorganica Chim Acta*, 1994, **221**, 165–167.
- 73 G. Anderegg, F. Arnaud-Neu, R. Delgado, J. Felcman and K. Popov, *Pure and Applied Chemistry*, 2005, **77**, 1445–1495.
- 74 A. Pasha, G. Tircsó, E. T. Benyó, E. Brücher and A. D. Sherry, *Eur<sup>3</sup>J<sub>HH</sub> Inorg Chem*, 2007, **2007**, 4340–4349.
- 75 C. A. Chang, *Handbook on the Physics and Chemistry of Rare Earths*, 2017, **51**, 169–299.
- 76 Z. Baranyai, I. Bányai, E. Brücher, R. Király and E. Terreno, *Eur<sup>3</sup>J<sub>HH</sub> Inorg Chem*, 2007, **2007**, 3639–3645.
- 77 K. Binnemans, *Coord Chem Rev*, 2015, **295**, 1–45.
- 78 M. J. Comstock, Ed., 1980, pp. i–iv.
- 79 P. Hänninen and H. Härmä, Eds., *Lanthanide Luminescence*, Springer Berlin Heidelberg, Berlin, Heidelberg, 2011, vol. 7.
- 80 W. R. Kitzmann, J. Moll and K. Heinze, *Photochemical & Photobiological Sciences*, 2022, **21**, 1309–1331.
- 81 S. J. A. Pope, B. J. Coe, S. Faulkner, E. V. Bichenkova, X. Yu and K. T. Douglas, *J Am Chem Soc*, 2004, **126**, 9490–9491.
- 82 S. V. Eliseeva and J.-C. G. Bünzli, *Chem. Soc. Rev.*, 2010, **39**, 189–227.

- 83 S. Faulkner, S. J. A. Pope and B. P. Burton-Pye, *Appl Spectrosc Rev*, 2005, **40**, 1–31.
- 84 J.-C. G. Bünzli and C. Piguet, *Chem Soc Rev*, 2005, **34**, 1048.
- 85 M. Hatanaka and S. Yabushita, *Theor Chem Acc*, 2014, **133**, 1517.
- 86 P. P. Ferreira da Rosa, Y. Kitagawa and Y. Hasegawa, *Coord Chem Rev*, 2020, **406**, 213153.
- 87 Y. Ning, Y.-W. Liu, Y.-S. Meng and J.-L. Zhang, *Inorg Chem*, 2018, **57**, 1332–1341.
- 88 D. Gao, X. Zhang and J. Zhang, *CrystEngComm*, 2014, **16**, 11115–11121.
- 89 S. F. Mason, R. D. Peacock and B. Stewart, *Chem Phys Lett*, 1974, **29**, 149–153.
- 90 F. S. Richardson, *Inorg Chem*, 1980, **19**, 2806–2812.
- 91 C. M. Dodson and R. Zia, *Phys Rev B*, 2012, **86**, 125102.
- 92 R. C. Leif, L. M. Vallarino, M. C. Becker and S. Yang, *Cytometry Part A*, 2006, **69A**, 767–778.
- 93 S. V. Eliseeva and J.-C. G. Bünzli, *Chem. Soc. Rev.*, 2010, **39**, 189–227.
- 94 R. Datta, T. M. Heaster, J. T. Sharick, A. A. Gillette and M. C. Skala,<sup>3</sup>*J<sub>HH</sub> Biomed Opt*, 2020, **25**, 1.
- 95 S. R. Kiraev, E. Mathieu, F. Siemens, D. Kovacs, E. Demeyere and K. E. Borbas, *Molecules*, 2020, **25**, 5282.
- 96 A. G. Cosby, J. J. Woods, P. Nawrocki, T. J. Sørensen, J. J. Wilson and E. Boros, *Chem Sci*, 2021, **12**, 9442–9451.
- 97 A. K. R. Junker, L. R. Hill, A. L. Thompson, S. Faulkner and T. J. Sørensen, *Dalton Transactions*, 2018, **47**, 4794–4803.
- 98 D. L. Dexter,<sup>3</sup>*J<sub>HH</sub> Chem Phys*, 1953, **21**, 836–850.
- 99 Th. Förster, *Discuss. Faraday Soc.*, 1959, **27**, 7–17.
- 100 N. S. Poluéktov, I. I. Zheltvai, G. I. Gerasimenko, M. A. Tishchenko and A. A. Kucher,<sup>3</sup>*J<sub>HH</sub> Appl Spectrosc*, 1976, **24**, 189–192.
- 101 Joseph. R. Lakowicz, in *Principles of Fluorescence Spectroscopy*, Springer US, Boston, MA, 2006, pp. 331–351.
- 102 A. Beeby, I. M. Clarkson, R. S. Dickins, S. Faulkner, D. Parker, L. Royle, A. S. de Sousa, J. A. G. Williams and M. Woods, *Journal of the Chemical Society, Perkin Transactions 2*, 1999, 493–504.
- 103 G. E. Buono-core, H. Li and B. Marciniak, *Coord Chem Rev*, 1990, **99**, 55–87.
- 104 W. D. Horrocks and D. R. Sudnick, *Acc Chem Res*, 1981, **14**, 384–392.
- 105 W. DeW. Horrocks and D. R. Sudnick, *J Am Chem Soc*, 1979, **101**, 334–340.

- 106 R. M. Supkowski and W. DeW. Horrocks, *Inorganica Chim Acta*, 2002, **340**, 44–48.
- 107 M. Tropiano, O. A. Blackburn, J. A. Tilney, L. R. Hill, T. Just Sørensen and S. Faulkner,  $^3J_{HH}$  *Lumin*, 2015, **167**, 296–304.
- 108 L. R. Hill, T. J. Sørensen, O. A. Blackburn, A. Brown, P. D. Beer and S. Faulkner, *Dalton Trans.*, 2013, **42**, 67–70.
- 109 I. Bertini, C. Luchinat, G. Parigi and E. Ravera, in *Solution NMR of Paramagnetic Molecules*, Elsevier, 2017, pp. 1–24.
- 110 A. Kumar and R. C. Rani Grace, in *Encyclopedia of Spectroscopy and Spectrometry*, Elsevier, 2017, pp. 1946–1955.
- 111 C. R. Jones, C. P. Butts and J. N. Harvey, *Beilstein J. Org. Chem*, 2011, **7**, 145–150.
- 112 M. P. Williamson, in *Modern Magnetic Resonance*, Springer Netherlands, Dordrecht, pp. 409–412.
- 113 M. Barbush and D. W. Dixon, *Biochem Biophys Res Commun*, 1985, **129**, 70–75.
- 114 X.-C. Su and J.-L. Chen, *Acc Chem Res*, 2019, **52**, 1675–1686.
- 115 J. Koehler and J. Meiler, *Prog Nucl Magn Reson Spectrosc*, 2011, **59**, 360–89.
- 116 V. S. SASTRI, J.-C. BÜNZLI, V. R. RAO, G. V. S. RAYUDU and J. R. PERUMAREDDI, in *Modern Aspects of Rare Earths and Their Complexes*, Elsevier, 2003, pp. 779–843.
- 117 A. Paulovicova, U. El-Ayaan, K. Umezawa, C. Vithana, Y. Ohashi and Y. Fukuda, *Inorganica Chim Acta*, 2002, **339**, 209–214.
- 118 S.-H. Lam, H.-Y. Hung, P.-C. Kuo, D.-H. Kuo, F.-A. Chen and T.-S. Wu, *Molecules*, 2020, **25**, 5383.
- 119 M. Vonci, K. Mason, E. A. Suturina, A. T. Frawley, S. G. Worswick, I. Kuprov, D. Parker, E. J. L. McInnes and N. F. Chilton, *J Am Chem Soc*, 2017, **139**, 14166–14172.
- 120 O. A. Gansow, P. A. Loeffler, R. E. Davis, M. R. Willcott and R. E. Lenkinsk, *J Am Chem Soc*, 1973, **95**, 3390–3392.
- 121 J. W. M. De Boer, P. J. D. Sackers, C. W. Hilbers and E. De Boer, *Journal of Magnetic Resonance (1969)*, 1977, **25**, 455–476.
- 122 J. A. Peters, J. Huskens and D. J. Raber, *Prog Nucl Magn Reson Spectrosc*, 1996, **28**, 283–350.
- 123 S. P. Babailov,  $^3J_{HH}$  *Incl Phenom Macrocycl Chem*, 2014, **80**, 377–381.
- 124 E. A. Suturina, K. Mason, C. F. G. C. Geraldès, I. Kuprov and D. Parker, *Angewandte Chemie*, 2017, **129**, 12383–12386.
- 125 A. M. Funk, K.-L. N. A. Finney, P. Harvey, A. M. Kenwright, E. R. Neil, N. J. Rogers, P. Kanthi Senanayake and D. Parker, *Chem Sci*, 2015, **6**, 1655–1662.

- 126 X. Jian, J. Qin and Q. Gu, *Phys Lett A*, 2010, **374**, 2580–2583.
- 127 D. Ranaut and K. Mukherjee, *Phys Lett A*, 2023, **465**, 128710.
- 128 L. C. Thompson, in *Handbook on the Physics and Chemistry of Rare Earths*, 1979, pp. 209–297.
- 129 A. S. Souza and M. A. Couto dos Santos, *Chem Phys Lett*, 2012, **521**, 138–141.
- 130 J. Sievers, *Zeitschrift für Physik B Condensed Matter*, 1982, **45**, 289–296.
- 131 J. D. Rinehart and J. R. Long, *Chem Sci*, 2011, **2**, 2078–2085.
- 132 D. Parker, E. A. Suturina, I. Kuprov and N. F. Chilton, *Acc Chem Res*, 2020, **53**, 1520–1534.
- 133 O. A. Blackburn, A. M. Kenwright, P. D. Beer and S. Faulkner, *Dalton Transactions*, 2015, **44**, 19509–19517.
- 134 O. A. Blackburn, A. M. Kenwright, A. R. Jupp, J. M. Goicoechea, P. D. Beer and S. Faulkner, *Chemistry - A European Journal*, 2016, **22**, 8929–8936.
- 135 S. E. Bodman and S. J. Butler, *Chem Sci*, 2021, **12**, 2716–2734.
- 136 B. Bleaney, C. M. Dobson, B. A. Levine, R. B. Martin, R. J. P. Williams and A. V. Xavier,<sup>3</sup>*J<sub>HH</sub> Chem Soc Chem Commun*, 1972, 791–793.
- 137 B. T. Kilbourn, *Journal of the Less Common Metals*, 1986, **126**, 101–106.
- 138 S. Dey and G. C. Dhal, *Mater Sci Energy Technol*, 2020, **3**, 6–24.
- 139 G. Pan, X. Bai, D. Yang, X. Chen, P. Jing, S. Qu, L. Zhang, D. Zhou, J. Zhu, W. Xu, B. Dong and H. Song, *Nano Lett*, 2017, **17**, 8005–8011.
- 140 X. Cui, T. Wu, J.-P. Cao, W. Tang, F.-L. Yang, B.-A. Zhu and Z. Wang, *Fuel*, 2021, **288**, 119683.
- 141 L. Sanzhong, Z. Baolian, X. Ming, A. Jańczuk, X. Wenhua, C. Jinpei and P. G. Wang, *Chinese Science Bulletin*, 2001, **46**, 1673–1681.
- 142 B. M. Trost, *Angewandte Chemie International Edition in English*, 1995, **34**, 259–281.
- 143 J. Becica and G. E. Dobereiner, *Org Biomol Chem*, 2019, **17**, 2055–2069.
- 144 S. Castellino and J. J. Sims, *Tetrahedron Lett*, 1984, **25**, 4059–4062.
- 145 Helen C. Aspinall, Jamie F. Bickley, Nicholas Greeves, Richard V. Kelly and Peter M. Smith, *Organometallics*, 2005, **24**, 3458–3467.
- 146 S. U. Pandya, R. S. Dickins and D. Parker, *Org Biomol Chem*, 2007, **5**, 3842.
- 147 M. Allen, *Synlett*, 2016, **27**, 1310–1317.
- 148 Y. Mei, P. Dissanayake and M. J. Allen, *J Am Chem Soc*, 2010, **132**, 12871–12873.
- 149 J. R. Morrow, L. A. Buttrey, V. M. Shelton and K. A. Berback, *J Am Chem Soc*, 1992, 114, 1903–1905

## Chapter-2: Exploring the catalytic behaviour of p.DO3A complexes

### 2.1 Aim and scope

The aim of this chapter is to fluorinate halocarboxylates using Ln.p.DO3A in a catalytic capacity, as a proof of concept for the use of heptadentate lanthanide complexes as homogenous catalysts. With this being exploited to label  $^{18}\text{F}$  in select biomolecules containing haloacids, opening up new avenues for radiolabelling in the field of medical imaging, specifically positron emission tomography (PET) imaging in which radiolabelling is a significant part.<sup>1-4</sup> This Chapter initially covers the synthesis and characterisation of these systems, followed by observation of their solution phase interactions with suitable anions through the use of luminescence, with the information then processed using DynaFit<sup>®</sup>.<sup>5</sup> The Ln.p.DO3A systems observed in this Chapter will confirm previous observations seen, detail the effects of a change in Ln(III) identity, and act as an experimental template for the DO3AM derivatives investigated in Chapters 3-5.<sup>6</sup>

### 2.2 Ln.p.DO3A a prototype system

Propargyl DO3A was the first ligand to be synthesised. This ligand has been synthesised extensively in the literature and is a good example of a heptadentate ligand, the subject of investigation in this thesis.<sup>7-10</sup> The propargyl group was selected due to the synthetic ease of addition and the precedent of use within the Faulkner group.<sup>11,12</sup> For the purposes of this thesis the propargyl group serves to saturate the fourth amine group on the ring, preventing unwanted side reactions.<sup>13</sup>

The presence of two inner-sphere solvating molecules in heptadentate complexes (DO3A based complexes), will facilitate the binding of mono- and bidentate anions for recognition at the metal centre. This will create two different sites for anion binding, an equatorial position as opposed to the axial binding position which is most often exploited in MRI contrast agents.<sup>14-16</sup> This equatorial binding position has a much greater binding strength than the axial binding position.<sup>6</sup> While the axial binding guests will be in fast exchange, which is required for them to be an effective contrast agent (CA), the equatorially binding guests will be in slower exchange (**Figure-2.1**).<sup>17</sup>

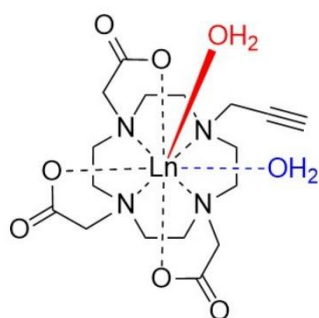


**Figure-2.1.** Structure of Ln.p.DO3A with two coordinating H<sub>2</sub>O molecules in an axial binding mode (red) and equatorial binding mode (blue).

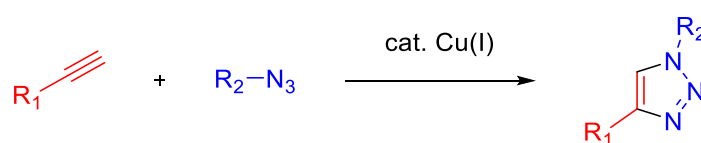
Luminescence measurements will be the primary source of data when investigating the nature of binding around the lanthanide centre, with the data processed using DynaFit<sup>®</sup>. Allowing determination of the number of binding anions and other information, such as the strength and denticity of binding.<sup>5</sup>

In comparison to other lanthanide complexes acting as CA's, the rate of guest exchange is of less importance in this thesis. With both anions chelating to the Eu(III) ion, this holds them in close proximity favouring a reaction between the species.<sup>6</sup> This process has been observed previously for the Eu.p.DO3A complex,

with the complex providing an increase in the initial rate of reaction for the fluorination of halocarboxylic acid derivatives.<sup>6</sup> More information has to be gathered on this complex to observe if the reaction goes to completion and the relevant timescales, with observations hoping to show a noticeable difference over a prolonged period. This system should provide a way of standardising measurements, which can then be used to compare with the DO3AM complexes studied later in this thesis. Although the field of lanthanides working within or as catalysts themselves is well established, cyclen based lanthanide complexes as catalysts is an area that is comparatively less researched.<sup>18</sup>

### 2.3 Previous applications and uses of p.DO3A

Propargyl DO3A has been the subject of investigation for many purposes within lanthanide chemistry.<sup>19-22</sup> The DO3A structure is derived from DOTA, which is a desirable ligand for lanthanide encapsulation due to the high kinetic stability of the formed complexes.<sup>23,24</sup> While DO3A is not as kinetically stable due to the loss of an acetate arm on the periphery of the ligand, this gives a vacant fourth position on the cyclen ring, enabling functionalisation on this position.<sup>13</sup> This has been explored extensively to create CA's and other useful molecules that are more targeting or sensitive to specific environments (e.g. pH, oxygen concentration etc.).<sup>25-27</sup> The alkyne functional group and its reactions have been observed extensively in organic chemistry, with a history of use within reactions such as Diels-Alder and 'click' reactions being two of its most well-known uses (**Scheme-2.1**).<sup>28,29</sup>

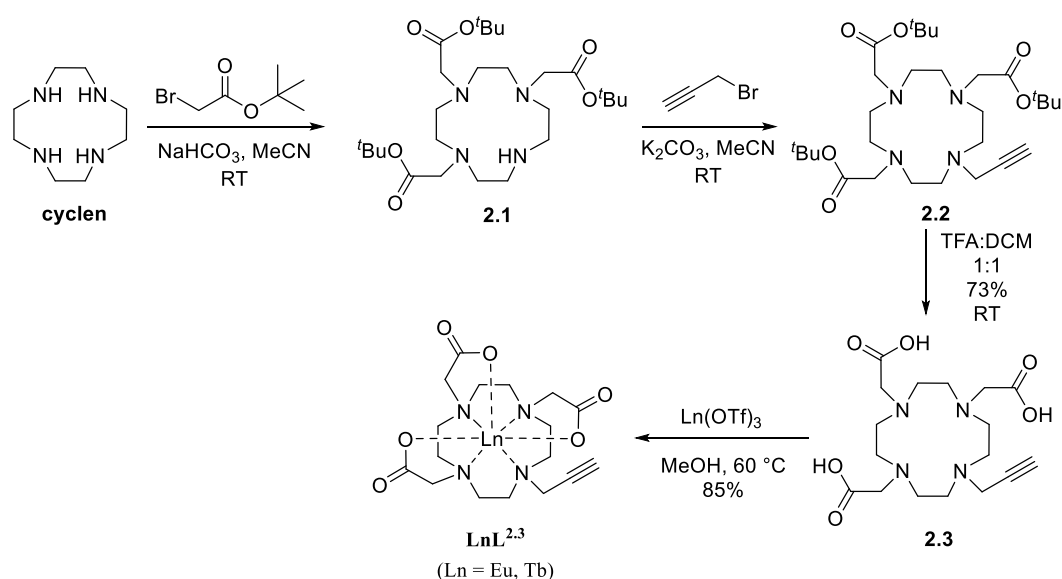


**Scheme-2.1.** General Cu(I) catalysed click reactions.

Its uses in ‘click’ reactions is what made the propargyl group interesting within the Faulkner Group, with the ability to ‘click’ specific moieties to the DO3A ligand.<sup>20,21,28,30</sup> However, within this thesis, the propargyl group will be used to saturate the fourth amine position on the ring. The reasons to use propargyl arm is the synthetic ease of addition to the cyclen ring and its small size should mean that sterically it will not hinder the binding of any guest anions in solution.<sup>6,13</sup>

## 2.4 Synthesis of p.DO3A

The synthesis of p.DO3A is a well-known pathway in the Faulkner group (**Scheme-2.2**).<sup>31–33</sup>



**Scheme-2.2:** Synthesis of Ln.p.DO3A (**LnL<sup>2,3</sup>**) for investigation as a prototype system.

Direct alkylation of cyclen with *tert*-butyl bromoacetate produces the protected ester of DO3A, DO3A(*t*BuO)<sub>3</sub> (**2.1**) in a good yield. DO3A(*t*BuO)<sub>3</sub> was further reacted with propargyl bromide which as aforementioned works well to yield the protected ester of p.DO3A (**2.2**). **2** undergoes removal of the ester groups in acidic

conditions to yield **2.3** as the TFA salt. **2.3** is then mixed with the appropriate lanthanide triflate salt and after appropriate basification and time, affords the complex Ln.p.DO3A (LnL<sup>2,3</sup>) (Ln(III)=Eu, Tb, Gd, Y, Yb) in good yield. The overall reaction proceeds with a good overall yield of 26 % and is highly reproducible.

Complexes were fully characterised by NMR, MS and luminescence spectroscopies. These values all corresponded well with literature values for the Ln.p.DO3A complexes (**Figure-2.2**).<sup>11,20</sup>

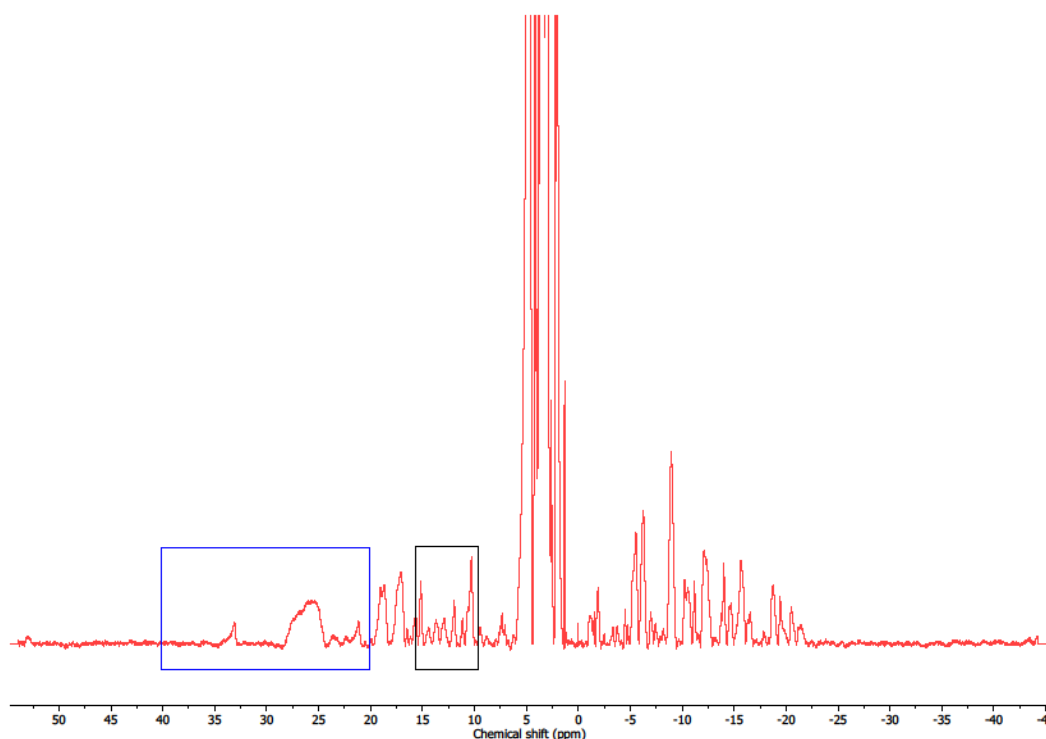


**Figure-2.2.** <sup>1</sup>H NMR spectrum of Eu.p.DO3A (EuL<sup>2,3</sup>) (298 K, D<sub>2</sub>O, 500 MHz), Highlighting peaks due to SAP isomer (blue box) and TSAP isomer (black box).

Eu(III) was prioritised due to previous research being focused on Eu(III) containing complexes, the emphasis being to confirm previous observations, then move on to more complex systems while retaining the same lanthanide.<sup>6</sup> Eu(III) is the only

metal in the lanthanide series where NMR spectroscopy and luminescence measurements are easily attainable.<sup>34</sup> While Tb(III) is more luminescent (higher quantum yield) and NMR spectroscopic data can be gained from the complexes, the NMR spectra are more difficult to assign in comparison to Eu(III) analogues.<sup>35-37</sup> Yb(III) was also considered but due to the lack of a spectrometer with a NIR (Near Infra-Red) detector, this was abandoned.<sup>38</sup>

Tb(III) was of interest as in comparison to Eu(III), Tb(III) is further along the period specifically the other side of the ‘gadolinium break’.<sup>39</sup> This effect details the shift in conformational preference of ‘DOTA-like’ compounds from SAP to TSAP. This conformational change will have far reaching effects within this thesis. The SAP conformation for DOTA like complexes has a lower hydration number ( $q$ ) than the TSAP conformation for the same complex.<sup>40</sup> Therefore, exploring Eu(III) and Tb(III) shows the effect of the ‘gadolinium break’ and to see how the impact of this conformational shift will affect the complexes ability to act as a catalyst. For Yb(III), being so far along the period, the mole fraction of TSAP in solution will be very high, theoretically providing less space for anion binding. As such it is of less significance in this thesis, making the focus of this chapter on the Eu(III) and Tb(III) analogue of p.DO3A (**Figure-2.3**).<sup>41</sup>

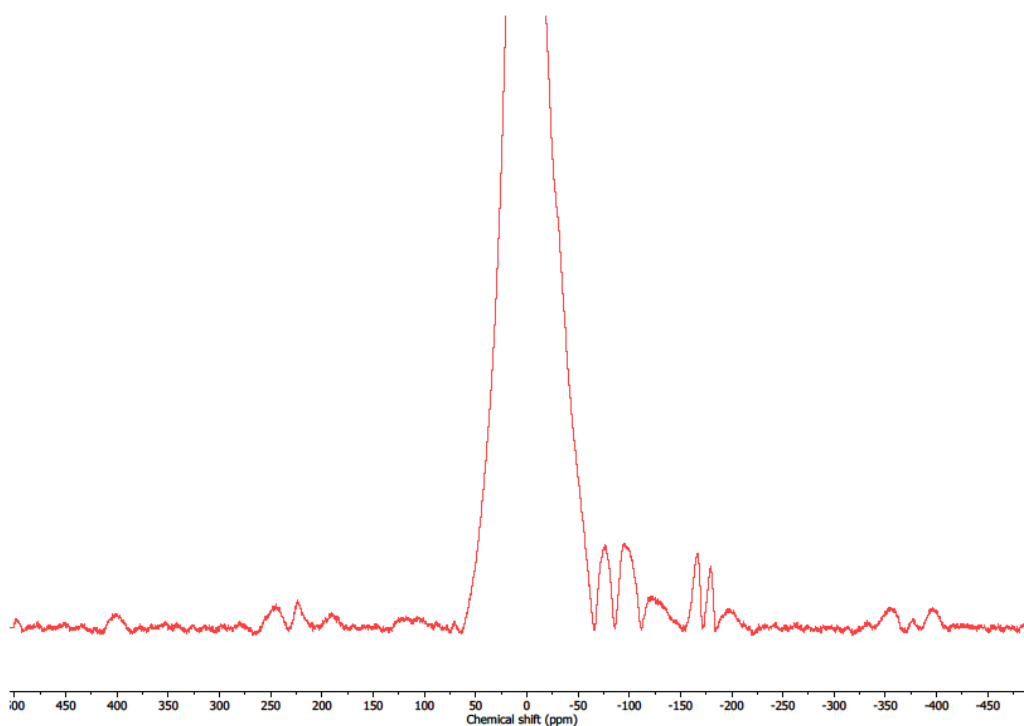


**Figure-2.3.**  $^1\text{H}$  NMR spectrum of Tb.p.DO3A (298 K,  $\text{D}_2\text{O}$ , 500 MHz)

## 2.5 Luminescence studies of Ln.p.DO3A complexes

Luminescence titrations of Ln.p.DO3A complexes were carried out on the Fluorolog-3 spectrometer using a non-dilution method to maintain complex concentration.<sup>42</sup> Once a suitable spectrum was obtained, detailing the relevant transitions, suitable peaks were monitored and processed to generate a binding isotherm using DynaFit<sup>®</sup>.

### 2.5.1 Eu.p.DO3A

Upon completion of this luminescence titration, suitable peaks were chosen for observation. In Eu.p.DO3A the peaks correspond to the transitions  $^5\text{D}_0 \rightarrow ^7\text{F}_1$ ,  $^5\text{D}_0 \rightarrow ^7\text{F}_2$ ,  $^5\text{D}_0 \rightarrow ^7\text{F}_3$  and  $^5\text{D}_0 \rightarrow ^7\text{F}_4$ .<sup>43</sup> These transitions can afford a large amount of information about the local lanthanide environment (**Table-2.1**).<sup>44</sup>

**Table-2.1.** Table detailing transitions observed in luminescence spectra of europium (III) compounds, highlighted transitions are studied extensively in this thesis. Reproduced from reference.<sup>44</sup>

Transition <sup>a</sup>	Dipole character <sup>b</sup>	Wavelength range (nm)	Relative intensity <sup>c</sup>	Remarks
$^5D_0 \rightarrow ^7F_0$	ED	570-585	vw to s	Only observed in $C_n$ , $C_{nv}$ and $C_5$ symmetry
$^5D_0 \rightarrow ^7F_1$	MD	<b>585-600</b>	<b>s</b>	<b>Intensity largely independent of environment</b>
$^5D_0 \rightarrow ^7F_2$	ED	<b>610-630</b>	<b>s to vs</b>	<b>Hypersensitive transition; Intensity very strongly dependent on environment</b>
$^5D_0 \rightarrow ^7F_3$	ED	640-660	vw to w	Forbidden transition
$^5D_0 \rightarrow ^7F_4$	ED	680-710	m to s	Intensity dependent on environment, but no hypersensitivity
$^5D_0 \rightarrow ^7F_5$	ED	740-770	vw	Forbidden transition
$^5D_0 \rightarrow ^7F_6$	ED	810-840	vw to m	Rarely measured and observed

<sup>a</sup> Only transitions starting from the  $^5D_0$  level are shown

<sup>b</sup> ED = induced magnetic dipole transition, MD magnetic dipole transition

<sup>c</sup> vw = very weak, w = weak, m = medium, s = strong, vs = very strong

While all the transitions can impart some useful information about this complex, the  $^5D_0 \rightarrow ^7F_2$  ( $\Delta J=2$ ) is of particular interest as it is a hypersensitive transition. This transition is particularly sensitive to the local environment, so is useful in elucidating structural information. Combined with the  $^5D_0 \rightarrow ^7F_1$  ( $\Delta J=1$ ) transition, which is magnetically sensitive, these transitions provide structural information throughout the titration reaction (**Figure-2.4**).<sup>44</sup>

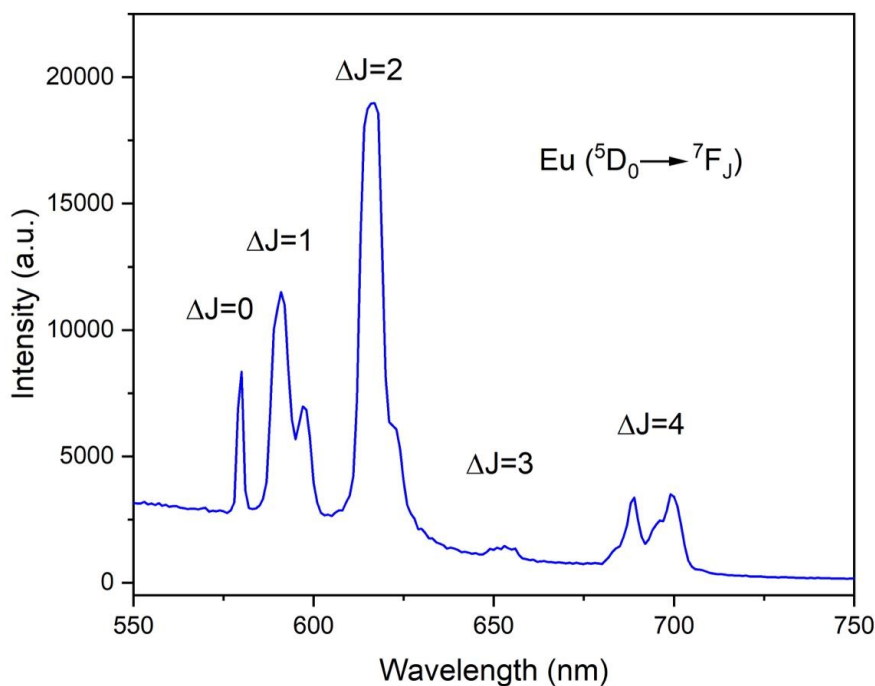


**Figure-2.4.** Steady-state luminescence spectrum of Eu.p.DO3A ( $1 \times 10^{-3}$  mol dm $^{-3}$ ) in HEPES buffer ( $0.02$  mol dm $^{-3}$ ) ( $\lambda_{\text{ex}} = 394$  nm).

This information can be gathered by monitoring the change in intensity of the individual transitions or specific wavelengths. These methods were used depending on the identity of the anionic guest. For ‘softer’ anions such as acetate ( $\text{AcO}^-$ ) there is an overall change in the intensity but peak shape remains consistent, integration of the transition peak to quantify the associated change with increasing anion concentration.<sup>45,46</sup> For ‘hard’ anions such as fluoride ( $\text{F}^-$ ), due to the strength of the binding, this can cause a change in magnetic field orientation.<sup>42</sup> A ‘flip’ from prolate to oblate or vice versa, causes a change in peak shape as the local magnetic field around the lanthanide changes upon anion binding.<sup>47</sup> This change in peak shape is a result of the reordering of  $m_J$  states in each transition. Reordering of the energy levels leads to different occupation of the states based on a Boltzmann-like distribution.<sup>42,47,48</sup> The change in peak shape means monitoring of the overall change in peak area upon guest addition is inaccurate. Instead, the magnitude of

individual wavelengths must be monitored, with the wavelengths selected being peak maxima which remain constant throughout the titration.<sup>46</sup>

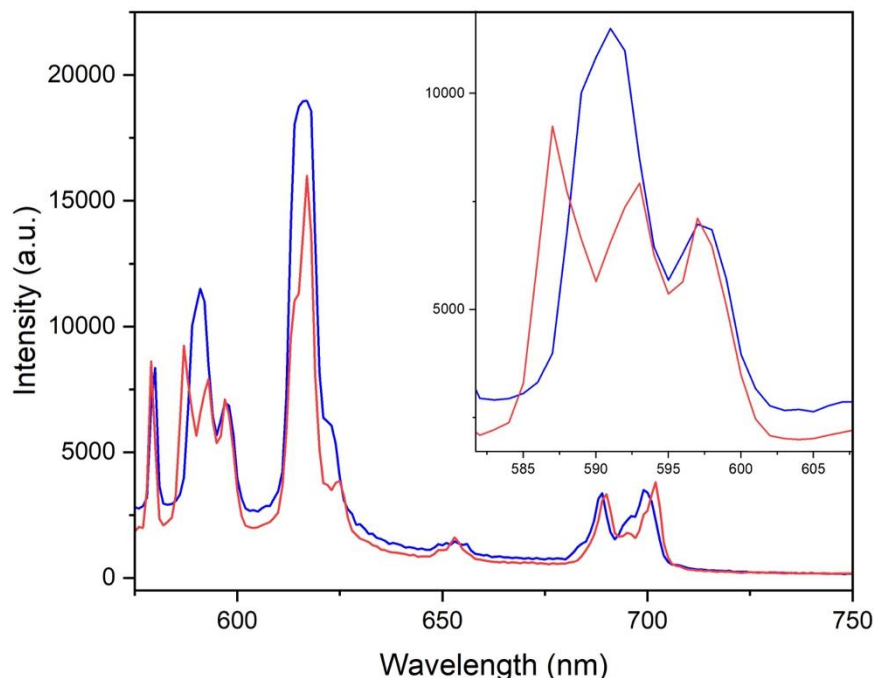


**Figure-2.5.** Steady-state luminescence spectra of Eu.p.DO3A ( $1 \times 10^{-3} \text{ mol dm}^{-3}$ ) showing the change in peak shape and intensity before (blue) and after (red) fluoride addition (8.57 eq),  $\lambda_{\text{ex}} = 394 \text{ nm}$ . *Inset:* magnification on the  $\Delta J=1$  transition showing the change in the anisotropic field surrounding the lanthanide centre, initial (blue), final (red).

A graph of peak or wavelength vs guest anion concentration can then be plotted. This data was processed using DynaFit<sup>®</sup>; this is an iterative fitting package that allows assignment binding events. These binding events correlate to changes in intensity, with the values of the binding constants being dependent upon factors such as the gradient of the curve, and the existence of any intermediate species.<sup>5</sup> Of interest is whether the intensity changes correspond to one or more binding events. This allows differentiation between one- and multiple-binding events, which is of interest in this thesis due to the proposed method of catalytic action of the complexes being studied.<sup>6</sup> The data used for fitting with DynaFit<sup>®</sup> was the guest anion concentration against the peak area of transitions  $\Delta J=1$ ,  $\Delta J=2$ ,  $\Delta J=3$  and  $\Delta J=4$

along with peak ratios  $\Delta J=2/\Delta J=1$  and  $\Delta J=2/\Delta J=4$ . Tracking the changes in intensity for each individual peak, but also how the peaks change with regard to each other.

As in **Table-2.1** the  ${}^5D_0-{}^7F_1$  ( $\Delta J=1$ ) peak remains largely independent of environment, the hypersensitive  ${}^5D_0-{}^7F_2$  ( $\Delta J=2$ ) peak is strongly dependent on environment so will change greatly upon anion binding.<sup>44</sup> Determination of the ratio  $\Delta J=2/\Delta J=1$  is advantageous,  $\Delta J=2$  describing in detail the changes in the local coordination sphere. While  $\Delta J=1$  includes changes during the titration, such as changes in solvent polarity and magnetic field, with these factors affecting the observed luminescence intensity.<sup>45,46,49</sup> This should allow observation of more pronounced changes in comparison to the guest anion concentration.

### 2.5.1.1 Eu.p.DO3A binding studies

Luminescence titrations of Eu.p.DO3A ( $1 \times 10^{-3}$  mol dm<sup>-3</sup>) were carried out in HEPES and Tris buffered solutions of MilliQ water (0.01 mol dm<sup>-3</sup>). In both cases these were titrated against known concentrations of acetate and fluoride as aliquots from a stock solution (0.02 mol dm<sup>-3</sup>).

When titrating against fluoride, the change in peak shape upon addition of a ‘hard’ guest anion must be taken into account.<sup>42</sup> Meaning, instead of the integral of transition  $\Delta J=1$ ,  $\Delta J=2$ ,  $\Delta J=3$  and  $\Delta J=4$ , the peak maxima are selected and the corresponding wavelength and associated intensity changes are monitored and these are used when attempting to generate binding events/constants.<sup>46</sup>

Upon the addition of fluoride to a solution of Eu.p.DO3A, a change is observed in the intensity of the peak at 587 nm highlighted in **Figure-2.6**. Due to the variance in the baseline upon changing ionic strength of the solution, this peak is baselined against the value at 582 nm: this serves to normalise the  $^5D_0 \rightarrow ^7F_0$  transition from which a binding isotherm is generated. In this experiment the metal is directly excited ( $\lambda_{\text{ex}} = 394 \text{ nm}$ ,  $^5D_0 \rightarrow ^7F_J$ ) due to the lack of a chromophore for efficient electron transfer (eT).

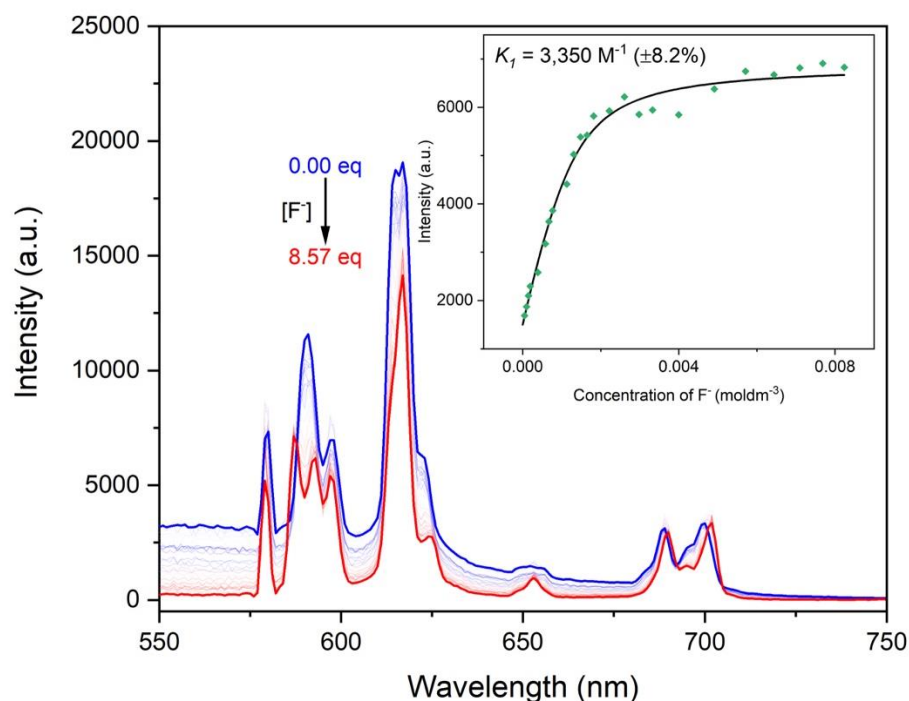


**Figure-2.6.** Graph showing the change in luminescence spectra of Eu.p.DO3A ( $1 \times 10^{-3} \text{ mol dm}^{-3}$ ) in HEPES buffer ( $0.01 \text{ mol dm}^{-3}$ ), upon the addition of increasing amounts of KF. With starting (blue) and end (red) concentrations highlighted,  $\lambda_{\text{ex}} = 394 \text{ nm}$ . *Inset:* binding isotherm from DYNAFIT®, plot of intensity of peak at 587 nm (baselined against 582 nm value, dark-green) vs concentration of  $\text{F}^-$ .

The first binding event observed ( $K_1 = 3,350 \text{ M}^{-1} (\pm 8.2 \%)$ ) indicates strong binding of the fluoride to the central lanthanide. While this fits well, there is some shape to the scatter of the points, indicating that there could be another potential binding event, however this is too weak to be fully resolved as a separate binding event.

This supports the working hypothesis that there is one anion bound and the second is only weakly bound in the axial position.<sup>6,31</sup>

Under the same conditions, an increasing concentration of acetate was added. This causes an increase in intensity reflected in the *Inset* of **Figure-2.8**. The initial lack of change in peak area is due to competitive binding, from HEPES buffer, or from deprotonation creating the isoelectronic  $^-OH$  ion which in turn binds to the lanthanide centre. While this initial competitive binding is weak, it is a noticeable effect in titrations with weakly binding anions such as acetate in this case.<sup>50,51</sup> This quickly turns into acetate binding to the lanthanide centre. The shape of the curve shows similarities to the fluoride analogue, the sigmoidal nature of the curve implies a binding event which cannot be fully distinguished. What could account for this is acetate binding in a bidentate fashion, input of this stoichiometric reaction into DynaFit<sup>®</sup> produced a binding isotherm for the theoretical termolecular collision. This physically corresponds to the initial binding of one of the oxygens on the acetate group, followed sequentially by the non-independent binding of the second oxygen, yielding a bidentate ligand with one overall binding constant ( $K_1 = 954 \text{ M}^{-1} (\pm 6.6 \%)$ ).

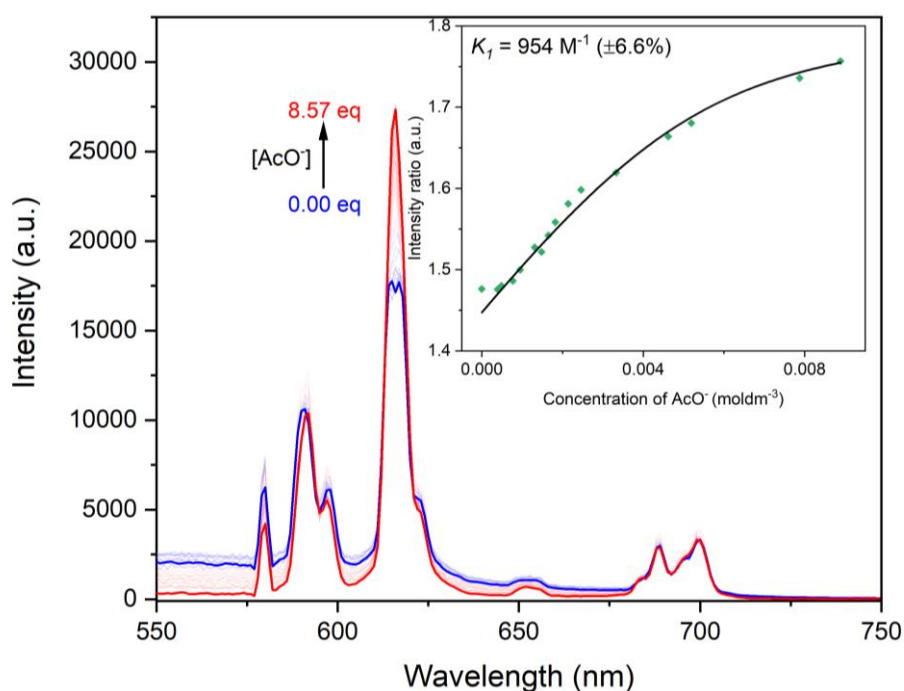


**Figure-2.7.** Graph showing the change in luminescence spectrum of Eu.p.DO3A ( $1 \times 10^{-3} \text{ mol dm}^{-3}$ ) in HEPES buffer ( $0.01 \text{ mol dm}^{-3}$ ), upon addition of increasing amounts of NaOAc. With starting (blue) and end (red) concentrations highlighted,  $\lambda_{\text{ex}} = 394 \text{ nm}$ . Inset: binding isotherm from DYNAFIT<sup>®</sup>, plot of Intensity ratio of the  $\Delta J=2/\Delta J=1$  (dark-green) vs concentration of  $\text{AcO}^-$ .

To confirm the effects and to explore the effect of buffer on binding strength, the same reaction was repeated in Tris buffer. The Tris buffer analogous experiment generated a weaker binding constant ( $K_1 = 1,155 \text{ M}^{-1}$  ( $\pm 2.9\%$ )) than the HEPES analogue (**Figure-2.8**). The shape of the curve was similar to the HEPES analogue, yet what was noticeable is the marked decrease in variability of the baseline. One contrasting observation is the decrease in spectral intensity when titrating with fluoride versus acetate as guest. This is due to fluoride being a more effective photoinduced electron transfer (PeT) quencher, leading to a decrease in spectral intensity. This is a notable effect reported in the literature, so is unsurprising to see reflected throughout this thesis.<sup>52,53</sup>

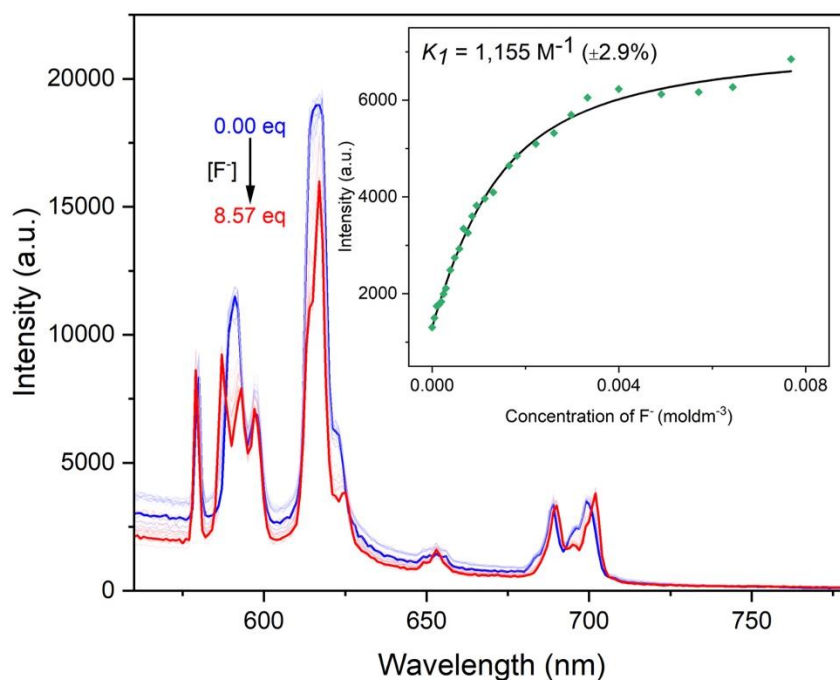


**Figure-2.8.** Graph showing the change in luminescence spectrum of Eu.p.DO3A ( $1 \times 10^{-3}$  mol dm $^{-3}$ ) in Tris buffer (0.01 mol dm $^{-3}$ ), upon addition of increasing amounts of KF. With starting (blue) and end (red) concentrations highlighted,  $\lambda_{\text{ex}} = 394$  nm. *Inset:* binding isotherm from DYNAFIT<sup>®</sup>, plot of intensity of peak at 587 nm (baselined against 582 nm value, dark-green) vs concentration of F $^{-}$ .

From work done by Lai *et al.*<sup>50</sup>, on buffer binding to divalent metal ions, it is shown that HEPES exhibits stronger and thus more competitive binding with respect to Tris. The displacement of HEPES by fluoride in **Figure-2.6** leads to a high rate of change in luminescence intensity, resulting in a higher binding constant in comparison to that observed in **Figure-2.8**. The higher binding affinity for HEPES as opposed to Tris is very apparent on comparison of **Figure-2.7** and **Figure-2.9**.

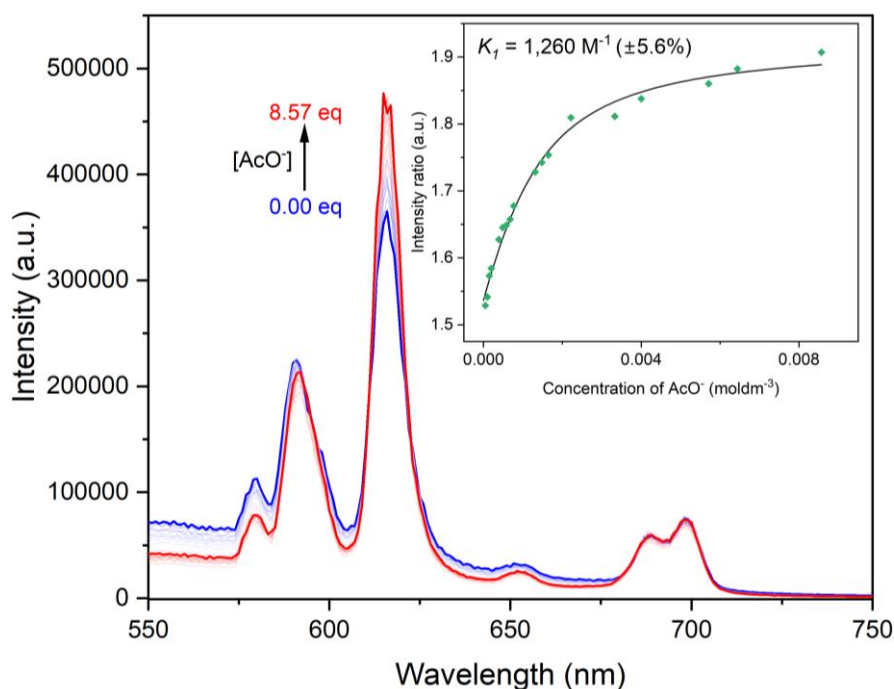


**Figure-2.9.** Graph showing the change in luminescence spectrum of Eu.p.DO3A ( $1 \times 10^{-3}$  mol dm $^{-3}$ ) in Tris buffer (0.01 mol dm $^{-3}$ ), upon addition of increasing amounts of NaOAc. With starting (blue) and end (red) concentrations highlighted,  $\lambda_{\text{ex}} = 394$  nm. *Inset:* binding isotherm from DYNAFIT<sup>®</sup>, plot of Intensity ratio of the  $\Delta J=2/\Delta J=1$  (dark-green) vs concentration of AcO $^{-}$ .

With **Figure-2.9** showing none of the competitive binding exhibited by the HEPES analogue, both titrations against acetate (HEPES and Tris buffered) show good correlation in binding constants.

Eu.p.DO3A and the luminescence titrations show good agreement with current comparable literature sources in the same area (**Table-2.2**).<sup>31</sup> The titrations confirm, what has long been suspected, that acetate binds in a bidentate fashion to the lanthanide centre.<sup>6</sup> The greater binding strength of fluoride as an anionic guest is apparent, allowing it to displace acetate from one binding mode. This should hold the anions in close proximity to one another and enable catalysis through the aforementioned hypothetical mechanism in **Section-2.2**.<sup>42,45,47</sup>

**Table-2.2.** Binding constants of anions with Eu.p.DO3A complexes in aqueous media. §

Anion	Media*	Binding constant (M <sup>-1</sup> )#
		$K_1 = [\text{EuLX}]^-$
		Eu.p.DO3A
F <sup>-</sup>	water-HEPES	3,350 (±270)
	water-Tris	1,160 (±33)
AcO <sup>-</sup>	water-HEPES	954 (±6.3)
	water-Tris	1,260 (±71)

\*All buffers are maintained at 0.01 M, pH 7.4; HEPES = N-(2-Hydroxyethyl)piperazine-N'-(2-ethanesulfonic acid) saline, Tris = trisaminomethane saline

# Error in brackets is represented as standard error in M<sup>-1</sup>. All data were plotted at the 95% confidence interval.

§ The binding of anions was studied by steady-state fluorescence titrations of the complexes with varying concentrations of potassium fluoride and sodium acetate with binding isotherms generated using DynaFit®.

The difficulty of rationalising a second binding event in the fluoride titrations can be explained in terms of the increased electrostatic repulsion. The addition of a second fluoride ion to the anionic [Ln.p.DO3A.F]<sup>-</sup> complex is highly unfavourable, leading to a weak and indistinguishable second binding event. This is corroborated by lifetime data and associated 'q' values from work done by Alexander et al.<sup>31</sup>

## 2.5.2 Tb.p.DO3A

To explore the effect of changing the central lanthanide ion in the same reaction set, the same titration experiments were repeated using Tb.p.DO3A (1×10<sup>-4</sup> mol dm<sup>-3</sup>) as the complex under investigation. The concentrations of the buffered solutions (0.001 mol dm<sup>-3</sup>) and anionic guests (0.002 mol dm<sup>-3</sup>) were modified accordingly. Tb(III) is more emissive with larger quantum yields than Eu(III) in isostructural complexes, as demonstrated by Kucher *et al.*<sup>54</sup> This necessitates a decreased concentration of host to not overwhelm the detector being used.

To address the issue of background luminescence, time-gating techniques were employed. As mentioned in Section-1.4, certain lanthanides exhibit long lanthanide luminescence lifetimes; this can be used to exclude the short-lived autofluorescence from other sources. This offers enhanced signal-to-noise ratios and very low limits of anion detection, making it highly advantageous in this case. This also allows direct comparison of how the individual bands increase either independently or with regard to other bands, offering high spatial and temporal resolution. Although this technique does not allow distinction of spectral fine structure and hence a decreased amount of information about the lanthanide environment, this data is more conducive to the determination of binding constants using DynaFit<sup>®</sup>.

An unexpected benefit of the change in lanthanide ion was the associated change in energy levels of the triplet excited state, as aforementioned in Section-1.4 this is the state which receives energy transfer from the ligand excited states when exploiting the 'antenna effect'. With a change in lanthanide ion identity comes a change in the triplet energy level, this brings it into proximity of the propargyl group triplet energy level, enabling effective sensitisation through this antenna. An observation not seen in the analogous Eu.p.DO3A complex. This allows exploitation of the propargyl group as a suitable antenna group. While not as efficient as other chromophore containing terbium complexes, it nonetheless facilitates indirect excitation.

This change from fluorescence to phosphorescence was accompanied by a change in instrumentation from the Fluorolog<sup>®</sup> to the PerkinElmer LS55. This instrument, while less sensitive than the Fluorolog<sup>®</sup>, was much more time-efficient and decreased the signal-to-noise ratio even more, providing an optimised route to carry

out titrations. Tb.p.DO3A measurements were thus carried out using this instrument. The shape of the luminescence spectrum changed with lanthanide identity giving  $^5D_4$  as the ground state (**Figure-2.10**).<sup>55</sup>

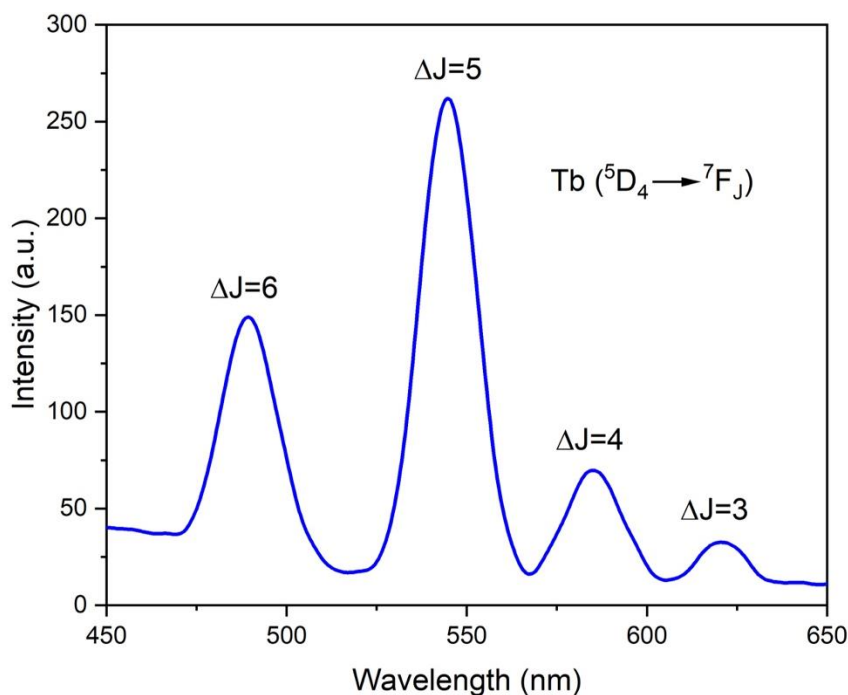


**Figure-2.10.** Fluorescence spectrum of Tb.p.DO3A ( $1 \times 10^{-4}$  mol  $\text{dm}^{-3}$ ) in Tris buffer (0.001 mol  $\text{dm}^{-3}$ ),  $\lambda_{\text{ex}} = 226$  nm (high initial intensity at 450 nm due to  $2\lambda$  peak from Raman scattering).

### 2.5.2.1 Tb.p.DO3A binding studies

Time-gating techniques allowed removal of background auto-fluorescence, yet due to the low excitation wavelength (226 nm) the double excitation peak around 450 nm results in some interference within the spectral data. Due to Terbium's smaller size and similar charge, it has a greater charge density which makes it much more polarising in solution. The associated binding constants for fluoride binding in HEPES ( $K_1 = 71,400 \text{ M}^{-1}$  ( $\pm 9.0\%$ ),  $K_2 = 90 \text{ M}^{-1}$  ( $\pm 18.9\%$ )) are much higher than the Eu(III) analogue (**Figure-2.11**).

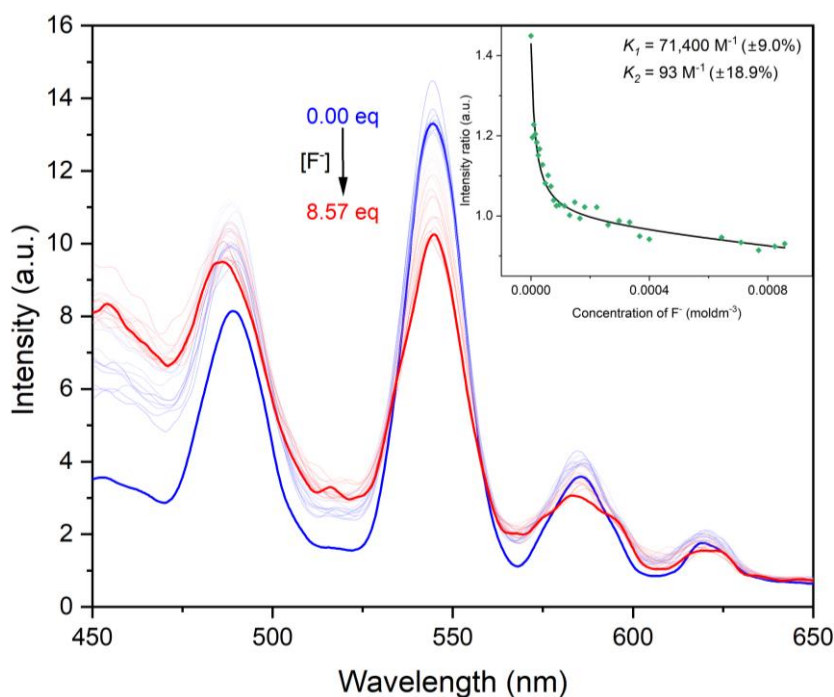


**Figure-2.11.** Graph showing the change in luminescence spectrum of Tb.p.DO3A ( $1 \times 10^{-4}$  mol dm $^{-3}$ ) in HEPES buffer (0.001 mol dm $^{-3}$ ), upon addition of increasing amounts of KF. With starting (blue) and end (red) concentrations highlighted,  $\lambda_{\text{ex}} = 226$  nm. *Inset:* binding isotherm from DynaFit $^{\text{®}}$ , plot of Intensity ratio of the  $\Delta J=6/\Delta J=5$  (dark-green) vs concentration of F $^{-}$ .

This reflects an increase in binding strength expected upon change of the lanthanide identity, making a second binding event distinguishable within the binding isotherm. This carries over into observations on **Figure-2.12** where a second binding mode for acetate to the lanthanide centre is distinguishable. This shows that even though acetate can bind in a bidentate fashion, there is the propensity for it to bind multiple times in a monodentate fashion, due to the preference for multiple hard anion donors due to the increasing Lewis acidity upon changing from Eu(III) to Tb(III).<sup>56</sup>

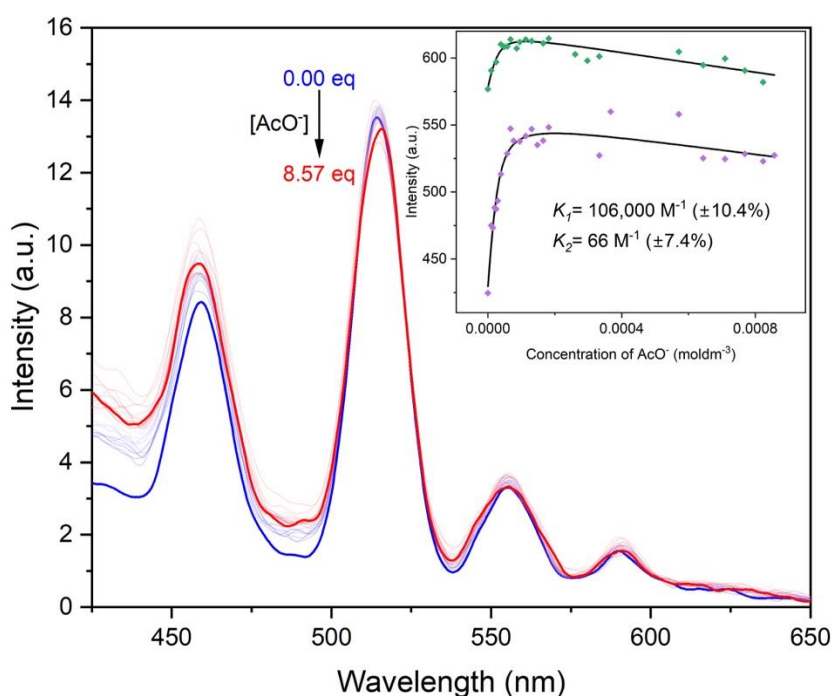


**Figure-2.12.** Graph showing the change in luminescence spectrum of Tb.p.DO3A ( $1 \times 10^{-4}$  mol dm $^{-3}$ ) in HEPES buffer (0.001 mol dm $^{-3}$ ), upon addition of increasing amounts of NaOAc. With starting (blue) and end (red) concentrations highlighted,  $\lambda_{\text{ex}} = 226$  nm. **Inset:** binding isotherm from DynaFit<sup>®</sup>, plot of the integrated intensity of  $\Delta J=6$  (dark-green) and  $\Delta J=5$  (purple) vs concentration of F $^{-}$ .

The binding constants for the Tris buffered titrations show similar values for the associated binding constants, also exhibiting the presence of a second binding event (Table-2.3).

**Table-2.3.** Binding constants of anions with Tb.p.DO3A complexes in aqueous media. <sup>§</sup>

Anion	Media*	Binding constant (M $^{-1}$ ) <sup>#</sup>	
		$K_1 = [\text{TbLX}]^{-}$	$K_2 = [\text{TbLX}_2]^{2-}$
Tb.p.DO3A			
F $^{-}$	water-HEPES	106,000 ( $\pm 11,000$ )	66.0 ( $\pm 4.9$ )
	water-Tris	176,000 ( $\pm 37,000$ )	97.3 ( $\pm 2.7$ )
AcO $^{-}$	water-HEPES	71,400 ( $\pm 6,500$ )	93.0 ( $\pm 18.0$ )
	water-Tris	37,600 ( $\pm 3,080$ )	75.0 ( $\pm 14.0$ )

\*All buffers are maintained at 0.01 M, pH 7.4; HEPES = N-(2-Hydroxyethyl)piperazine-N'-(2-ethanesulfonic acid) saline, Tris = trisaminomethane saline

<sup>#</sup> Error in brackets is represented as standard error in M $^{-1}$ . All data were plotted at the 95% confidence interval.

<sup>§</sup> The binding of anions was studied by steady-state fluorescence titrations of the complexes with varying concentrations of potassium fluoride and sodium acetate with binding isotherms generated using DynaFit<sup>®</sup>

These luminescence titrations have further explored the nature of the binding around these p.DO3A based complexes, confirming previously observed results and seeing the dramatic increase in binding strength with the use of a more charge dense lanthanide. Exploring the nature of the binding around the lanthanide centre is of importance as this serves to construct an image of how the anions will behave in a potential catalytic situation. Both complexes exhibit strong binding constants for anionic guests, this combined with the observation of two binding modes makes them good candidates for catalytic studies.

## **2.6 Catalytic studies**

In scoping studies done by Laura Mason.<sup>6</sup> The ability of lanthanide containing complexes to catalyse basic fluorination reactions was explored with the aim to create a facile way of fluorinating specific molecules. The reaction chosen to explore whether this was possible was the fluorination of halocarboxylic acids. A range of substrates were chosen that varied based upon several different factors such as steric constraints and electronic stability.

Chloroacetic acid was the most basic substrate, providing very little steric hindrance, with the leaving chloride group being in close proximity to the lanthanide at the centre of the complex. 3-Chloropropanoic acid introduces a -CH<sub>2</sub>- group in between the acetate binding moiety and the leaving group, probing the effectiveness of the catalyst over varying distances, as well as to observe any potential regioselectivity (**Figure-2.13**). With 2-chloro-2-phenylacetic acid, the presence of a phenyl group introduces a large degree of steric hindrance, yet also serves to stabilise the transition state of this substitution reaction. The product of this reaction will also be an enantiomer due to the presence of a chiral centre,

allowing the observation of whether there is an enantiomeric preference within these complexes.

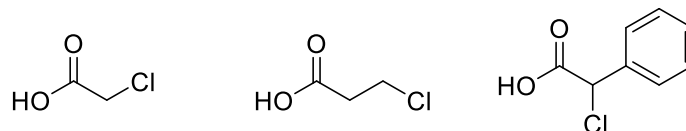


**Figure-2.13.** Chemical structures of chloroacetic acid (*left*), 3-chloropropanoic acid (*centre*) and 2-chloro-2-phenylacetic acid (*right*)

2-chloro-2-phenylacetic acid is insoluble in a D<sub>2</sub>O reaction medium. Therefore, it was converted to the sodium salt (sodium 2-chloro-2-phenylacetate) through addition of sodium hydroxide (**Figure-2.14**).

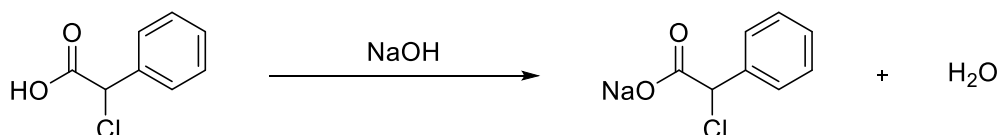


**Figure-2.14.** Conversion of 2-chloro-2-phenylacetic acid to sodium 2-chloro-2-phenylacetate.

## 2.6.1 NMR spectroscopy studies of fluorination

Chloroacetic acid was the first substrate studied. Physically for each measurement, for a volume of 0.6 mL the appropriate amounts were weighed out to have concentrations for TBAF, 0.1 mol dm<sup>-3</sup>; halocarboxylic acid substrate, 0.1 mol dm<sup>-3</sup>; catalyst under investigation, 0.01 mol dm<sup>-3</sup>. An initial control reaction was done to ensure that the reaction proceeded when the substrate and a fluoride source were combined in the same reaction vessel. This, and subsequent reactions were monitored for 12 hours, plotting the change in intensity of the fluorinated product's NMR signal (**Figure-2.15**).

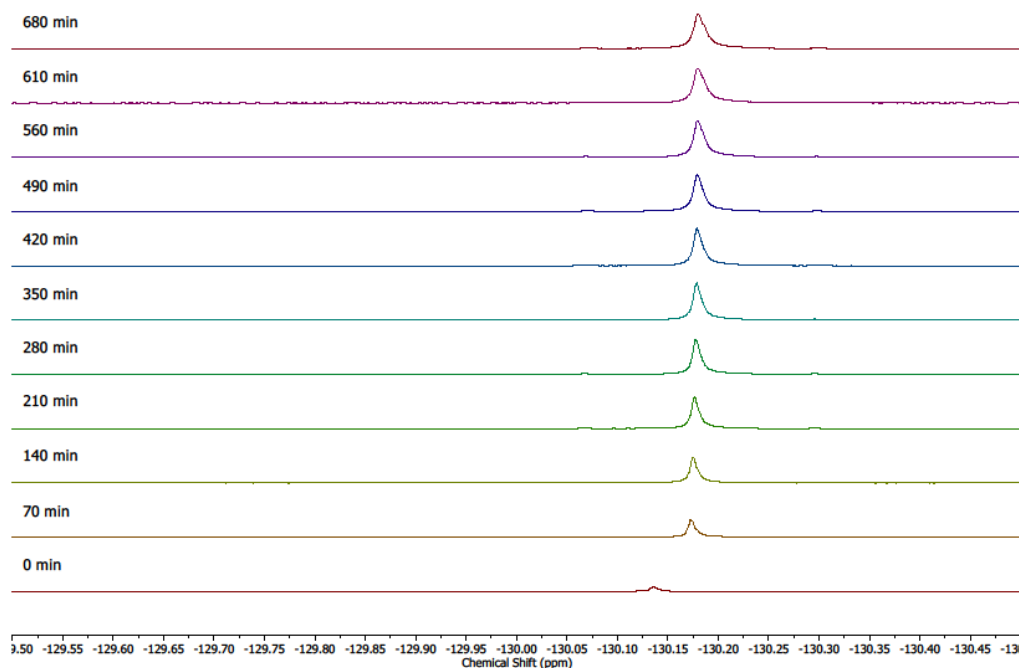


**Figure-2.15.**  $^{19}\text{F}$  NMR spectra of the control reaction between TBAF and chloroacetic acid over a 12-hour period.

This integrated intensity was then compared to the catalysed reactions. Particular interest was paid to the difference in initial rates of reaction, the effect of the catalyst on this and whether the reaction was believed to have gone to completion. Over the course of the reactions there is a change in the ionic charge of the solvent as the identity of the free ions in solution change during the course of the reaction.

This has the effect of the location of the TBAF fluoride peak migrating over the course of the reaction, causing it to cross the fluorinated product peak location, giving rise to an apparent spike in the intensity of the product peak. The points corresponding to this area are omitted to get an accurate description of the reaction progress, this was repeated for Eu.p.DO3A and some other examples further into this thesis. The first data set for Eu.p.DO3A (**Figure-2.16, top**) and Tb.p.DO3A (**Figure-2.16, bottom**) show a curious set of observations. Eu.p.DO3A works as

desired, causing an increase in both the initial rate and long-range rate. Despite this, the reaction does not appear to have gone to completion over the course of 12 h. Tb.p.DO3A initially exhibits a higher reaction rate but shows a decrease in reaction rate over time in comparison to the control reaction. This may indicate that, at lower concentrations of reactant, the concentration of reactants may become rate limiting as the reaction progresses.

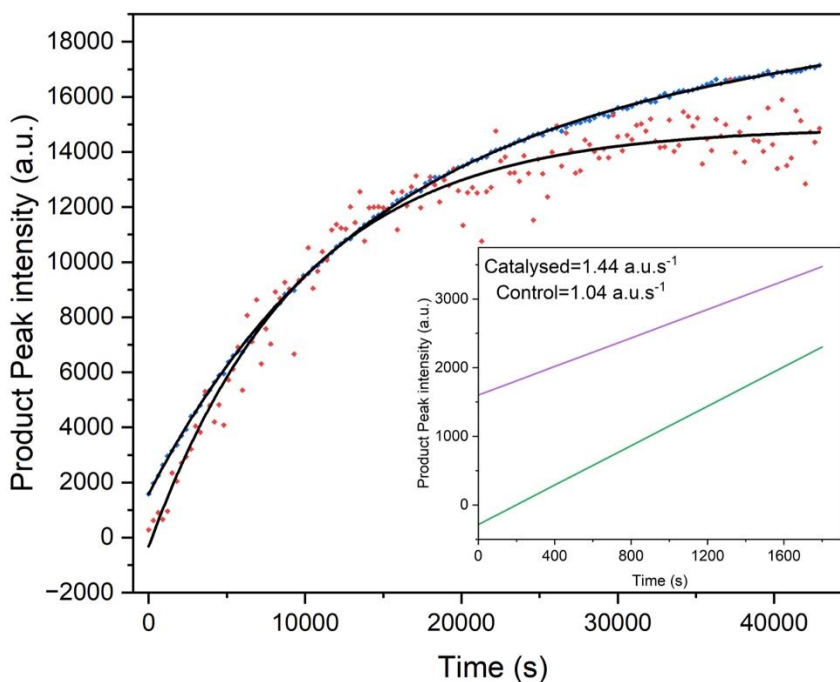
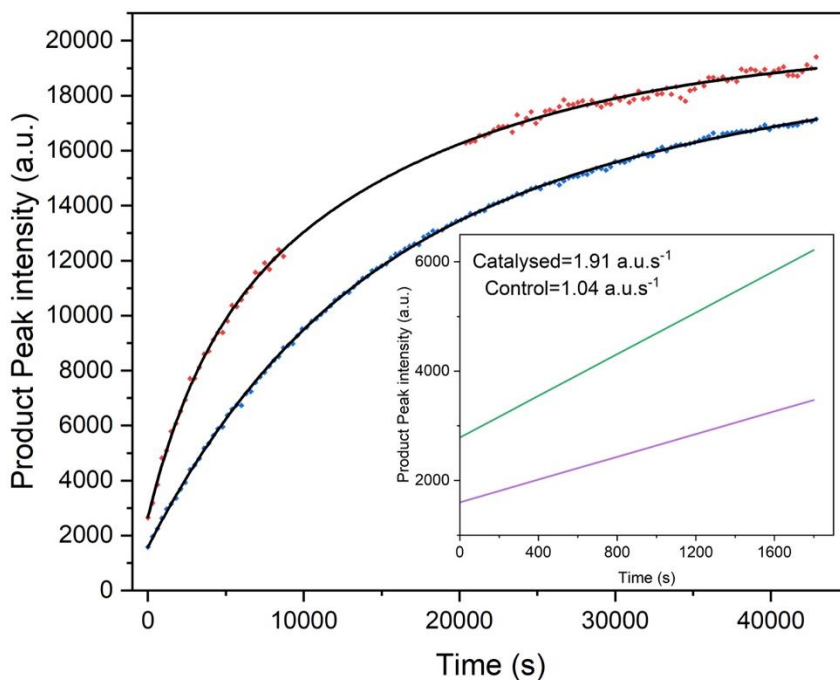


**Figure-2.16.** Graph of catalysed (10%mol) (red-scatter) and control (blue-scatter) reactions for the reaction of TBAF with chloroacetic acid with catalysts Eu.p.DO3A (*top*) and Tb.p.DO3A (*bottom*). Inset: Comparison of the initial rates of reaction between catalysed (dark-green) and control (purple) reactions, deduced by determining the gradient of a linear fit for the first 1800 s of the reaction being catalysed by Eu.p.DO3A (*top*) and Tb.p.DO3A (*bottom*).

To determine whether there was a regio-dependency of the observed catalysis, the experiment was repeated with a 3-chloropropanoic acid substrate. The control

reaction shows greatly decreased initial and overall reaction rates. This is to be expected due to the lack of a neighbouring carbonyl group to stabilise transition state formation through hyperconjugation (**Figure-2.17**).

A similar set of observations for the reactions with 3-chloropropanoic acid is observed. Eu.p.DO3A (**Figure-2.17, top**) works well to catalyse the progress of the reaction (points removed due to migration of the TBAF peak). Tb.p.DO3A (**Figure-2.17, bottom**) complex shows a similar observation as previously seen, with the complex initially catalysing then inhibiting the reaction as it progresses. This could be due to reagent concentrations limiting reaction rate or may reflect demetallation of the complex by precipitation of the associated lanthanide fluoride ( $\text{LnF}_3$ ).

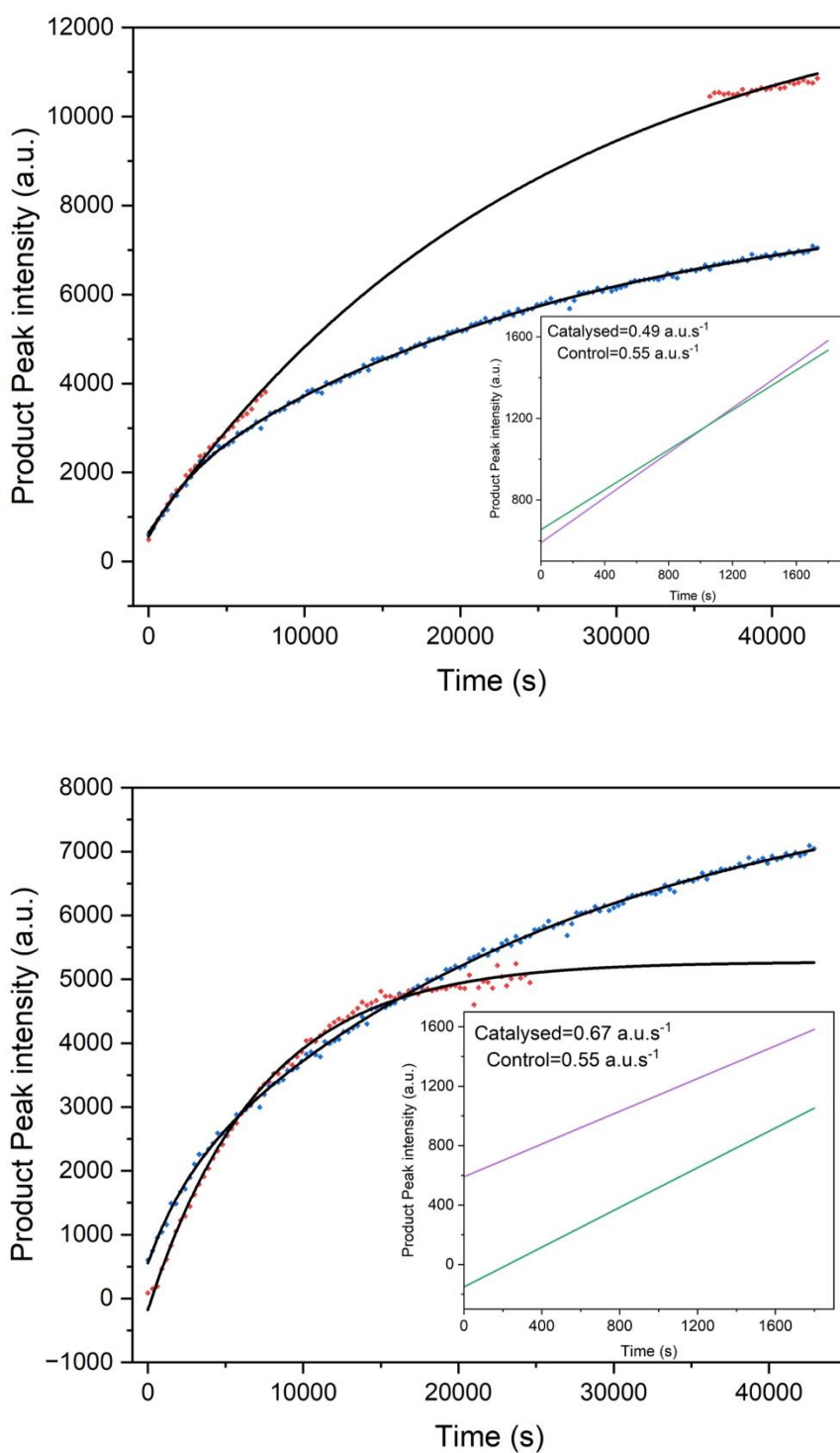


**Figure-2.17.** Graph of catalysed (10%mol) (red-scatter) and control (blue-scatter) reactions for the reaction of TBAF with 3-chloropropanoic acid with catalysts Eu.p.DO3A (*top*) and Tb.p.DO3A (*bottom*). Inset: Comparison of the initial rates of reaction between catalysed (dark-green) and control (purple) reactions, deduced by determining the gradient of a linear fit for the first 1800 s of the reaction being catalysed by Eu.p.DO3A (*top*) and Tb.p.DO3A (*bottom*).

To investigate how the presence of steric bulk would affect the catalytic ability of the complexes in question. The experiment was repeated using sodium

2-chloro-2-phenylacetate as the carboxylate substrate. This allowed observation of the potential for enantioselectivity and steric bulk dependence with the latter potentially hindering the reaction. The presence of a phenyl ring should serve to stabilise the transition state through conjugation with the  $\pi$ -system of the phenyl ring. The shape of the graphs differs greatly from the previous observations (**Figure-2.18**). The rate of reaction, for both control and catalysed variants, is greatly decreased and thus over the 12 h timescale an exponential decay cannot be fitted. The graph would imply initial inhibition of the reaction, potentially by the sodium ion in solution, with the slow initial increase in product peak intensity. With this being followed by the reaction rate increasing and proceeding at a uniform rate from 7500 s to the end of the 12 h period at 42900 s. In concordance with previous observations, both complexes catalyse the initial rate of reaction to the same degree. However, due to the slow rate of reaction, the reagent concentration does not get low enough to observe any reaction inhibition by the Tb.p.DO3A complex.

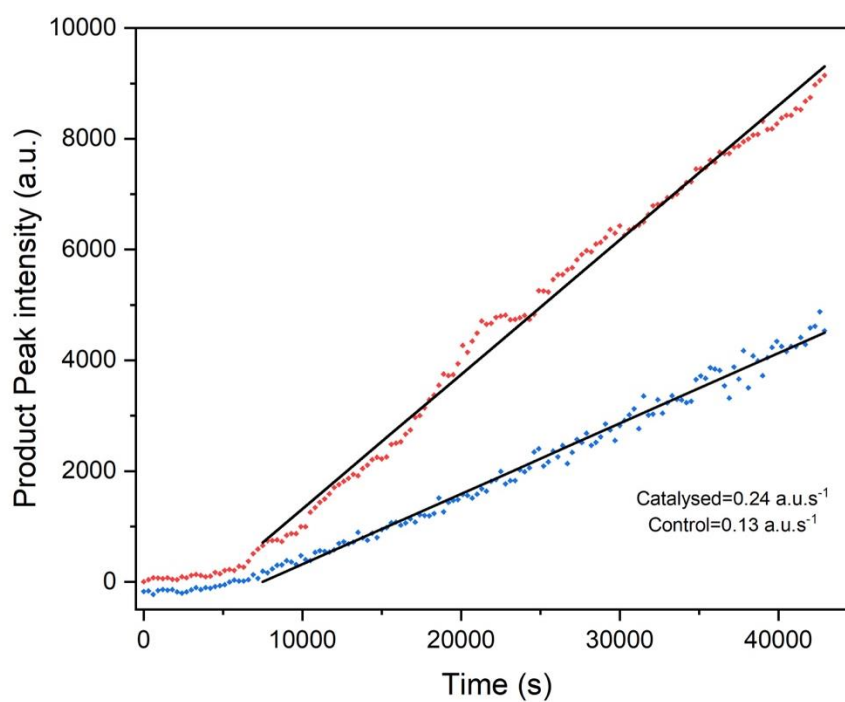
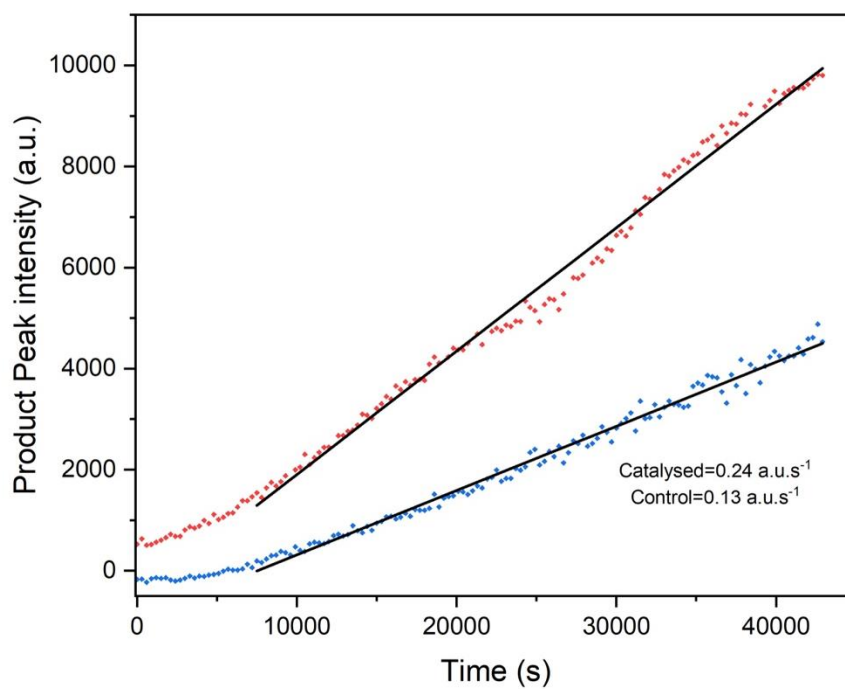


**Figure-2.18.** Graph of catalysed (10%mol) (red-scatter) and control (blue-scatter) reactions for the reaction of TBAF with sodium 2-chloro-2-phenylacetate with catalysts Eu.p.DO3A (*top*) and Tb.p.DO3A (*bottom*). Comparison of rates of reaction through corresponding linear fits (black).

The lack of solubility of the pure substrate and thus inclusion of a sodium ion introduces unwanted variables into this reaction, such as solvent polarity due to the inclusion of a cation. However, there is an overall effect on the rate of reaction as observed by the change upon inclusion of either of the complexes. This along with an associated change in the gradient of the linear fit, in this case representing the reaction rate, shows the complex's impact on the rate of reaction showing their activity as catalysts.

### 2.6.2 Conclusions on catalytic studies

The investigation into the potential catalytic abilities of the Ln.p.DO3A complexes was promising. Confirming and expanding upon previous observations, while exploring how the variation of lanthanide identity affected these properties.<sup>6</sup> Solubility limitations in the third substrate (2-chloro-2-phenylacetic acid) meant less useful data could be extracted, yet they were still deemed to provide significant evidence of catalysis of the sodium salt of the substrate (sodium 2-chloro-2-phenylacetate). The first two substrates provided compelling evidence for catalysis of fluorination reactions in aqueous media, with Eu.p.DO3A proving to be an effective catalyst. In both support and contrast of this, Tb.p.DO3A showed high initial rates of reaction, but the rate decreased over the course of the 12 h time period. This decrease in reaction rate could be due to several factors, chiefly lanthanide precipitation. The high binding constants observed in **Table-2.2**, demonstrate a strong interaction between Tb(III) and F<sup>-</sup>, the extreme of this would be formation of TbF<sub>3</sub>. TbF<sub>3</sub> being insoluble in aqueous media would precipitate out of solution, resulting in removal of both the fluoride source and the reaction catalyst. This hypothesis seems the most likely case, precipitation is observed for

all of the catalytic reactions due to the instability of heptadentate complexes in both aqueous media and fluoride containing solutions over time. This combined with observations by Cordfunke *et al*<sup>57</sup>. on the formation enthalpies of lanthanide oxides, demonstrating the greater binding strength of Tb(III) with hard anions in comparison to Eu(III), leading to the conclusion that precipitation of terbium fluoride, or alternatively terbium hydroxide as the most likely cause of reaction inhibition.

## 2.7 Summary and conclusions

This Chapter has covered the initial synthesis of a series of Ln.p.DO3A complexes, to act as prototype systems for the DO3AM derivatives covered later in this thesis. From initial synthesis an Eu(III) and Tb(III) complex were carried forward. Luminescence titrations were carried out on both complexes with KF and NaOAc, in aqueous media. This data was processed and through the use of DynaFit<sup>®</sup> iterative fitting software, binding events and their associated binding constants were assigned and quantified respectively.<sup>5</sup> From this data was concluded that these complexes exhibit two binding modes, with one of greater strength (equatorial) and the other comparatively weaker (axial). As such, they were deemed suitable for use as catalysts in an appropriate reaction set. The fluorination of halocarboxylic acids was chosen as a suitable reaction set, with the application of selective fluorination for PET imaging being deemed of interest. Catalytic studies were carried out, this comprised observing the appearance of a given product peak over a 12 h period and monitoring the rate of change at different points, most importantly in the initial reaction stages. This provided conclusive evidence for these complexes acting as catalysts. The Eu(III) containing complexes showed an acceleration in reaction rate

across all reactions and all timeframes. However, the Tb(III) analogues showed limitations upon prolonged exposure as they precipitated out of solution, removing both substrate and catalyst from the reaction. As such it was decided to proceed with only Eu(III) containing complexes later in this thesis, to prevent repetition of the same observations covered in **Section-2.7.1**.

## 2.8 References

- 1 J. S. Fowler and T. Ido, *Semin Nucl Med*, 2002, **32**, 6–12.
- 2 J. S. Wright, T. Kaur, S. Preshlock, S. S. Tanzey, W. P. Winton, L. S. Sharninghausen, N. Wiesner, A. F. Brooks, M. S. Sanford and P. J. H. Scott, *Clin Transl Imaging*, 2020, **8**, 167–206.
- 3 M. Failla, G. Floresta and V. Abbate, *RSC Med Chem*, 2023, **14**, 592–623.
- 4 J. Rong, A. Haider, T. E. Jeppesen, L. Josephson and S. H. Liang, *Nat Commun*, 2023, **14**, 3257.
- 5 P. Kuzmič, *Anal Biochem*, 1996, **237**, 260–273.
- 6 Laura. Mason, DPhil thesis, University of Oxford, 2017.
- 7 R. Mansi, X. Wang, F. Forrer, S. Kneifel, M.-L. Tamma, B. Waser, R. Cescato, J. C. Reubi and H. R. Maecke, *Clinical Cancer Research*, 2009, **15**, 5240–5249.
- 8 S. I. Presolski, V. P. Hong and M. G. Finn, *Curr Protoc Chem Biol*, 2011, **3**, 153–162.
- 9 M. Wagner, R. Ruloff, E. Hoyer and W. Gründer, *Zeitschrift für Naturforschung C*, 1997, **52**, 508–515.
- 10 P. Caravan, J. J. Ellison, T. J. McMurry and R. B. Lauffer, *Chem Rev*, 1999, **99**, 2293–2352.
- 11 G. McMullon, DPhil thesis, University of Oxford, 2022.
- 12 L. Tear, DPhil thesis, University of Oxford, 2018.
- 13 T. J. Sørensen and S. Faulkner, *Acc Chem Res*, 2018, **51**, 2493–2501.
- 14 D. Parker, R. S. Dickins, H. Puschmann, C. Crossland and J. A. K. Howard, *Chem Rev*, 2002, **102**, 1977–2010.
- 15 S. J. Butler and D. Parker, *Chem. Soc. Rev.*, 2013, **42**, 1652–1666.
- 16 S. E. Bodman and S. J. Butler, *Chem Sci*, 2021, **12**, 2716–2734.
- 17 P. Caravan, C. T. Farrar, L. Frullano and R. Uppal, *Contrast Media Mol Imaging*, 2009, **4**, 89–100.
- 18 M. Allen, *Synlett*, 2016, **27**, 1310–1317.
- 19 S. Hapuarachchige and D. Artemov, *Topics in Magnetic Resonance Imaging*, 2016, **25**, 205–213.
- 20 M. Tropiano, A. M. Kenwright and S. Faulkner, *Chemistry - A European Journal*, 2015, **21**, 5697–5699.
- 21 A. K. R. Junker, M. Tropiano, S. Faulkner and T. J. Sørensen, *Inorg Chem*, 2016, **55**, 12299–12308.

- 22 C. Allain, P. D. Beer, S. Faulkner, M. W. Jones, A. M. Kenwright, N. L. Kilah, R. C. Knighton, T. J. Sørensen and M. Tropicano, *Chem. Sci.*, 2013, **4**, 489–493.
- 23 C. Cossy, L. Helm and A. E. Merbach, *Inorg Chem*, 1988, **27**, 1973–1979.
- 24 A. Takács, R. Napolitano, M. Purgel, A. C. Bényei, L. Zékány, E. Brücher, I. Tóth, Z. Baranyai and S. Aime, *Inorg Chem*, 2014, **53**, 2858–2872.
- 25 J. W. Walton, A. Bourdolle, S. J. Butler, M. Soulie, M. Delbianco, B. K. McMahon, R. Pal, H. Puschmann, J. M. Zwier, L. Lamarque, O. Maury, C. Andraud and D. Parker, *Chem. Commun.*, 2013, **49**, 1600–1602.
- 26 M. L. P. Reddy, K. S. Bejoymohandas and V. Divya, *Dyes and Pigments*, 2022, **205**, 110528.
- 27 T. Boltersdorf, F. N. E. Gavins and N. J. Long, *Chem Sci*, 2021, **12**, 8740–8745.
- 28 G. J. Stasiuk and M. P. Lowe, *Dalton Trans.*, 2009, 9725–9727.
- 29 H.-J. Wu, F.-H. Ying and W.-D. Shao, *J. Org. Chem*, 1995, **60**, 6168–6172.
- 30 N. H. Evans, *Chempluschem*, 2020, **85**, 783–792.
- 31 C. Alexander, J. A. Thom, A. M. Kenwright, K. E. Christensen, T. J. Sørensen and S. Faulkner, *Chem Sci*, 2023, **14**, 1194–1204.
- 32 L. R. Tear, M. L. Maguire, M. Tropicano, K. Yao, N. J. Farrer, S. Faulkner and J. E. Schneider, *Dalton Trans.*, 2020, **49**, 2989–2993.
- 33 L. R. Tear, C. Carrera, E. Gianolio and S. Aime, *Chem. Eur. J.*, 2020, **26**, 6056–6063.
- 34 G. P. Castro, L. L. L. S. Melo, F. Hallwass, S. M. C. Gonçalves and A. M. Simas, *Dalton Trans.*, 2021, **50**, 10193–10205.
- 35 J.-C. G. Bünzli and C. Piguet, *Chem Soc Rev*, 2005, **34**, 1048.
- 36 S. V. Eliseeva and J.-C. G. Bünzli, *Chem. Soc. Rev.*, 2010, **39**, 189–227.
- 37 D. Parker, J. D. Fradgley and K.-L. Wong, *Chem Soc Rev*, 2021, **50**, 8193–8213.
- 38 A. V. Orlova, V. Yu. Kozhevnikova, A. S. Goloveshkin, L. S. Lepnev and V. V. Utochnikova, *Dalton Trans.*, 2022, **51**, 5419–5425.
- 39 S. P. Sinha, *Helv Chim Acta*, 1975, **58**, 1978–1983.
- 40 G. Tircso, B. C. Webber, B. E. Kucera, V. G. Young and M. Woods, *Inorg Chem*, 2011, **50**, 7966–7979.
- 41 C. Kumas, W. S. Fernando, P. Zhao, M. Regueiro-Figueroa, G. E. Kiefer, A. F. Martins, C. Platas-Iglesias and A. D. Sherry, *Inorg Chem*, 2016, **55**, 9297–9305.
- 42 O. A. Blackburn, A. M. Kenwright, P. D. Beer and S. Faulkner, *Dalton Trans.*, 2015, **44**, 19509–19517.

- 43 A. de Bettensourt-Dias, *Luminescence of Lanthanide Ions in Coordination compounds and Nanomaterials*, 1st edn., 2014.
- 44 K. Binnemans, *Coord Chem Rev*, 2015, **295**, 1–45.
- 45 L. R. Hill, T. J. Sørensen, O. A. Blackburn, A. Brown, P. D. Beer and S. Faulkner, *Dalton Trans.*, 2013, **42**, 67–70.
- 46 M. Tropiano, O. A. Blackburn, J. A. Tilney, L. R. Hill, M. P. Placidi, R. J. Aarons, D. Sykes, M. W. Jones, A. M. Kenwright, J. S. Snaith, T. J. Sørensen and S. Faulkner, *Chem. Eur. J.*, 2013, **19**, 16566–16571.
- 47 O. A. Blackburn, A. M. Kenwright, A. R. Jupp, J. M. Goicoechea, P. D. Beer and S. Faulkner, *Chem. Eur. J.*, 2016, **22**, 8929–8936.
- 48 O. A. Blackburn, R. M. Edkins, S. Faulkner, A. M. Kenwright, D. Parker, N. J. Rogers and S. Shuvaev, *Dalton Trans.*, 2016, **45**, 6782–6800.
- 49 A. K. R. Junker, L. R. Hill, A. L. Thompson, S. Faulkner and T. J. Sørensen, *Dalton Trans.*, 2018, **47**, 4794–4803.
- 50 C.-Q. Xiao, Q. Huang, Y. Zhang, H.-Q. Zhang and L. Lai, *Thermochim Acta*, 2020, **691**, 178721.
- 51 G. J. Pielak, *Biochemistry*, 2021, **60**, 3436–3440.
- 52 T. Kowada, H. Maeda and K. Kikuchi, *Chem Soc Rev*, 2015, **44**, 4953–4972.
- 53 B. Daly, J. Ling and A. P. de Silva, *Chem. Soc. Rev.*, 2015, **44**, 4203–4211.
- 54 N. S. Poluéktov, I. I. Zheltvai, G. I. Gerasimenko, M. A. Tishchenko and A. A. Kucher, *<sup>3</sup>J<sub>HH</sub> Appl Spectrosc*, 1976, **24**, 189–192.
- 55 S. V. Eliseeva and J.-C. G. Bünzli, *Chem. Soc. Rev.*, 2010, **39**, 189–227.
- 56 J. C. G. Bünzli, *<sup>3</sup>J<sub>HH</sub> Coord Chem*, 2014, **67**, 3706–3733.
- 57 E. H. P. Cordfunke and R. J. M. Konings, *Thermochim Acta*, 2001, **375**, 65–79.

## Chapter 3: Synthesis of DO3AM derivatives

### 3.1 DO3AM and DOTAM complexes

DOTAM is the tetra amide analogue of DOTA (**Figure 3.1**).<sup>1,2</sup> Like DOTA, DOTAM forms lanthanide complexes with high kinetic stability but comparatively lower thermodynamic stability; yet the high kinetic stability makes it suitable for purposes similar to DOTA, as contrast agents and in medical imaging applications.<sup>3-5</sup> One of the main points of interest of DOTAM is the possibility of further functionalisation of the amide pendant arms on the periphery of the ligand.<sup>6</sup> With two hydrogen atoms available for substitution, this allows for the creation of more diverse ligands.

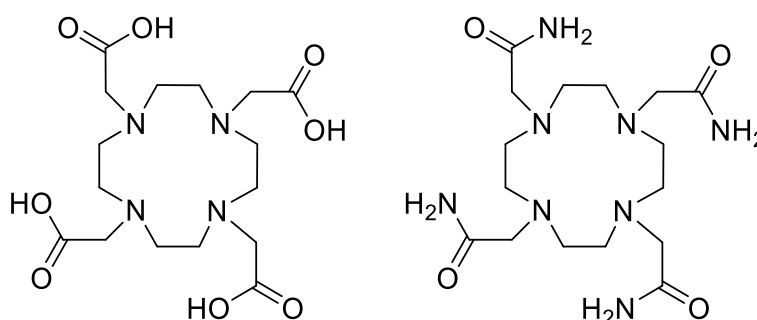


**Figure 3.1.** Chemical structures of DOTA (*left*) and DOTAM (*right*).

For the purposes of this thesis, the inclusion of an amide pendant arm enables modification of the coordination sphere significantly by exploiting electronic effects on amide substituents.<sup>7</sup> Desirable properties such as solubility and rigidity can be incorporated and these could potentially influence a complexes first solvation sphere.<sup>8</sup> DO3AM is the tri-amide analogue of DO3A (**Figure 3.2**). DO3AM differs from DOTAM, as it forms complexes with dramatically reduced kinetic stability, as does its acidic analogue, DO3A to DOTA. This makes tailoring

the ligand properties of paramount importance as creation of a rigid ligand through the inclusion of specific arms will help prevent demetallation and hence a loss of functionality.

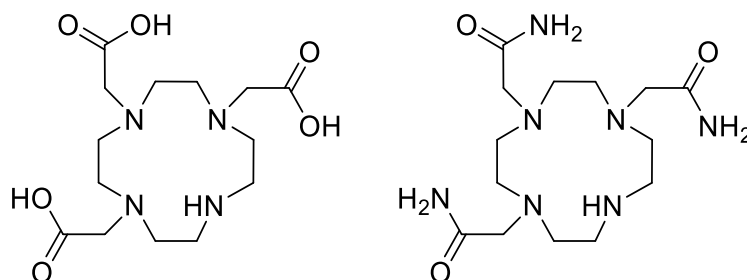


**Figure 3.2.** Chemical structures of DO3A (*left*) and DO3AM (*right*).

Incorporation of rigid and bulky groups is necessary in these cases, so the selection of pendant arms played a major role in deciding which complexes to make.

### 3.1.1 Applications and uses of DO3AM and DOTAM

DOTAM based macrocycles have been used as chelating ligands to create novel Ln(III) complexes, for many applications.<sup>9,10</sup> Investigations by Dunand *et al.*<sup>11</sup> sought to optimise water exchange rates in DOTAM, DTMA and DOTMAM complexes (**Figure-3.3**). Where the presence of a methyl group bound to an amide or  $\alpha$  to the cyclen ring affects both the number of potential isomers present, and their specific water exchange rates. To probe their structure the Eu(III) complexes were made, showing the ratio of TSAP/SAP isomerism present. With water exchange being favoured in the TSAP form over the SAP form ( $[\text{Eu}(\text{dtma})(\text{H}_2\text{O})]^{3+}:k_{\text{ex}}^{298}$  SAP =  $8.2 \pm 0.2 \times 10^3 \text{ s}^{-1}$ , TSAP =  $352 \pm 97 \times 10^3 \text{ s}^{-1}$ ), the rate of water exchange was shown to depend upon the ratio of these isomers hence the rate of interconversion of the TSAP and SAP isomers.

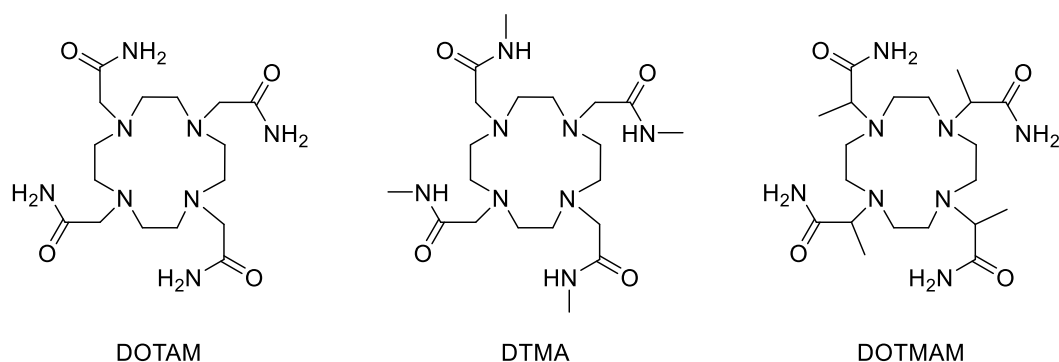


**Figure-3.3.** Chemical structures of DOTAM (1,4,7,10-tetrakis(carbamoylmethyl)-1,4,7,10-tetraazacyclododecane, *left*), DTMA (1,4,7,10-tetrakis- (N-methylcarbamoylmethyl)-1,4,7,10-tetraazacyclododecane, *centre*) and DOTMAM (1,4,7,10-tetrakis(methylcarbamoylmethyl)-1,4,7,10-tetraazacyclododecane, *right*)

DOTAM has also been exploited as a ligand separate for inclusion in metal complexes. For example, Nazare *et al.* altered the DOTAM scaffold.<sup>12</sup> Onto this ligand was appended three targeting groups and one fluorescent moiety, with the macrocyclic cavity remaining empty (**Figure-3.4**). Ligands such as these are becoming more prevalent as their use as multimodal imaging agents becomes more researched.

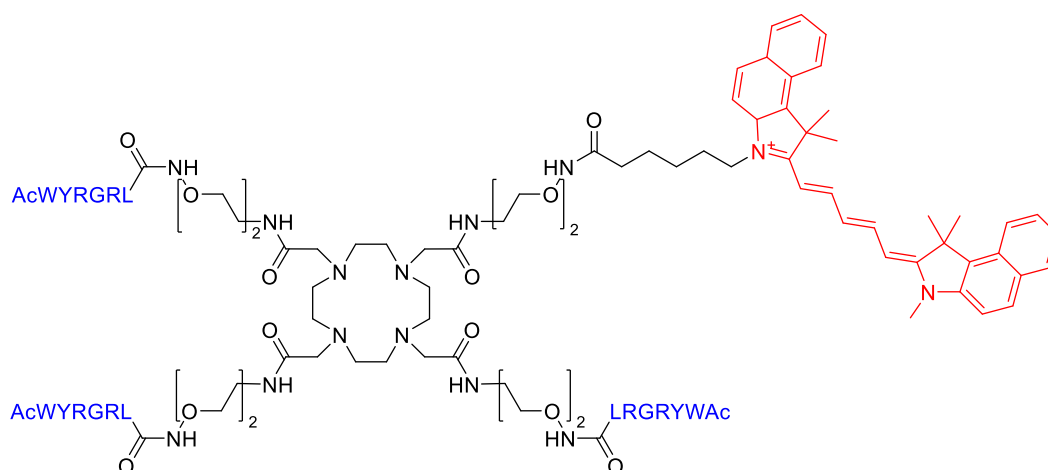


**Figure-3.4.** Chemical structure of (AcWYRGRL)<sub>3</sub>-DOTAM-Cy5.5 **3TP**, containing three collagen II targeting peptides (**blue**) and a fluorescing (Cy5.5) moiety (**red**). AcWYRGRL = acetylated-tryptophan-tyrosine-arginine-glycine-arginine-leucine, Cy 5.5 = Cyanine-5.5.

Other research carried out by Hudson *et al.* has investigated DOTAMs applications for *in vivo* cartilage imaging (**Figure-3.5**).<sup>13</sup>

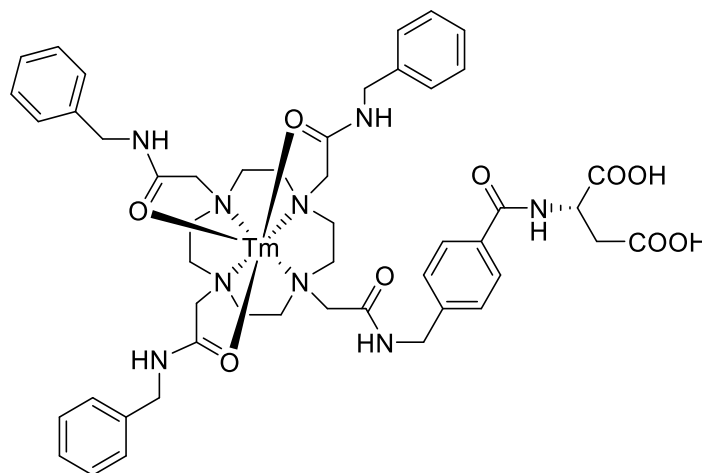


**Figure-3.5.** Tm(III) DOTAM alkyl complexes for application as PARACEST and MRI contrast agents.

In combination with a central lanthanide ion (Tm(III)) these have seen promising potential as CEST or PARACEST agents, with the overall aim to decrease the positive charge associated with these molecules thus increasing their biocompatibility. Despite these myriad uses and research into DOTAM, both as a ligand in complexes and as a molecule, DO3AM has not seen such extensive research. Its relatively low kinetic and thermodynamic stability renders it ineffective for most complex applications, especially for *in vivo* applications, as lanthanide *in vivo* deposition can lead to extensive health issues.<sup>14</sup>

### 3.2 Aim and scope

The aim of this work is to further explore the nature of lanthanide complexes based upon a DO3AM framework and to utilise them for catalytic fluorination. This area has been underexplored in comparison to DOTA, DO3A and DOTAM based complexes. The initial aim will be to synthesise an appropriate set of ligands with

desirable qualities such as rigidity and solubility. These ligands will be complexed with Eu(III), and their photophysics explored. Photophysical and NMR spectroscopic characterisation of the complexes will allow deduction of the conformational preference of each complex. This will yield more information on the local solvation sphere, and provide information on the potential catalytic ability of the complexes. The catalytic activity is investigated in Chapter-6. This Chapter focuses on investigating the effect these ligands have on chirality at the metal centre and provide the means to explore enantioselectivity in fluorination reactions. Furthermore, these systems give the option to retain positive charge, as neutral coordinating amide groups create an overall positive charge on the complex. Variation of the functional groups present in the ligands created will allow exploration of the role of charge in various factors primarily the solubility of DO3AM derived complexes. A specific aim being to increase the positive charge on the ligand periphery, such that upon formation of a complex with a positively charged periphery, this will prevent aggregation between neighbouring molecules through electrostatic interactions. This overall positive charge will persist throughout the complexation of a pair of anionic guests, making them an ideal candidate for application as homogeneous catalysts (**Figure-3.6**).

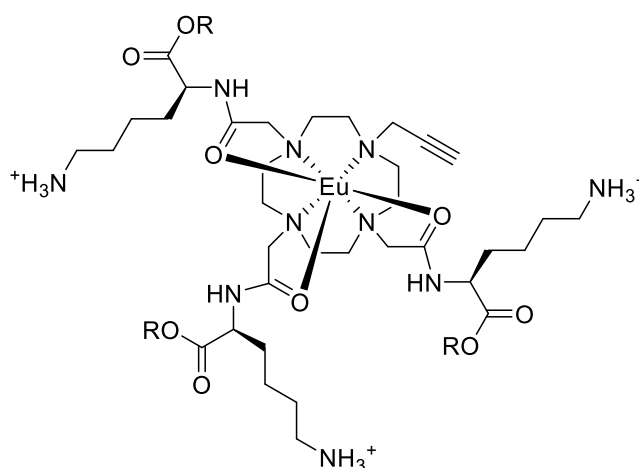


**Figure-3.6.** General chemical structure of  $[\text{Eu.p.DO3AM.Lys.OR}]^{6+}$  ( $\text{R} = \text{-Me, -'Bu}$ ) with amine arms protonated in aqueous solution.

### 3.3 Design strategy for p.DO3AM ligands

The DO3AM motif initially required modification by blocking the fourth amine position on the ring. Blocking this position with a small group allows for anion binding in this empty coordination site. Previous work done by the Faulkner group has proved the existence of two different anion binding modes in complexes based on a DO3AM motif, with this initially being discovered for the Eu.p.DO3AM.Asp.O<sup>t</sup>Bu complex (**Figure-3.7**).<sup>15</sup>

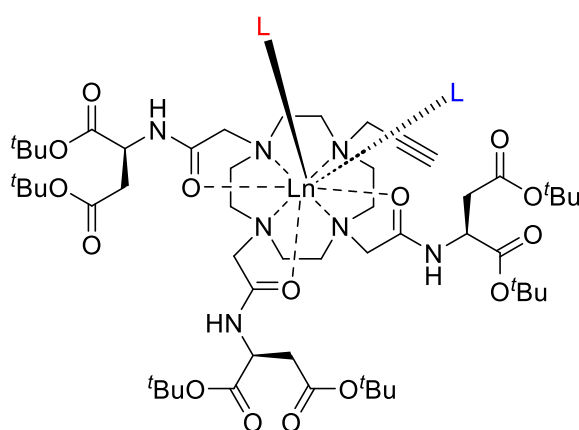


**Figure-3.7.** Chemical structure of Eu.p.DO3AM.Asp.O<sup>t</sup>Bu with axial (red) and equatorial (blue) binding modes.

These two binding modes, one axial and one equatorial, have different binding constants with the axial being smaller than the equatorial.<sup>13</sup> The axial binding mode is much weaker hence the ligand in this position is deemed to be in fast exchange. The equatorial binding mode is comparatively stronger, with this position being exchanged on a slower timeframe.<sup>13</sup> This was a promising catalyst for fluorination reactions. However, Eu.p.DO3AM.Asp.O<sup>t</sup>Bu was insoluble in water, a desirable solvent for this reaction. This, along with Eu.p.DO3AM.Asp.OH aggregating in solution made these unfeasible catalysts (**Figure-3.8**).

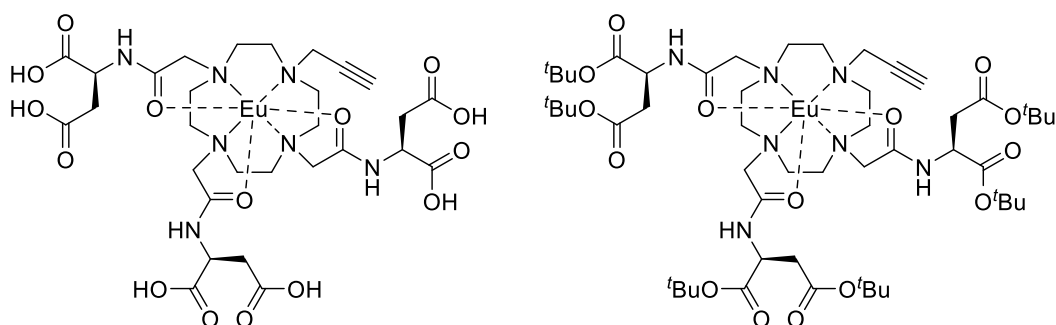


**Figure-3.8.** Chemical structures of Eu.p.DO3AM.Asp.OH (*left*) and Eu.p.DO3AM.Asp.O<sup>t</sup>Bu (*right*).

To allow ion coordination at both positions, a suitably small blocking group must be utilised to prevent unwanted side reactions on the unsubstituted amine position on the ring. Previous research carried out in the Faulkner group sought to compare the anion binding positions of the complexes Eu.p.DO3A and Eu.m.DO3A (**Figure 3.9**).

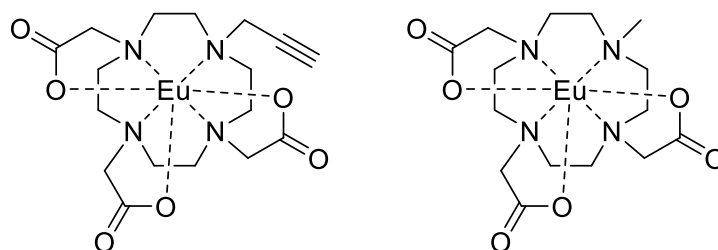


**Figure-3.9.** Chemical structures of Eu.p.DO3A (*left*) and Eu.m.DO3A (*right*).

Inclusion of a methyl group as in Eu.m.DO3A (**Figure-3.9**, *left*), as opposed to a propargyl group Eu.p.DO3A (**Figure-3.9**, *right*), led to comparatively lower solubility of the overall complex. Studies were therefore continued with propargyl, due to the synthetic ease with which this group could be appended to the cyclen ring, along with the increased solubility of the complex. The propargyl group is a well-researched addition to DO3A and DO3AM based ligands. It has been researched extensively as a handle for ‘click’ chemistry, providing a facile way to append desirable groups to a large macrocycle.<sup>16,17</sup> Based upon the synthetic ease and precedent within this field it was selected as a blocker for the fourth amine position on the ring.

### 3.3.1 Selection of pendant arms

The pendant arms on the periphery of the cyclen based macrocycles dictate a lot of the overall properties of the complex. This allows engineering of desirable properties by the inclusion or exclusion of specific functional groups, combined with well-known protecting groups and facile protecting strategies, this can afford multiple ligands for investigation. For example, in previous research done by the Faulkner group on the Eu.p.DO3AM.Asp.OH complex (**Figure-3.7**) in water; aggregation was observed and the complex precipitated out of solution, meaning

the ligand must be designed to avoid this observation.<sup>15</sup> From evidence gathered from photophysical studies, it was deduced that this was due to binding between neighbouring complexes by bridging acetate groups. This demonstrates that modification of the pendant arms can cause drastic changes in solution phase properties such as hydrophilicity, hence the opportunity for modification can vary greatly. This has mainly been exploited to add targeting moieties onto the ligand periphery, such as in work carried out by Brennecke *et al* (**Figure-3.10**), this aspect of DOTAMs structure continues to encourage novel research in this area.<sup>18</sup>

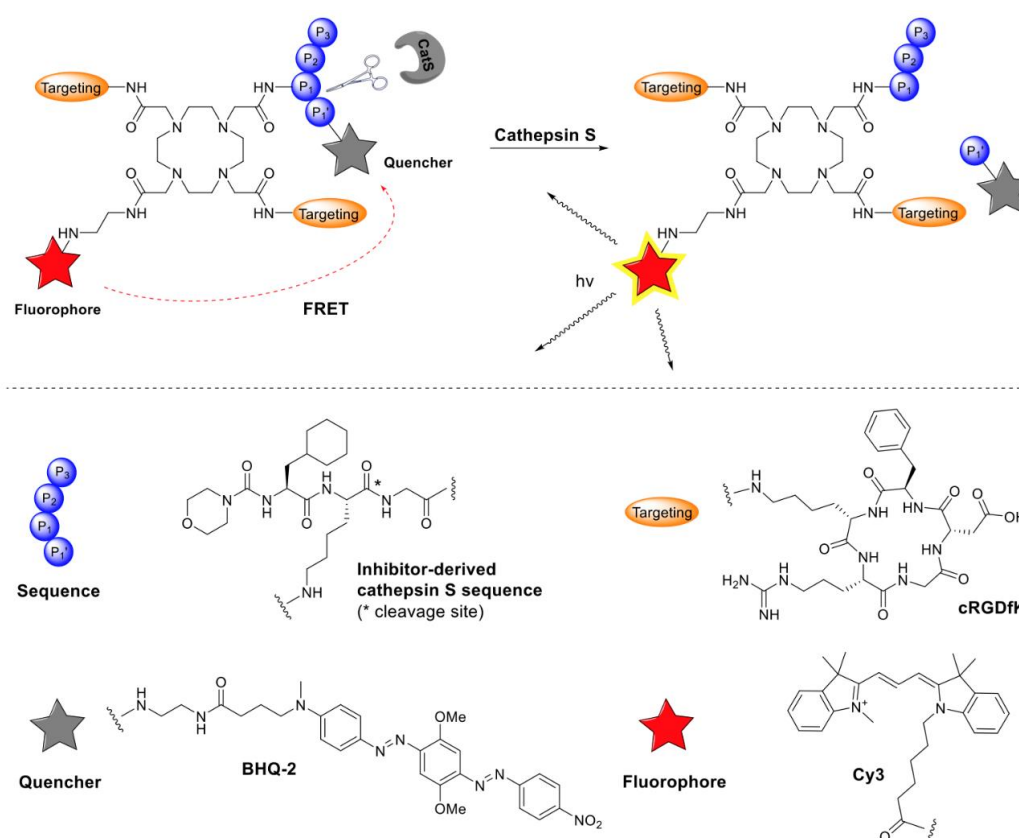


**Figure-3.10.** Example of a DOTAM based macrocycle with modified pendant arms that can act as targeting, quenching and fluorescing moieties. *Top:* Schematic representation of a targeted, activatable cathepsin S fluorescent probe on a DOTAM based macrocycle. *Bottom:* structural representation of the appended moieties, including cRGDfK targeting unit, BHQ-2 quencher, and Cy3 dye. Reproduced from reference.<sup>18</sup>

Chiral catalysis is a growing and important field and to achieve enantioselectivity a catalyst must contain a pre-organised active site, this enables the reaction to proceed via a specific conformational reaction pathway resulting in one enantiomer.<sup>19</sup> Inclusion of chiral pendant arms enforces this chirality around the lanthanide centre, leading to a predominant isomer for the ligand and complex as a whole. A series of chiral molecules was therefore needed, an easy source of chiral molecules is the  $\alpha$ -amino acid series. The amino acids used are available commercially as one enantiomer, allowing the potential for a conformational preference due to the use of a single isomer, in this thesis L-enantiomers were used.

The  $\alpha$ -amino acid series has many structural attributes, the presence of a chiral carbon and a R group that can be varied. The R group allows incorporation of desired functional groups, with these groups having good aqueous solubility, high rigidity and exhibiting chirality. A specific aim is to negate the propensity for complex aggregation, as seen in complexes with negatively charged complex arms.<sup>15</sup> L-lysine contains an amine group as the 'R' sidechain, with a  $pK_a$  in the 9.5-11.0 range this will be protonated in aqueous media (**Figure-3.11**). Decreasing the propensity for aggregation and promoting solubility through charge separation. This thesis employs a range of protected lysine amino acid derivatives. Orthogonal protection is of great importance in these arms. The inclusion of two different protecting groups on lysine, one on the side chain amine and the second on the carboxylic acid, allows selective deprotection of the amine group. Four such mixed systems were chosen (**Figure-3.11**).

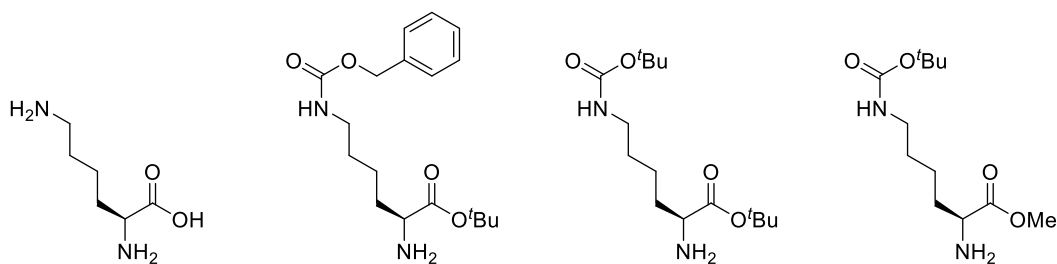


**Figure-3.11** Chemical structures of L-lysine (furthest-left), tert-butyl N<sup>6</sup>-((benzyloxy)carbonyl)-L-lysinate (centre-left), tert-butyl N<sup>6</sup>-(tert-butoxycarbonyl)-L-lysinate (centre-right) and methyl N<sup>6</sup>-(tert-butoxycarbonyl)-L-lysinate (furthest-right). Referred to as Lys, Lys.CBz.O<sup>t</sup>Bu, Lys.O<sup>t</sup>Bu.O<sup>t</sup>Bu and Lys.O<sup>t</sup>Bu.OMe respectively.

Due to synthetic constraints mentioned later in this thesis Lys.O<sup>t</sup>Bu.OMe became desirable due to the ease of removal of the amine ‘Boc’ protecting group. Phenylalanine (**Figure-3.12**) was the second pendant arm. With a phenyl group as the ‘R’ group in this case. While having a negative impact upon the solubility in aqueous media, the phenyl group could act as a chromophore for the lanthanide centre.

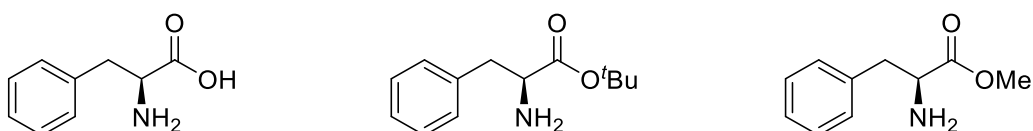


**Figure-3.12.** Chemical structures of L-phenylalanine (left), tert-butyl L-phenylalaninate (centre), methyl L-phenylalaninate (right). Referred to as Phen, Phen.O<sup>t</sup>Bu, Phen.OMe respectively.

This efficient method of lanthanide excitation proved to be less useful for these complexes due to poor overlap between the phenyl chromophore and lanthanide excited states. This chromophore does not offer an effective excitation pathway for these complexes, as excitation at the chromophores absorption wavelength did not yield a characteristic Eu(III) luminescence spectrum. Despite this, direct excitation still worked well for this complex, enabling probing of the coordination environment around the Eu(III) ion.

Proline (**Figure-3.13**) differs from the other ligands in that the side chain group includes a five-membered ring that includes the amine group.

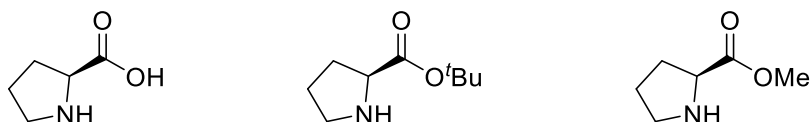


**Figure-3.13.** Chemical structures of L-proline (left), tert-butyl L-prolinate (centre), methyl L-prolinate (right). Referred to as Pro, Pro.O<sup>t</sup>Bu, Pro.OMe respectively.

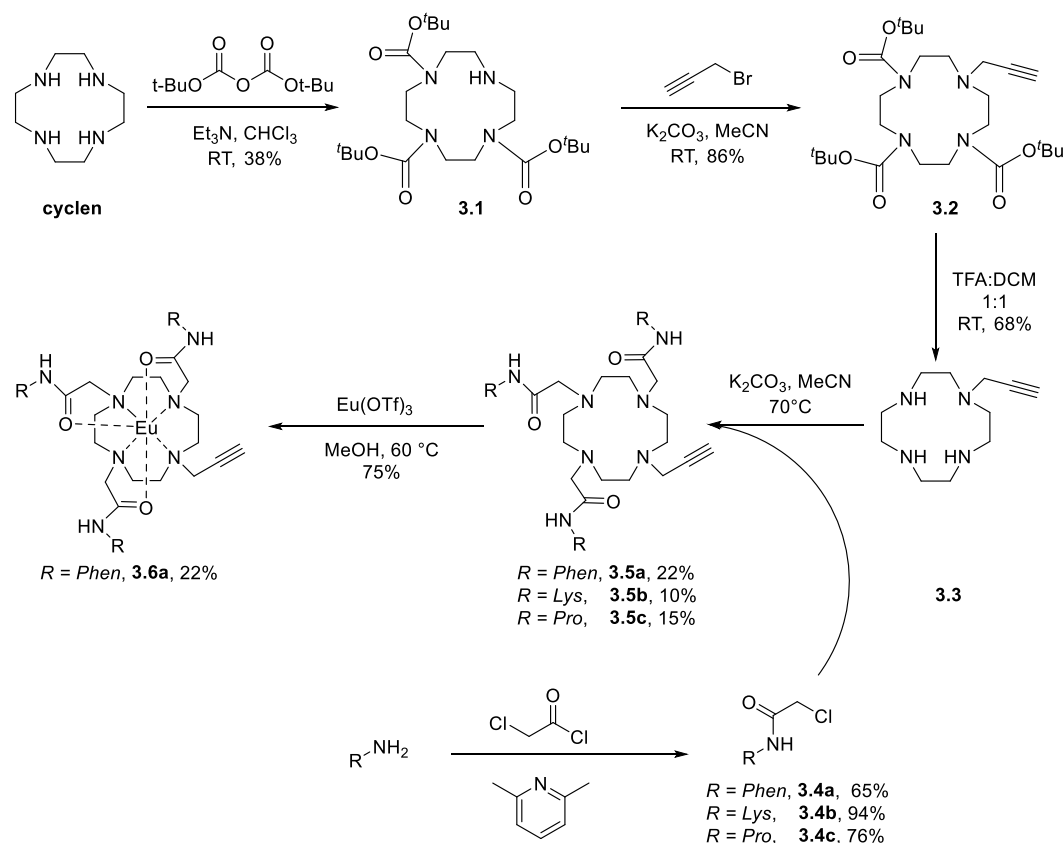
This secondary amine changes to a tertiary amine upon formation of the final ligand. The formation of a tertiary amine removes any amide oscillators on the complex, with amide oscillators offering a quenching pathway for lanthanides in solution.<sup>20</sup> Yet the main motivation behind the inclusion of proline is that the five-membered ring should enforce rigidity in the pendant arms. Rigidity in the complex should prevent conformational interconversion of the complex between TSAP and SAP conformations, preserving the ideal catalytic TSAP configuration, with this conformer having much faster exchange rates.<sup>21</sup> Faster exchange rates are sought to make sure that there is exchange of anions between the inner and outer coordination sphere, as if the anions irreversibly bind then the catalyst is rendered inert after one reaction cycle. Due to its rigidity proline was deemed the most likely to demonstrate a conformational preference.

In each of these pendant arms there is a selection of different protecting groups. The main driving reason behind this is synthetic ease, to prevent unwanted side reactions. Secondary to this was to investigate the role that steric bulk could have, on the solution phase coordination chemistry of the complexes under investigation. While other pendant arms were theorised if not explored, these substrates were

picked as the most suitable to explore the role of charge, lipophilicity and rigidity within Ln(III) complexes.

### 3.3.2 Initial synthetic pathway

The initial synthetic pathway comprised the use of protecting chemistry to achieve a monoalkylated propargyl cyclen intermediate, before direct alkylation to yield the final ligands (**Scheme-3.1**).



**Scheme-3.1.** Initial synthetic route for Eu.p.DO3AM derivatives.

The initial synthetic pathway has been used previously within the Faulkner group and in the wider community there is extensive literature on this topic.<sup>15,22</sup> This method involves a protection/deprotection methodology. Initially alkylating cyclen with Boc anhydride to create the protected ester **3.1**, this molecule **3.1** has been used extensively to access monoalkylated products due to the great degree of difficulty

directly alkylating the cyclen ring. This protected ester **3.1** was then alkylated with propargyl bromide to give product **3.2**. The protecting ester groups of **3.2** were then removed by an ester acidic hydrolysis, yielding the cyclen ring with one position substituted with a propargyl group (**3.3**) (**Figure-3.14**): this molecule is then used for all syntheses of the different DOTAM derivatives.

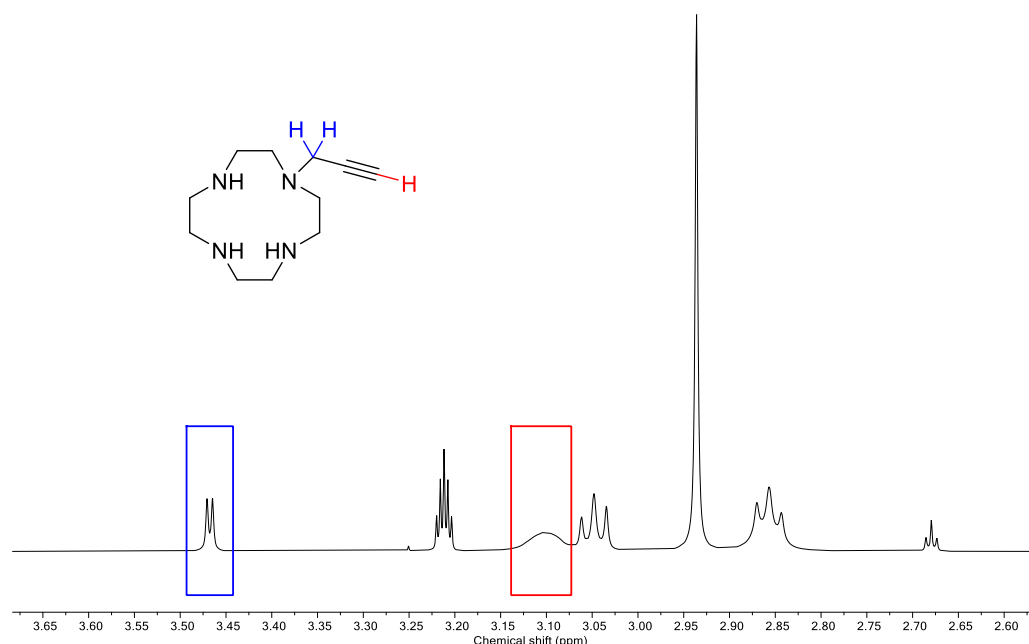


**Figure-3.14.**  $^1\text{H}$  NMR spectrum of compound **3.3**, with the propargyl protons highlighted in blue and red.

To create suitable pendant arms the respective L-amino acids were functionalised using chloroacetyl chloride, allowing them to be appended to the cyclen ring. These functionalised amino acids **3.4a-c** were then reacted with **3.3** to yield the trisubstituted products **3.5a-c** before being complexed with  $\text{Eu}(\text{OTf})_3$  to give  $[\text{EuL}^{3.6a-c}]$ .

### 3.3.3 Synthetic adaptation and optimisation.

The original synthetic pathway (while well-established) has significant drawbacks. The use of protecting group chemistry and lack of facile purification leads to low

yields in the initial steps of the synthesis to create compound **3.3** (22 % overall yield). To reach **3.6a**, the overall yield is 1.1 %, with the other final complexes being synthesised in yields too low to be measurable.

The chloroacetylation procedure was the most limiting factor initially. The reaction is carried out in the presence of base, literature sources quote  $\text{Et}_3\text{N}$  as a viable base for this reaction, with a  $\text{pK}_a$  of 10.64 at room temperature.<sup>23</sup> Yet upon addition to the reaction mixture, the colour became black and after work up according to literature procedures, no product was observed.<sup>24</sup> Reactions with substitute bases such as DIPEA ( $\text{pK}_a = 10.98$ ) also resulted in no observable product, so it was considered to use a more sterically hindered base. 2,6-di-tert-butylpyridine ( $\text{pK}_a = 3.58$ ) is a highly sterically hindered base, preventing it from acting as a nucleophile. Based on initial success with 2,6-ditert-butyl pyridine, a similar, equally effective but cheaper analogue 2,6-lutidine ( $\text{pK}_a = 6.67$ ) was used (**Figure-3.15**).

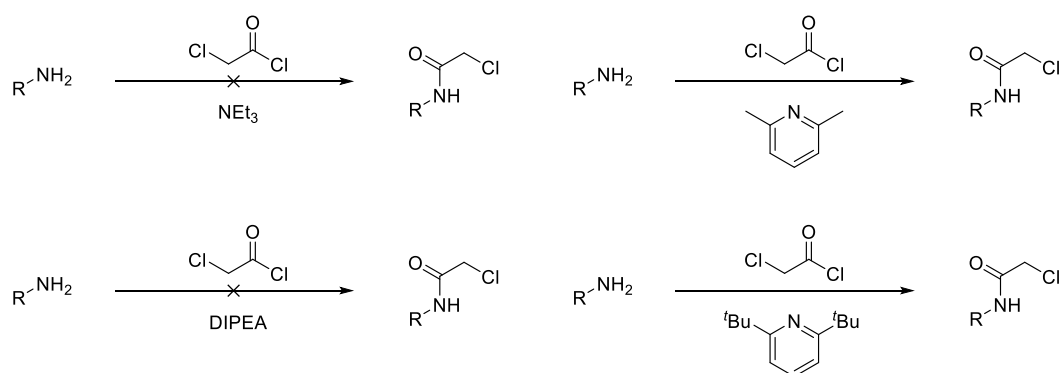


**Figure-3.15.** Chloroacetylation of amino acid derivatives with differing bases:  $\text{Et}_3\text{N}$  (*top left*), DIPEA (*bottom left*), 2,6-lutidine (*top right*) and 2,6-di-tert-butylpyridine (*bottom right*)

The synthesis of protected ester **3.1**, commonly known as ‘tri-boc cyclen’ has been well documented and used to access monoalkylated cyclen. Despite this, the presence of the tetra-substituted variant posed synthetic issues as separation from the desired tri-protected ester is difficult due to their chemical similarity, with

similar  $R_f$  values in both silica and alumina-based chromatography. This prompted investigation into an efficient way to monoalkylate cyclen with a suitable protecting group, which upon protection with boc-anhydride and removal of the first protecting group, would yield the desired protected ester **3.1**.

Direct alkylation of cyclen with propargyl bromide would be the most direct method, thus was investigated. While this reaction is cited in the literature, when attempted practically, it instead formed a mix of di- and unsubstituted cyclen, while little propargyl cyclen (**3.3**) that was formed was inseparable from the reaction mixture (**Figure-3.16**).<sup>16</sup> Despite continued effort to optimise the reaction conditions and/or purification, the ratio of propargyl cyclen compared to the generated by-products did not improve, prompting no further exploration down this synthetic pathway.

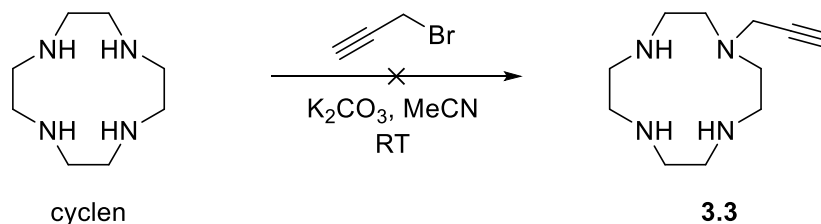


**Figure-3.16.** Attempted alkylation of cyclen with propargyl bromide to create intermediate **3.3**.

Direct protection of a single position with a carboxybenzyl 'CBz' protecting group on the cyclen ring (**Figure-3.17**) via benzyl chloroformate was considered. This reaction works well and is achieved with a moderate yield, and has a well-known deprotection pathway (**Figure-3.18**).<sup>25</sup>

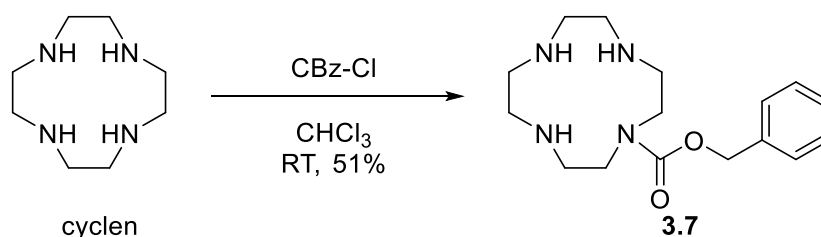


**Figure-3.17.** Monoalkylation of cyclen with a carboxybenzyl (CBz) group to afford a monosubstituted cyclen based ligand.

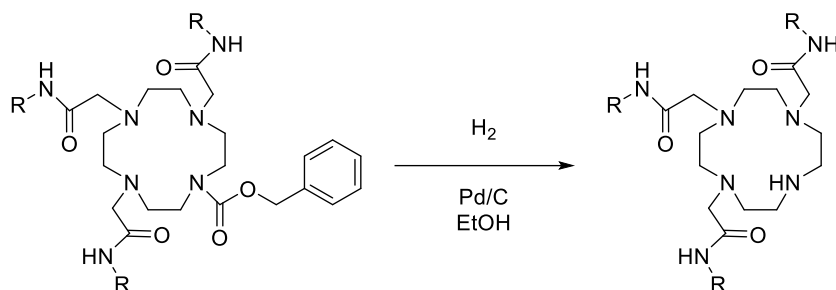
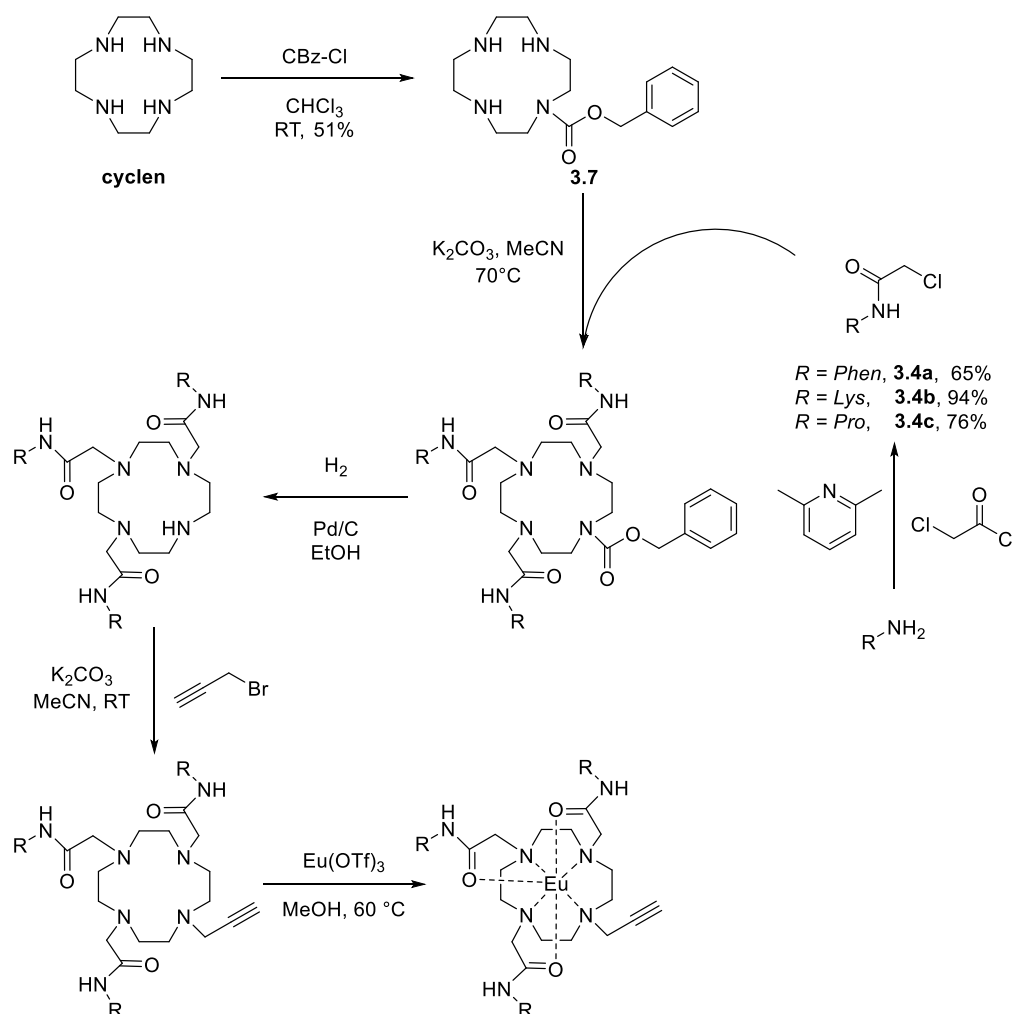


**Figure-3.18.** Theorised deprotection reaction of -CBz protected DO3AM derivatives.

This monoalkylation, while working well, increases the number of synthetic steps, which while improving selectivity does not change the overall yield as desired

(Scheme-3.2).



**Scheme-3.3.** Theoretical reaction scheme for alkylation of compound 3.7 and subsequent steps.

This scheme also introduced other problems such as deprotection of Lys.Cbz.O<sup>t</sup>Bu over the course of the reaction scheme, due to no longer being orthogonally protected, in summary this new pathway introduced more problems than it solved and was thus abandoned.

Appending the amino acid pendant arms to propargyl cyclen (**3.3**) had many difficulties, with the propensity for variable substitution being the main one. Despite various attempts varying the reaction conditions, temperature, equivalents, time etc. with all amino acid pendant arms, these reactions continued to give a spread of mono-, di- and trisubstituted products. While purification is possible

through the use of alumina and silica flash column chromatography, multiple columns are required to give the desired DO3AM products, reducing an already low yield. The pathway shown in **Scheme-3.1** only gave EuL<sup>3.6a</sup> in quantities to proceed with further studies. Therefore, another method had to be found to synthesise the desired ligands in high enough yields to enable creation of the complexes indicated.

### 3.3.4 Acid-amide coupling

After analysis of the literature concerning the synthesis of DOTAM derivatives. A paper by León-Rodríguez *et al.* was of particular interest.<sup>26</sup> It concerned the creation of DOTAM derivatives and the limitations surrounding direct alkylation of the cyclen ring. It included further ways to optimise the above synthetic process. Yet the fundamental limitation is summarised as '*N*-substitution of cyclen as a first step increases the steric hindrance around the macrocycle and thereby restricts further substitutions'. Meaning that upon addition of one of the functionalised intermediates **3.4a-c** it becomes increasingly more difficult to create further substituted products. To synthesise DOTAMR<sub>4</sub> derivatives, an acid-amide coupling pathway is proposed which circumvents the issues summarised in **Table-3.1**.

**Table-3.1.** Summary of advantages of acid-amide coupling condensation reactions versus nucleophilic substitution reactions.

	Advantages
(1)	Quarternarisation of compounds containing tertiary amines is eliminated.
(2)	Steric hindrance is minimal since the reaction centers will be the non-constrained COOH substituents of DOTA instead of the amino groups of cyclen.
(3)	The reaction rates are faster for condensation-type reactions than for nucleophilic substitutions.

This inspired a different approach to synthesis of ligands **3.5a-c**. This new method combines the effective synthetic pathway to produce ligand **2.3** (p.DO3A), along with commercially available protected amino acid derivatives (**Figures-3.11, 3.12, 3.13**).

Initial coupling reactions with this method proved to be highly successful with the synthesis of ligand **3.5d** achieving a 65% yield after optimisation of this reaction by variance of reaction time (16 h to 48 h), equivalents of coupling agent (3 eq to 6 eq) and coupling agent identity (switched from 2-(1H-Benzotriazole-1-yl)-1,1,3,3-tetramethylammonium tetrafluoroborate (TBTU) to Hexafluorophosphate Azabenzotriazole Tetramethyl Uronium (HATU)) (**Figure-3.19**).

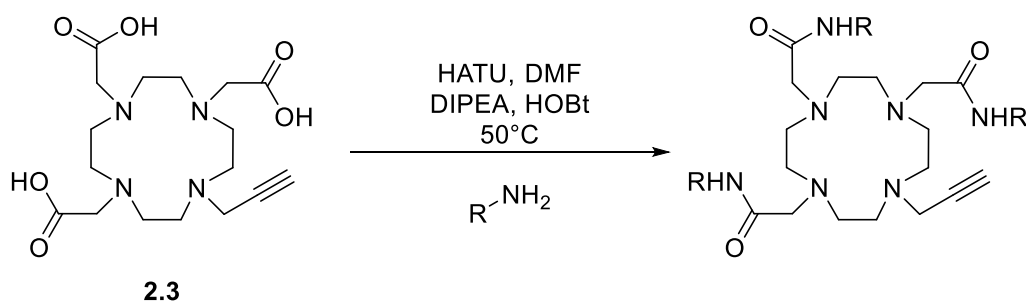
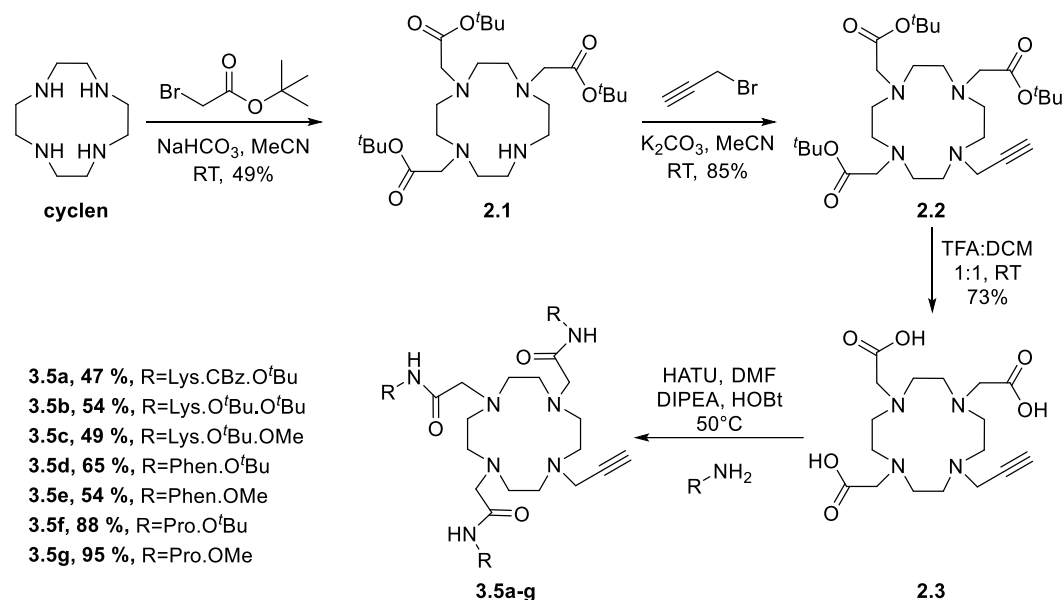


**Figure-3.19.** Proposed general reaction route for ligand synthesis. Reaction proceeds via an acid-amide coupling mechanism. HATU = Hexafluorophosphate Azabenzotriazole Tetramethyl Uronium, DIPEA = N,N-Diisopropylethylamine, HOBt = Hydroxybenzotriazole, DMF = N,N-Dimethylformamide.

A standard procedure was developed that worked in both DMF and MeCN, the solvent being important for ligand solubility. This method was then applied to all future ligand syntheses within this thesis. This method enabled amino acids to be rapidly incorporated onto the p.DO3A motif, creating a whole new range of

p.DO3AMR<sub>3</sub> derivatives, along with a reproducible synthetic method. This resulted in **Scheme-3.4** being the final optimised synthetic route for ligand synthesis.



**Scheme-3.4.** Full synthetic route implementing an acid-amide coupling mechanism to achieve ligands **3.5a-g**.

This updated synthesis pathway allows incorporation of any desired amino acid derivatives. One problem encountered was the removal of the CBz protecting group on the pendant arm of the p.DO3AM.Lys.CBz.O<sup>t</sup>Bu complex (**3.5a**, **Scheme-3.4**), this was resistant to gaseous hydrogenation (10% Pd/C, H<sub>2</sub> balloon, EtOH) and transfer hydrogenation (10% Pd/C, ammonium formate, IPA) conditions. Due to the high yield and ease of coupling to **2.3**, another amino acid derivative methyl N<sup>6</sup>-(tert-butoxycarbonyl)-L-lysinate (Lys.O<sup>t</sup>Bu.OMe) was used. The deprotection of which was much easier, with a simple TFA deprotection reaction working well (**Figure-3.20**).

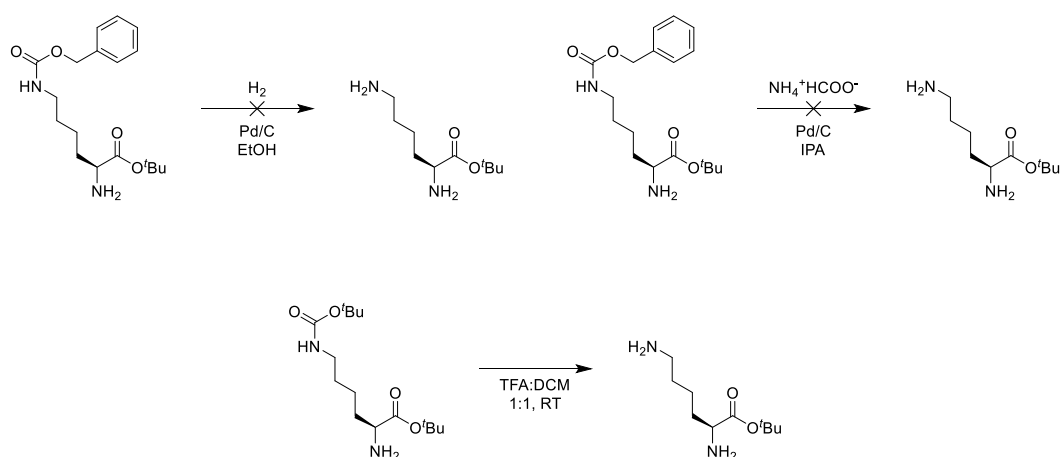
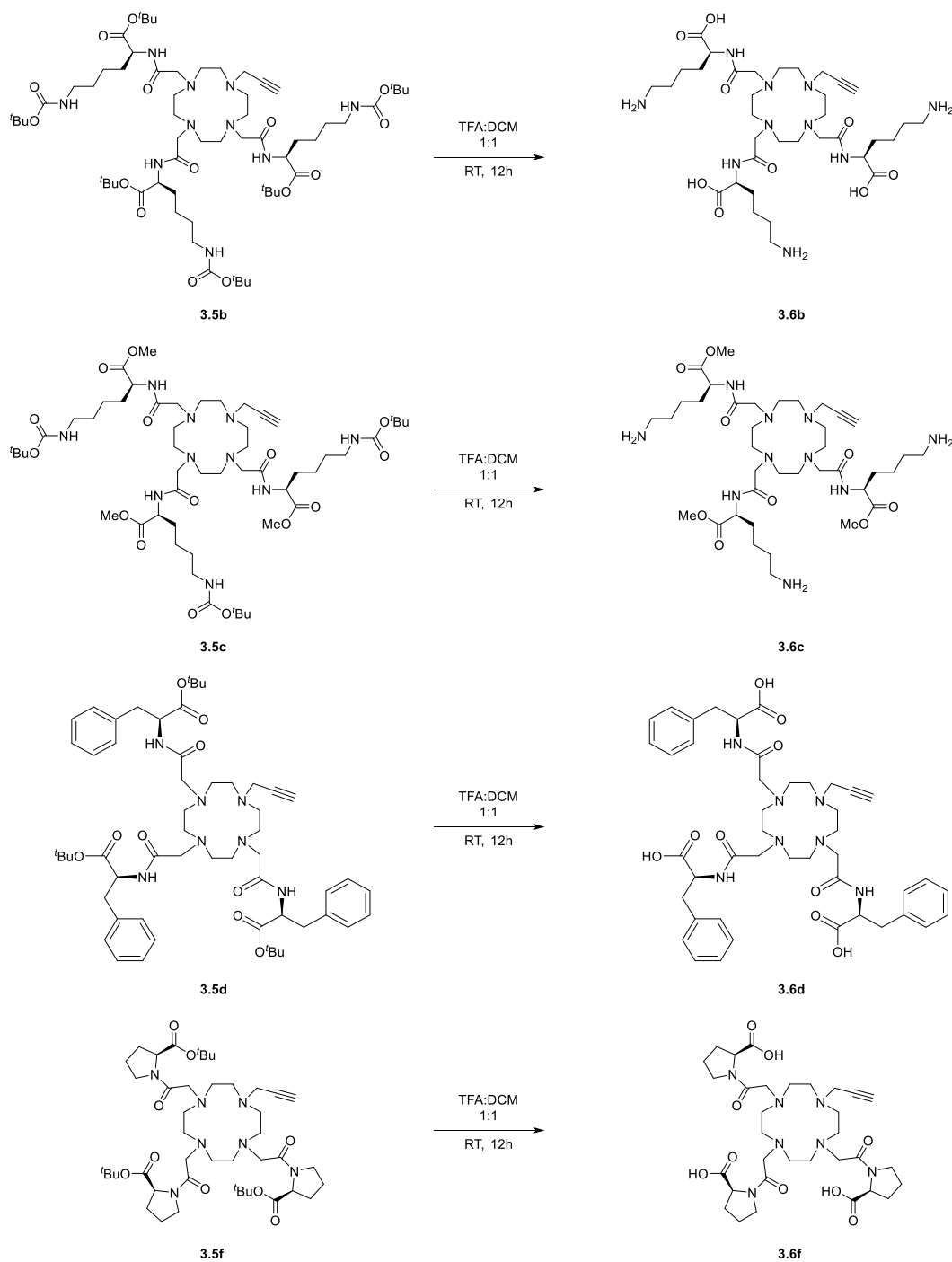


**Figure-3.20.** Reaction Schemes for the unsuccessful removal of a CBz group by hydrogenation (*top left*), transfer hydrogenation (*top right*) and the successful Boc deprotection reaction (*bottom*).

### 3.3.5 Final steps and complexation

To explore the potential catalytic activity of DO3AM derivatives, several different Eu(III) complexes were made. The aim being to gain more structural information from photophysical studies, allowing a more informed choice to be made as to which to carry forward for catalytic studies later in the thesis. While deprotection of the carboxylic acids group on the pendant arms was discouraged, due to the propensity for complex aggregation, it was deemed of interest. Firstly, to see whether aggregation would occur, and secondly, to see the impact this would have on the observed spectra and associated binding constants produced. Most importantly though, deprotecting the carboxylic acid groups should assist in aqueous solubility of these complexes in water. With catalytic studies being carried out in aqueous media, as it has been observed that fluorination reactions occur faster in aqueous rather than organic media, such as MeOH.<sup>15</sup>

The removal of the carboxylic acid protecting groups (**Scheme-3.5**) went smoothly in TFA and DCM to give the final deprotected ligands appended with amino acid arms based on proline (**3.6f**), phenylalanine (**3.6d**) and lysine (**3.6b** and **3.6c**).



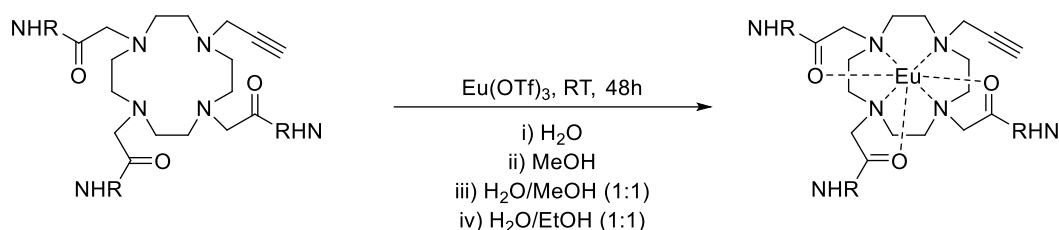
**Scheme-3.5.** TFA deprotection reactions of **3.5b-d,f** to yield final ligands **3.6b-d,f**.

The final ligands (**Table-3.2**) were then complexed with  $\text{Eu}(\text{OTf})_3$  in a range of solvents.

**Table-3.2.** DO3AM derivatives for complexation with  $\text{Eu}(\text{OTf})_3$ .

Final Ligands	
p.DO3AM.Lys.CBz.O <sup>t</sup> Bu	<b>3.5a</b>
p.DO3AM.Lys.OMe	<b>3.6c</b>
p.DO3AM.Phen.O <sup>t</sup> Bu	<b>3.5d</b>
p.DO3AM.Phen.OMe	<b>3.5a</b>
p.DO3AM.Phen.OH	<b>3.6d</b>
p.DO3AM.Pro.O <sup>t</sup> Bu	<b>3.5e</b>
p.DO3AM.Pro.OMe	<b>3.5g</b>
p.DO3AM.Pro.OH	<b>3.6f</b>

The solvent mixes varied depending on the nature of the protecting groups used, the aim being to prevent scrambling of the ester protecting groups, while also trying to ensure solubility of both ligand and lanthanide to enable effective complexation (**Scheme-3.6**). Depending on the basicity or acidity of the ligand in question, basification was required to deprotonate the cyclen ring nitrogens, allowing the lanthanide to be fully encapsulated by the ligand and the pendant arms.<sup>27</sup>



**Scheme-3.6.** General complexation reaction with  $\text{Eu}(\text{OTf})_3$ , differing solvents due to identity of protecting groups used.

### 3.3.6 Characterisation

The ligands were fully characterised by NMR and luminescence spectroscopy with the latter detailed in Chapter-4. The LIS gives rise to proton spectra with a much greater spectral width as aforementioned in Section-1.5.

These spectra also give an indication of the relative presence of both SAP and TSAP isomers. The TSAP configuration has the pendant arm protons in closer proximity to the lanthanide centre, promoting a stronger contribution to the pseudocontact (through space) shift. This pushes these protons to higher chemical shifts indicating the presence of the TSAP isomer. In DOTA and DOTAM based complexes it is common to see preference for one isomer over the other, they are deemed to be conformationally locked due to the high energetic barrier for interconversion.<sup>28</sup> This is not the case for DO3A and DO3AM based complexes, the lack of a fourth pendant arm lowers this energetic barrier, making it common to see the presence of SAP and TSAP as both of these isomers will be thermally populated at room temperature.

Due to the low barrier to interconversion of the isomers of DO3AM-based complexes, it is expected to observe both isomers present in solution. **Figure-3.21** shows the presence of both isomers in Eu.p.DO3AM.Lys.OMe in solution at a roughly 1:1 ratio, showing that there is no conformational preference for this complex. This is an observation seen for all other complexes synthesised.

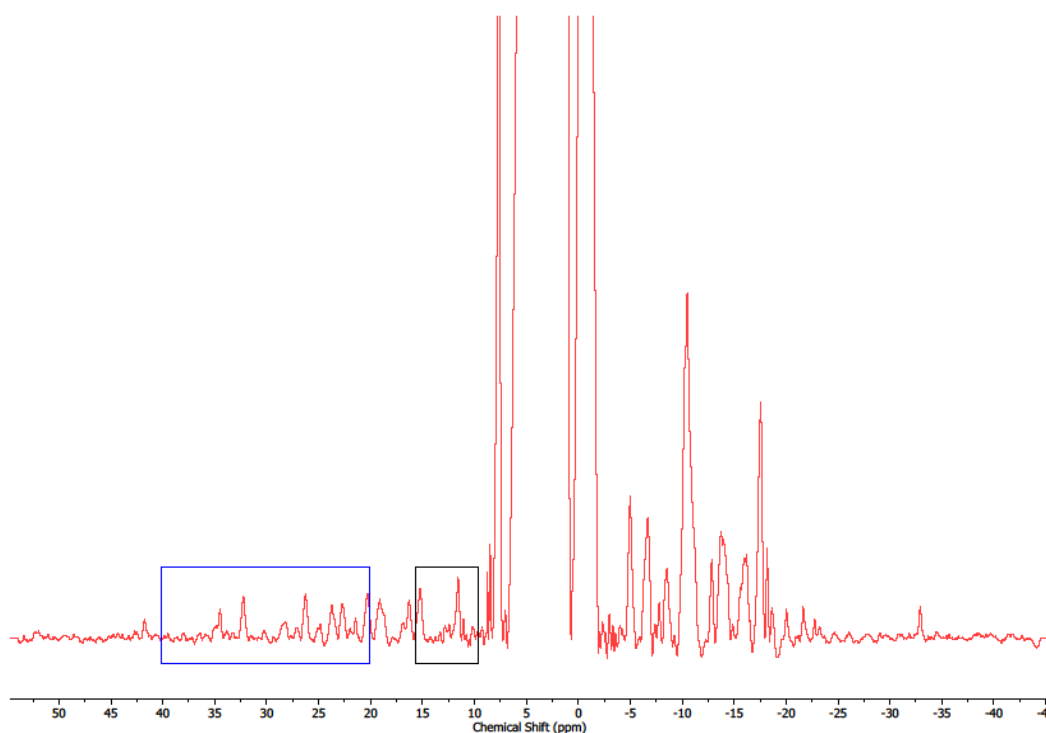


**Figure-3.21.**  $^1\text{H}$  NMR spectrum of Eu.p.DO3AM.Lys.OMe (298 K,  $\text{D}_2\text{O}$ , 500 MHz). Highlighting peaks due to SAP isomer (blue box) and TSAP isomer (black box).

### 3.4 Summary and conclusions

After considerable adjustment to the original synthetic route, the complexes  $\text{EuL}^{3.5\text{a,c-g}}$  and  $\text{EuL}^{3.6\text{b-d,f}}$  were successfully synthesised. There is much scope to improve upon this synthetic method to increase yields, with purification being a critical step. The use of size-exclusion chromatography and preparative HPLC would be of great use in this pursuit. Yet the research covered in this chapter shows that successful methods for DOTAM synthesis can be applied to specific DO3AM derivatives with good results. Preliminary studies with NMR spectroscopy for characterisation purposes have shown that there is a mix of TSAP and SAP isomers which was to be assumed due to fluxional nature of the ligands involved. Full luminescence titrations and lifetimes are detailed in Chapter-4 to investigate their anion specific binding in solution.

### 3.5 References

- 1 F. Wojciechowski, M. Suchy, A. X. Li, H. A. Azab, R. Bartha and R. H. E. Hudson, *Bioconjug Chem*, 2007, **18**, 1625–1636.
- 2 S. J. Ratnakar, S. Viswanathan, Z. Kovacs, A. K. Jindal, K. N. Green and A. D. Sherry, *J Am Chem Soc*, 2012, **134**, 5798–5800.
- 3 Z. Baranyai, I. Bányai, E. Brücher, R. Király and E. Terreno, *Eur<sup>3</sup>J<sub>HH</sub> Inorg Chem*, 2007, **2007**, 3639–3645.
- 4 G. Tircsó, Z. Garda, F. K. Kálmán, Z. Baranyai, I. Pócsi, G. Balla and I. Tóth, *<sup>3</sup>J<sub>HH</sub> Inorg Biochem*, 2013, **127**, 53–61.
- 5 C. A. Chang, *Handbook on the Physics and Chemistry of Rare Earths*, 2017, **51**, 169–299.
- 6 K. Ferreira, H.-Y. Hu, V. Fetz, H. Prochnow, B. Rais, P. P. Müller and M. Brönstrup, *Angew. Chem. Int. Ed.*, 2017, **56**, 8272–8276.
- 7 V. Lagostina, L. Leone, F. Carniato, G. Digilio, L. Tei and M. Botta, *Inorganics (Basel)*, 2019, **7**, 43.
- 8 S. Udomsub and S. Hannongbua, *J. Chem. Soc., Faraday Trans.*, 1997, **93**, 3045–3052.
- 9 C. Peukert, K. Rox, B. Karge, S.-K. Hotop and M. Brönstrup, *ACS Infect Dis*, 2023, **9**, 330–341.
- 10 H.-Y. Hu, N.-H. Lim, D. Ding-Pfennigdorff, J. Saas, K. U. Wendt, O. Ritzeler, H. Nagase, O. Plettenburg, C. Schultz and M. Nazare, *Bioconjug Chem*, 2015, **26**, 383–388.
- 11 F. A. Dunand, R. S. Dickins, D. Parker and A. E. Merbach, *Chemistry - A European Journal*, 2001, **7**, 5160–5167.
- 12 H.-Y. Hu, N.-H. Lim, D. Ding-Pfennigdorff, J. Saas, K. Ulrich Wendt, O. Ritzeler, H. Nagase, O. Plettenburg, C. Schultz and M. Nazare, *Bioconjug Chem*, 2015, **26**, 383–388.
- 13 M. Suchý, M. Milne, A. A. H. Elmehriki, N. McVicar, A. X. Li, R. Bartha and R. H. E. Hudson, *<sup>3</sup>J<sub>HH</sub> Med Chem*, 2015, **58**, 6516–6532.
- 14 D. J. Todd and J. Kay, *Curr Rheumatol Rep*, 2008, **10**, 195–204.
- 15 Laura. Mason, DPhil thesis, University of Oxford, 2017.
- 16 J. K. Molloy, O. Kotova, R. D. Peacock and T. Gunnlaugsson, *Org Biomol Chem*, 2012, **10**, 314–322.
- 17 K. Jobe, C. H. Brennan, M. Motevalli, S. M. Goldup and M. Watkinson, *Chem. Commun.*, 2011, **47**, 6036–6038.
- 18 B. Brennecke, Q. Wang, W. Haap, U. Grether, H.-Y. Hu and M. Nazaré, *Bioconjug Chem*, 2021, **32**, 702–712.

- 19 X. Guo, C. Xu and H. Kuang, in *Encyclopedia of Nanomaterials*, Elsevier, 2023, pp. 3–13.
- 20 D. Kovacs, D. Kocsi, J. A. L. Wells, S. R. Kiraev and K. E. Borbas, *Dalton Trans.*, 2021, **50**, 4244–4254.
- 21 G. Tircso, B. C. Webber, B. E. Kucera, V. G. Young and M. Woods, *Inorg Chem*, 2011, **50**, 7966–7979.
- 22 M. Suchý, A. X. Li, R. Bartha and R. H. E. Hudson, *Bioorg Med Chem*, 2008, **16**, 6156–6166.
- 23 A. V. Rayer, K. Z. Sumon, L. Jaffari and A. Henni,<sup>3J<sub>HH</sub></sup> *Chem Eng Data*, 2014, **59**, 3805–3813.
- 24 B. S. Balaji and N. Dalal, *Green Chem Lett Rev*, 2018, **11**, 534–543.
- 25 Y. Yamamoto, E. Shimizu, K. Ban, Y. Wada, T. Mizusaki, M. Yoshimura, Y. Takagi, Y. Sawama and H. Sajiki, *ACS Omega*, 2020, **5**, 2699–2709.
- 26 L. M. De León-Rodríguez, S. Viswanathan and A. D. Sherry, *Contrast Media Mol Imaging*, 2010, **5**, 121–125.
- 27 J. Moreau, E. Guillon, J.-C. Pierrard, J. Rimbault, M. Port and M. Aplincourt, *Chem. Eur. J.*, 2004, **10**, 5218–5232.
- 28 A. Kovács, *ACS Omega*, 2021, **6**, 13321–13330.

## Chapter-4: Photophysical studies on DO3AM derivatives

### 4.1 Aim and Scope

In the previous Chapter the synthesis of a series of heptadentate DO3AM derived complexes was detailed. This Chapter details the motivation behind creating each of these distinct complexes alongside its luminescence behaviour in aqueous and organic media. Several of these complexes are similar to one another leading them to be grouped into sets, for phenylalanine, proline and lysine (**Figure-4.1**). Within each set there are differing degrees of steric hindrance and different functional groups present, the effect of which will be studied in this Chapter.

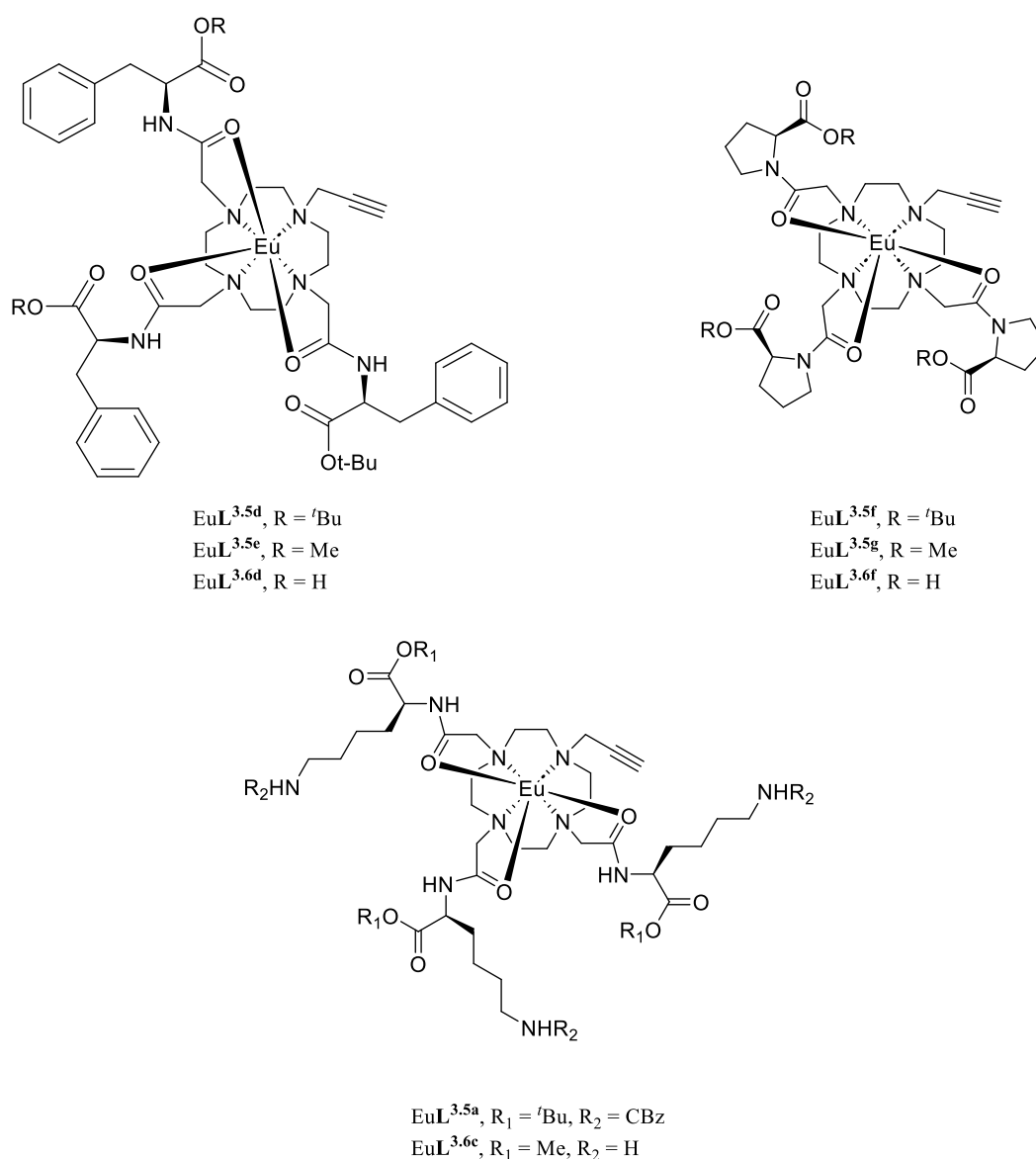


**Figure-4.1.** Chemical complexes studied in this Chapter. *Top-left:* Eu.p.DO3AM.Phen.OR motif variants (phenylalanine), *top-right:* Eu.p.DO3AM.Pro.OR motif variants (proline), *bottom:* Eu.p.DO3AM.Lys.OR.X motif variants (lysine).

The primary method of investigation in this Chapter will be luminescence titrations, allowing the distinction of binding events and their quantification. Luminescence lifetimes will be taken for the complexes in non-deuterated solvent, complex in non-deuterated solvent with anionic guests and complex in deuterated solvent. This allows observation of the change in lifetime upon binding of anions giving information about potential quenching pathways due to anion binding. And the

combination of deuterated and non-deuterated observed lifetimes allowing determination of hydration number ' $q$ ' for each complex. From these measurements, a suitable set will then be chosen to progress to catalytic studies detailed in Chapter-5.

## 4.2 Introduction to luminescence studies methodology

To investigate the local magnetic field around each of the lanthanide centres and to assign values for the binding of anionic guests to the lanthanide centre, luminescence titrations were carried out. Employing the same method and instruments, as used and detailed for Tb.p.DO3A in Chapter-2. For each of the complexes synthesised in Chapter 3, luminescence titrations were performed. Due to the catalytic measurements detailed in Chapter-5 being in aqueous media, the titrations in MilliQ water were prioritised. MeOH titrations were also carried out as some of the complexes were insoluble in aqueous media. To investigate this reaction between halocarboxylic acids and fluoride, luminescence titrations were carried out with anionic guests, acetate and fluoride. Fluoride will come from two sources, potassium fluoride (KF) and *tert*-butylammonium fluoride (TBAF). This is due to the solubility of potassium fluoride in MeOH being different to its solubility in water, making TBAF a useful comparison as it is very soluble in both solvents, sodium acetate was again used as the acetate source. Therefore, for most complexes six datasets were acquired, three for MeOH and three for H<sub>2</sub>O.

## 4.3 Eu.p.DO3AM.Phen

The p.DO3AM.Phen ligand-based systems were initially designed to incorporate a chromophore to enable antenna sensitisation. However, it is not an effective antenna

due to poor overlap between the excited states of the chromophore and the Eu(III) ion (**Figure-4.2**). Yet the inclusion of the phenyl group enables investigation of the effect of a lipophilic group's inclusion onto the ligand. This could either prevent the potential for aforementioned aggregation through the inclusion of more steric bulk or could promote aggregation through introduction of potential  $\pi$ -stacking interactions. From the p.DO3AM.Phen framework, protecting groups of -O'Bu and -OMe will show how steric bulk can affect a system. An OH group included on the ligand will show the effect an O-H oscillator will have on the electronic (luminescence investigated) and solution phase properties in comparison to the other Eu.p.DO3AM.Phen.OR complexes.

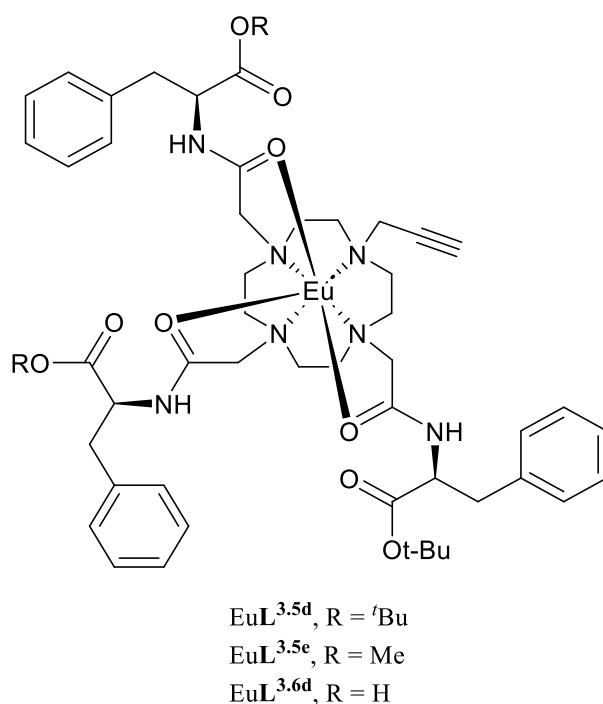


**Figure-4.2.** General chemical structure of Eu.p.DO3AM.Phen.OR complexes.

### 4.3.1 Eu.p.DO3AM.Phen.O'Bu

Luminescence studies began with bulky lipophilic complex Eu.p.DO3AM.Phen.O'Bu. Due to ineffective sensitisation there was a return to

direct excitation as seen in **Section-2.5** where similar studies were done on Eu.p.DO3A. Due to insolubility of the complex in water, measurements were only carried out in MeOH.

#### 4.3.1.1 Luminescence in MeOH

Initial measurements with acetate showed a trend which became more prevalent as titrations progressed. The decrease in intensity at an acetate concentration  $\approx 0.0015 \text{ mol dm}^{-3}$  is one of many similar observations in these luminescence titrations (**Figure-4.3**). The working hypothesis is that this concentration is the equilibrium point between the binding of two acetate guests or an acetate guest binding in a bidentate fashion to the Eu(III) centre. Which upon further anion addition, leads to the bidentate binding mode being chosen preferentially. Corresponding to one binding constant being resolvable instead of two separate binding events.

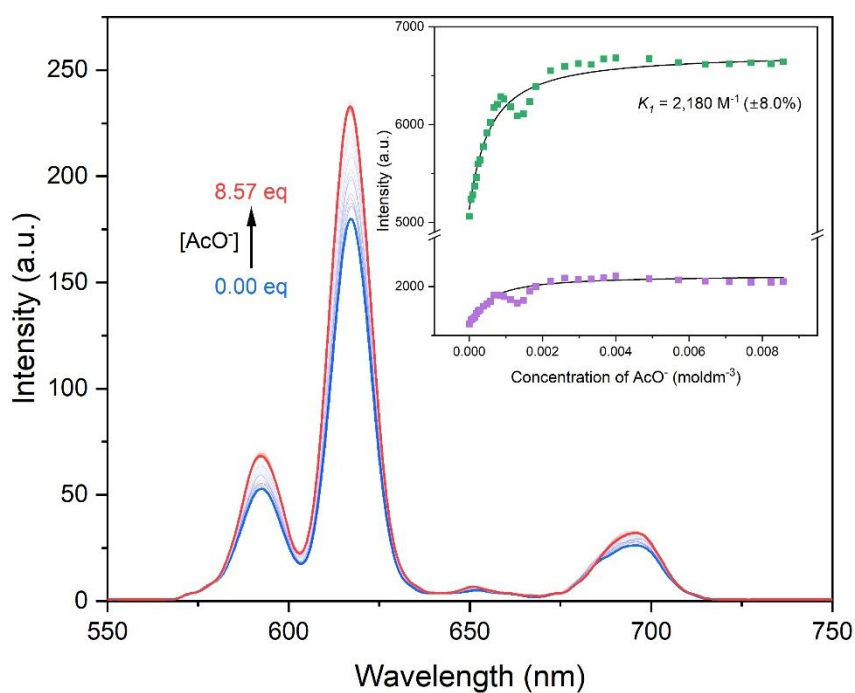


**Figure-4.3.** Graph showing the change in luminescence spectrum of Eu.p.DO3AM.Phen.O'Bu ( $1 \times 10^{-3}$  mol dm $^{-3}$ ) in MeOH, upon addition of increasing amounts of NaOAc ( $0.02$  mol dm $^{-3}$ ). With starting (blue) and end (red) concentrations highlighted,  $\lambda_{\text{ex}} = 393$  nm. *Inset:* binding isotherm from DynaFit $^{\text{®}}$ , plot of intensity area of  $\Delta J=2$  (dark green) and area of  $\Delta J=1$  (purple) vs concentration of AcO $^{-}$ .

This exemplifies a trend seen in most of the acetate binding where, dependant on the binding strength, it is observed that the equilibrium between a bidentate acetate binding and two monodentate binding events are energetically very similar.

The luminescence titrations carried out with potassium fluoride proved to be more difficult to converge to a specific binding constant (**Figure-4.4**). While the titration curves would imply the presence of two binding events, due to the change in intensity at fluoride concentration  $\approx 0.0015$  mol dm $^{-3}$ . This could not be resolved into binding events, likely due to the sharp nature of the intensity decrease of peaks  $\Delta J = 1$  and  $\Delta J = 2$ .

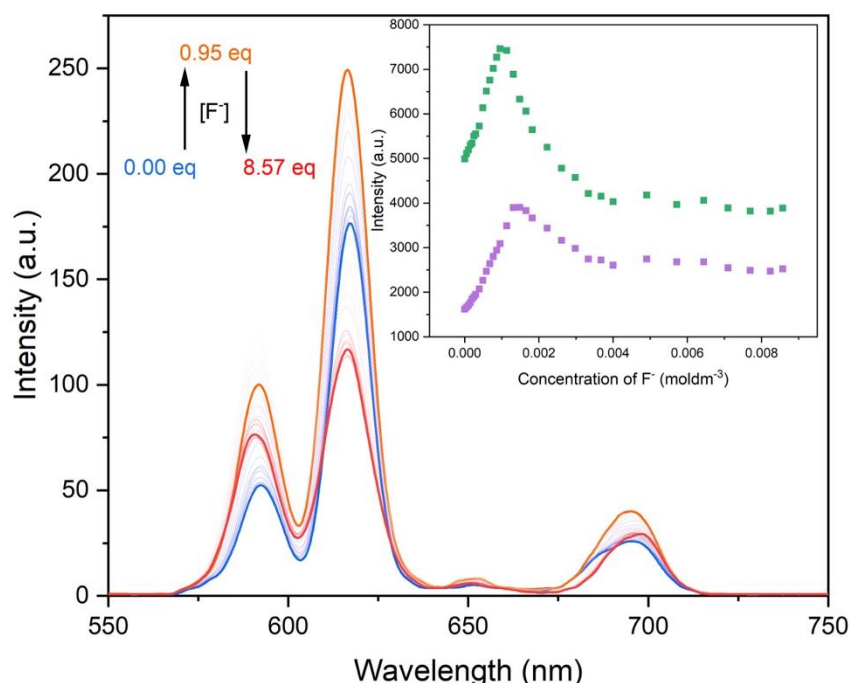


**Figure-4.4.** Graph showing the change in luminescence spectrum of Eu.p.DO3AM.Phen.O'Bu ( $1 \times 10^{-3}$  mol dm $^{-3}$ ) in MeOH, upon addition of increasing amounts of KF ( $0.02$  mol dm $^{-3}$ ). With starting (blue), maximum intensity (orange) and end (red) concentrations highlighted,  $\lambda_{\text{ex}} = 393$  nm. *Inset:* Change in intensity of area  $\Delta J=2$  (dark green) and area  $\Delta J=1$  (purple) vs concentration of F $^{-}$ .

For the analogous titration with TBAF as the fluoride source, this fitted well to two separate binding events (**Figure-4.5**). This reiterates the differences between the two different anion sources, potassium fluoride exhibits poor solubility at higher ionic strengths, potentially making this the reason for being unable to resolve the binding constants in **Figure-4.4**. The improved solubility of TBAF allows ready binding of fluoride in MeOH, making these binding constants clearly resolvable and quantifiable.

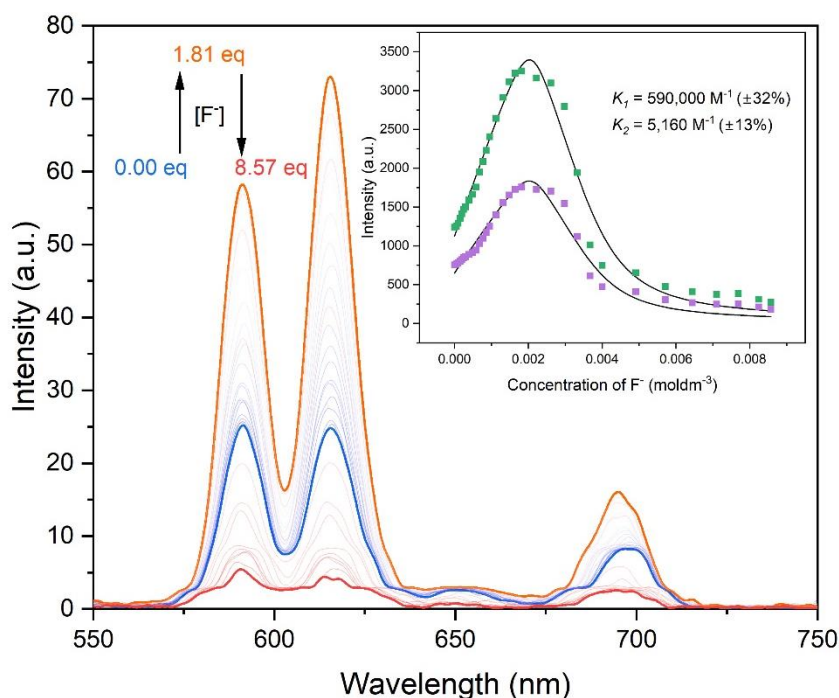


**Figure-4.5.** Graph showing the change in luminescence spectrum of Eu.p.DO3AM.Phen.O'Bu ( $1 \times 10^{-3}$  mol dm<sup>-3</sup>) in MeOH, upon addition of increasing amounts of TBAF (0.02 mol dm<sup>-3</sup>). With starting (blue), maximum intensity (orange) and end (red) concentrations highlighted,  $\lambda_{\text{ex}} = 393$  nm. *Inset:* binding isotherm from DynaFit<sup>®</sup>, plot of intensity of peak at 591 nm (amber), 616 nm (cyan), area of  $\Delta J=2$  (dark green) and area of  $\Delta J=1$  (purple) vs concentration of F<sup>-</sup>.

**Table-4.1** Summary of binding constants of Eu.p.DO3AM.Phen.O<sup>t</sup>Bu with anionic guests in MeOH.

Anionic source	Media	Binding constant (M <sup>-1</sup> ) <sup>#</sup>	
		$K_1 = [\text{EuLX}]^-$ EuL <sup>3.5d</sup>	$K_2 = [\text{EuLX}_2]^{2-}$
NaOAc	MeOH	2,180 (±175)	-
KF	MeOH	-	-
TBAF	MeOH	590,000 (±190,000)	5,160 (±671)

<sup>#</sup>  $K_1$  = first binding event;  $K_2$  = second binding event-deduced from binding isotherm generated from DynaFit<sup>®</sup>

<sup>±</sup> Error in brackets is represented as standard error in M<sup>-1</sup>. All data were plotted at the 95% confidence interval

<sup>§</sup> The binding of anions was studied by time-gated phosphorescence titrations of the complexes with varying concentrations of sodium acetate, potassium fluoride and tetrabutylammonium fluoride with binding isotherms generated using DynaFit<sup>®</sup>

The binding constants summarised in **Table-4.1** show the differences between fluoride (hard anion) and acetate (relatively soft) binding strength and the preference between them. This is ideal for the proposed catalytic system with tightly bound fluoride and acetate-based substrate in equilibrium with bulk solvent. Despite the binding of fluoride in MeOH being assignable to a binding event, due to the magnitude of the binding constant

### 4.3.1.2 Luminescence lifetimes

Luminescence lifetimes of the complex before and after addition of guest were measured, to further understand the coordination sphere around the lanthanide. With the increase in lifetime upon addition of anionic guest being higher due to the replacement of solvent molecules, hence offering less efficient quenching pathways (**Table-4.2**).

**Table-4.2** Summary of luminescence lifetimes\* of Eu.p.DO3AM.Phen.O'Bu before and after anionic guest addition in MeOH (Conc of host is 0.001 mol dm<sup>-3</sup>, guest conc is 0.02 mol dm<sup>-3</sup>).

EuL <sup>3.5d</sup>	Lifetime in MeOH (ms)
Complex	0.45 (± 0.84%)
Complex + 8.57 eq NaOAc	0.50 (± 0.43%)
Complex + 8.57 eq KF	0.72 (± 0.64%)
Complex + 8.57 eq TBAF	0.26 (± 4.9%)

± Error in brackets is represented as standard error in M<sup>-1</sup>. All data were plotted at the 95% confidence interval

\* Lifetimes were best fit to a mono-exponential decay unless otherwise stated.

The decrease in lifetime with the addition of TBAF is likely due to the presence of a more efficient quenching pathway, facilitating fast quenching something not seen by the more insoluble KF. A value for 'q' was determined through measurement of a lifetime in the analogous deuterated solvent. A value of 3.6 indicates a very high hydration number, despite the tendency for overestimation of 'q' for high values.<sup>1</sup> This indicates the presence of an alternate quenching pathway within this complex, as the fluoride binding constants would indicate the presence of only two guest binding modes.

**Table-4.3** Luminescence lifetimes in MeOH and MeOD of Eu.p.DO3AM.Phen.O'Bu (Conc of host is 1×10<sup>-3</sup> mol dm<sup>-3</sup>)\*.

Media	EuL <sup>3.5d</sup>		
	Lifetime in Hydrated solvent (ms)	Lifetime in Deuterated solvent (ms)	Hydration number (q)
MeOH	0.45	2.64	3.6

\* All lifetime values are subject to an error of ± 10% or less.

This observation is not what was expected for this complex, but nonetheless is useful in determining its suitability for catalytic applications.

### 4.3.2 Eu.p.DO3AM.Phen.OMe

By changing the acid protecting group from a *tert*-butyl ester to a methyl ester group in this complex, the aim was to create a similar complex which experienced less steric hindrance. The aims were to improve solubility and space for anion binding, while retaining some steric bulk to prevent complex aggregation and fluxional isomerism between TSAP and SAP, with the TSAP being preferred for aforementioned reasons.

#### 4.3.2.1 Luminescence in MeOH

Measurements in MeOH began with acetate binding, a similar perturbation in the curve  $\approx 0.00075 \text{ mol dm}^{-3}$  was observed (**Figure-4.6-*Inset***) due to the equilibrium between binding options upon increasing acetate concentration.

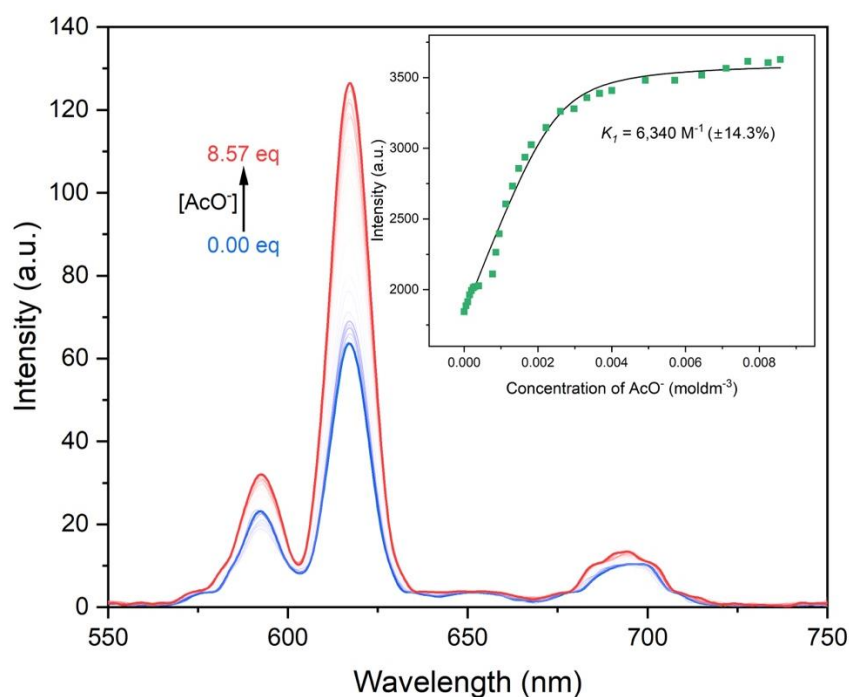


**Figure-4.6.** Graph showing the change in luminescence spectrum of Eu.p.DO3AM.Phen.OMe ( $1 \times 10^{-3} \text{ mol dm}^{-3}$ ) in MeOH, upon addition of increasing amounts of NaOAc ( $0.02 \text{ mol dm}^{-3}$ ),  $\lambda_{\text{ex}} = 393 \text{ nm}$ . With starting (blue) and end (red) concentrations highlighted. *Inset*: binding isotherm from DynaFit®, plot of intensity of area  $\Delta J=2$  (dark green) vs concentration of  $\text{AcO}^-$ .

For the fluoride binding studies, in both KF and TBAF luminescence titrations produced very similar datasets (**Figure-4.7**). The observation of a sudden decrease in spectral intensity could be a consequence of multiple factors. The first and most apparent is lanthanide precipitation, removal of the lanthanide from the complex through formation of the insoluble europium fluoride ( $\text{EuF}_3$ ).<sup>2</sup>

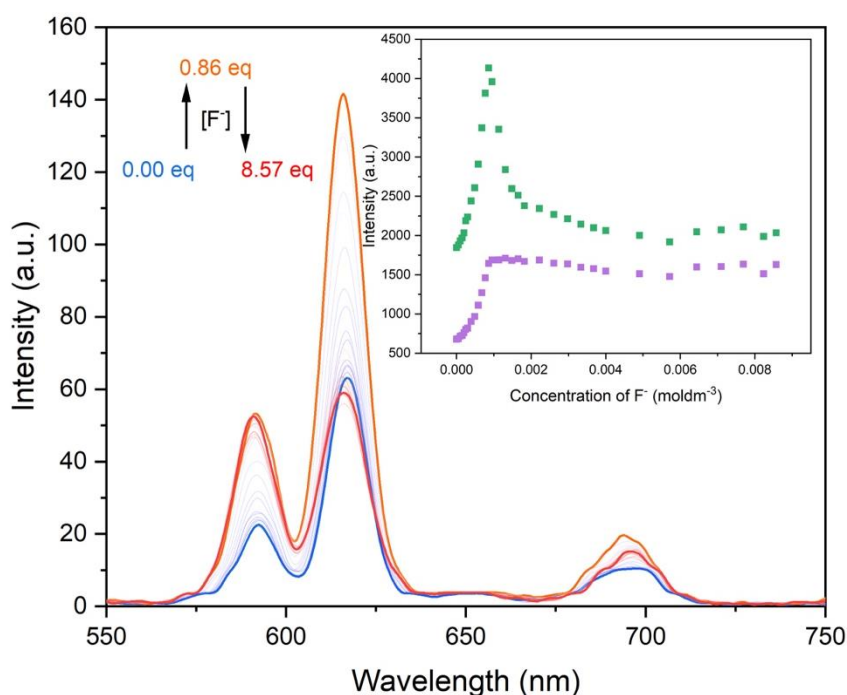


**Figure-4.7.** Graph showing the change in luminescence spectrum of Eu.p.DO3AM.Phen.OMe ( $1 \times 10^{-3}$  mol  $\text{dm}^{-3}$  in MeOH, upon addition of increasing amounts of KF ( $0.02$  mol  $\text{dm}^{-3}$ ). With starting (blue), maximum intensity (orange) and end (red) concentrations highlighted,  $\lambda_{\text{ex}} = 393$  nm. *Inset:* Change in intensity of area  $\Delta J=2$  (dark green) and area  $\Delta J=1$  (purple) vs concentration of  $\text{F}^-$ .

The shape and changes in the titration with KF are replicated in the titration with TBAF, with no binding constant being able to be assigned. This could reflect two very strong binding events that cannot be assigned due to the change in gradient (which correlates with the binding strength) being too great to quantify.

### 4.3.2.2 Luminescence in H<sub>2</sub>O

Eu.p.DO3AM.Phen.OMe exhibited low solubility in MilliQ water, but at the low concentrations that the titrations were carried out at it was soluble enough. This was important as over the course of anionic addition, the ionic strength of the aqueous medium gets stronger, solubilising the complexes an observation that is not seen for the -O<sup>t</sup>Bu analogue. It was of obvious importance to observe intensity changes due to an increase in binding intensity, rather than an increase in solubility over the course of the titration. There is evidence of acetate binding to the complex in solution, though very weak, meaning the anion is likely in fast exchange with bulk (Figure-4.8).

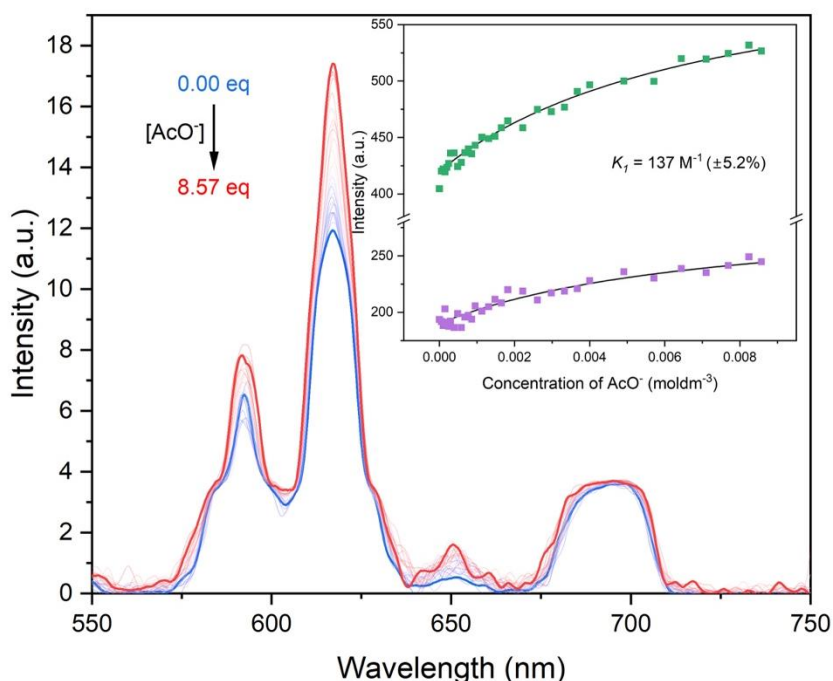


**Figure-4.8.** Graph showing the change in luminescence spectrum of Eu.p.DO3AM.Phen.OMe ( $1 \times 10^{-3}$  mol dm<sup>-3</sup>) in MilliQ water, upon addition of increasing amounts of NaOAc ( $0.02$  mol dm<sup>-3</sup>). With starting (blue) and end (red) concentrations highlighted,  $\lambda_{\text{ex}} = 393$  nm. *Inset:* binding isotherm from DynaFit<sup>®</sup>, plot of intensity of area  $\Delta J=2$  (dark green) and area  $\Delta J=1$  (purple) vs concentration of AcO<sup>-</sup>.

Titration with both fluoride sources (KF and TBAF) showed strong binding with only one binding event present (Figure-4.9), exhibiting graphs of similar shape and change.

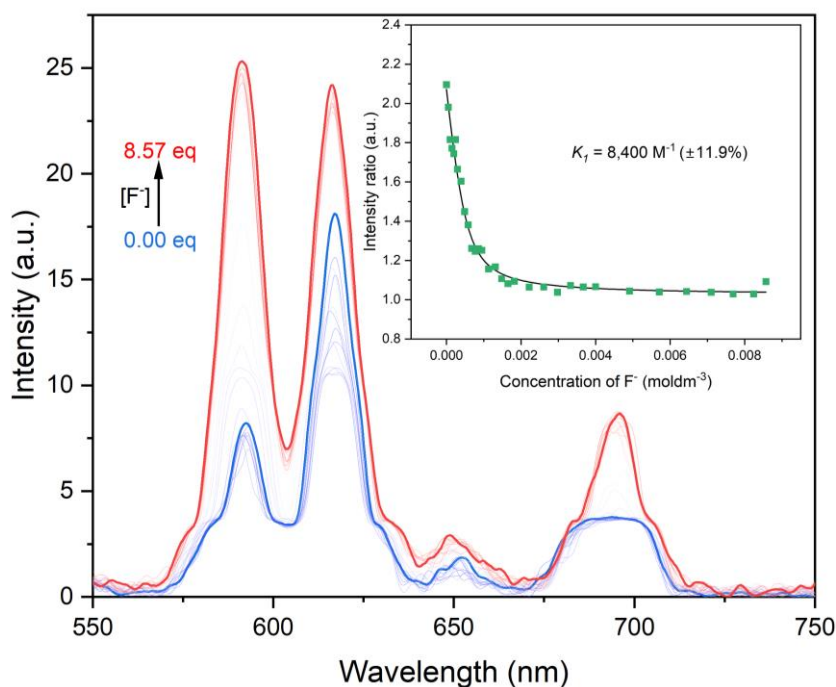


**Figure-4.9.** Graph showing the change in luminescence spectrum of Eu.p.DO3AM.Phen.OMe ( $1 \times 10^{-3}$  mol dm $^{-3}$ ) in MilliQ water, upon addition of increasing amounts of KF (0.02 mol dm $^{-3}$ ). With starting (blue) and end (red) concentrations highlighted,  $\lambda_{\text{ex}} = 393$  nm. *Inset:* binding isotherm from DynaFit<sup>®</sup>, plot of intensity ratio of  $\Delta J=2/\Delta J=1$  (dark green) vs concentration of F $^{-}$ .

Despite the low solubility of this complex, binding constants are assignable, showing that solubility is not a limiting factor at this low concentration. This could also prove potentially useful, as the variable solubility dependent on anion concentration could provide a facile method of separation. As the reaction progresses, the complex could precipitate out of solution as it is insoluble at lower anion concentrations, making separation easy in comparison to the more soluble complexes.

The binding constants observed for Eu.p.DO3AM.Phen.OMe show great variability (Table-4.4). The difference in binding constants with acetate as the guest anion, will be down to the competitive nature of the solvent. Water is a strongly coordinating solvent, resulting in the small change observed. The large change in the MeOH analogue is due to the poor solvating nature of MeOH, meaning that upon binding, there is a large change in the intensity and hence a larger binding constant. The lack of a second binding event here is not a cause for concern, acetate can bind in a bidentate fashion to these complexes, while

fluoride exhibits good binding strengths likely to result in a weak unresolvable second binding event.

**Table-4.4.** Summary of binding constants of Eu.p.DO3AM.Phen.OMe with anionic guests in MeOH and water.

Anionic source	Media	Binding constant ( $M^{-1}$ ) <sup>#</sup>
		$K_1 = \frac{[EuLX]}{EuL^{3.5a}}$
NaOAc	MeOH	6,340 ( $\pm 907$ )
	Water	137 ( $\pm 7.12$ )
KF	MeOH	-
	Water	8,400 ( $\pm 1,000$ )
TBAF	MeOH	-
	Water	4,520 ( $\pm 203$ )

<sup>#</sup>  $K_1$  = first binding event;  $K_2$  = second binding event-deduced from binding isotherm generated from DynaFit<sup>®</sup>

<sup>±</sup> Error in brackets is represented as standard error in  $M^{-1}$ . All data were plotted at the 95% confidence interval

<sup>§</sup> The binding of anions was studied by time-gated phosphorescence titrations of the complexes with varying concentrations of sodium acetate, potassium fluoride and tetrabutylammonium fluoride with binding isotherms generated using DynaFit<sup>®</sup>

### 4.3.2.3 Luminescence lifetimes

Luminescence lifetimes for the complexes before and after anion addition were taken (**Table-4.5**). For the MeOH system, there is an increase in lifetime for the complex with bound fluoride, due to replacement of solvent molecules capable of quenching the lanthanide. For acetate there is a decrease in observed lifetime, replacement of a solvent molecule with a more effective acetate quencher will cause this decrease. For the water system, there is a decrease in lifetime with all guests, this is due to the increasing ionic strength enabling more effective solvation and hence more effective quenching pathways, resulting in a small decrease for all values despite anionic substitution. With acetate showing a larger than expected decrease as guest binding also cause a decrease in lifetime as aforementioned.

**Table-4.5.** Summary of luminescence lifetimes\* of Eu.p.DO3AM.Phen.OMe before and after anionic guest addition in MeOH and water (Conc of host is  $1 \times 10^{-3}$  mol dm<sup>-3</sup>, guest conc is 0.02 mol dm<sup>-3</sup>).

EuL <sup>3.5a</sup>	Lifetime in MeOH (ms)	Lifetime in H <sub>2</sub> O (ms)
Complex	0.73 ( $\pm$ 0.50%)	0.69 ( $\pm$ 0.86%)
Complex + 8.57 eq NaOAc	0.54 ( $\pm$ 0.32%)	0.33 ( $\pm$ 1.1%)
Complex + 8.57 eq KF	0.93 ( $\pm$ 0.63%)	0.57 ( $\pm$ 0.95%)
Complex + 8.57 eq TBAF	1.05 ( $\pm$ 0.62%)	0.59 ( $\pm$ 0.80%)

$\pm$  Error in brackets is represented as standard error in M<sup>-1</sup>. All data were plotted at the 95% confidence interval

\* All lifetime values are subject to an error of  $\pm$  10% or less.

Lifetimes in deuterated and non-deuterated solvents were taken to determine a value for ‘*q*’ (**Table-4.6**). These values make apparent the problems of solubility with this complex. A value of 0.9 for the complex in MeOH fits well with the observed data which shows the presence of one binding event. The value of 0 is believed to be due to the presence of aggregation between the complex molecules, potentially from  $\pi$ -stacking between the aryl rings, and would indicate an increased solvent interaction in a deuterated solvent.<sup>3</sup> This would correspond with an increase in solubility upon anion addition, as the anion binding would break up these aggregates, increasing their solubility and decreasing their lifetime as observed in **Table-4.5**.

**Table-4.6.** Luminescence lifetimes in deuterated and undeuterated solvent of Eu.p.DO3AM.Phen.OMe (Conc of host is  $1 \times 10^{-3}$  mol dm<sup>-3</sup>)\*.

Media	EuL <sup>3.5a</sup>		
	Lifetime in Hydrated solvent (ms)	Lifetime in Deuterated solvent (ms)	Hydration number (q)
MeOH	0.73	1.52	0.9
H <sub>2</sub> O	0.69	0.93	0

\* Lifetimes were best fit to a mono-exponential decay unless otherwise stated.

While this system does have issues with solubility, the ability to adjust the solubility through anion addition nevertheless makes it an interesting subject for catalytic studies.

### 4.3.3 Eu.p.DO3AM.Phen.OH

The removal of the protecting groups was out of curiosity. With the acetate groups giving the option to either promote aggregation, by acting as a bridging ligand between ligand arms and lanthanide centres, or by enabling more effective solvation and hence solubility.

#### 4.3.3.1 Luminescence in MeOH

Titration began with the complex in MeOH, titrating against acetate as the guest anion (**Figure-4.10**). This fit to a single binding event but with a very high error in this measurement. The equilibrium between the acetate binding in a bidentate versus two monodentate ligand binding modes can be seen clearly, with the slowing increase to  $\approx 0.0025 \text{ mol dm}^{-3}$  detailing the first binding event. The large increase after that showing the preference for the bidentate mode. If the curve were to describe a second binding event, there would be a negative gradient after  $\approx 0.0025 \text{ mol dm}^{-3}$ .

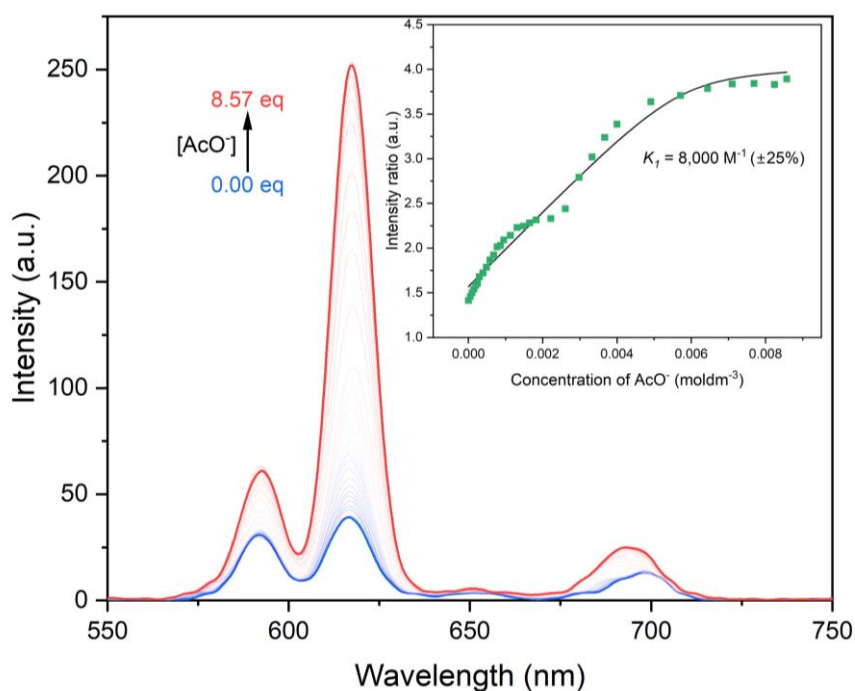


**Figure-4.10.** Graph showing the change in luminescence spectrum of Eu.p.DO3AM.Phen.OH ( $1 \times 10^{-3}$  mol dm $^{-3}$ ) in MeOH, upon addition of increasing amounts of NaOAc (0.02 mol dm $^{-3}$ ). With starting (blue) and end (red) concentrations highlighted,  $\lambda_{\text{ex}} = 393$  nm. *Inset:* binding isotherm from DynaFit<sup>®</sup>, plot of change in intensity ratio of  $\Delta J=2/\Delta J=1$  (dark green) vs concentration of AcO $^{-}$ .

This was followed by a titration against KF (**Figure-4.11**). While two binding events were observed in this titration, the error in these values was very high, with the shape of the peak also being a curious observation. The overall shape of the curve is one which would describe two binding events with an initial increase and then decrease. Yet there is a small dip at the top of the curve which gives rise to most of the uncertainty detailed by the errors within the binding constants. Despite this large error the figure does show two binding events as expected for this complex, with increased strength in comparison to the similar complexes detailed earlier in this Chapter.

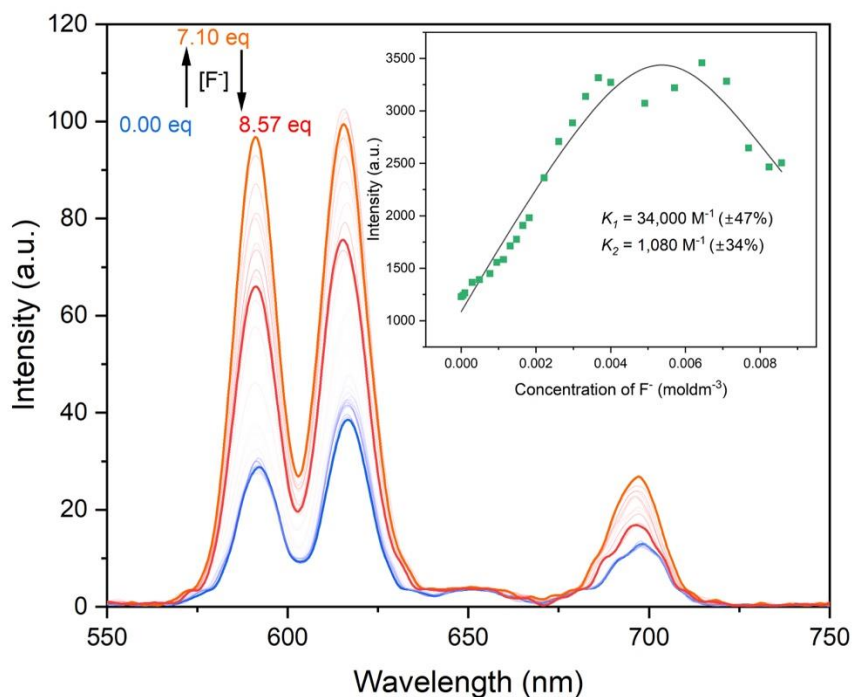


**Figure-4.11.** Graph showing the change in luminescence spectrum of Eu.p.DO3AM.Phen.OH ( $1 \times 10^{-3}$  mol dm $^{-3}$ ) in MeOH, upon addition of increasing amounts of KF (0.02 mol dm $^{-3}$ ). With starting (blue), maximum intensity (orange) and end (red) concentrations highlighted,  $\lambda_{\text{ex}} = 393$  nm. *Inset:* binding isotherm from DynaFit<sup>®</sup>, plot of change in intensity of area  $\Delta J=2$  (dark green) vs concentration of F $^{-}$ .

Although two binding events were resolvable from this titration in MeOH, due to the complex being completely insoluble in water, it was determined early on to not continue with measurements for this system. As the investigation was to focus on those soluble in aqueous media. The binding constants for these systems showed increased values in comparison to earlier iterations of this complex (**Table-4.7**). With the values of the second binding constant being large enough to be clearly resolvable into distinct separate binding events.

**Table-4.7.** Summary of binding constants of Eu.p.DO3AM.Phen.OH ( $1 \times 10^{-3}$  mol dm<sup>-3</sup>) with anionic guests (8.57 eq) in MeOH and water.

Anionic source	Media	Binding constant (M <sup>-1</sup> ) <sup>#</sup>	
		$K_1 = \frac{[\text{EuLX}^-]}{\text{EuL}^{3,6d}}$	$K_2 = \frac{[\text{EuLX}_2]^{2-}}{\text{EuL}^{3,6d}}$
NaOAc	MeOH	8,000 ( $\pm 2,000$ )	-
KF	MeOH	34,000 ( $\pm 16,000$ )	1,080 ( $\pm 367$ )

<sup>#</sup>  $K_1$  = first binding event;  $K_2$  = second binding event-deduced from binding isotherm generated from DynaFit<sup>®</sup>

$\pm$  Error in brackets is represented as standard error in M<sup>-1</sup>. All data were plotted at the 95% confidence interval

<sup>§</sup> The binding of anions was studied by time-gated phosphorescence titrations of the complexes with varying concentrations of sodium acetate, potassium fluoride and tetrabutylammonium fluoride with binding isotherms generated using DynaFit<sup>®</sup>

### 4.3.3.2 Luminescence lifetimes

Luminescence lifetimes were taken before and after anionic additions, showing the expected decrease upon acetate addition, as well as an increase in fluoride addition for aforementioned reasons (**Table-4.8**).

**Table-4.8.** Summary of luminescence lifetimes\* of Eu.p.DO3AM.Phen.OH before and after anionic guest addition in MeOH (Conc of host is  $1 \times 10^{-3}$  mol dm<sup>-3</sup>, guest conc is 0.02 mol dm<sup>-3</sup>).

EuL <sup>3,6d</sup>	Lifetime in MeOH (ms)
Complex	0.71 ( $\pm 0.54\%$ )
Complex + 8.57 eq NaOAc	0.50 ( $\pm 0.14\%$ )
Complex + 8.57 eq KF	0.92 ( $\pm 0.70\%$ )

$\pm$  Error in brackets is represented as standard error in M<sup>-1</sup>. All data were plotted at the 95% confidence interval

\* All lifetime values are subject to an error of  $\pm 10\%$  or less.

Lifetimes in deuterated and non-deuterated solvents were taken to determine a value for 'q' (**Table-4.9**). These observations corroborated well with the results of the luminescence titrations, a value of 1.3 for q would indicate variation between one and two guests binding, showing the presence of two binding modes with one weaker than the other.

**Table-4.9.** Luminescence lifetimes in MeOH and MeOD of Eu.p.DO3AM.Phen.OH (Conc of host is  $1 \times 10^{-3}$  mol dm<sup>-3</sup>)\*.

Media	EuL <sup>3.6d</sup>		
		Lifetime in Hydrated solvent (ms)	Lifetime in Deuterated solvent (ms)
			Hydration number ( <i>q</i> )
MeOH		0.71	1.3

\* All lifetime values are subject to an error of  $\pm 10\%$  or less.

The complex Eu.p.DO3AM.Phen.OH has many of the attributes desired for an efficient fluorination catalyst. The combination of luminescence titrations and lifetimes demonstrates a good fit for two binding modes with different binding strengths. However, the complete insolubility of the complex in water limits its application for the experiments detailed in Chapter-5 of this thesis, hence fewer experiments were done on this complex because of this crucial limitation.

#### 4.3.4 System summary

The p.DO3AM.Phen.OR ligand motif offered some promising observations, yet also some limiting factors as well. Solubility is the main factor in these complexes, with Eu.p.DO3AM.Phen.O'Bu exhibiting insolubility due to the bulky alkyl groups, Eu.p.DO3AM.Phen.OH aggregating within solution and Eu.p.DO3AM.Phen.OMe exhibiting variable solubility dependent on ionic strength. The -O'Bu and -OH analogues insolubility meant no luminescence titrations were carried out in water, meaning catalytic studies could not be carried out on these complexes. The -OMe analogue was partially soluble due to providing a balance between steric bulk and functional group coverage, as such it exhibited partial solubility. This partial solubility could be desirable for purification processes where the catalyst needs to be removed at the end of the reaction, which can be difficult for homogenous reactions where everything is in the same phase. Therefore, while the complexes

made did not offer facile excitation through the antenna or water solubility as was their design aim, they nonetheless offer exciting opportunities for catalysis in the Eu.p.DO3AM.Phen.OMe complex which is detailed in Chapter-5.

#### 4.4 Eu.p.DO3AM.Pro

The Eu.p.DO3AM.Pro complex-based systems, incorporate the rigid 5-membered ring from the amino acid proline into the ligand backbone. Creating a higher degree of rigidity will create a greater stereochemical preference at room temperature, which is desirable in these systems where the presence of three arms instead of four means there is less conformational rigidity. This system should therefore form only one major isomer creating the possibility for an enantioselective catalyst if the coordination sphere around the lanthanide is much more rigid and defined. The inclusion of -O'Bu, -OMe and -OH groups are for the same reasons mentioned in **Section 4.2 (Figure-4.12)**. While the initial aim of the inclusion of these arms was rigidity, the aqueous solubility and small size of the surrounding ligand made it of great import in the aqueous catalytic studies carried out in Chapter-5.

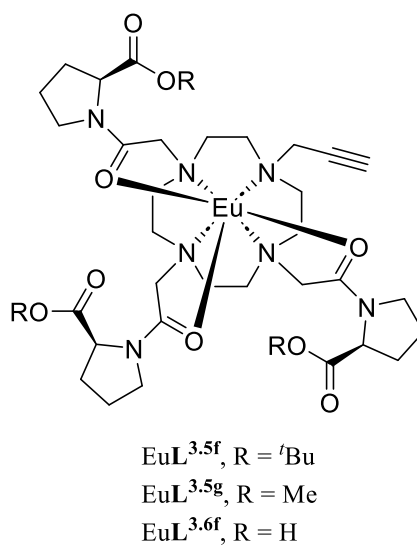


**Figure-4.12.** General chemical structure of Eu.p.DO3AM.Pro.OR complexes.

#### 4.4.1 Eu.p.DO3AM.Pro.O<sup>t</sup>Bu

Starting with the -O<sup>t</sup>Bu analogue of this complex, investigations were carried out to observe the effect of increased steric bulk.

##### 4.4.1.1 Luminescence in MeOH

Luminescence titrations started with titrating against a solution of sodium acetate (**Figure-4.13**). Two binding events were clearly observed with the first ( $K_1 = 10,460 \text{ M}^{-1} (\pm 397 \text{ M}^{-1})$ ) being much stronger than the second ( $K_2 = 3.8 \text{ M}^{-1} (\pm 0.40 \text{ M}^{-1})$ ), which is such a small value that while it was assignable, it implies that the second ligand will be in very fast exchange. This shows a notable difference in comparison to the Eu.p.DO3AM.Phen.OMe system. In those complexes, the curve shape showed a local minimum which was ascribed as the equilibrium point between acetate binding in a bidentate fashion versus two separate binding events. That local minimum is not present in this graph, showing the preference for two individual binding events. This could also be due to less sterically demanding groups around the lanthanide, allowing more anionic guests to approach the lanthanide.

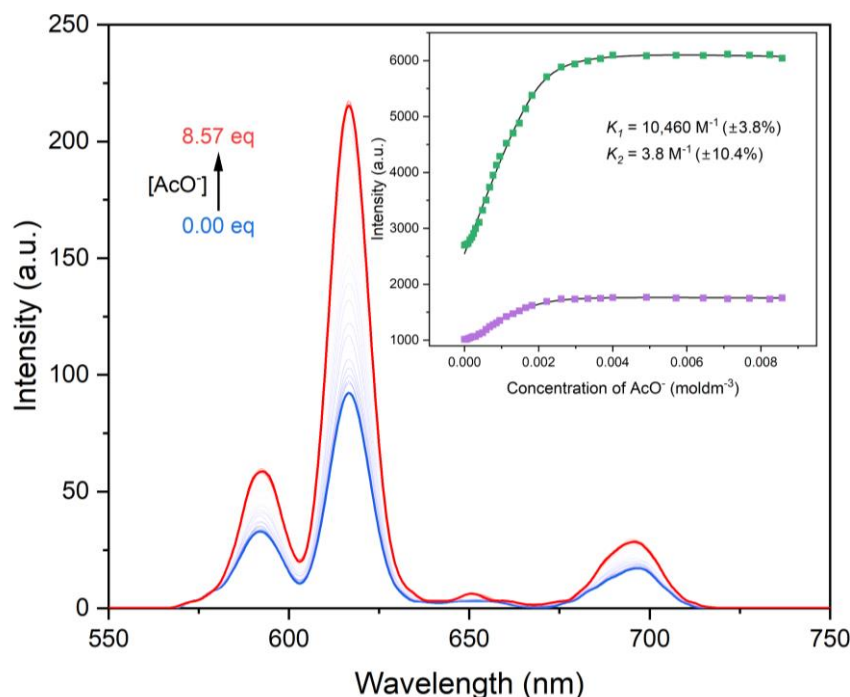


**Figure-4.13.** Graph showing the change in luminescence spectrum of Eu.p.DO3AM.Pro.O'Bu ( $1 \times 10^{-3} \text{ mol dm}^{-3}$ ) in MeOH, upon addition of increasing amounts of NaOAc ( $0.02 \text{ mol dm}^{-3}$ ). With starting (blue) and end (red) concentrations highlighted,  $\lambda_{\text{ex}} = 393 \text{ nm}$ . *Inset:* binding isotherm from DynaFit<sup>®</sup>, plot of intensity of area of  $\Delta J=2$  (dark green) and area of  $\Delta J=1$  (purple) vs concentration of  $\text{AcO}^-$ .

The complex was then titrated against KF (**Figure-4.14**). A similar set of observations were recorded for this titration, with a strong first binding event ( $K_1 = 60,000 \text{ M}^{-1} (\pm 11,000 \text{ M}^{-1})$ ), followed by a weaker second binding event ( $K_1 = 173 \text{ M}^{-1} (\pm 3.50 \text{ M}^{-1})$ ). This provides further evidence for more space available for the binding of anionic guests, as there are two binding constants of appreciable strength. It is to be expected that the magnitude of the binding events would be larger than those of acetate, due to the hard binding nature of fluoride anions in solution. This provides further evidence for the in-solution binding of both acetate and fluoride in two differing modes, one in slow and the other in fast exchange.

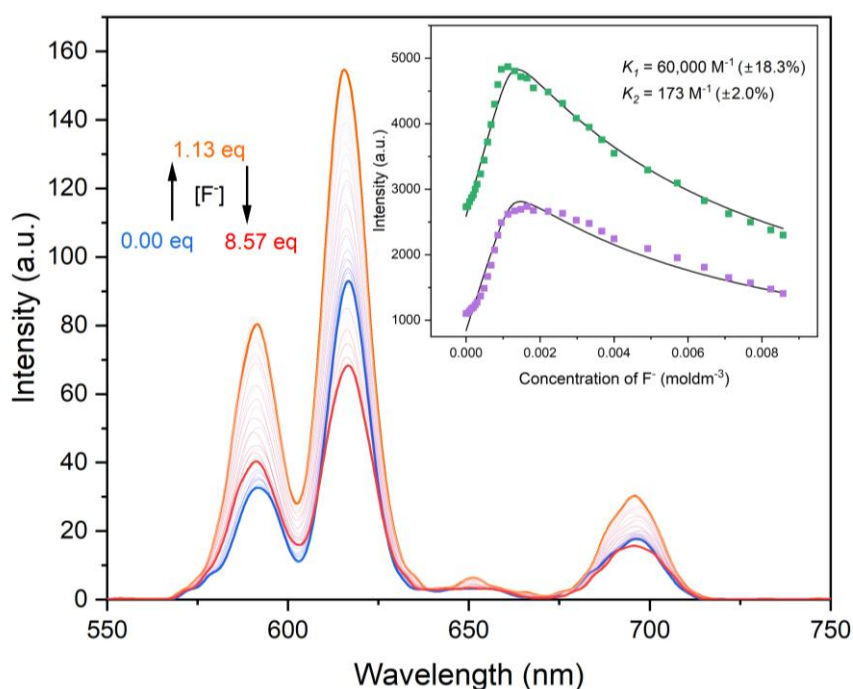


**Figure-4.14.** Graph showing the change in luminescence spectrum of Eu.p.DO3AM.Pro.O'Bu ( $1 \times 10^{-3}$  mol dm $^{-3}$ ) in MeOH, upon addition of increasing amounts of KF (0.02 mol dm $^{-3}$ ). With starting (blue), maximum intensity (orange) and end (red) concentrations highlighted,  $\lambda_{\text{ex}} = 393$  nm. *Inset:* binding isotherm from DynaFit<sup>®</sup>, plot of intensity of area of  $\Delta J=2$  (dark green) and area of  $\Delta J=1$  (purple) vs concentration of F $^{-}$ .

The combination of both the observed binding constants and 'q' values give great certainty in the assignment of two binding events to this complex (**Table-4.10, 4.12**).

**Table-4.10.** Summary of binding constants of Eu.p.DO3AM.Pro.O'Bu ( $1 \times 10^{-3}$  mol dm $^{-3}$ ) with anionic guests in MeOH.

Anionic source	Media	Binding constant (M $^{-1}$ ) <sup>#</sup>	
		$K_1 = [\text{EuLX}]^{-}$	$K_2 = [\text{EuLX}_2]^{2-}$
		$\text{EuL}^{3.5\text{f}}$	
NaOAc	MeOH	10,460 ( $\pm 397$ )	3.8 ( $\pm 0.40$ )
KF	MeOH	60,000 ( $\pm 11,000$ )	173 ( $\pm 3.50$ )

<sup>#</sup>  $K_1$  = first binding event;  $K_2$  = second binding event-deduced from binding isotherm generated from DynaFit<sup>®</sup>

$\pm$  Error in brackets is represented as standard deviation. All data were plotted at the 95% confidence interval

<sup>§</sup> The binding of anions was studied by time-gated phosphorescence titrations of the complexes with varying concentrations of sodium acetate, potassium fluoride and tetrabutylammonium fluoride with binding isotherms generated using DynaFit<sup>®</sup>

#### 4.4.1.2 Luminescence lifetimes

The luminescence lifetimes taken of this complex before and after anion addition, indicate extensive ligation by the observation of an increase in lifetimes upon binding of anionic guests (**Table-4.11**). With the guests displacing solvent molecules and preventing more efficient quenching pathways, causing an increase in lifetime. An observed increase in lifetime for the binding of acetate, as the complex itself offers efficient quenching pathways, rather than inefficient pathways as observed in Eu.p.DO3AM.Phen.OR complexes.

**Table-4.11.** Summary of luminescence lifetimes\* of Eu.p.DO3AM.Pro.O'Bu before and after anionic guest addition in MeOH (Conc of host is 0.001 mol dm<sup>-3</sup>, guest conc is 0.02 mol dm<sup>-3</sup>).

EuL <sup>3,5f</sup>	Lifetime in MeOH (ms)
Complex	0.55 (± 0.52%)
Complex + 8.57 eq NaOAc	0.67 (± 0.42%)
Complex + 8.57 eq KF	0.93 (± 0.49%)

± Error in brackets is represented as standard error in M<sup>-1</sup>. All data were plotted at the 95% confidence interval

\* Lifetimes were best fit to a mono-exponential decay unless otherwise stated.

Lifetimes were taken in deuterated and non-deuterated solvents to determine a value for 'q' (**Table-4.12**). A q-value of 1.9 correlates very well with the results of the luminescence titrations, showing the presence of two binding events, with an appreciable but not fully bound second ligand. The Eu.p.DO3AM.Pro.O'Bu is therefore a very suitable complex for the purposes of complex catalysis, with the smaller ligand enabling more effective ligation and solvation.

**Table-4.12.** Luminescence lifetimes in MeOH and deuterated MeOD of Eu.p.DO3AM.Pro.O'Bu (Conc of host is  $1 \times 10^{-3}$  mol dm<sup>-3</sup>)\*.

Media	EuL <sup>3.5f</sup>		
	Lifetime in Hydrated solvent (ms)	Lifetime in Deuterated solvent (ms)	Hydration number ( <i>q</i> )
MeOH	0.55	1.47	1.9

\* All lifetime values are subject to an error of  $\pm 10\%$  or less.

## 4.4.2 Eu.p.DO3AM.Pro.OMe

The -OMe analogue of the Eu.p.DO3AM.Pro.OR motif was investigated extensively in this thesis. The reduction in steric hindrance could allow for the potential of greater space for binding, yet the reduction of steric hindrance also lessens the energetic barrier to demetallation.

### 4.4.2.1 Luminescence in MeOH

Luminescence titrations began in MeOH with acetate as the first anionic guest (**Figure-4.15**). Only one strong binding event ( $K_1 = 5,250 \text{ M}^{-1}$  ( $\pm 158 \text{ M}^{-1}$ )) is seen, as opposed to two binding events seen with the -O'Bu analogue. A small perturbation in the curve  $\approx 0.001 \text{ mol dm}^{-3}$  shows the point of equilibrium between bidentate and multiple monodentate binding events.

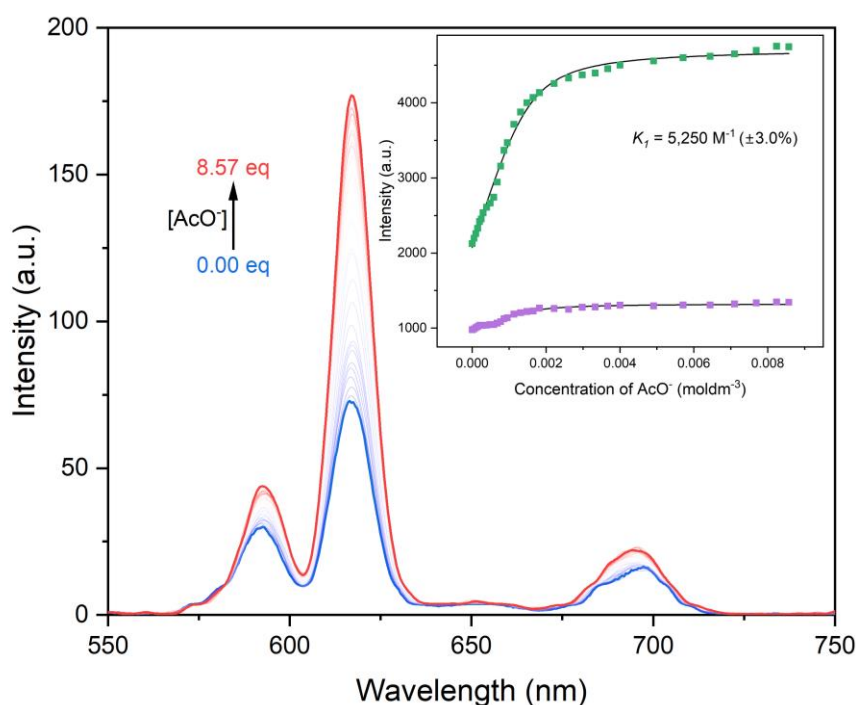


**Figure-4.15.** Graph showing the change in luminescence spectrum of Eu.p.DO3AM.Pro.O'Bu ( $1 \times 10^{-3} \text{ mol dm}^{-3}$ ) in MeOH, upon addition of increasing amounts of NaOAc ( $0.02 \text{ mol dm}^{-3}$ ). With starting (blue) and end (red) concentrations highlighted,  $\lambda_{\text{ex}} = 393 \text{ nm}$ . *Inset:* binding isotherm from DynaFit®, plot of intensity of peak  $\Delta J=1$  (purple) and area of  $\Delta J=2$  (dark green) vs concentration of  $\text{AcO}^-$ .

Luminescence titrations with KF and TBAF gave very similar results (Figure-4.16). There is a sharp increase in spectral intensity upon anion addition, then a sharp decrease at 0.77 anion equivalents. Despite many attempts to quantify the strength of the binding events seen, they were not distinguishable. The shape of the curve would correlate with two binding events with the drastic change in the gradient of the graph. However, this could be due to precipitation as the critical concentration is reached, causing a drop in spectral intensity as the lanthanide is removed from solution.

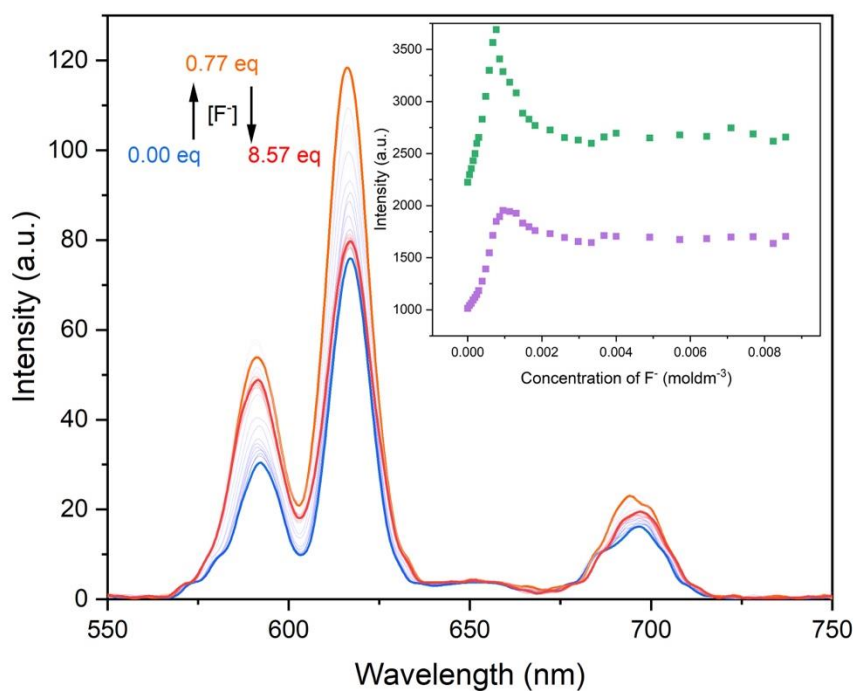


**Figure-4.16.** Graph showing the change in luminescence spectrum of Eu.p.DO3AM.Pro.OMe ( $1 \times 10^{-3} \text{ mol dm}^{-3}$ ) in MeOH, upon addition of increasing amounts of KF ( $0.02 \text{ mol dm}^{-3}$ ). With starting (blue), maximum intensity (orange) and end (red) concentrations highlighted,  $\lambda_{\text{ex}} = 393 \text{ nm}$ . *Inset:* Change in intensity of area  $\Delta J=2$  (dark green) and area  $\Delta J=1$  (purple) vs concentration of  $\text{F}^-$ .

This sharp decrease is observed in both KF and TBAF titrations, making the 0.77 anion equivalents of import, while also giving credence to the theory of lanthanide precipitation.

#### 4.4.2.2 Luminescence in $\text{H}_2\text{O}$

The same titrations were repeated in aqueous media. The first titration showed a much weaker binding constant, consistent with the observations of decreased binding strength when dissolved in a solvent with greater coordinating power (Figure-4.17). A clear single binding event is seen ( $K_1 = 664 \text{ M}^{-1} (\pm 17.3 \text{ M}^{-1})$ ), with no perturbation in the shape of the curve implying clear preference of the bidentate binding mode of acetate.

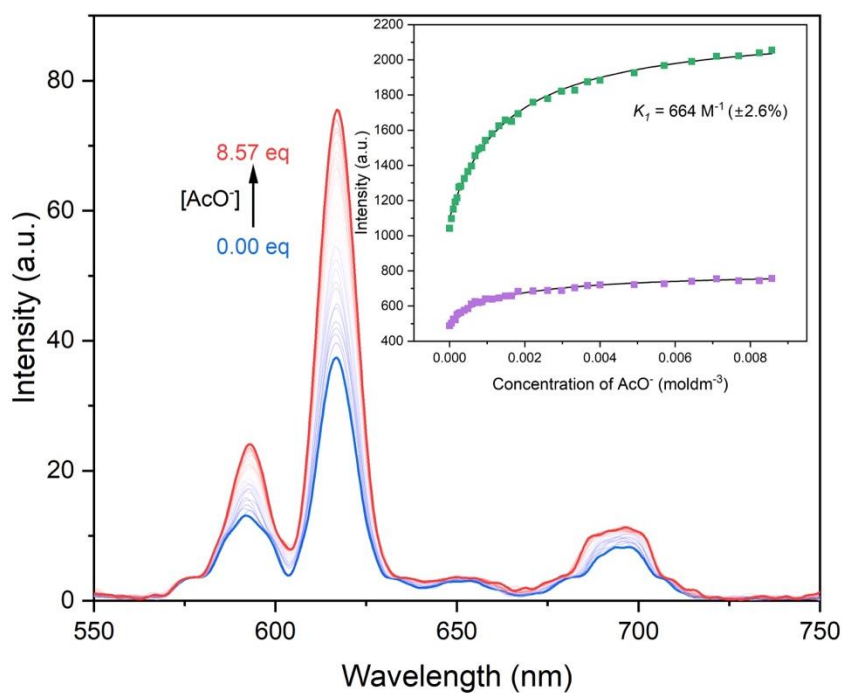


**Figure-4.17.** Graph showing the change in luminescence spectrum of Eu.p.DO3AM.Pro.OMe ( $1 \times 10^{-3} \text{ mol dm}^{-3}$ ) in MilliQ water, upon addition of increasing amounts of NaOAc ( $0.02 \text{ mol dm}^{-3}$ ). With starting (blue) and end (red) concentrations highlighted,  $\lambda_{\text{ex}} = 393 \text{ nm}$ . *Inset:* binding isotherm from DynaFit<sup>®</sup>, plot of intensity of area  $\Delta J=2$  (dark green) and area  $\Delta J=1$  (purple) vs concentration of  $\text{AcO}^-$ .

The complex was then titrated against both KF and TBAF, exhibiting similar results in both cases (**Figure-4.18**). Only a single binding event was distinguishable ( $K_1 = 3,880 \text{ M}^{-1}$  ( $\pm 427 \text{ M}^{-1}$ )), as opposed to the two binding events seen in the  $-\text{O}^t\text{Bu}$  analogous complex.

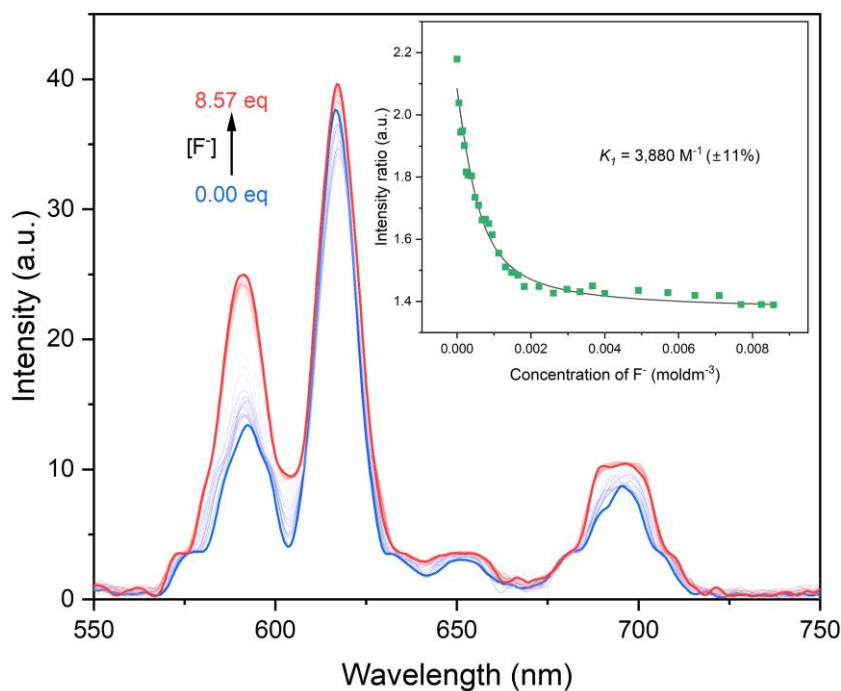


**Figure-4.18.** Graph showing the change in luminescence spectrum of Eu.p.DO3AM.Pro.OMe ( $1 \times 10^{-3} \text{ mol dm}^{-3}$ ) in MilliQ water, upon addition of increasing amounts of KF ( $0.02 \text{ mol dm}^{-3}$ ). With starting (blue) and end (red) concentrations highlighted,  $\lambda_{\text{ex}} = 393 \text{ nm}$ . *Inset:* binding isotherm from DynaFit<sup>®</sup>, plot of intensity ratio of  $\Delta J=2/\Delta J=1$  (dark green) vs concentration of  $\text{F}^-$ .

This goes against the presupposition that the decrease in steric hindrance would lead to greater availability of the lanthanide centre, more space leading to greater number of coordinating ligands. The results of the luminescence titrations with Eu.p.DO3AM.Pro.OMe show great variability, with great differences occurring with a change in the medium of the titration (**Table-4.13**). With MeOH as medium, the values for binding constants are much higher as the anionic guest is vastly preferred over the solvent. In aqueous media, strong coordination of water molecules offers competitive binding, resulting in comparatively lower binding constants. In this regard it may be that fluoride deprotonation of water creates the isoelectronic  $\text{OH}^-$  ion, which promotes Eu(III) excited state quenching (O-H oscillators), while also competing for the same binding pocket.<sup>4</sup> A combination of both of these factors results in decreased luminescence.

**Table-4.13.** Summary of binding constants of Eu.p.DO3AM.Pro.OMe with anionic guests in MeOH and water.

Anionic source	Media	Binding constant ( $M^{-1}$ ) <sup>#</sup>
		$K_1 = \frac{[EuLX]^-}{EuL^{3.5g}}$
NaOAc	MeOH	5,250 ( $\pm 158$ )
	Water	664 ( $\pm 17.3$ )
KF	MeOH	-
	Water	3,880 ( $\pm 427$ )
TBAF	MeOH	-
	Water	5,500 ( $\pm 440$ )

<sup>#</sup>  $K_1$  = first binding event;  $K_2$  = second binding event-deduced from binding isotherm generated from DynaFit<sup>®</sup>

$\pm$  Error in brackets is represented as standard error in  $M^{-1}$ . All data were plotted at the 95% confidence interval

<sup>§</sup> The binding of anions was studied by time-gated phosphorescence titrations of the complexes with varying concentrations of sodium acetate, potassium fluoride and tetrabutylammonium fluoride with binding isotherms generated using DynaFit<sup>®</sup>

#### 4.4.2.3 Luminescence lifetimes

The luminescence lifetimes before and after anion addition were taken (**Table-4.14**). They exhibit the expected result upon replacement of a solvating ligand with an anionic guest, that is an increase in the lifetime due to removal of quenching pathways, with a decrease between MeOH and water due to the greater efficacy of water molecules as quenchers.

**Table-4.14.** Summary of luminescence lifetimes\* of Eu.p.DO3AM.Pro.OMe before and after anionic guest addition in MeOH and water (Conc of host is  $1 \times 10^{-3}$  mol dm<sup>-3</sup>, guest conc is 0.02 mol dm<sup>-3</sup>).

EuL <sup>3.5g</sup>	Lifetime in MeOH (ms)	Lifetime in H <sub>2</sub> O (ms)
Complex	0.67 ( $\pm 0.45\%$ )	0.49 ( $\pm 0.57\%$ )
Complex + 8.57 eq NaOAc	0.70 ( $\pm 0.40\%$ )	0.65 ( $\pm 0.48\%$ )
Complex + 8.57 eq KF	1.03 ( $\pm 0.44\%$ )	0.61 ( $\pm 0.40\%$ )
Complex + 8.57 eq TBAF	1.03 ( $\pm 0.44\%$ )	0.63 ( $\pm 0.42\%$ )

$\pm$ Error in brackets is represented as standard error in  $M^{-1}$ . All data were plotted at the 95% confidence interval

\*Lifetimes were best fit to a mono-exponential decay unless otherwise stated.

While the results before and after anion addition are as expected, the values for ‘ $q$ ’ in these complexes are not (**Table-4.15**). It was hypothesised that a reduction in steric hindrance would lead to an increase in space for ligating molecules, both solvent and guest species. Yet these values of ‘ $q$ ’ are comparatively lower than the more sterically hindered -O’Bu analogue.

**Table-4.15.** Luminescence lifetimes in non-deuterated and deuterated solvent of Eu.p.DO3AM.Pro.OMe (Conc of host is  $1 \times 10^{-3}$  mol dm<sup>-3</sup>)\*.

Media	EuL <sup>3.5g</sup>	Lifetime in Hydrated solvent (ms)	Lifetime in Deuterated solvent (ms)	Hydration number ( $q$ )
MeOH		0.67	1.76	1.4
H <sub>2</sub> O		0.49	1.37	1.0

\* All lifetime values are subject to an error of  $\pm 10\%$  or less.

While these lower ‘ $q$ ’ values are in agreement with the results from luminescence titrations, it was curious to observe the lack of a second binding event in any of the titrations. While this does not preclude the existence of a second binding event, it does imply that the second binding event is too weak to quantify, there is evidence for additional binding events at much higher concentrations of guest elsewhere in the literature.<sup>5</sup>

### 4.4.3 Eu.p.DO3AM.Pro.OH

The deprotected -OH analogue of the Eu.p.DO3AM.Pro.OR complex motif was synthesised to explore the potential for improved aqueous solubility. The lack of steric hindrance in comparison to the -O’Bu and -OMe analogues could also lead to differing observations. The presence of -OH groups close to the lanthanide was also

of interest as this could affect the solution phase chemistry, as well as affecting the luminescence lifetime of the Ln(III) ion in the complex.

#### 4.4.3.1 Luminescence in MeOH

Titration began in MeOH, titrating against acetate as the anionic guest (**Figure-4.19**). There was a large increase in spectral intensity, showing an overall single binding event, with a strong binding constant ( $K_1 = 99,000 \text{ M}^{-1}$  ( $\pm 65,300 \text{ M}^{-1}$ )). This is a high value that is expected of complexes like this in methanolic solution, yet the error in this measurement is very high. This could be due to the presence of an equilibrium between a bidentate binding mode and two monodentate binding modes, preventing clear determination hence yielding a large error. In this case, the bidentate binding mode is preferred giving a value for a first binding event.

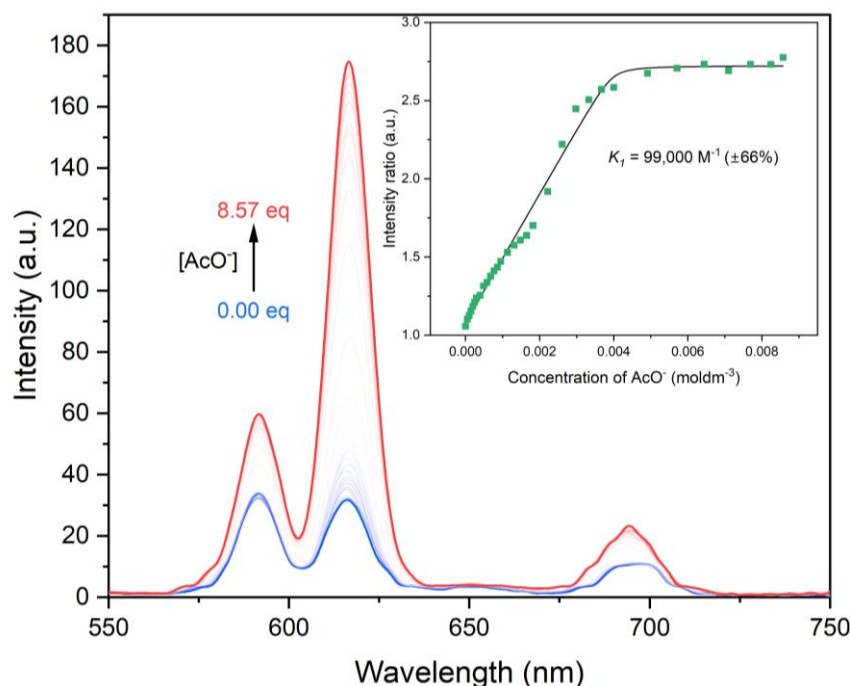


**Figure-4.19.** Graph showing the change in luminescence spectrum of Eu.p.DO3AM.Pro.OH ( $1 \times 10^{-3} \text{ mol dm}^{-3}$ ) in MeOH, upon addition of increasing amounts of NaOAc ( $0.02 \text{ mol dm}^{-3}$ ). With starting (blue) and end (red) concentrations highlighted,  $\lambda_{\text{ex}} = 393 \text{ nm}$ . *Inset:* binding isotherm from DynaFit<sup>®</sup>, plot of intensity ratio  $\Delta J=2/\Delta J=1$  (dark-green) vs concentration of  $\text{AcO}^-$ .

Luminescence titrations with KF and TBAF afforded a similar result, at an anionic guest concentration of 1.82 eq. In this case lanthanide demetallation from the complex is clearly observed. This is evident by the sharp decrease in spectral intensity, along with the observation of a loose precipitate in the cuvette at the time of running this experiment (**Figure-4.20**). The removal of all steric hinderance, upon creation of the OH group destabilised the complex to such an extent that upon exposure to a hard anionic guest, a precipitate was formed. This precipitate was white in colour so is likely  $\text{EuF}_3$  or  $\text{Eu}(\text{OH})_3$ , this occurred in both titrations which eliminates the probability that the fluoride source used caused precipitation.

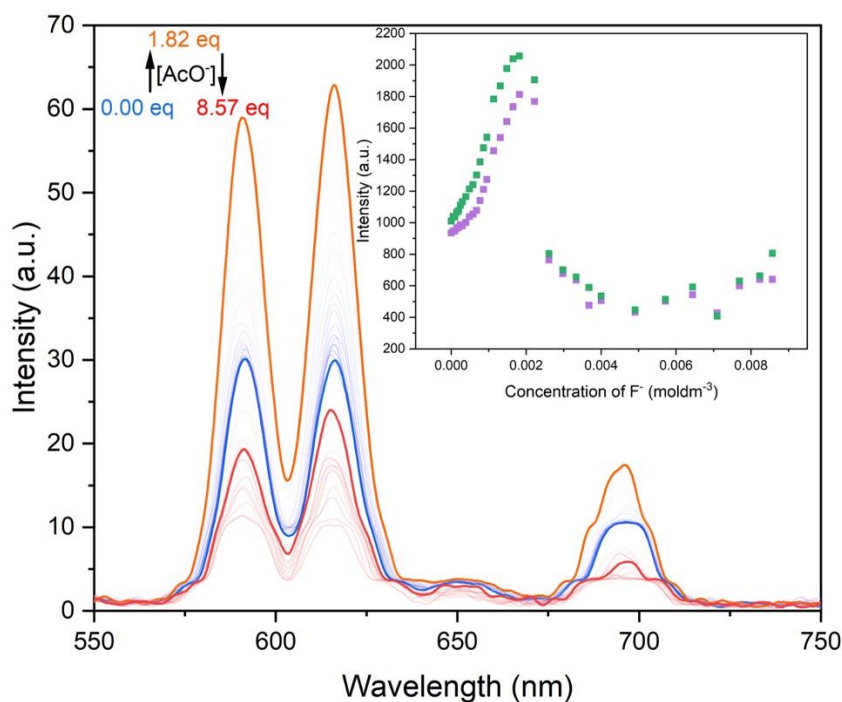


**Figure-4.20.** Graph showing the change in luminescence spectrum of Eu.p.DO3AM.Pro.OH ( $1 \times 10^{-3}$  mol dm $^{-3}$ ) in MeOH, upon addition of increasing amounts of KF (0.02 mol dm $^{-3}$ ). With starting (blue), maximum intensity (orange) and end (red) concentrations highlighted,  $\lambda_{\text{ex}} = 393$  nm. *Inset:* Change in intensity of area  $\Delta J=2$  (dark green) and area  $\Delta J=1$  (purple) vs concentration of F $^{-}$ .

In this case, the lattice enthalpy for the europium precipitate is much higher than any stabilisation gained from being embedded in a macrocyclic complex.<sup>2</sup> This demonstrates the drastic decrease in thermodynamic and kinetic stability upon reduction of the energetic barrier to demetallation in these complexes.<sup>6</sup>

#### 4.4.3.2 Luminescence in H $_2$ O

In aqueous media the same titrations were performed, starting out with a titration against anionic guest acetate (**Figure-4.21**). This titration fits well to one binding event with a very weak binding constant ( $K_1 = 89 \text{ M}^{-1} (\pm 3.03 \text{ M}^{-1})$ ). This is a very small binding constant, meaning that the guest will likely be in fast exchange with the bulk solvent.

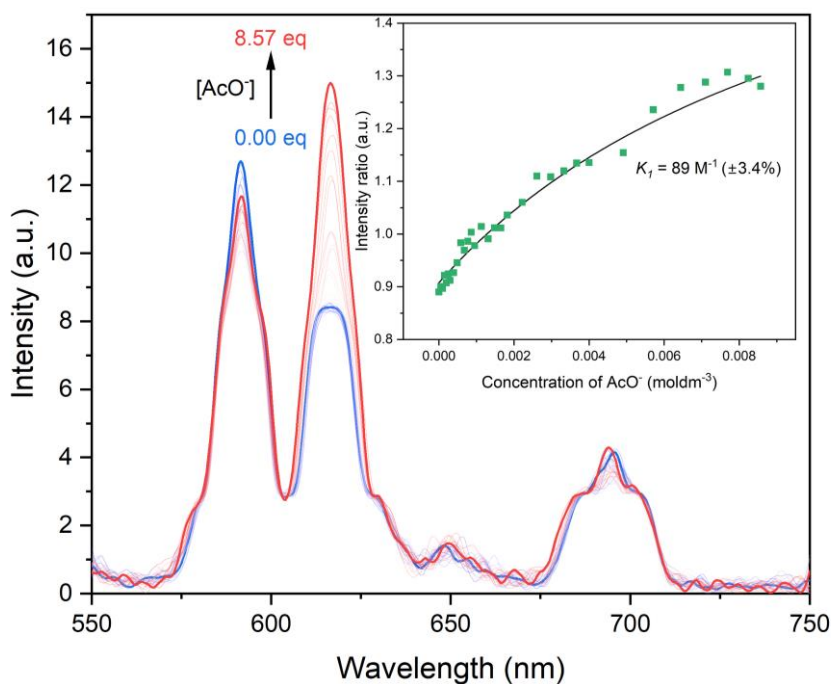


**Figure-4.21.** Graph showing the change in luminescence spectrum of Eu.p.DO3AM.Pro.OH ( $1 \times 10^{-3}$  mol dm $^{-3}$ ) in MilliQ water, upon addition of increasing amounts of NaOAc ( $0.02$  mol dm $^{-3}$ ). With starting (blue) and end (red) concentrations highlighted,  $\lambda_{\text{ex}} = 393$  nm. *Inset:* binding isotherm from DynaFit<sup>®</sup>, plot of intensity ratio  $\Delta J=2/\Delta J=1$  (dark green) vs concentration of AcO $^{-}$ .

Titration against both fluoride sources led to very distinct differences in the shape of each curve, with the titration with KF not fitting to any number of binding events, while titrating against TBAF fit to two binding events as hypothesised earlier in this thesis.

The titration against KF shows competitive binding through the first initial additions of fluoride: this is evident due to the lack of change in spectral intensity (**Figure-4.22**). This competitive binding may arise from the initial deprotonation of the hydroxyl groups on the ligand by fluoride anions in solution.

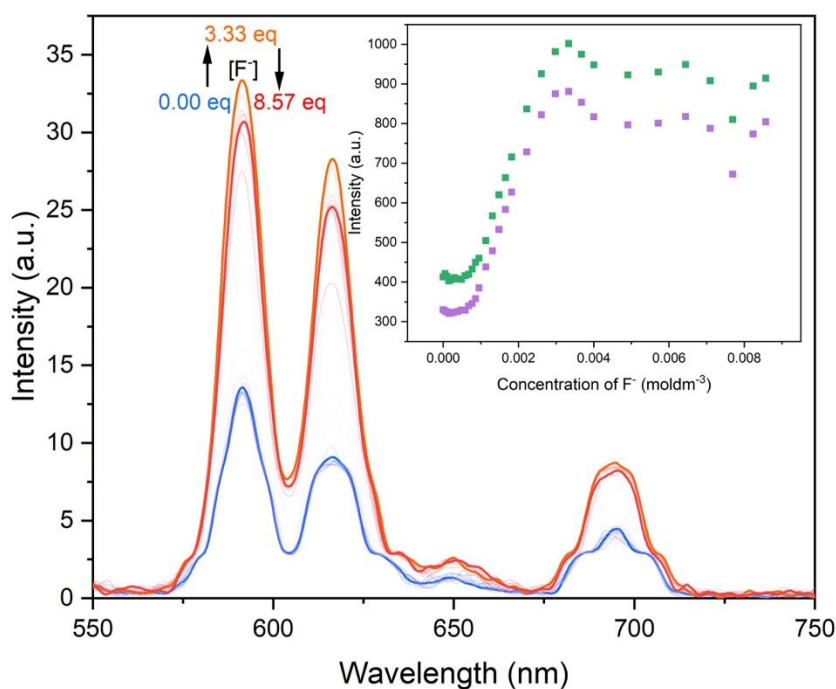


**Figure-4.22.** Graph showing the change in luminescence spectrum of Eu.p.DO3AM.Pro.OH ( $1 \times 10^{-3} \text{ mol dm}^{-3}$ ) in MilliQ water, upon addition of increasing amounts of KF ( $0.02 \text{ mol dm}^{-3}$ ). With starting (blue), maximum intensity (orange) and end (red) concentrations highlighted,  $\lambda_{\text{ex}} = 393 \text{ nm}$ . *Inset:* Change in intensity of area  $\Delta J=2$  (purple) and area  $\Delta J=1$  (dark green) vs concentration of  $\text{F}^-$ .

This would mean that in the initial stages of the titration, the ligand is being deprotonated by the added fluoride, before any binding takes place.<sup>7</sup> As upon reaching a fluoride concentration of greater than  $\approx 0.001 \text{ mol dm}^{-3}$ , the spectral intensity increases to a maximum before there is a slight decrease, which is the shape expected from a two binding event. These two binding events can be observed in the titration with TBAF (**Figure-4.23**).

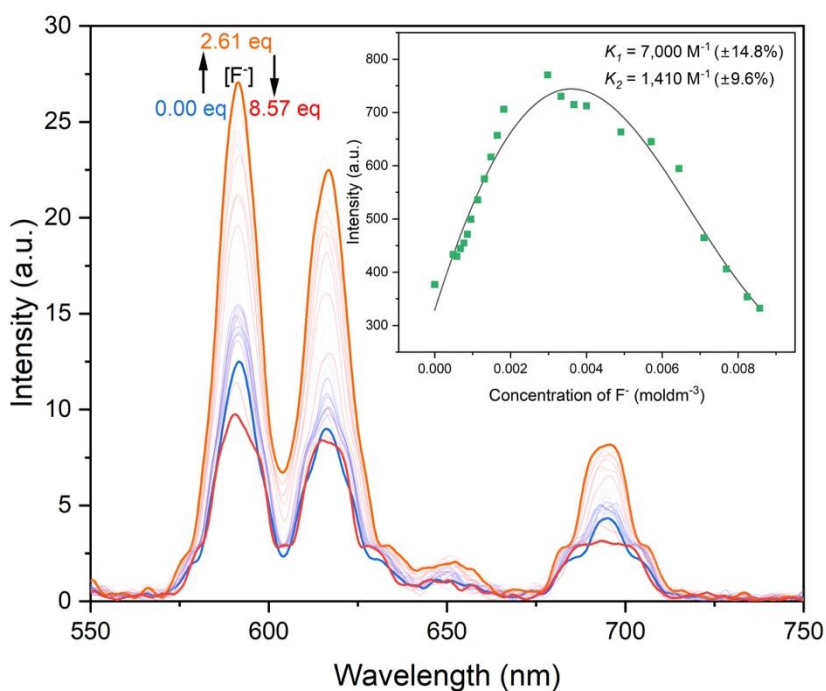


**Figure-4.23.** Graph showing the change in luminescence spectrum of Eu.p.DO3AM.Pro.OH ( $1 \times 10^{-3} \text{ mol dm}^{-3}$ ) in MilliQ water, upon addition of increasing amounts of TBAF ( $0.02 \text{ mol dm}^{-3}$ ). With starting (blue), maximum intensity (orange) and end (red) concentrations highlighted,  $\lambda_{\text{ex}} = 393 \text{ nm}$ . *Inset:* binding isotherm from DynaFit<sup>®</sup>, plot of intensity of area  $\Delta J=1$  (dark green) vs concentration of  $\text{F}^-$ .

By masking a few of the initial points in processing this data, a suitable fit for a two binding event was deduced. With this being separated into a strong first binding event ( $K_1 = 7,000 \text{ M}^{-1} (\pm 1,020 \text{ M}^{-1})$ ) and a weaker second binding event ( $K_1 = 1,410 \text{ M}^{-1} (\pm 135 \text{ M}^{-1})$ ). While there is still some initial competitive binding in this complex, there is not the same extent as was present in the titration against KF. What differs is the counterion for the fluoride in solution, specifically between a potassium ion ( $\text{K}^+$ ) and a tetra-*n*-butyl ammonium ion ( $[\text{N}((\text{CH}_2)_3\text{CH}_3)_4]^+$ ,  $\text{TBA}^+$ ). The potassium ion will have a greater charge density in comparison with the larger  $\text{TBA}^+$  ion. This greater charge density will lead to it being solvated well by water molecules and the acetate groups on the periphery of the complex in solution. This coordination to the acid arms on the complex makes the hydrogen atoms on each -COOH group much more acidic.<sup>8</sup> These more acidic protons therefore react first

with the fluoride added to solution and as such exhibit a greater extent of competitive binding, so causing no change in luminescence intensity until these protons have been fully removed by incoming fluoride ions. The binding constants would infer a picture of a complex with two binding modes (**Table-4.16**). Acetate binding in a bidentate fashion, fluoride showing two separate binding events. However this complex shows severe limitations due to its tendency to precipitate on standing in aqueous solution.

**Table-4.16.** Summary of binding constants of Eu.p.DO3AM.Pro.OH with anionic guests in MeOH and water (ppt. = precipitate).

Anionic source	Media	Binding constant ( $M^{-1}$ ) <sup>#</sup>	
		$K_1 = [EuLX]^-$ EuL <sup>3.6f</sup>	$K_2 = [EuLX_2]^{2-}$
NaOAc	MeOH	99,000 ( $\pm 65,300$ )	-
	Water	89 ( $\pm 3.03$ )	-
KF	MeOH	ppt.	-
	Water	-	-
TBAF	MeOH	ppt.	-
	Water	7,000 ( $\pm 1,020$ )	1,410 ( $\pm 135$ )

<sup>#</sup>  $K_1$  = first binding event;  $K_2$  = second binding event-deduced from binding isotherm generated from DynaFit<sup>®</sup>

$\pm$  Error in brackets is represented as standard error in  $M^{-1}$ . All data were plotted at the 95% confidence interval

<sup>§</sup> The binding of anions was studied by time-gated phosphorescence titrations of the complexes with varying concentrations of sodium acetate, potassium fluoride and tetrabutylammonium fluoride with binding isotherms generated using DynaFit<sup>®</sup>

#### 4.4.3.3 Luminescence lifetimes

Luminescence lifetimes before and after anion addition were recorded for the luminescence titrations (**Table-4.17**). In both titrations involving fluoride in MeOH there are reduced lifetimes due to quenching of the fluorescence through formation of a solid precipitate. The increase in lifetime with acetate again due to the replacement of a solvent molecule with a less effectively quenching anion guests.

For the titration in water, the values for fluoride titrations are predictable with the replacement of solvent with less effective fluoride quenchers.

**Table-4.17.** Summary of luminescence lifetimes of Eu.p.DO3AM.Pro.OH before and after anionic guest addition in MeOH and water (Conc of host is 0.001 mol dm<sup>-3</sup>, guest conc is 0.02 mol dm<sup>-3</sup>).

EuL <sup>3,6f</sup>	Lifetime in MeOH (ms)	Lifetime in H <sub>2</sub> O (ms)
Complex	0.41 (± 1.22%)	0.33 (± 1.43%)
Complex + 8.57 eq NaOAc	0.64 (± 0.38%)	0.20 (± 0.74%)
Complex + 8.57 eq KF	0.36 (± 1.07%)	0.45 (± 1.64%)
Complex + 8.57 eq TBAF	0.30 (± 2.8%)	0.41 (± 1.69%)

± Error in brackets is represented as standard error in M<sup>-1</sup>. All data were plotted at the 95% confidence interval

\* Lifetimes were best fit to a mono-exponential decay unless otherwise stated.

Yet upon addition of an acetate guest the lifetime for the complex decreases, meaning there is the inclusion of a more effective quenching pathway. This could be through photoelectron transfer from the electrons on the oxygen atoms on the ligating acetate ligand.<sup>9</sup> Lifetimes in deuterated and non-deuterated solvents were also collected to determine values for ‘*q*’ (Table-4.18).

**Table-4.18.** Luminescence lifetimes in non-deuterated and deuterated solvent of Eu.p.DO3AM.Pro.OH (Conc of host is 0.001 mol dm<sup>-3</sup>)\*.

Media	EuL <sup>3,6f</sup>		
	Lifetime in Hydrated solvent (ms)	Lifetime in Deuterated solvent (ms)	Hydration number ( <i>q</i> )
MeOH	0.41	3.26	1.0
H <sub>2</sub> O	0.33	2.68	1.1

\* All lifetime values are subject to an error of ± 10% or less.

The ‘*q*’ values corroborate well with the lifetime observations of one single binding event, with the potential for a second very weak binding event, that is too weak to be distinguishable by DynaFit<sup>®</sup> as a binding event.

#### 4.4.4 System summary

The Eu.p.DO3AM.Pro.OR complex exhibits the lowest thermodynamic and kinetic stability of any in this thesis, showing precipitation in the presence of fluoride, making it highly unsuitable for any further applications in this thesis which require it to be in fluoride containing solutions to act as a catalyst. Both the -OMe and -O<sup>t</sup>Bu analogues showed the presence of two binding events with differing strengths, one strong one weak. Contrary to what was hypothesised, the reduction in steric hindrance did not lead to stronger binding, with the opposite case being true to an extent of second binding events being unresolvable. Due to the second binding event in the Eu.p.DO3AM.Pro.OMe complex being much weaker than the second binding event in the Eu.p.DO3AM.Pro.O<sup>t</sup>Bu complex, this was deemed to be the deciding factor for carrying this complex forward to catalytic studies in Chapter-5. The second binding event must be very weak to enable fast exchange with other guest anions, as the guests must bind and unbind quickly to give an effective catalyst. In the -O<sup>t</sup>Bu analogue, the binding strength is such that the guests would remain bound even after a reaction had occurred.

#### 4.5 Eu.p.DO3AM.Lys

The Eu.p.DO3AM.Lys based complex systems were designed to localise a positive charge on the ligand periphery. This positive charge will act to keep the complexes apart and prevent the aggregation previously observed within similarly constructed complexes. The inclusion of an amine group should also improve water solubility, with this being one of the most desirable properties as the catalytic studies are in water. The inclusion of -O<sup>t</sup>Bu, -OMe and -OH groups is for the same reasons mentioned in **Section-4.2**.

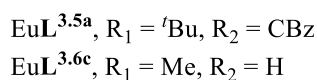
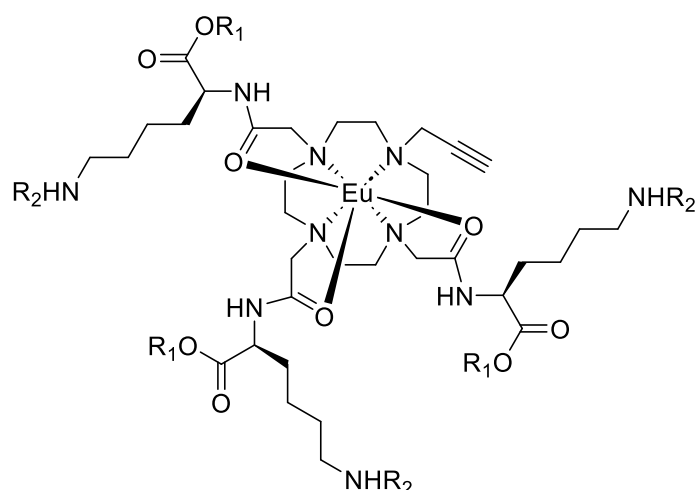


**Figure-4.24.** General chemical structure of Eu.p.DO3AM.Lys.OR complexes.

### 4.5.1 Eu.p.DO3AM.Lys.O<sup>t</sup>Bu.CBz

The Eu.p.DO3AM.Lys.O<sup>t</sup>Bu.CBz complex has all bulky protecting groups still in place. These groups prevent it from being soluble in aqueous media, yet the binding around this complex was investigated to determine the role that steric hindrance plays in binding to this complex motif.

#### 4.5.1.1 Luminescence in MeOH

Titration were carried out in MeOH alone for this complex, with the first titration being with acetate as the guest anion (**Figure-4.25**). The change in spectral intensity fit well with the presence of two binding events, a strong first binding event ( $K_1 = 2,690 \text{ M}^{-1} (\pm 70.0 \text{ M}^{-1})$ ) followed by a weaker second binding event ( $K_2 = 10.4 \text{ M}^{-1} (\pm 0.30 \text{ M}^{-1})$ ). The curve fitting very well to this across all monitored peaks. This would indicate that there are two binding modes within this complex. Luminescence titrations were then carried out for both fluoride sources. For the

luminescence titration with KF, the shape of the graph of peak spectral intensity vs guest concentration would appear to correlate with two binding events. Yet this was unresolvable into binding events, making determination of the binding strength impossible.

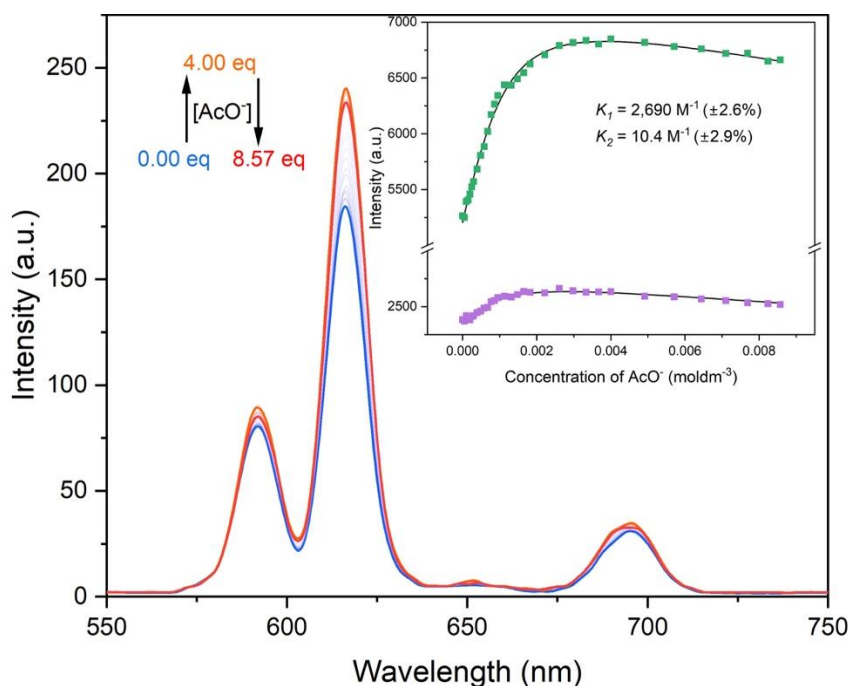


**Figure-4.25.** Graph showing the change in luminescence spectrum of Eu.p.DO3AM.Lys.O'Bu.CBz ( $1 \times 10^{-3} \text{ mol dm}^{-3}$ ) in MeOH, upon addition of increasing amounts of NaOAc ( $0.02 \text{ mol dm}^{-3}$ ). With starting (blue), maximum intensity (orange) and end (red) concentrations highlighted,  $\lambda_{\text{ex}} = 393 \text{ nm}$ . Inset: binding isotherm from DynaFit<sup>®</sup>, plot of intensity of area  $\Delta J=2$  (dark green) and area  $\Delta J=1$  (purple) vs concentration of AcO<sup>-</sup>.

The same titration carried out with TBAF as the fluoride source, generated a binding isotherm that fit to two binding events. With a strong first binding event ( $K_1 = 17,600 \text{ M}^{-1} (\pm 4,750 \text{ M}^{-1})$ ) and weaker second binding event ( $K_2 = 30.6 \text{ M}^{-1} (\pm 0.83 \text{ M}^{-1})$ ) (Figure-4.26). Confirming the difference between KF and TBAF as fluoride sources, with KF having limited solubility in MeOH, while TBAF exhibits good solubility in MeOH. This could be the limiting factor but there are other factors such as the presence of a charge dense  $\text{K}^+$  ion in solution meaning this cannot be said with certainty due to other variables present. However, the titration

with TBAF does show the presence of two binding events that were hypothesised from the titration with KF. Based on previous luminescence titrations the two fluoride sources yield results that are within error of each other, yet in some MeOHic systems they show stark differences.

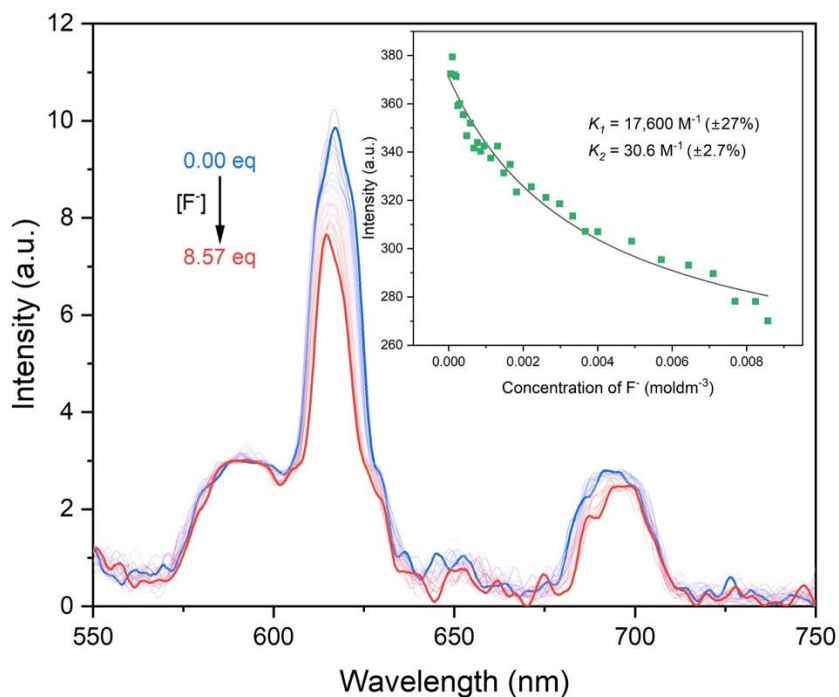


**Figure-4.26.** Graph showing the change in luminescence spectrum of Eu.p.DO3AM.Lys.O'Bu.CBz ( $1 \times 10^{-3}$  mol dm $^{-3}$ ) in MeOH, upon addition of increasing amounts of TBAF (0.02 mol dm $^{-3}$ ). With starting (blue), maximum intensity (orange) and end (red) concentrations highlighted,  $\lambda_{\text{ex}} = 393$  nm. *Inset:* binding isotherm from DynaFit<sup>®</sup>, plot of intensity of area  $\Delta J=2$  (dark green) vs concentration of AcO $^{-}$ .

While frustrating that the binding constant for the KF luminescence titration was undeterminable, the results from the other titrations carried out would infer the presence of two binding modes (**Table-4.19**). With the complex exhibiting strong binding for all the anionic guests it was titrated against.

**Table-4.19.** Summary of binding constants of Eu.p.DO3AM.Lys.O'Bu.Cbz with anionic guests in MeOH.

Anionic source	Media	Binding constant ( $M^{-1}$ ) <sup>#</sup>	
		$K_1 = [EuLX]^-$ EuL <sup>3.5d</sup>	$K_2 = [EuLX_2]^{2-}$
NaOAc	MeOH	2,690 ( $\pm 70.0$ )	10.4 ( $\pm 0.30$ )
KF	MeOH	-	-
TBAF	MeOH	17,600 ( $\pm 4,750$ )	30.6 ( $\pm 0.83$ )

<sup>#</sup>  $K_1$  = first binding event;  $K_2$  = second binding event-deduced from binding isotherm generated from DynaFit<sup>®</sup>

$\pm$  Error in brackets is represented as standard error in  $M^{-1}$ . All data were plotted at the 95% confidence interval

<sup>§</sup> The binding of anions was studied by time-gated phosphorescence titrations of the complexes with varying concentrations of sodium acetate, potassium fluoride and tetrabutylammonium fluoride with binding isotherms generated using DynaFit<sup>®</sup>

#### 4.5.1.2 Luminescence lifetimes

Luminescence lifetimes of the complex before and after anion additions were taken (**Table-4.20**). These exhibited some curious observations, while the lifetime with acetate as guest is in the range that would be expected, the lifetimes with the fluoride guests differ greatly. The addition of KF to a complex solution provides the expected result with coordination of the fluoride to the Eu (III) centre preventing effective luminescence quenching. In contrast, the inclusion of TBAF into the solution produces the opposite result, a decrease in the luminescence lifetime, corresponding to more effective quenching upon anion addition. This is likely due to fluorides effectiveness as a good photoinduced electron transfer (PeT) quencher, with this effect not being seen for KF due to solubility constraints.

**Table-4.20.** Summary of luminescence lifetimes of Eu.p.DO3AM.Lys.O'Bu.CBz before and after anionic guest addition in MeOH (Conc of host is  $1 \times 10^{-3}$  mol dm<sup>-3</sup>, guest conc is 0.02 mol dm<sup>-3</sup>).

EuL <sup>3.5a</sup>	Lifetime in MeOH (ms)
Complex	0.68 ( $\pm$ 0.53%)
Complex + 8.57 eq NaOAc	0.65 ( $\pm$ 0.38%)
Complex + 8.57 eq KF	0.98 ( $\pm$ 0.77%)
Complex + 8.57 eq TBAF	0.56 ( $\pm$ 1.46%)

$\pm$  Error in brackets is represented as standard error in M<sup>-1</sup>. All data were plotted at the 95% confidence interval

\* Lifetimes were best fit to a mono-exponential decay unless otherwise stated.

A *q*-value was determined for this complex, through the measurement of the lifetime in deuterated and non-deuterated solvent (**Table-4.21**). A value of 0.7 for 'q' would imply binding of only one solvent molecule which is in exchange with the bulk solvent, which given the size of the complex and associated steric hindrance seems likely.

**Table-4.21.** Luminescence lifetimes in MeOH and MeOD of Eu.p.DO3AM.Lys.O'Bu.CBz (Conc of host is 0.001 mol dm<sup>-3</sup>)\*

Media	EuL <sup>3.5a</sup>		
	Lifetime in Hydrated solvent (ms)	Lifetime in Deuterated solvent (ms)	Hydration number ( <i>q</i> )
MeOH	0.68	1.21	0.7

\* All lifetime values are subject to an error of  $\pm$  10% or less

This does make sense in terms of the complex binding hard anionic guests. 'Hard' anions bind strongly to the Eu(III) centre, allowing them to overcome steric hindrance inherent in the complex, something that the poorly solvating MeOH molecules will be unable to do.

## 4.5.2 Eu.p.DO3AM.Lys.OMe

The Eu.p.DO3AM.Lys.OMe complex was designed to maximise the chance of aqueous solubility and prevent aggregation in solution, through the inclusion of positively-charged amine groups on the arms of the complex. This complex proved to be highly soluble in water, showing the importance of ligand design and how this can yield desirable properties. As such, the observations from the experiments in aqueous conditions were of great interest, yet the MeOH-based experiments gave a good base for comparison with other complexes in this Chapter.

### 4.5.2.1 Luminescence in MeOH

Luminescence titrations began with titration against acetate as the anionic guest (**Figure-4.27**). The complex exhibited a very strong first binding event ( $K_1 = 33,800 \text{ M}^{-1}$  ( $\pm 7,270 \text{ M}^{-1}$ )). With no second binding event it can be inferred that the guest bound in a bidentate fashion, with both oxygen atoms binding to the central Eu(III) ion. While there is evidence of strong binding, the curve itself is sigmoidal, this could be due to aforementioned reasons of the equilibrium between two mono- and one bidentate binding modes for acetate, or the inclusion of an amine in solution could create targets for offsite interactions. These off-site targets would be a competitive binding site at low concentrations of anionic guest, hence the perturbation to the curve early in the titration. At higher concentrations the preference for anionic guest binding, would be the Eu(III) ion which exhibits a much stronger electrostatic force of attraction.

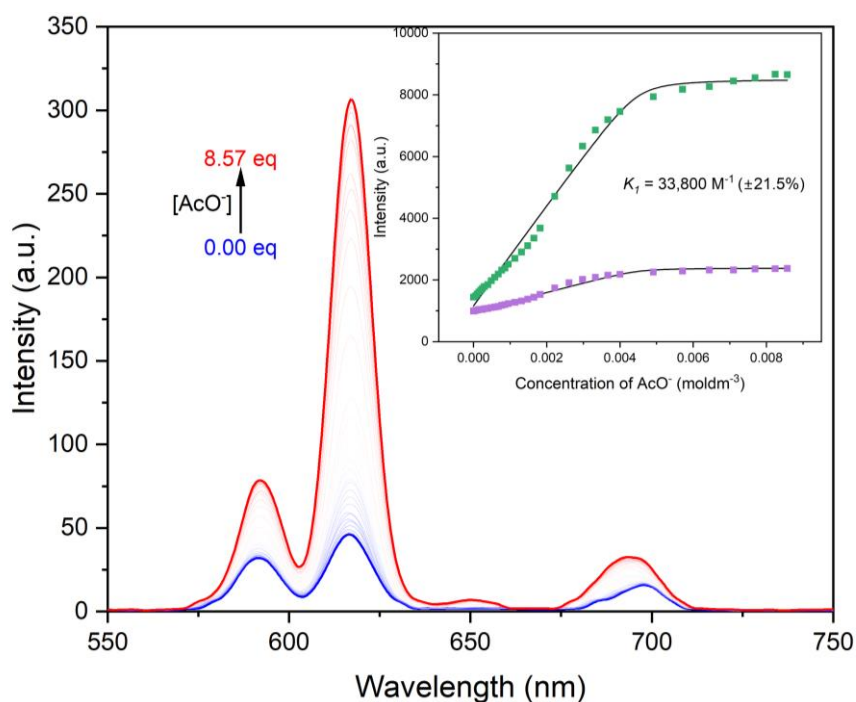


**Figure-4.27.** Graph showing the change in luminescence spectrum of Eu.p.DO3AM.Lys.OMe ( $1 \times 10^{-3} \text{ mol dm}^{-3}$ ) in MeOH, upon addition of increasing amounts of NaOAc ( $0.02 \text{ mol dm}^{-3}$ ). With starting (blue) and end (red) concentrations highlighted,  $\lambda_{\text{ex}} = 393 \text{ nm}$ . *Inset:* binding isotherm from DynaFit<sup>®</sup>, plot of intensity of area  $\Delta J=2$  (dark green) and area  $\Delta J=1$  (purple) vs concentration of  $\text{AcO}^-$ .

Titration against both fluoride sources showed a high degree of correlation with both showing the presence of two binding events, with the values being within the error regions with respect to one another (**Figure-4.28**).

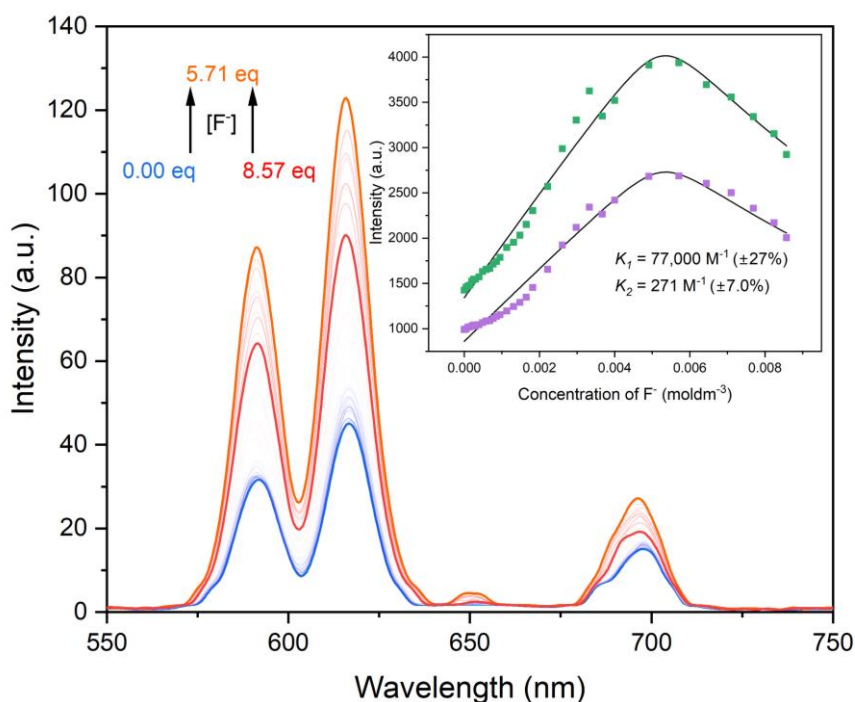


**Figure-4.28.** Graph showing the change in luminescence spectrum of Eu.p.DO3AM.Lys.OMe ( $1 \times 10^{-3} \text{ mol dm}^{-3}$ ) in MeOH, upon addition of increasing amounts of KF ( $0.02 \text{ mol dm}^{-3}$ ). With starting (blue), maximum intensity (orange) and end (red) concentrations highlighted. *Inset:* binding isotherm from DynaFit<sup>®</sup>, plot of intensity of area  $\Delta J=2$  (dark green) and area  $\Delta J=1$  (purple) vs concentration of  $F^-$ .

#### 4.5.2.2 Luminescence in H<sub>2</sub>O

The main area of interest for this complex was its aqueous binding with guests, due to its applications later in this thesis requiring aqueous solubility. The difference of note now being that the amine furthest away from the cyclen ring is protonated, for reasons mentioned in **Section-3.3.1**. The titration against acetate showed a weak single binding event ( $K_1 = 147 \text{ M}^{-1} (\pm 0.88)$ ) (**Figure-4.29**).

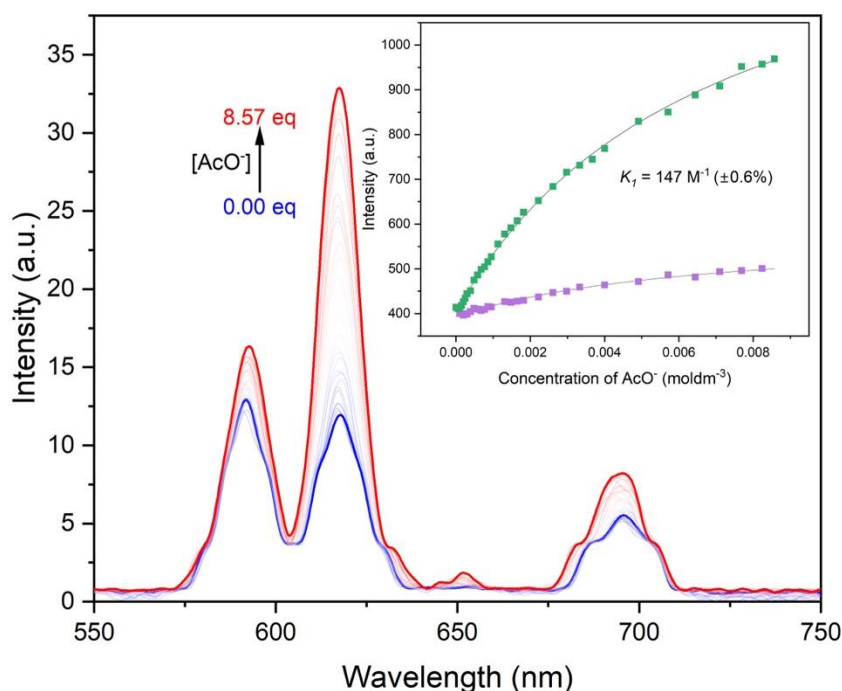


**Figure-4.29.** Graph showing the change in luminescence spectrum of Eu.p.DO3AM.Lys.OMe ( $1 \times 10^{-3} \text{ mol dm}^{-3}$ ) in MilliQ water, upon addition of increasing amounts of NaOAc ( $0.02 \text{ mol dm}^{-3}$ ). With starting (blue) and end (red) concentrations highlighted,  $\lambda_{\text{ex}} = 393 \text{ nm}$ . *Inset:* binding isotherm from DynaFit<sup>®</sup>, plot of intensity of area  $\Delta J=2$  (dark green) and area  $\Delta J=1$  (purple) vs concentration of  $\text{AcO}^-$ .

Yet there is small evidence of competitive binding, likely arising from the protonated amine. The clustering of points ( $0\text{--}5 \times 10^{-4} \text{ mol dm}^{-3}$ ) initially gives evidence for competitive binding of acetate to the peripheral amine groups. Yet this competitive binding is almost negligible with the error within this measurement being very low despite this.

The titrations with fluoride were more difficult to resolve into distinct binding events. Changing the identity of guest from acetate to fluoride produces a much greater degree of competitive binding as evidenced in the initial lack of change in the area of peak intensity (**Figure-4.30**).

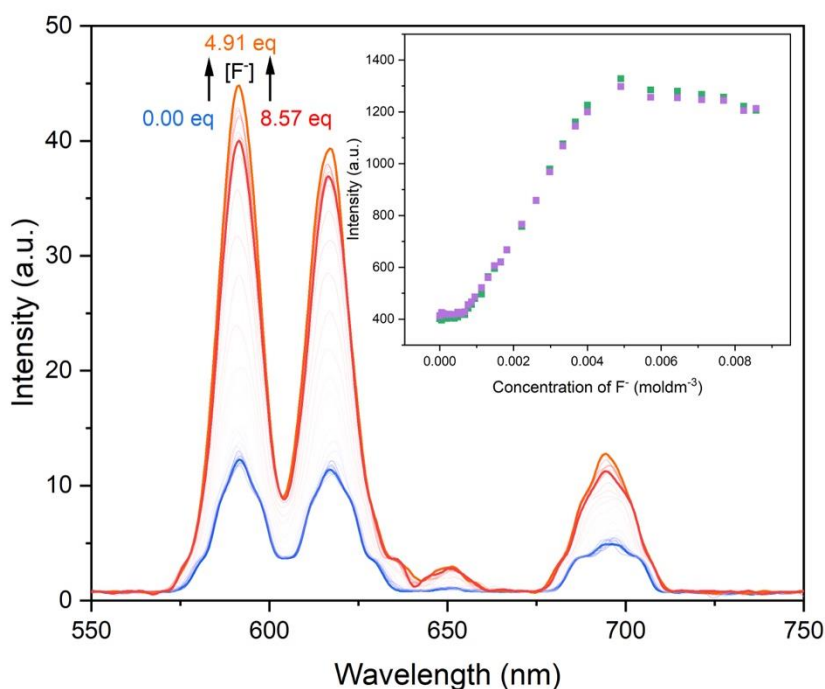


**Figure-4.30.** Graph showing the change in luminescence spectrum of Eu.p.DO3AM.Lys.OMe ( $1 \times 10^{-3} \text{ mol dm}^{-3}$ ) in MilliQ water, upon addition of increasing amounts of KF ( $0.02 \text{ mol dm}^{-3}$ ). With starting (blue), maximum intensity (orange) and end (red) concentrations highlighted,  $\lambda_{\text{ex}} = 393 \text{ nm}$ . *Inset:* Change in intensity of area  $\Delta J=2$  (purple) and area  $\Delta J=1$  (dark green) vs concentration of  $F^-$ .

The presence of this competitive binding makes the titration with KF unassignable to any potential binding isotherm. The same can be said for the titration with TBAF, yet through removal of the initial competitive binding data points binding events are resolvable. While the two binding constants generated cannot be taken to be completely accurate, the presence of two binding constants of differential strength ( $K_1 = 144,000 \text{ M}^{-1} (\pm 34,600 \text{ M}^{-1})$ ,  $K_2 = 115 \text{ M}^{-1} (\pm 3.11 \text{ M}^{-1})$ ) was implied by the shape of the curve with an initial decrease followed by a decrease in intensity (Figure-4.31).

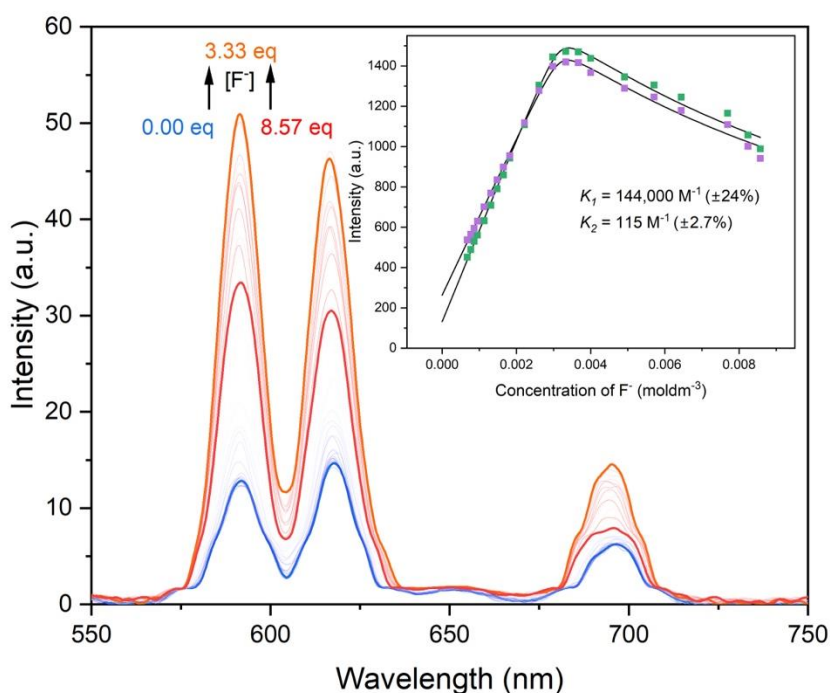


**Figure-4.31.** Graph showing the change in luminescence spectrum of Eu.p.DO3AM.Lys.OMe ( $1 \times 10^{-3} \text{ mol dm}^{-3}$ ) in MilliQ water, upon addition of increasing amounts of TBAF ( $0.02 \text{ mol dm}^{-3}$ ). With starting (blue), maximum intensity (orange) and end (red) concentrations highlighted,  $\lambda_{\text{ex}} = 393 \text{ nm}$ . *Inset:* binding isotherm from DynaFit<sup>®</sup>, plot of intensity of area  $\Delta J=2$  (purple) and area  $\Delta J=1$  (dark green) vs concentration of  $\text{F}^-$ .

This evidence all points towards the presence of two binding events, but with distinct competitive binding at the outset of the titration. Likely due to the protonated amines in aqueous media binding to the ‘hard’ fluoride anions. The binding constants are in good agreement with the current hypothesis of two guests binding to the heptadentate Eu(III) complexes (**Table-4.22**).

**Table-4.22.** Summary of binding constants of Eu.p.DO3AM.Lys.OMe with anionic guests in MeOH and water.

Anionic source	Media	Binding constant ( $M^{-1}$ ) <sup>#</sup>	
		$K_1 = [EuLX]^-$ EuL <sup>3.5g</sup>	$K_2 = [EuLX_2]^{2-}$
NaOAc	MeOH	33,800 ( $\pm 7,440$ )	-
	Water	147 ( $\pm 0.89$ )	-
KF	MeOH	77,000 ( $\pm 20,800$ )	271 ( $\pm 19.0$ )
	Water	-	-
TBAF	MeOH	61,000 ( $\pm 25,000$ )	36 ( $\pm 3.67$ )
	Water*	144,000 ( $\pm 34,600$ )	115 ( $\pm 3.11$ )

<sup>#</sup>  $K_1$  = first binding event;  $K_2$  = second binding event-deduced from binding isotherm generated from DynaFit<sup>®</sup>

<sup>±</sup> Error in brackets is represented as standard error in  $M^{-1}$ . All data were plotted at the 95% confidence interval

<sup>§</sup> The binding of anions was studied by time-gated phosphorescence titrations of the complexes with varying concentrations of sodium acetate, potassium fluoride and tetrabutylammonium fluoride with binding isotherms generated using DynaFit<sup>®</sup>

\* Data points associated with this binding constant were modified considerably to attain values for the separate binding constants

### 4.5.2.3 Luminescence lifetimes

Luminescence lifetimes were taken before and after anion addition. The results in MeOH showed expected values with fluoride inhibiting the quenching of the Eu(III) ion by solvent molecules, and acetate showing an overall similarity due to the provision of alternate quenching pathways (**Table-4.23**). For the values in water, both fluoride titrations result in a longer lifetime, along with a reduction in lifetime with acetate providing more effective quenching pathways for luminescence.

**Table-4.23.** Summary of luminescence lifetimes of Eu.p.DO3AM.Lys.OMe before and after anionic guest addition in MeOH and water (Conc of host is 0.001 mol dm<sup>-3</sup>, guest conc is 0.02 mol dm<sup>-3</sup>).

EuL <sup>3.6c</sup>	Lifetime in MeOH (ms)	Lifetime in H <sub>2</sub> O (ms)
Complex	0.55 (±0.59%)	0.57 (±0.39%)
Complex + 8.57 eq NaOAc	0.62 (±0.25%)	0.43 (±0.86%)
Complex + 8.57 eq KF	0.95 (±0.55%)	0.59 (±1.16%)
Complex + 8.57 eq TBAF	0.90 (±0.63%)	0.69 (±0.66%)

± Error in brackets is represented as standard error in M<sup>-1</sup>. All data were plotted at the 95% confidence interval

\* Lifetimes were best fit to a mono-exponential decay unless otherwise stated.

Lifetimes in deuterated and non-deuterated solvents were taken to determine the solvation number ‘*q*’ in each solvent (**Table-4.24**).

**Table-4.24.** Luminescence lifetimes in non-deuterated and deuterated solvent of Eu.p.DO3AM.Lys.OMe (Conc of host is 0.001 mol dm<sup>-3</sup>)\*.

Media	EuL <sup>3.6c</sup>		
	Lifetime in Hydrated solvent (ms)	Lifetime in Deuterated solvent (ms)	Hydration number ( <i>q</i> )
MeOH	0.55	2.26	2.5
H <sub>2</sub> O	0.57	1.70	0.8

\* All lifetime values are subject to an error of ±10% or less.

The ‘*q*’ number for the complex in MeOH shows good agreement with the data from binding titrations, specifically the presence of more than one binding species. The ‘*q*’ value in aqueous media correlates somewhat with previous observations, showing that there is coordination of solvent and guest species, yet differs with the MeOH value as 0.8 implies binding of only one solvent molecule. This could be due to differing binding strengths between solvent molecules and hard anionic guests, with the identity of the solvent changing, this impacts degree of competition for binding slots. As the complex will bind more anionic guests due to the increased binding strength, in comparison to the weaker binding solvent molecules. Yet binding of only one acetate molecule, even in a bidentate fashion, would indicate there is less room for binding. Leading to the conclusion that only in higher

concentrations of fluoride is the second binding event visible, and the complex is capable of binding two guests with one in very fast exchange.

### **4.5.3 System summary**

The Eu.p.DO3AM.Lys.OR motif produced interesting results. Confirming the hypothesis developed so far that reduction of steric hindrance, through deprotection or changing identity of protecting groups, does not necessarily create more room for guest binding. In some cases, introducing additional groups can lead to interference with guest binding, such as the -NH<sub>2</sub> group included in the Eu.p.DO3AM.Lys.OMe complex. The design of the macrocyclic ligand worked well to solubilise this complex, again showing the effect of hydrophobic protecting groups on complex solubility, along with the positive impact of cationic groups on aqueous solubility.

## 4.6 Conclusions

In this Chapter, it has been demonstrated for a large range of heptadentate complexes that there are two binding modes with differing strengths, specifically one much stronger than the other, with the weaker being in fast exchange as a result. This has been confirmed through carrying out luminescence titrations to determine the number of binding events and quantifying their strengths, observation of the lifetimes before and after guest addition and determination of hydration numbers ( $q$ ) for each complex-solvent pair (Figure-4.32).

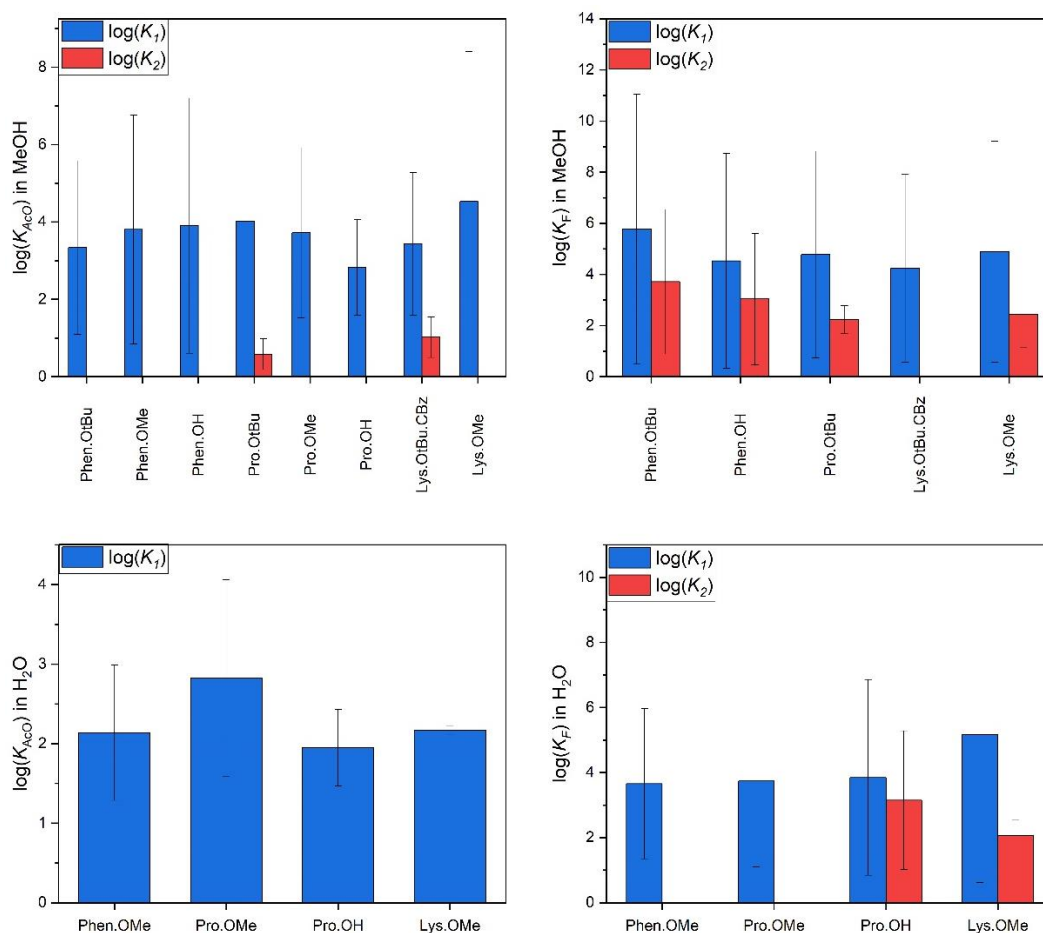


**Figure-4.32.** Summary of all binding constants outlined in Chapter-4 for each complex (Eu.p.DO3AM.X). Where  $K_F$  represents the binding constant with fluoride,  $K_{AcO}$  represents the binding constant with acetate, black bars represent the associated errors.

The complexes exhibited variable solubility with some incapable of dissolving in water and preventing results being gained for these complexes in aqueous media. Due to the further application of these complexes requiring aqueous solubility, a suitable group of water-soluble complexes had to be chosen. This need arises because the specific fluorination reactions being investigated, take place faster in water than in MeOH.<sup>10</sup> Therefore the complexes chosen to carry forward to catalytic studies, were selected for their aqueous solubility and stability within solution, the chosen complexes are summarised in **Figure-4.33**.

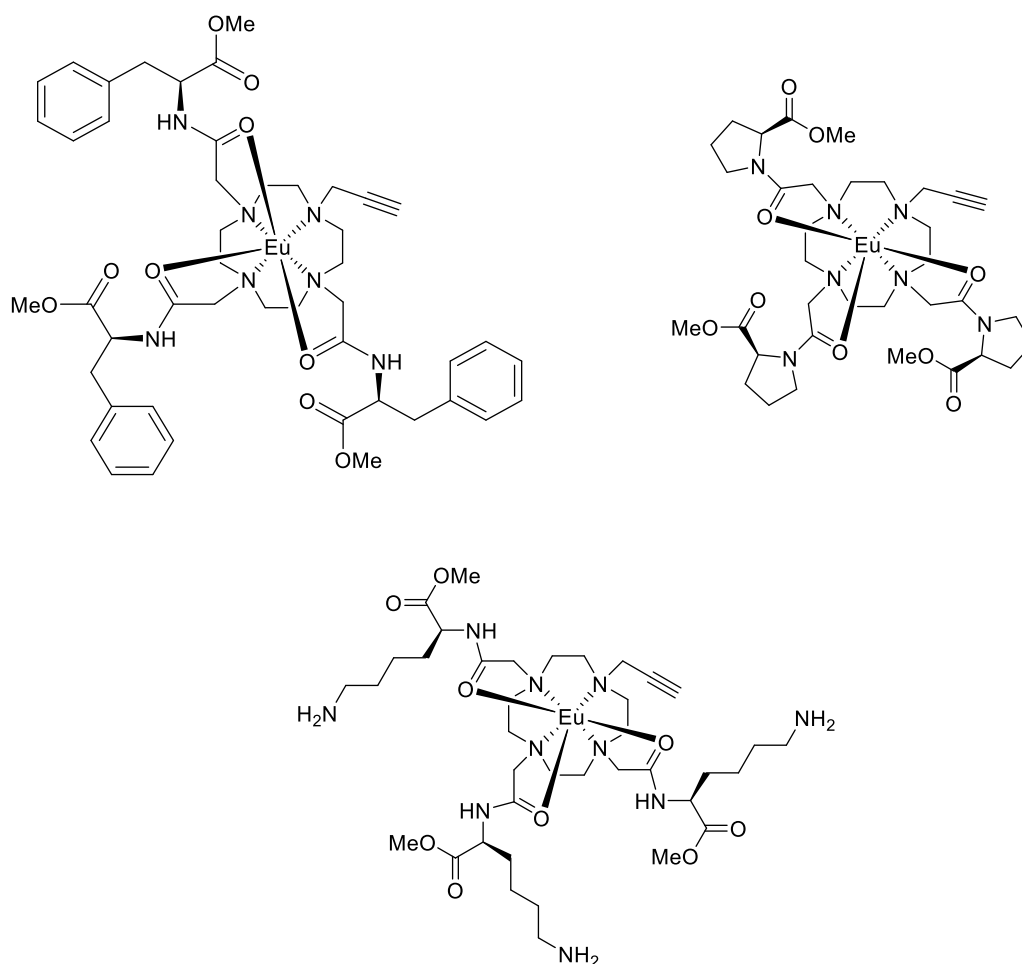


**Figure-4.33.** Chemical structures of complexes chosen for catalytic studies. Eu.p.DO3AM.Phen.OMe (*top left*), Eu.p.DO3AM.Pro.OMe (*top right*), Eu.p.DO3AM.Lys.OMe (*bottom*).

The -OMe analogues of each complex motif showed improved aqueous solubility, the presence of two binding events and no precipitation upon exposure to hard anions. All desirable properties to have for their application as homogenous catalysts for the fluorination of halocarboxylic acids in aqueous media.

## 4.7 References

- 1 R. M. Supkowski and W. DeW. Horrocks, *Inorganica Chim Acta*, 2002, **340**, 44–48.
- 2 M. L. Parker, J. Jian and J. K. Gibson, *Phys. Chem. Chem. Phys.*, 2021, **23**, 11314–11326.
- 3 A. K. R. Junker, M. Tropicano, S. Faulkner and T. J. Sørensen, *Inorg Chem*, 2016, **55**, 12299–12308.
- 4 A. Beeby, I. M. Clarkson, R. S. Dickins, S. Faulkner, D. Parker, L. Royle, A. S. de Sousa, J. A. G. Williams and M. Woods, *J. Chem. Soc., Perkin. Trans.*, 1999, 493–504.
- 5 C. Alexander, J. A. Thom, A. M. Kenwright, K. E. Christensen, T. J. Sørensen and S. Faulkner, *Chem Sci*, 2023, **14**, 1194–1204.
- 6 T. J. Sørensen and S. Faulkner, *Acc Chem Res*, 2018, **51**, 2493–2501.
- 7 C. Caltagirone, G. W. Bates, P. A. Gale and M. E. Light, *Chem. Commun.*, 2008, 61–63.
- 8 F. Cotton, G. Wilkinson, C. A. Murillo and M. Bochmann, *Advanced Inorganic Chemistry*, 6th edn., 1999.
- 9 D. Parker, J. D. Fradgley and K.-L. Wong, *Chem Soc Rev*, 2021, **50**, 8193–8213.
- 10 Laura. Mason, DPhil thesis, University of Oxford, 2017.

## Chapter-5: Catalytic studies on DO3AM derivatives

### 5.1 Aim and Scope

To assess the catalytic ability of the DO3AM derivatives (Chapters 3 and 4), and to confirm the catalytic cycle observed in Chapter-2, three Eu.p.DO3AM derivatives were carried forward to catalytic studies (**Figure-5.1**).

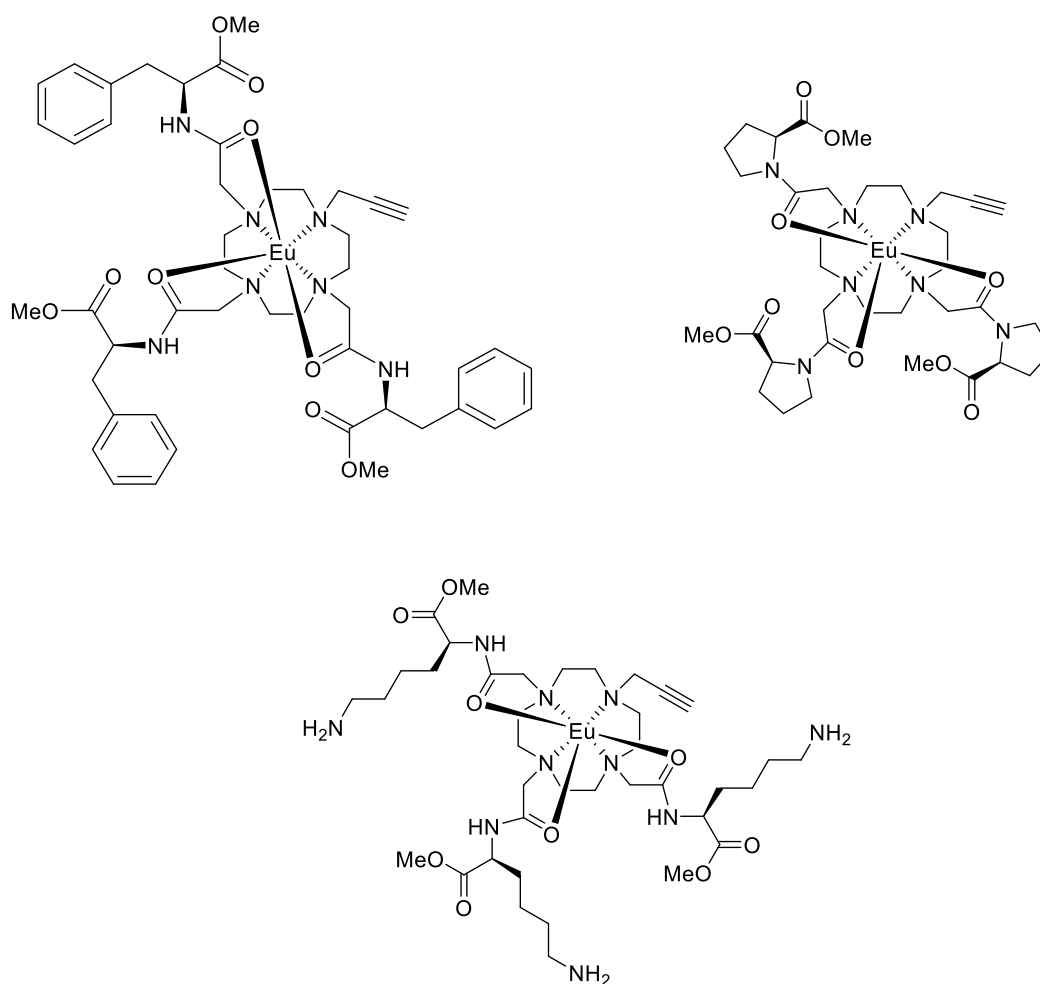


**Figure-5.1.** Chemical structures of complexes chosen for catalytic studies. Eu.p.DO3AM.Phen.OMe (*top left*), Eu.p.DO3AM.Pro.OMe (*top right*), Eu.p.DO3AM.Lys.OMe (*bottom*).

With more tailored ligand spheres in contrast to Ln.p.DO3A systems detailed in Chapter-2, the aim is to create more effective catalysts while still retaining aqueous solubility.

## 5.2 Proposed catalytic route

Previously in the Faulkner group, catalytic activity was observed on Eu.p.DO3AM.Asp.OH.OH and Eu.p.DO3AM.Asp.O'Bu.O'Bu complexes, when a series of halocarboxylic acids underwent an S<sub>N</sub>2 reaction with fluorine (**Figure-5.2**).<sup>1</sup> Given the importance of fluorine-18 in radio imaging, this reaction has the potential to provide a route for late stage labelling of radiopharmaceuticals in water if effective catalysis can be achieved.

It is proposed that the lanthanide complex acts as a catalyst, holding both reactants in close proximity while they are coordinated to the Eu(III) centre. With the addition of fluorine regio- and potentially stereoselectively onto specific biomolecules, this is of great interest for the creation of novel agents for Positron Emission Tomography (PET) imaging.

It is proposed that once the S<sub>N</sub>2 reaction has occurred, the substrates are exchanged with bulk solution, restoring the catalyst to its starting condition. With the catalyst being restored due to the transient nature of bonding at the Eu(III) centre in aqueous media. As the catalyst is dissolved in aqueous media, this represents the potential for an effective, water soluble and homogenous catalyst.

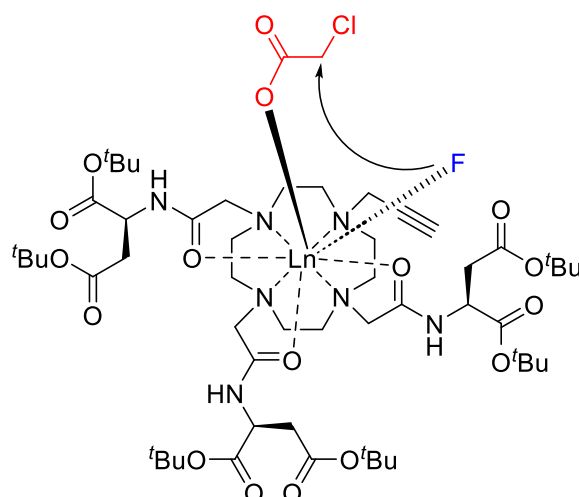
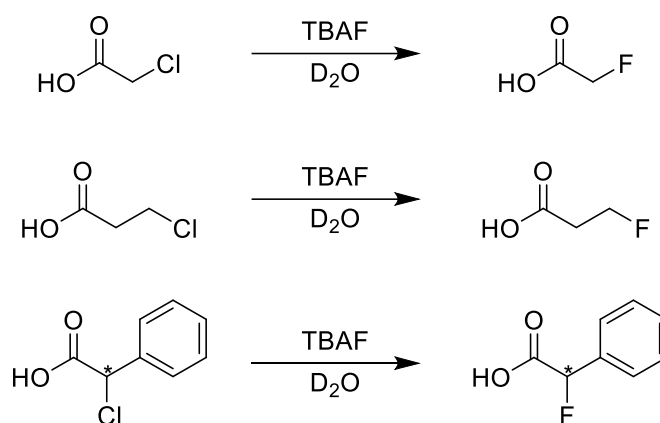


**Figure-5.2.** Formation of a quaternary lanthanide-based complex for the fluorination of halocarboxylic acids, with proposed mechanism of  $S_N2$  action. Bound Fluoride ion (blue), general halocarboxylic acid substrate (red).

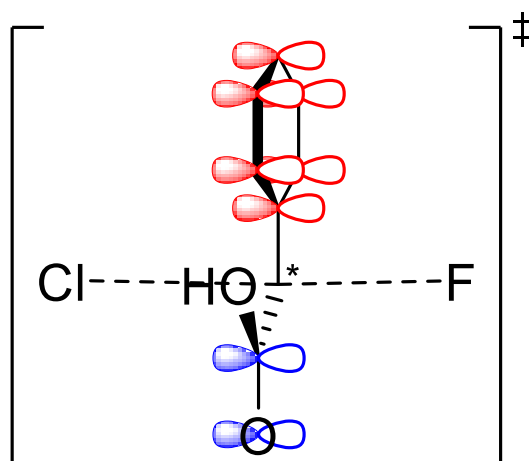
### 5.3 Catalysis investigation by Multinuclear NMR spectroscopy

To understand the catalytic ability of each of the complexes, a model set of reactions were chosen. The fluorination of halocarboxylic acids. This reaction set was chosen due to both fluorine and carboxylic acids being known to bind to lanthanide centres, both within this thesis and in wider literature.<sup>2-4</sup> These reactions can occur in MeOH and other protic solvents, but have been shown to have higher rate constants in aqueous media.<sup>1</sup> These catalysts are able to accelerate these reactions at RT, with only a chloride ion being produced over the course of the reaction, with this not inhibiting the reaction through competitive binding due to the higher binding constants associated with fluoride binding.<sup>5</sup> The specific halocarboxylic acids and their control reactions are detailed in **Scheme-5.1**.



**Scheme-5.1.** Fluorination of chloroacetic acid (*top*), 3-chloropropanoic acid (*middle*), sodium 2-chloro-2-phenylacetate. Reaction conditions; TBAF (0.1 mol dm<sup>-3</sup>), halocarboxylic acid substrate (0.1 mol dm<sup>-3</sup>), D<sub>2</sub>O (0.6 mL), catalyst under investigation (0.01 mol dm<sup>-3</sup>). \* indicates the presence of stereogenic centre.

Chloroacetic acid is the simplest halocarboxylic acid investigated with the chlorine alpha to the -COOH functional group, enabling ready substitution upon binding of both acetate and fluoride in the proposed catalytic pathway in **Figure-5.1**. 3-chloropropanoic acid was investigated to see whether there was a degree of regioselectivity with this catalysis, with the -CH<sub>2</sub>- group increasing the distance of the leaving group from the catalyst itself. The last substrate investigated was sodium 2-chloro-2-phenylacetate, to see the effect of steric bulk and whether the presence of a phenyl group would accelerate the reaction by hyperconjugative stabilisation of the transition state formed in the course of this reaction (**Scheme-5.2**).



**Scheme-5.2.** Proposed transition state for the control reaction of TBAF with 2-chloro-2-phenylacetate, showing resonance stabilisation with neighbouring carbonyl (blue) and phenyl (red)  $\pi$ -orbitals.

The resulting fluorinated product of sodium 2-chloro-2-phenylacetate could also show an enantiomeric preference, chiral carbon adjacent to the -COOH group (\*, **Scheme-5.1**), enabling exploration of a complexes ability to act as an enantioselective catalyst. For all halocarboxylic acids, it was chosen to use the chlorinated version. Previous experiments have examined the use of brominated reagents, with the corresponding rates for brominated versus chlorinated being faster due to the greater stability of the leaving bromide versus chloride group.<sup>1</sup> It was chosen to keep the leaving group the same to observe how the reaction depended on sterics, proximity and electronic factors.

### 5.3.1 NMR spectroscopy catalysis lanthanide catalyst choice

From the results in Chapter-2, Eu.p.DO3A was shown to catalyse the fluorination of halocarboxylic acids to a greater extent in both their initial rates and long-range rates, as opposed to Tb.p.DO3A. Therefore, Eu(III) was the lanthanide of choice for complexation with the DO3AM derivatives synthesised. Of the derivatives synthesised in Chapter-4, the Eu.p.DO3AM complexes containing -OMe as a

protecting group were selected for catalytic investigation. This was due to a number of effects observed in Chapter-4. With some complexes showing precipitation at critical fluoride concentrations (Eu.p.DO3AM.Pro.OH), their removal from solution preventing their use in these reactions. Others showed limited solubility with some being completely insoluble (Eu.p.DO3AM.Lys.O'Bu.CBz, Eu.p.DO3AM.Phen.O'Bu). While some also showed a great degree of competitive binding from functional groups located on the macrocyclic ring, such as -OH groups requiring deprotonation by fluoride guests before binding is observed to the Eu(III) centre (Eu.p.DO3AM.Pro.OH). The -OMe derivatives outlined in **Figure-5.1** remain dissolved in aqueous solution over the entire 12h period, minimise steric bulk and provide a degree of comparability between the complexes under investigation. While Eu.p.DO3AM.Lys.OMe and Eu.p.DO3AM.Pro.OMe show good aqueous solubility, Eu.p.DO3AM.Phen.OMe shows only partial solubility but is well solubilised upon anion addition.

#### **5.4 Catalytic NMR spectroscopy methodology**

The reactions were carried out in D<sub>2</sub>O (0.6 mL), with the control test consisting of 1:1 TBAF.3H<sub>2</sub>O to halocarboxylic acid (0.1 mol dm<sup>-3</sup>). A <sup>19</sup>F NMR spectrum was measured every 5 minutes for 12 hours, with the initial point being after 5 minutes equilibration time where the solution was allowed to stand after vigorous mixing. The catalysed test was performed under the same conditions with the addition of 10% loading of the complex under investigation. The fluorinated carboxylic acid peak was integrated for both the complex and control tests, which were then compared over time to determine any catalytic activity.

## 5.5 Eu.p.DO3AM.Pro.OMe catalytic studies

Eu.p.DO3AM.Pro.OMe was the most promising candidate out of the proline derivatives, due to its solubility within water and its improved stability upon exposure to anions in aqueous solution. This complex proved to be a highly effective catalyst for the fluorination of chloroacetic acid with TBAF (**Figure-5.3**) with a clear increase in catalytic activity upon lanthanide addition compared to the control.

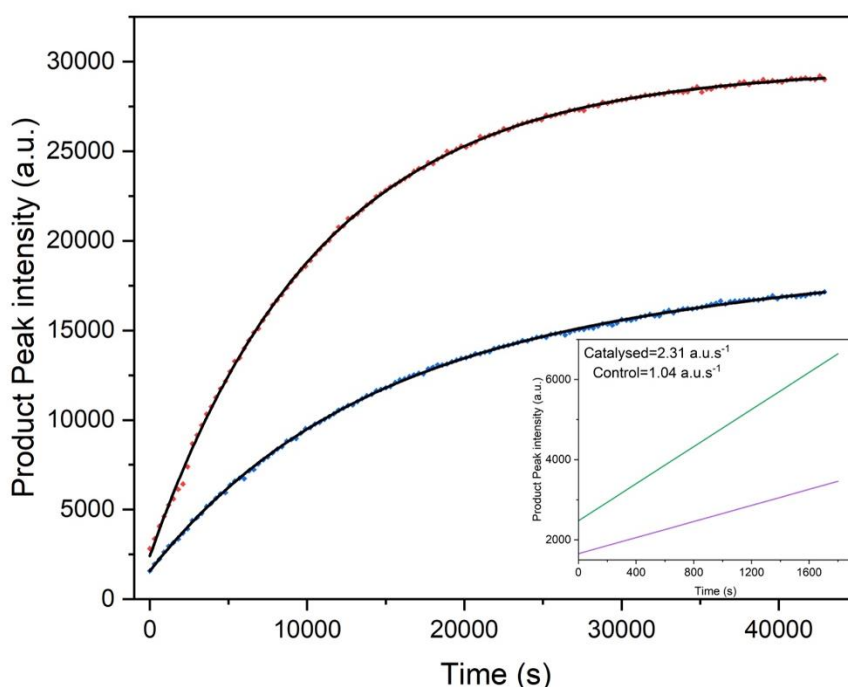


**Figure-5.3.** Graph monitoring the integrated intensity of product (fluoroacetic acid) peak formation in the Eu.p.DO3AM.Pro.OMe catalysed reaction (red-scatter) and control reaction (blue-scatter) of chloroacetic acid and TBAF over the course of 12h. *Inset:* Comparison of initial reaction rate for the catalysed (dark-green) and control (purple) reactions between 0-1800 s.

The complex has a much higher initial ( $cat. = 2.31 \text{ s}^{-1}$ ,  $control. = 1.04 \text{ s}^{-1}$ ) and final rate of reaction, alongside these improvements the intensity change in the latter stages of the reaction starts to plateau. This would indicate that this reaction is reaching completion over the 12-hour observation window.

When Eu.p.DO3AM.Pro.OMe is combined with 3-chloropropanoic acid, again lanthanide catalytic activity is demonstrated (**Figure-5.4**).

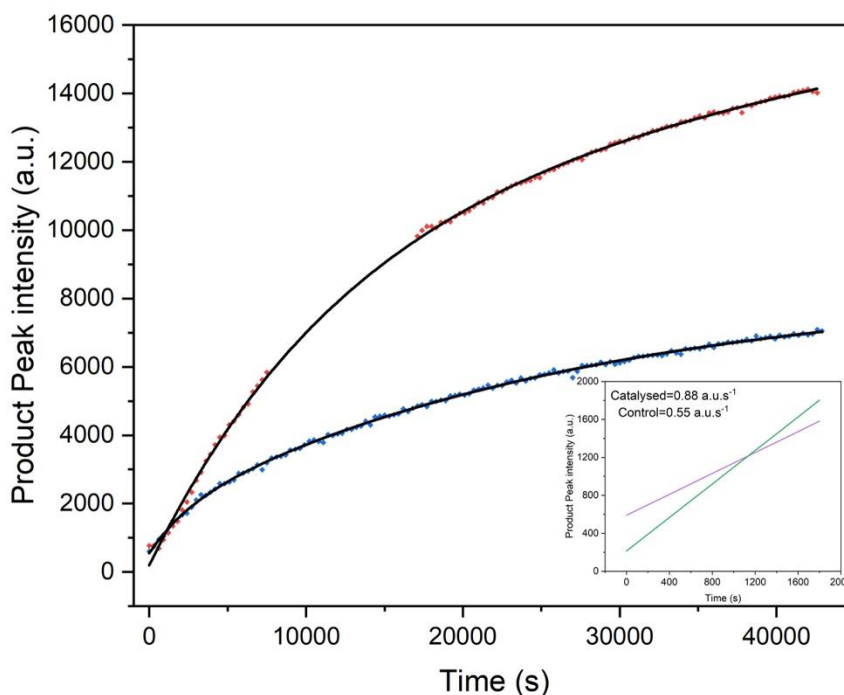


**Figure-5.4.** Graph monitoring the integrated intensity of product (3-fluoropropanoic acid) peak formation in the Eu.p.DO3AM.Pro.OMe catalysed reaction (red-scatter) and control reaction (blue-scatter) of 3-chloropropanoic acid and TBAF over the course of 12h. *Inset:* Comparison of initial reaction rate for the catalysed (dark-green) and control (purple) reactions between 0-1800 s.

As expected, the initial rates of reaction are lower (*cat.* =  $0.88 \text{ s}^{-1}$ , *control.* =  $0.55 \text{ s}^{-1}$ ) in this analogue due to the greater distance between the Eu(III) and substituted chlorine atom. Yet the results are still very promising, with a much higher initial and long-range reaction rate when catalysed, despite this the reaction has not gone to completion over the course of 12 hours.

Over the course of this reaction, due to the changing ionic strength of the solution, the TBAF peak ‘migrates’ across the NMR spectrum (**Figure-5.5**); with this migration being a reported effect when changes in pH and ionic strength occur.<sup>6</sup> This migration causes the TBAF peak to cross the product peak under observation in some cases, causing a large hump in the NMR spectra integration. These data has

been cut to allow fitting of an exponential decay curve to this reaction. Upon removing this section of data, the experiments fit well to an exponential decay that is expected over the course of a reaction with limited reagents.

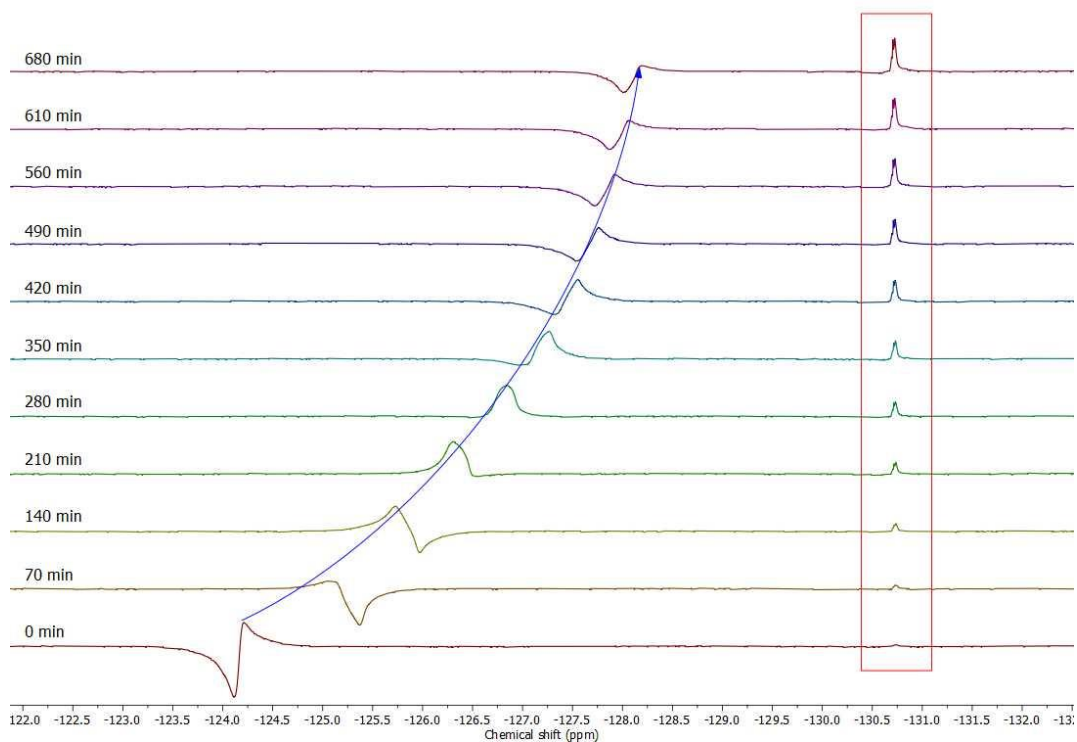


**Figure-5.5.** Stacked plot of  $^{19}\text{F}$  NMR spectra of reaction between TBAF and sodium 2-chloro-2-phenylacetate ( $0.1 \text{ mol dm}^{-3}$ ) with Eu.p.DO3AM.Pro.OMe as catalyst (10% loading) over a 12h period. With the emerging product (2-fluoro-2-phenylacetate) peak (red-box) and migrating TBAF peak (blue-line) highlighted.

In contrast to the previous two reactions where the majority of the reaction takes place, the analogous reaction with sodium 2-chloro-2-phenylacetate shows a very slow rate of reaction preventing the data being fit to an exponential decay. Although the 12 h window is not a long enough timeframe to allow fitting to an exponential decay, the initial rates of reaction can be determined. The experimental data with Eu.p.DO3AM.Pro.OMe plotted in **Figure-5.6**, show an increase in the initial rate of reaction compared to the control reaction ( $cat. = 0.19 \text{ s}^{-1}$ ,  $control. = 0.13 \text{ s}^{-1}$ ).

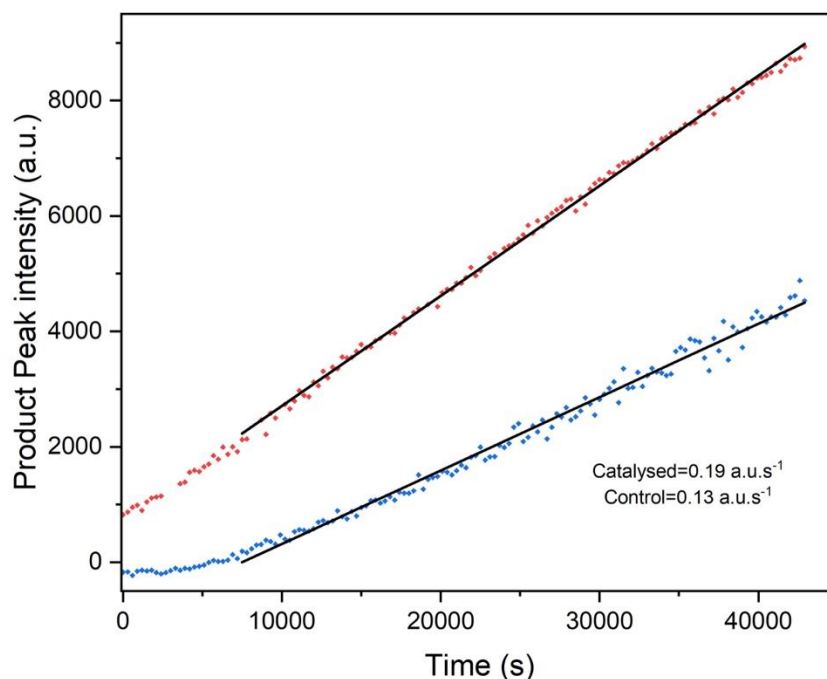


**Figure-5.6.** Graph monitoring the integrated intensity of product (2-fluoro-2-phenyl acetate) peak formation in the Eu.p.DO3AM.Pro.OMe catalysed reaction (**red-scatter**) and control reaction (**blue-scatter**) of sodium 2-chloro-2-phenyl acetate and TBAF over the course of 12h with their associated linear fits for initial rate determination (black).

While the results of the experiment with sodium 2-chloro-2-phenylacetate do demonstrate the catalytic ability of Eu.p.DO3AM.Pro.OMe and show the expected trend, it is postulated that the presence of sodium ions in solution affects the validity of this experiment. It is likely the sodium ions affect the ionic strength of solution, but they also offer an alternate binding option for the fluoride ions. Despite this there is an increase in the rate of product peak formation on the inclusion of the catalyst in comparison to the control, showing that the complex does have catalytic activity in this system (**Table-5.1**).

**Table-5.1.** Initial rates of reaction for the control and Eu.p.DO3AM.Pro.OMe catalysed reactions of TBAF with halocarboxylic acid substrates.

Catalyst	Substrate reaction rate (s <sup>-1</sup> ) <sup>#</sup>		
	Chloroacetic acid	3-chloropropanoic acid	sodium 2-chloro-2-phenylacetate
Control	1.04	0.55	0.13
Eu.p.DO3AM.Pro.OMe	2.31	0.88	0.19

<sup>#</sup> All initial rate values are subject to an error of  $\pm 10\%$  or less.

For the three halocarboxylic acids tested, Eu.p.DO3AM.Pro.OMe has been shown to have a catalytic effect on the rate S<sub>N</sub>2 substitution with fluorine. There is a notable difference in the initial rate of reaction between the control and lanthanide catalysed sample in all cases. The distance between the chlorine leaving group and the lanthanide reduces the overall conversion to the product, and the inclusion of the sodium salt of halocarboxylic acids negatively impacts the conversion through alteration of the solutions ionic charge along with the presence of a competitive binder.

## 5.6 Eu.p.DO3AM.Phen.OMe catalytic studies

Eu.p.DO3AM.Phen.OMe is only partially soluble in aqueous media, but is soluble when added to an aqueous solution with TBAF (0.1 mol dm<sup>-3</sup>), allowing examination of its catalytic activity. It's increased solubility in TBAF solution means that Eu.p.DO3AM.Phen.OMe preferentially binds fluoride very selectively in solution, as solvation by water is not effective enough to dissolve it in solution. This higher affinity for fluoride in aqueous solution means it could promote the catalytic reaction by readily binding with fluoride, or inhibit the reaction by binding irreversibly with fluoride and preventing the reaction from working as desired. When Eu.p.DO3AM.Phen.OMe (10% loading) is combined in a 1:1 TBAF:

chloroacetic acid solution in  $D_2O$ , a very curious result is observed (**Figure-5.7**). A linear increase in the product peak integral of fluoroacetic acid is observed for the first  $\approx 10000$  s. This would imply that the reaction rate is constant over this period (*cat.* = *control.* =  $1.04 \text{ s}^{-1}$ ). After this the rate begins to plateau to a constant intensity. The control without Eu.p.DO3AM.Phen.OMe gives the same result as observed in other similar experiments.

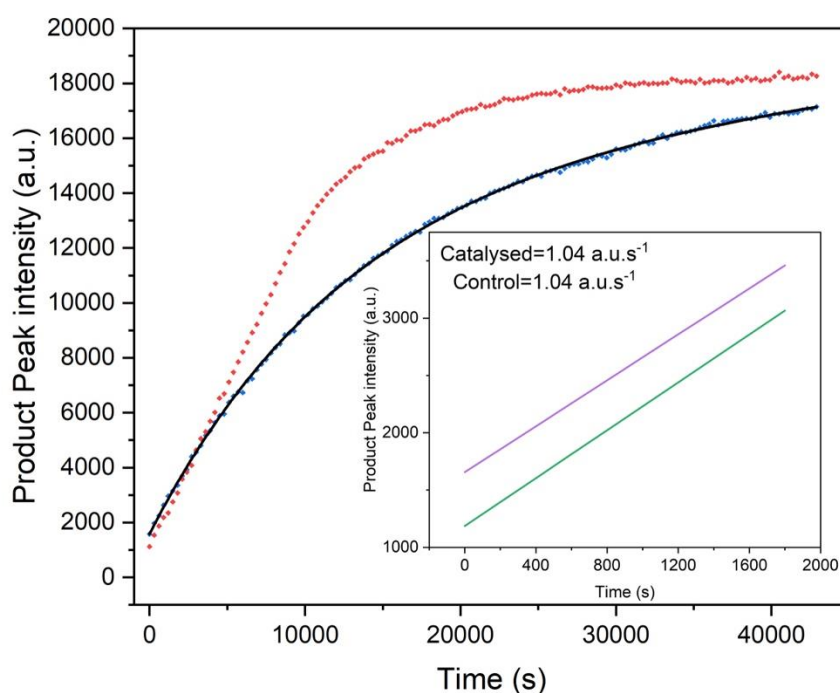


**Figure-5.7.** Graph monitoring the integrated intensity of product (fluoroacetic acid) peak formation in the Eu.p.DO3AM.Phen.OMe catalysed reaction (**red-scatter**) and control reaction (**blue-scatter**) of chloroacetic acid and TBAF over the course of 12h. *Inset:* Comparison of initial reaction rate for the catalysed (**dark-green**) and control (**purple**) reactions between 0-1800 s.

The working hypothesis is that the catalyst offers a pathway with a lower activation energy, making this the preferred pathway for the reaction. Due to Eu.p.DO3AM.Phen.OMe having a greater binding strength with fluoride as opposed to water, it is then coordinatively saturated with fluoride and progresses at a constant reaction rate. This proceeds until the concentration of fluoride decreases enough for the complex to not be fully saturated, then the reaction rate decreases.

Due to this effect, an exponential decay cannot be fitted to this reaction, but the initial reaction rate can be determined ( $cat. = control. = 1.04 \text{ s}^{-1}$ ). While these rates are very similar between the catalysed and controlled reactions, the catalysed maintains this rate for a longer period, resulting in the reaction almost going to completion over the 12-hour time period.

Similarly, the reaction of Eu.p.DO3AM.Phen.OMe with 3-chloropropanoic acid returns shows the same initial rate of reaction ( $cat. = control. = 0.55 \text{ s}^{-1}$ ), but with a higher long-range reaction rate compared to the control (**Figure-5.8**). Yet in this case an exponential decay can be fit to the data, but due to the aforementioned increased distance between substrate and catalyst this reaction is slower and thus does not go to completion.

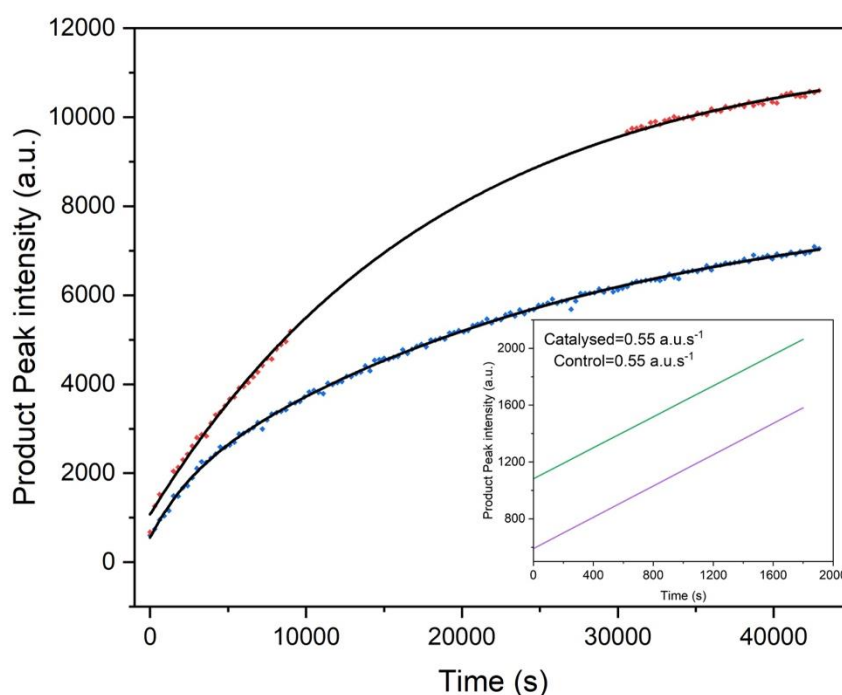


**Figure-5.8.** Graph monitoring the integrated intensity of product (3-fluoropropanoic acid) peak formation in the Eu.p.DO3AM.Phen.OMe catalysed reaction (red-scatter) and control reaction (blue-scatter) of 3-chloropropanoic acid and TBAF over the course of 12 h. *Inset:* Comparison of initial reaction rate for the catalysed (dark-green) and control (purple) reactions between 0-1800 s.

The analogous experiment with sodium-2-chloro-2-phenylacetate showed a similar acceleration of the reaction rate as previously seen (*cat.* =  $0.19 \text{ s}^{-1}$ , *control.* =  $0.13 \text{ s}^{-1}$ ) albeit with a slower overall rate in comparison (**Figure-5.9**).

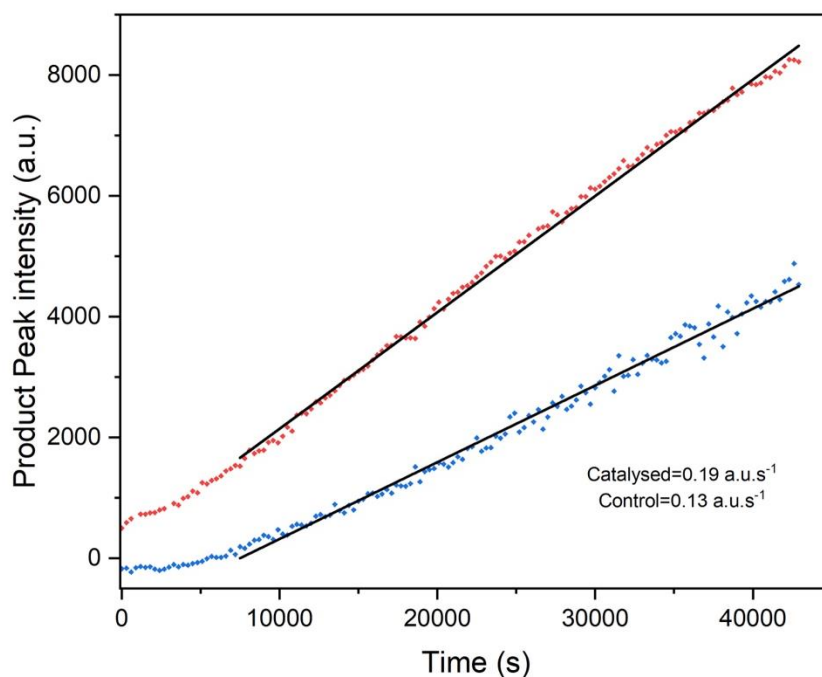


**Figure-5.9.** Graph monitoring the integrated intensity of product (2-fluoro-2-phenyl acetate) peak formation in the Eu.p.DO3AM.Phen.OMe catalysed reaction (**red-scatter**) and control reaction (**blue-scatter**) of 2-sodium-2-chlorophenylacetate and TBAF over the course of 12 h with their associated linear fits for initial rate determination (black).

For the chosen halocarboxylic acids the Eu.p.DO3AM.Phen.OMe complex has acted as a catalyst for all three reactions (**Table-5.2**). Despite some interesting observations this catalyst has proven to be effective at accelerating the rate of reaction, specifically when in aqueous media of high enough ionic strength to solubilise it.

**Table-5.2.** Initial rates of reaction for the control and Eu.p.DO3AM.Phen.OMe catalysed reactions of TBAF with halocarboxylic acid substrates.

Catalyst	Substrate reaction rate (s <sup>-1</sup> ) <sup>#</sup>		
	Chloroacetic acid	3-chloropropanoic acid	sodium 2-chloro-2-phenylacetate
Control	1.04	0.55	0.13
Eu.p.DO3AM.Phen.OMe	1.04*	0.55*	0.19

\* Anomalous result with same initial rate but maintains rate for a longer period of time.

<sup>#</sup> All initial rate values are subject to an error of  $\pm 10\%$  or less.

### 5.7 Eu.p.DO3AM.Lys.OMe catalytic studies

The lysine-based complexes were specifically designed for their water solubility, the positively charged groups on the complex periphery will be protonated in aqueous media and therefore should not interfere in reaction catalysis.

The Eu.p.DO3AM.Lys.OMe catalysed reaction of chloroacetic acid and TBAF proceeds at a much greater initial rate (*cat.* = 3.82 s<sup>-1</sup>, *control.* = 1.04 s<sup>-1</sup>) and looks to have gone much further towards completion than the control (**Figure-5.10**).

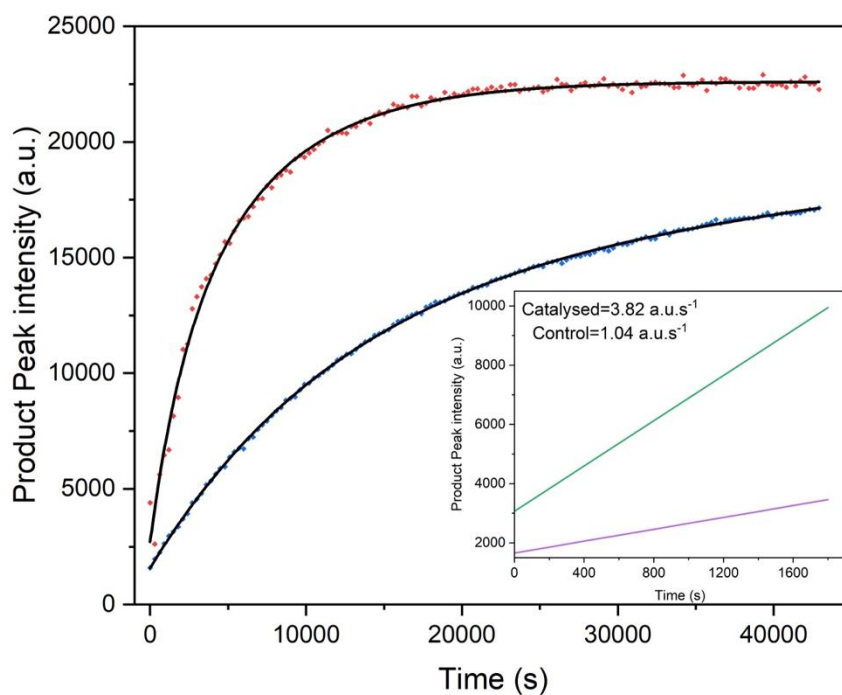


**Figure-5.10.** Graph monitoring the integrated intensity of product (fluoroacetic acid) peak formation in the Eu.p.DO3AM.Lys.OMe catalysed reaction (red-scatter) and control reaction (blue-scatter) of chloroacetic acid and TBAF over the course of 12h. *Inset:* Comparison of initial reaction rate for the catalysed (dark-green) and control (purple) reactions between 0-1800 s.

The initial rate is much faster, and with the graph plateauing  $\approx 30000$ s, this reaction can be said to have reached completion fastest with this complex as catalyst for this chlorinated substrate.

A similar catalysis of reaction rate is seen in the 3-chloropropanoic acid substrate reaction (**Figure-5.11**). The reaction does not go to completion but shows a large increase in reaction rate in comparison to the control reaction ( $cat. = 1.22 \text{ s}^{-1}$ ,  $control. = 0.56 \text{ s}^{-1}$ ).

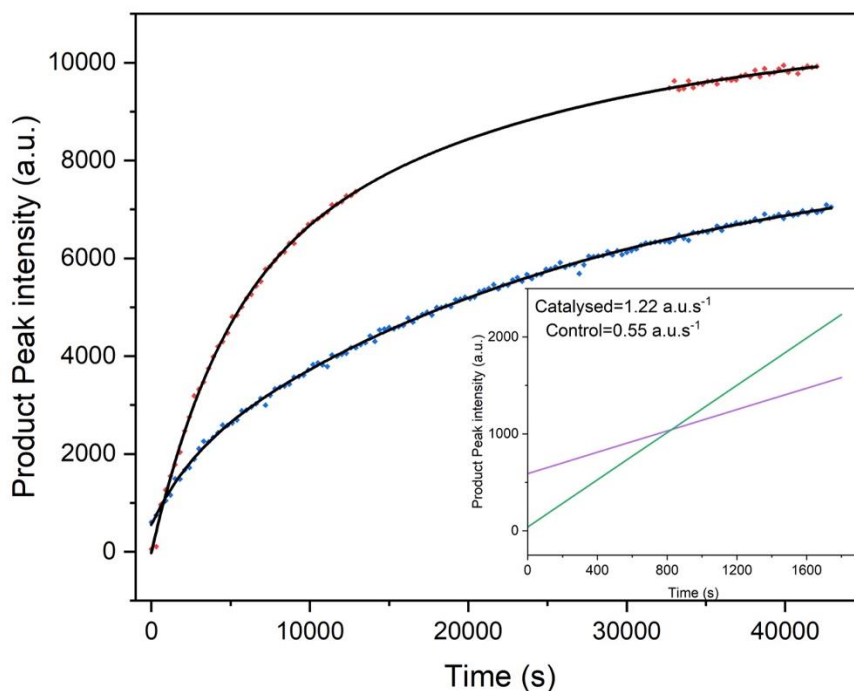


**Figure-5.11.** Graph monitoring the integrated intensity of product (3-fluoropropanoic acid) peak formation in the Eu.p.DO3AM.Lys.OMe catalysed reaction (**red-scatter**) and control reaction (**blue-scatter**) of 3-chloropropanoic acid and TBAF over the course of 12h. *Inset:* Comparison of initial reaction rate for the catalysed (**dark-green**) and control (**purple**) reactions between 0-1800 s.

The reactions thus far with Eu.p.DO3AM.Lys.OMe have shown an increase in the rate of reaction in comparison to the control. Yet for the reaction with the sodium 2-chloro-2-phenylacetate substrate, while there is still an increase in rate in comparison to the control ( $cat. = 0.16 \text{ s}^{-1}$ ,  $control. = 0.13 \text{ s}^{-1}$ ), but a similar significant increase in rate is not observed (**Figure-5.12**).

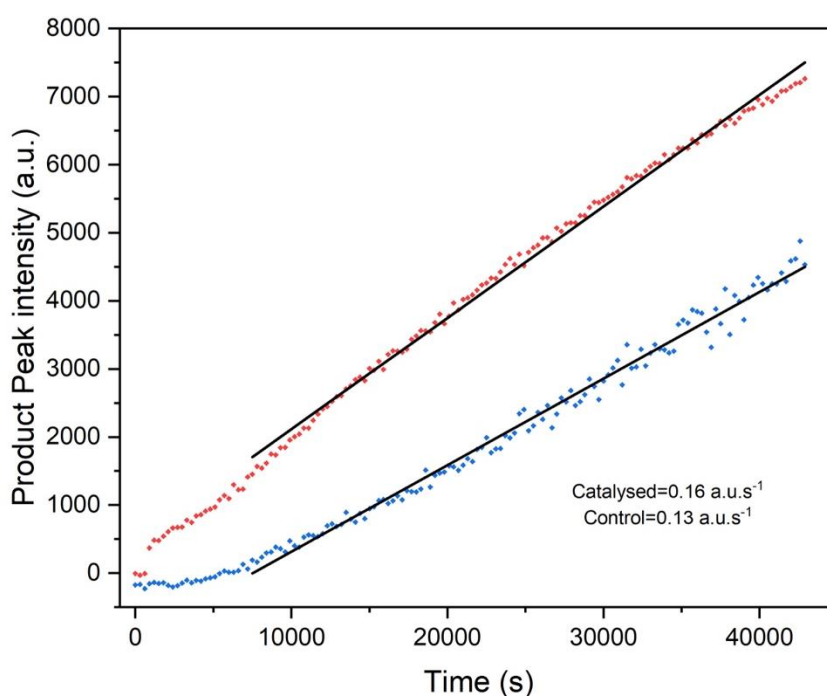


**Figure-5.12.** Graph monitoring the integrated intensity of product (sodium 2-fluoro-2-phenyl acetate) peak formation in the Eu.p.DO3AM.Phen.OMe catalysed reaction (**red-scatter**) and control reaction (**blue-scatter**) of 2-sodium-2-chlorophenylacetate and TBAF over the course of 12 h; with their associated linear fits for initial rate determination (black).

While this last reaction shows less evidence of a highly effective catalyst, there are aforementioned limitations within this experiment. Therefore, despite this result, the -Lys.OMe complex shows some of the most promising results for an effective Eu(III) based catalyst (**Table-5.3**).

**Table-5.3.** Initial rates of reaction for the control and Eu.p.DO3AM.Lys.OMe catalysed reactions of TBAF with halocarboxylic acid substrates.

Catalyst	Substrate reaction rate (s <sup>-1</sup> ) <sup>#</sup>		
	Chloroacetic acid	3-chloropropanoic acid	sodium 2-chloro-2-phenylacetate
Control	1.04	0.55	0.13
Eu.p.DO3AM.Lys.OMe	3.82	1.22	0.16

<sup>#</sup> All initial rate values are subject to an error of  $\pm 10\%$  or less.

## 5.8 Discussion

The catalytic propensity of three Eu(III) containing-complexes was investigated for a set of S<sub>N</sub>2 fluorination reactions for a set of halocarboxylic acid substrates in aqueous media. For all the complexes investigated, all were found to accelerate the reaction in comparison to an uncatalysed control reaction. While there were some unexpected observations, reaction rates were increased by catalyst inclusion (**Table-5.4**).

**Table-5.4.** Table summarising the initial rates of control and catalysed reactions with variable halocarboxylic acid substrates.

Catalyst	Substrate reaction rate (s <sup>-1</sup> ) <sup>#</sup>		
	Chloroacetic acid	3-chloropropanoic acid	sodium 2-chloro-2-phenylacetate
Control	1.04	0.55	0.13
Eu.p.DO3AM.Pro.OMe	2.31	0.88	0.19
Eu.p.DO3AM.Phen.OMe	1.04*	0.55*	0.19
Eu.p.DO3AM.Lys.OMe	3.82	1.22	0.16

\* Anomalous result with same initial rate but maintains rate for a longer period of time.

<sup>#</sup> All initial rate values are subject to an error of ± 10 % or less.

From these results, the most effective catalyst would appear to be Eu.p.DO3AM.Lys.OMe which shows a large difference in the rate of reaction in comparison to the control reactions for all halocarboxylic substrates tested. By contrast the Eu.p.DO3AM.Phen.OMe catalyst shows little difference from the control reaction, yet as **Figures-5.7** and **5.8** detail, the overall rate is increased with respect to the control, rendering this an effective catalyst also. The Eu.p.DO3AM.Pro.OMe complex shows intermediate values between the other two

complexes under investigation, but still working as an effective catalyst in these conditions.

For the first two substrates (chloroacetic acid and 3-chloropropanoic acid) there is a marked difference in the rates of reaction, across both control and catalysed reactions, showing the regio-dependancy of both the reactions and catalysts. This effect will be partially down to the presence of a neighbouring carbonyl group stabilising the transition state in the  $S_N2$  reaction for chloroacetic acid. Yet the decrease in reaction rate for the control is on the order of a half, with the reaction rates of the catalysed processes decreasing by greater factors. This demonstrates there is a high degree of interaction between the lanthanide centre and the incoming/outgoing halides, as the greater distance from the lanthanide centre has caused a larger than expected decrease in the observed reaction rate.

With the third substrate (sodium 2-chloro-2-phenylacetate), the aim was to probe the potential for enantioselectivity with these catalysts. Yet the observed products from all reactions coalesced into one peak within the NMR spectra. While this does not prove there is no preference in the product distribution, the prevalence of both diastereomers in the  $^1\text{H}$  NMR spectra of the complexes utilised as catalysts within these reactions proves that the catalysts used are racemic (Chapter-3). This combined with the observation of a broad singlet peak in the  $^{19}\text{F}$  NMR spectra, seen in this Chapter for all catalysed reactions, indicate a spread of products. Despite the inclusion of rigid and bulky amino acid-based side arms onto three of the four of the nitrogens, this is not enough to enforce a conformational and hence enantiomeric preference on the complex and they show a high degree of

fluxionality. This lack of preference in the complex conformation is then translated onto the product distribution which is a racemic mix also.

## 5.9 Conclusions

Detailed in this Chapter are the catalytic experiments carried out on a set of DO3AM based derivatives monitored by  $^{19}\text{F}$  NMR spectroscopy, the complexes selected according to the guidelines outlined in Chapter-4. These complexes were shown to accelerate the  $\text{S}_{\text{N}}2$  displacement of chlorine ions by fluoride ions, for a set of halocarboxylic acid substrates. The halocarboxylic acid substrates were chosen to explore the ability of the catalysts to be regio- and enantioselective. The regioselectivity of the catalysts was profound, with much greater reaction rates observed with the substituted groups being held in closer proximity to the lanthanide centre. Evidenced by the marked difference for the 3-chloropropanoic acid substrate reaction set compared to the analogous chloroacetic acid set, with the latter being more proximal to the lanthanide centre. The most successful catalyst was the Eu.p.DO3AM.Lys.OMe complex, showing the greatest acceleration in initial reaction rate and some reactions appearing to reach completion. This is attributed to the decreased degree of steric crowding, due to the inclusion of more conformationally flexible groups. The presence of a rigid 5-member ring in Eu.p.DO3AM.Pro.OMe and the bulky, hydrophobic phenyl group present in Eu.p.DO3AM.Phen.OMe act to decrease the available space for coordination of guest species. For 2-sodium-2-chloro-phenylacetate the potential for enantioselectivity was investigated, due to the lack of enantiomeric preference inherent within the complexes themselves due to the conformational flexibility of the heptadentate ligands, there was no enantiomeric selectivity on the products of

the catalysed reactions. Throughout this Chapter the ability of p.DO3AM based Eu(III) complexes as catalysts has been readily apparent, showing their ability to accelerate reactions across the range of halocarboxylic acid substrates. While the specifics of their catalytic ability are limited, the evidence for this ability has been covered extensively within this Chapter.

## 5.10 References

- 1 Laura. Mason, DPhil thesis, University of Oxford, 2017.
- 2 O. A. Blackburn, A. M. Kenwright, P. D. Beer and S. Faulkner, *Dalton Trans.*, 2015, **44**, 19509–19517.
- 3 L. R. Hill, T. J. Sørensen, O. A. Blackburn, A. Brown, P. D. Beer and S. Faulkner, *Dalton Trans.*, 2013, **42**, 67–70.
- 4 O. A. Blackburn, A. M. Kenwright, A. R. Jupp, J. M. Goicoechea, P. D. Beer and S. Faulkner, *Chem. Eur. J.*, 2016, **22**, 8929–8936.
- 5 C. Alexander, J. A. Thom, A. M. Kenwright, K. E. Christensen, T. J. Sørensen and S. Faulkner, *Chem Sci*, 2023, **14**, 1194–1204.
- 6 P. Kukic, F. O’Meara, C. Hewage and J. Erik Nielsen, *Chem Phys Lett*, 2013, **579**, 114–121.

## Chapter-6: Conclusions and Future Work

This thesis has explored the utility of DO3AM derivatives in the field of homogenous catalysis. While catalysis using rare-earth elements has been employed in a wide range of uses and industries, the creation of novel homogenous lanthanide complexes for catalysis is now garnering great interest in the scientific community. The lanthanides unique solution phase chemistry, which requires extensive tailoring, provides the opportunity to introduce desired functional groups onto ligands, enhancing the stereo- or regioselectivity of lanthanide complexes. The ability to catalyse reactions stereo selectively has been the purview of enzymes, or facial catalysts historically. The potential for lanthanide complexes to enable easier synthetic pathways to enantiomerically pure compounds is of great academic and commercial interest.

In the course of this work, a number of different complexes were created for investigation. Chapter-2 detailed the successful synthesis and investigation into a prototype Ln.p.DO3A system. This system was explored due to its links with previous studies and to create a consistent method for application later in the thesis. Chapter-3 documented the synthetic challenges of creating DO3AM derivatives. With extensive optimisation conducted in this area, more facile creation of amide derived, cyclen-based complexes should now be feasible. The inclusion of amide-coupling within these synthetic routes was of great use in this thesis. Chapter-4 covers luminescence investigations of eight distinct DO3AM derived Ln(III) complexes, with a focus on binding behaviour to anionic guests (fluoride, acetate). Their solution phase chemistry was investigated extensively during this section of

the thesis, allowing selection of a suitable set of complexes to carry forward. Chapter-5 detailed the investigation into the catalytic ability of three selected DO3AM derivatives, specifically on the  $S_N2$  addition of fluoride to three chlorinated halocarboxylic acid substrates. An accelerated reaction rate was observed for all complexes, with the most promising showing reaction completion within the 12 h observation window. These results reveal that the selected complexes are capable of homogeneous catalysis as hypothesised earlier in this thesis.

Future work in this area is limited by the kinetic stability of the DO3AM derivatives studied. Some of the complexes precipitated at very low anionic concentrations, with all complexes showing kinetic instability over a prolonged time period in aqueous solution. This is one of the major limitations in this area. The use of ester links instead of amide links, could allow for the inclusion of stronger coordinating groups. These stronger coordinating groups would increase the kinetic stability by increasing the energetic barrier to demetallation. This work could also be expanded upon by greater variation of Ln(III) identity, with the larger/earlier Ln(III) ions facilitating more space for binding of anions for catalytic purposes, yet being less Lewis acidic as such not having the prerequisite binding strength to hold anions in close proximity. In contrast to this the smaller/later Ln(III) ions are much more Lewis acidic and have greater binding strengths, as exhibited by Tb(III) in this thesis, yet could have less space for substrate binding to enable catalysis. One of the main pursuits after this thesis regarding catalysis, will be to quantify the turnover number. While this thesis provides a starting point for qualitatively understanding the effect these complexes have as catalysts, they do not provide

substantial quantitative proof. The turnover number (TON) should be calculated to describe the catalysts lifetime robustness, with other quantities such as the turnover frequency (TOF) calculated to describe the instantaneous efficiency of the catalyst, variation of reaction conditions such as temperature and pressure would also be of interest in this area.

This thesis documents a more facile way to synthesise heptadentate DO3AM derivatives, increasing the potential of functionalisation. This new synthetic pathway is an improvement on the suboptimal synthetic pathways previously adopted in this area. The inclusion of other desirable functional groups, could greatly expand the synthetic scope of DO3AM complexes, creating new ways to include moieties for targeting, probing and other desired applications.

For further catalytic studies, the determination of the enantiomeric purity of reaction products would be of great interest, showing how successful they are in this regard. Greater understanding would be required before applying these catalysts to the fluorination of biomolecules for PET imaging. So far this area shows great promise for the creation of novel homogeneous catalysts.

## Chapter-7: Experimental procedures

### 7.1 Reagents and solvents

Sodium bicarbonate (99.7%), sodium hydroxide (98%), propargyl bromide solution (80 wt% in toluene, 0.3% MgO stabiliser), Tris-HCl (Trizma<sup>®</sup> hydrochloride) (99%), HEPES sodium salt ( $\geq 99.5\%$ , titration), europium (III) trifluoromethanesulfonate hydrate (98%), terbium (III) trifluoromethanesulfonate (98%), magnesium sulfate (anhydrous, ReagentPlus<sup>®</sup>,  $\geq 99.5\%$ ), sodium chloride (puriss. P.a., ACS reagent, ISO,  $\geq 99.5\%$ ), potassium carbonate (ACS reagent,  $\geq 99\%$ ), ammonium formate (granular, 97%), chloroacetyl chloride (98%), triethylamine, acetone (ACS, ISO, Reag. Ph Eur-used to wash glasswares), CD<sub>3</sub>OD  $\geq 99.8$  atom% D, CD<sub>2</sub>Cl<sub>2</sub>  $\geq 99.8$  atom% D, DMSO-*d*<sub>6</sub> 99.8 atom% D and D<sub>2</sub>O 99.9 atom% D were from Sigma Aldrich and used as received. Other solvents (acetone, acetonitrile, chloroform, methanol, ethanol, tetrahydrofuran, diethyl ether, pentane, ethyl acetate, toluene, *N,N*-dimethyl formamide, dimethyl sulfoxide (anhydrous,  $\geq 99.9\%$ )) were all reagent grade and also from Sigma Aldrich.

Cyclen (CheMatech, Dijon, France); caesium carbonate, *N*'-Boc-L-lysine methyl ester hydrochloride (95%), *N*'-Boc-L-lysine tert-butyl ester hydrochloride (95%), *N*'-Cbz-L-lysine tert-butyl ester hydrochloride (95%), L-proline methyl ester hydrochloride (95%), L-proline tert-butyl ester hydrochloride (95%), L-phenylalanine methyl ester hydrochloride (95%), L-phenylalanine tert-butyl ester hydrochloride (95%), di-tert-butyl-dicarbonate, *N,N*-diisopropylethylamine (99%), HATU (98%) and 20% palladium on carbon (wet, 55-65%) (Fluorochem);

Trifluoroacetic acid (99%) (Sigma-Aldrich), 1-hydroxybenzotriazole (98%) (Acros Organics); dichloromethane (reagent grade,  $\geq 95\%$ ) (Honeywell); hydrochloric acid ( $\sim 37\%$ , analytical reagent grade), nitric acid (70%), glacial acetic acid (laboratory reagent grade), and potassium iodide (Fisher Scientific); anhydrous sodium acetate (99%), anhydrous sodium sulfate (99.99%), neutral alumina (activated, Brockmann grade II), tert-butylbromoacetate (98%), terbium (III) trifluoromethanesulfonate (98%) and potassium fluoride (Riedel-de Haën<sup>®</sup>) were used as received.

Melting point tubes (100 mm, soda glass sealed ends) were from Sigma Aldrich. Anhydrous solvents were obtained from an MBraun SPS800 and used without further purification (solvents purchased from commercial suppliers as stated above). Deionised water was used throughout the study which was obtained from Elga PURELAN<sup>®</sup> Chorus 1 complete with conductivity of 18.2 M $\Omega$ .cm.

## **7.2 Vacuum processing, Dialysis, Centrifugation, Filtration, TLC and Column chromatography.**

Buchi Rotavapor<sup>®</sup> R-300 and Heidolph Laborota 4000-efficient Rotary Evaporator were used to evaporate solvents under reduced pressure. Compounds were dried on a Schlenk line with a high-vac Edwards RV3 Vacuum pump. Dialysis of the complexes were performed using Spectra-Por<sup>®</sup> Float-A-Lyzer<sup>®</sup> G2 dialysis membrane tubing made from cellulose ester (Spectrum Labs) with a molecular weight cut-off of either 100-500 Da or 500-1000 Da. Centrifugations were performed using Beckman Coulter<sup>®</sup> Allegra<sup>®</sup> X-12R Benchtop Centrifuge. All centrifugations were performed at 3750 rpm for 15 min at 4 °C. Filtrations during the reaction workup were performed under gravity using a Whatman filter paper

(grade 1 circles) on a glass funnel or using celite (Filteraid, Celite Hyflo Super-cel<sup>®</sup> from Alfa-Aeser) under vacuum. Column chromatography was performed using Geduran<sup>®</sup> silica gel 60 (0.040-0.063 mm mesh, Sigma Aldrich) and neutral alumina (activated, Brockmann grade II). Analytical thin layer chromatography (TLC) was performed on aluminium sheet supported silica gel plates coated with silica gel 60 F<sub>254</sub> (0.2 mm, Merck) using different solvent systems as mobile phase. The compounds were visualised in TLC by potassium permanganate stain prepared as per literature protocol,<sup>1</sup> or by using a UV TLC chamber in short wavelength (254 nm) and long wavelength (365 nm) as appropriate.

### **7.3 Preparation of buffers in water**

Tris-HCl buffer (0.01 M, pH 7.4) was prepared by dissolving 242 mg of Trizma base in 100 mL deionised water followed by the dropwise addition of 138  $\mu$ L of concentrated HCl (37%. 12.1 M) and made up to 200 mL using deionised water.

HEPES buffer (0.1 M, pH 7.40) was prepared by dissolving 2.60 g of *N*-(2-Hydroxyethyl)piperazine-*N'*-(2-ethanesulfonic acid) sodium salt in 80 mL deionised water and adjusting the pH using 0.01 M aqueous NaOH to 7.40. The final volume was adjusted to 100 mL using deionised water.

Aqueous NaOH (1.00 M) was prepared by dissolving 40.0 g of NaOH in 250 mL deionised water and making up to 1.00 L in a standard flask.

## 7.4 Physical Methods

### 7.4.1 NMR spectra

NMR spectra were recorded on a Bruker Biospin AG Avance III HD Nanobay 400 MHz NMR spectrometer equipped with a 9.4 T magnet ( $^1\text{H}$  400.2 MHz,  $^{13}\text{C}$  100.6 MHz,  $^{19}\text{F}$  376.5 MHz) or Bruker Avance III NMR equipped with a 11.75 T magnet ( $^1\text{H}$  500 MHz,  $^{13}\text{C}$  125.7 MHz,  $^{19}\text{F}$  470.4 MHz) or Bruker Avance Ultrashield Neo 600 MHz NMR Spectrometer equipped with a 14.1 T magnet ( $^1\text{H}$  600.4 MHz,  $^{13}\text{C}$  151 MHz). All NMR spectra were recorded in deuterated solvents (Sigma Aldrich). Chemical shifts were assigned by comparison with residual proton and carbon resonances of the solvents.<sup>2</sup> The NMR spectrometers were set with  $(\text{CH}_3)_4\text{Si}$  in  $\text{CDCl}_3$  as the internal reference for  $^1\text{H}$  and  $^{13}\text{C}$ ;  $\text{CFCl}_3$  in  $\text{CDCl}_3$  for  $^{19}\text{F}$  ( $\delta = 0$  ppm). NMR samples were placed in Norrell<sup>®</sup> standard series<sup>™</sup> 5 mm NMR tubes (600 MHz frequency, Sigma Aldrich) and the spectra recorded.

#### 7.4.1.1 NMR spectroscopy catalysis experiments

All NMR spectroscopy catalysis experiments were run on a Bruker Avance III NMR equipped with a 11.75 T magnet ( $^{19}\text{F}$  470.4 MHz). Measurements were performed over a 12 hour period using the following parameters: number of scans, 16; acquisition time, 32 s. The data was processed using Mestrenova, integrating across the desired chemical shift (ppm) range to monitor product peak formation, before being transferred to Origin for replotting. In Origin the product peak formation data was fitted to an exponential decay function, except for instances where this could not be fitted to the current dataset. Certain points were masked to improve the fit of the data but did not affect the overall results yielded by the data; more extensive masking was done on an *ad hoc* basis, this was due to migration of

the peak associated with TBAF across the spectrum over the course of the reaction. This is due to the change in ionic strength causing a change in the chemical shift that TBAF appears at, over the course of the reaction this peak migrates across the product peak distorting the integrated peak data.<sup>3</sup> Therefore, this data was redacted and an exponential decay fitted to the remaining data. Physically for each measurement, for a volume of 0.6 mL the appropriate amounts were weighed out to have concentrations for TBAF,  $0.1 \text{ mol dm}^{-3}$ ; halocarboxylic acid substrate,  $0.1 \text{ mol dm}^{-3}$ ; catalyst under investigation,  $0.01 \text{ mol dm}^{-3}$ . These were weighed out in three separate vials, 0.3 mL of D<sub>2</sub>O was added to the vial containing TBAF and 0.3 mL was added to the vial containing the halocarboxylic acid substrate. The total volume in the vial containing the halocarboxylic acid substrate was then transferred to the vial containing the catalyst under investigation. The total volume from the vial containing TBAF was then added to the vial containing both the halocarboxylic acid substrate and catalyst under investigation, this vial was then agitated using a vortexer mixer for 10 seconds. The total volume was then transferred to the NMR tube and the experiment run with the parameters detailed above.

#### **7.4.2 Mass Spectrometry**

ESI mass spectra were recorded on the Thermofisher Exactive™ Plus mass spectrometer with a Waters Acuity UPLC system and Waters Bioaccord 2 Loop injection MS (HIGH MASS, + ion, and data processed using spectral works remote analyzer®). LRMS was recorded on a Waters LCT Premier XE bench-top orthogonal acceleration time-of-flight ESI mass spectrometer and data processed in Mestrenova. MALDI-TOF mass spectra were recorded on a Bruker AutoFlex Mass

Spectrometer. All MALDI-TOF MS were run in a DCTB (trans-2-[3-(4-tert-Butylphenyl)-2-methyl-2-propenylidene]malononitrile) matrix.

### 7.4.3 Luminescence spectra

Steady-state excitation and emission spectra were recorded on a Horiba Jobin Yvon Fluorolog<sup>®</sup> 3-12 Fluorometer equipped with a Hamamatsu R928 detector and a double-grating emission monochromator. A 2" square unmounted longpass 550 nm filter (FGL 550S) or 400 nm filter (FGL 400S) fabricated using a 2 mm thick Schott<sup>®</sup> coloured glass (Thor Labs) was used while recording the steady-state emission spectra of Eu(III) and Tb(III) complexes respectively. For Eu.p.DO3A, slits of 20 nm with a band pass of 1 nm for excitation at 393 nm was used. Points were recorded at 1 nm intervals with a 0.1 s to 0.5 s integration time. S1/R1 (S1 = signal 1, R1 = error 1) was used throughout to obtain the steady-state luminescence output.

Time-resolved phosphorescence emission spectra were recorded with time per flash of 41 ms, flash count as 10 ms, delay after flash as 0.05 ms, and sample window as 0.2 ms for Eu(III) complexes. Slit width in phosphorescence; for Eu.p.DO3AM.Lys.Cbz.O'Bu, Eu.DO3AM.Lys.OMe, Eu.p.DO3AM.Phen.O'Bu, Eu.p.DO3AM.Phen.OMe, Eu.p.DO3AM.Phen.OH, Eu.p.DO3AM.Pro.O'Bu, Eu.p.DO3AM.Pro.OMe and Eu.p.DO3AM.Pro.OH slits of 15 nm with a band pass of 5 nm for excitation at 393 nm was used. Lifetime measurements were made on the same instrument for the Eu(III) complexes with a max delay of 2 or 8 or 12 ms. Luminescence lifetimes were obtained by tail fit for Eu(III) complexes using exponential decay function in Origin 8 operated with FluorEssence<sup>™</sup> software for Windows<sup>®</sup>. All lifetimes gave satisfactory fitting using a mono exponential decay

function; fitting to a double exponential decay did not improve the fit. S1 response was used throughout for obtaining the time-resolved, and steady-state excitation output. Luminescence lifetimes were calculated for Eu(III) complexes using the modified Horrocks' equation as detailed in Chapter-1. The steady-state and time resolved measurements were carried out for solutions of the complexes mentioned above, these were taken in a 3500  $\mu$ L quartz macro fluorescence cuvette with a PTFE fold lid (Starna Scientific, type: 3/GL14/Q/10). All measurements were performed at ambient temperature and averaged to three measurements.

Additionally, time-resolved phosphorescence emission spectra were recorded on a Perkin Elmer LS55. A 2" square unmounted longpass 550 nm filter (FGL 550S) or 400 nm filter (FGL 400S) fabricated using a 2 mm thick Schott<sup>®</sup> coloured glass (Thor Labs) was used while recording the time-resolved emission spectra of Eu(III) and Tb(III) complexes. For Tb.p.DO3A, slits of 15 nm with a band pass of 5 nm for excitation at 212 nm was used; for Eu.p.DO3AM.Lys.Cbz.O'Bu, Eu.DO3AM.Lys.OMe, Eu.p.DO3AM.Phen.O'Bu, Eu.p.DO3AM.Phen.OMe, Eu.p.DO3AM.Phen.OH, Eu.p.DO3AM.Pro.O'Bu, Eu.p.DO3AM.Pro.OMe and Eu.p.DO3AM.Pro.OH slits of 15 nm with a band pass of 5 nm for excitation at 393 nm. Flash count: 10, Sample window: 0.20 ms, Time per flash 41.00 ms. The S1 response was used throughout to obtain the time-resolved luminescence output, with all measurement being performed at ambient temperature, averaged to three measurements with dark offset active.

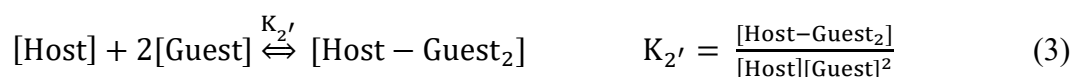
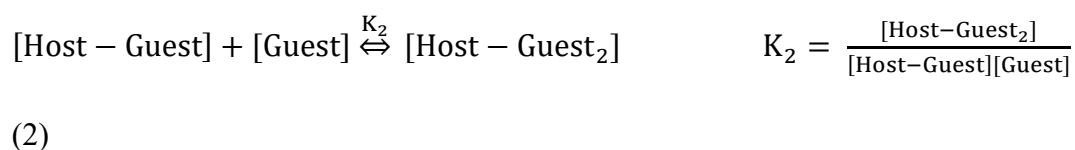
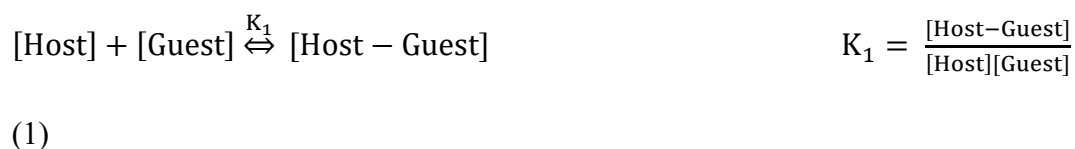
#### **7.4.3.1 Luminescence titration protocol**

The binding of anionic guests (fluoride, acetate) to the complexes was quantified to compute the binding constants ( $K$ ) by steady-state luminescence titration,

employing the non-dilution method,<sup>4</sup> by fixing the concentration of the host complex and varying the concentration of the guest (fluoride, acetate). This was accomplished by carrying out the luminescence titrations by adding aliquots of guest, pre-dissolved in a solution containing the host complex, to a solution of a fixed concentration of the host complex (at an equal concentration of host in solution 1) to maintain the concentration of the complex as uniform, while increasing the concentration of the guest in solution. Stock solution of the host complex (2 mL) was taken in a cuvette and the solution of the guest added in aliquots using Gilson<sup>®</sup> micropipettes. After each aliquot addition (varying amounts between 5-150  $\mu\text{L}$ ), the solution was mixed through agitation using a 1000  $\mu\text{L}$  micropipette inside the cuvette. After complete addition the sample was left to stand for 2 min prior to the measurement being taken. For titrations, the concentration of the stock solution for all Eu(III) containing complexes was 1 mM and the stock concentration of the guest (fluoride, acetate) was 20 mM; for Tb.p.DO3A, the stock concentration was  $1 \times 10^{-5}$  M and the stock guest concentration was  $2 \times 10^{-4}$  M.

Eu(III) containing complexes have sharp line-like emission spectra, which allow ratiometric analysis through measurement of the absolute change or the relative intensity change in comparison to other bands.<sup>5</sup> Anion binding occurs directly at the Ln(III) metal centre, displacing the bound inner-sphere solvent or water molecules; resulting in variations in the Ln(III) coordination environment and the local ligand field, resulting in changes in the corresponding emission intensity, spectral shape and complex lifetime.<sup>4</sup> For Eu(III) containing complexes this is typically characterised by a large change in the intensity of the electric-dipole allowed, hypersensitive  ${}^5\text{D}_0 \rightarrow {}^7\text{F}_2$  ( $\Delta J = 1$ ) emission band whose splitting and intensity is

relative to the local symmetry at the metal centre and to the magnetic anisotropy factor,  $\delta$ .<sup>5</sup> This ratiometric change in binding was monitored upon the addition of each aliquot portion of the guest by comparing the integral of the hypersensitive  $\Delta J = 1$  band, compared to the other visible  $\Delta J$  transitions on the Eu spectrum detailed in Table 1.2. This change in spectrum is then plotted as a function of the concentration of the guest added to the host (equivalent guests) and the concentration of the halides is determined alongside a known concentration curve.<sup>5</sup> The resulting titration curve, referred to as the binding isotherm in this thesis, is then best fitted to a mathematical model corresponding to the postulated chemical equilibria (eq (1)-(3) mentioned below) to obtain the association constants for one- ( $K_1$ ) or two- ( $K_2$ ) or two- (non-independent) ( $K_{2'}$ ) binding events in  $M^{-1}$  via an iterative least square fitting process using DYNAFIT<sup>®</sup> software with uncertainty ( $\pm$ ) expressed as coefficient of variation in percentage and standard error.<sup>6</sup>



In certain luminescence titrations involving fluoride binding in neat solvents, the form and shape of the emission bands can change shape over the course of fluoride addition, making the integration of the emissive bands unrepresentative of the crystal-field splitting.<sup>5</sup> This results in the maxima from the  $\Delta J = 0$  and  $\Delta J = 1$  bands

being used to quantify binding by plotting their intensity via an iterative least square fitting process,<sup>4,5</sup> similar to the method mentioned above. Luminescence titrations were performed at least twice and the best was chosen based upon the strongest binding constant and associated errors.

#### **7.4.3.2 Generation of binding isotherms using DYNAFIT<sup>®</sup>**

Data on all luminescence titrations of the host Eu(III) and Tb(III) complexes with guest anions (fluoride, acetate) were processed and plotted using Origin software. For the ratiometric study of binding interactions, the area under the emission bands were integrated by summing over the wavelength range under each band and the ratio calculations and comparison performed in Origin. For luminescence titrations involving fluoride binding in neat solvents: for Eu.p.DO3A binding isotherms were generated after a baseline subtraction from an emission wavelength; for all other Eu(III) containing complexes, due to the use of time-resolved phosphorescence, there was no significant change in spectral shape observed so the method aforementioned in section-7.4.3.1 worked in these instances. All binding isotherms were generated from DynaFit<sup>®</sup> version 4.08 using its default setting (Trust region algorithm in confidence intervals at 95% probability level) which was transferred to and replotted in Origin. Some outliers were masked to improve data quality, with any significant removal being mentioned on an *ad hoc* basis, with this masking only improving the fit and not changing the overall result.

### **7.5 Software details**

Structures were drawn using Chem Draw 20 and IUPAC names predicted using the same program. NMR and mass spectrometry data were processed using Mestrenova

software version 14.2. All luminescence, binding isotherms and fitted data were plotted using Origin software version 2020b.

### 7.5.1 DynaFit®

Luminescence titration data was fitted to binding constants with the iterative least-squares fitting software DynaFit®, which is able to derive mathematical models for the binding mechanism.<sup>6</sup> DynaFit® is advantageous due to the postulated equilibrium reaction being inputted symbolically, avoiding the use of more complicated alternatives or higher order differential equations. DynaFit® uses the relationship between emission intensity and concentration of the guest chemical species to generate a binding constant from the change in intensity over the course of the titration. After initial manual data processing, an automated process was designed using Excel and Origin in concert. This involved integration of all peaks deemed relevant in the spectrum (summing over wavelength range for each peak) and calculating the responses. The response of the host complex was calculated from the emission intensity and concentration of the guest species, calculated at the start and when the adduct was deemed to have fully binded (binding isotherm plateau or titration endpoint). This data along with the concentrations of host and guest along with binding model information, is then inserted into a script in a suitable format for DynaFit®. To remove human error in this process, macro scripts were written to output the guest concentration and relevant responses into text files in an appropriate directory, these could then be added directly or linked through console commands to an applicable DynaFit® fitting script (**Figure-7.1**). This script generates a set of parameters for optimisation of the fitting program (**Figure-7.2**) and an associated binding isotherm (**Figure-7.3**)

```

;Model Discrimination
;Eu_p_DO3AM_Phen_OH_Acetate_MeOH, complex (1e-3), Guest binding (0.02), 0-1500 microlitres
[task]
  task = fit
  data = equilibria
  model = 1:1 ?
[mechanism]
  Eu + guest <==> complex1 : K1 assoc
[constants]
  K1 = 10e4 ??
[concentrations]
  Eu = 0.001 ??
[data]
variable guest
  file C:\Users\SFGGroup\Documents\DPhil\Louis_Dynafit_data\Scripts\Eu_p_DO3AM_Lys_OMe_Ace'
  file C:\Users\SFGGroup\Documents\DPhil\Louis_Dynafit_data\Scripts\Eu_p_DO3AM_Lys_OMe_Ace'
  file C:\Users\SFGGroup\Documents\DPhil\Louis_Dynafit_data\Scripts\Eu_p_DO3AM_Lys_OMe_Ace'
  file C:\Users\SFGGroup\Documents\DPhil\Louis_Dynafit_data\Scripts\Eu_p_DO3AM_Lys_OMe_Ace'
  file C:\Users\SFGGroup\Documents\DPhil\Louis_Dynafit_data\Scripts\Eu_p_DO3AM_Lys_OMe_Ace'
  file C:\Users\SFGGroup\Documents\DPhil\Louis_Dynafit_data\Scripts\Eu_p_DO3AM_Lys_OMe_Ace'
[output]
  directory C:\Users\SFGGroup\Documents\DPhil\Louis_Dynafit_data\Results\Eu_p_DO3AM_Lys_OMe'
[task]
  task = fit
  data = equilibria
  model = monodentate 2:1 ?
[mechanism]
  Eu + guest <==> complex1 : K1 assoc
  complex1 + guest <==> complex2 : K2 assoc
[constants]
  K1 = 10e4 ??
  K2 = 10e4 ??
  ;K3 = 10e4 ??
[task]
  task = fit
  data = equilibria
  model = termolecular 2:1 ?
[mechanism]
  Eu + guest + guest<==> complex1 : K1 assoc

[constants]
  K1 = 10e4 ??
[end]

```

Figure-7.1. Excerpt from a DynaFit<sup>®</sup> script.

## Parameters

### Trust Region Algorithm

#### Optimized Parameters

No.	Par#Set	Initial	Final	Std. Error	CV (%)	Low <sup>(a)</sup>	High <sup>(a)</sup>	Note
#1	K1	100000	151	27	17.6	144	> 158	
#2	[Eu]	9.558e-007	2e-009	0.00099	49433407.3	< 1.1e-009	0.00033	
#3	r(Eu)#1	4e+008	1.9e+011	9.4e+016	49691862.4	1.2e+006	> 3.7e+011	
#4	r(complex1)#1	6.6e+008	2.9e+011	1.4e+017	48447308.9	1.8e+006	> 5.5e+011	
#5	r(Eu)#2	4e+008	2e+011	9.7e+016	48547283.6	1.2e+006	> 4.1e+011	
#6	r(complex1)#2	1.4e+009	6.9e+011	3.4e+017	48732116.9	4.3e+006	> 6.9e+011	
#7	r(Eu)#3	1.249e+007	6.2e+009	3e+015	49102292.1	39000	> 6.2e+009	
#8	r(complex1)#3	1.796e+007	9.2e+009	4.5e+015	48675214.0	56000	> 9.2e+009	
#9	r(Eu)#4	1.161e+007	5.9e+009	2.9e+015	48957194.9	37000	6.6e+009	
#10	r(complex1)#4	4.62e+007	2.5e+010	1.2e+016	47940127.8	150000	> 2.5e+010	
#11	r(Eu)#5	998800	5.2e+008	2.5e+014	48725505.6	< 2.1	1.2e+009	
#12	r(complex1)#5	2.276e+006	1.3e+009	6.4e+014	49133555.7	< 5.3	> 2.9e+009	
#13	r(Eu)#6	919000	4.8e+008	2.4e+014	49231242.2	< 2	1.2e+009	
#14	r(complex1)#6	2.54e+006	1.5e+009	7.2e+014	48204445.0	< 6	> 3.2e+009	

<sup>(a)</sup> Confidence intervals at 95 % probability level.

**Figure-7.2.** Example DynaFit® data output of binding constant and other parameters.

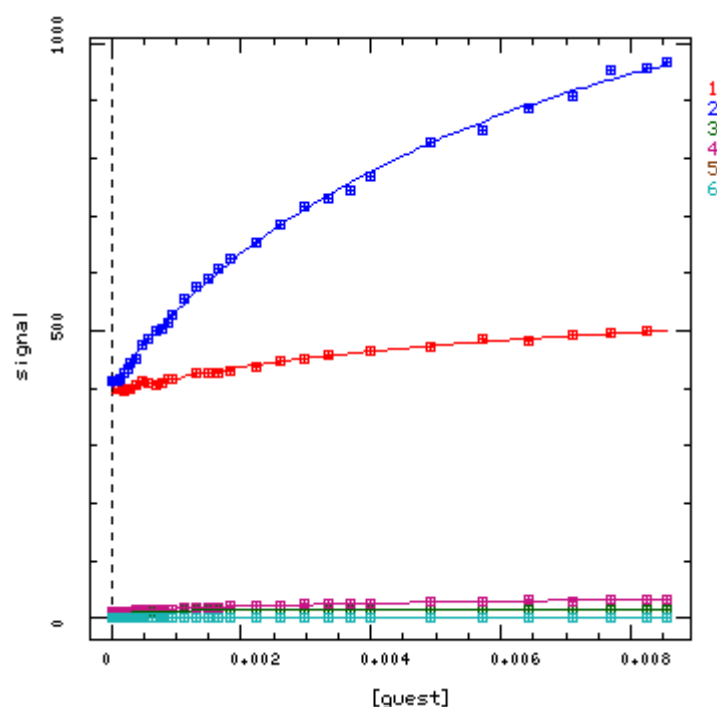


**Figure-7.3.** Example first attempt at fitted binding isotherm output from DynaFit<sup>®</sup>.

Model Discrimination Analysis allowed attempted fitting to multiple models, showing which model fitted the data best.<sup>7</sup> The models considered were 1:1 binding (host binds to one guest molecule), 2:1 binding (host binds to two guest molecules) and termolecular 2:1 binding (simultaneous binding of two guests to one host – physically unlikely but rationalises the propensity for bidentate binding in guest ions such as acetate, allows determination of one overall binding constant if DynaFit<sup>®</sup> is unable to separate the two binding constants  $K_{\text{tot}} = K_1 \cdot K_2$  for 2:1 binding) (Figure-7.4).

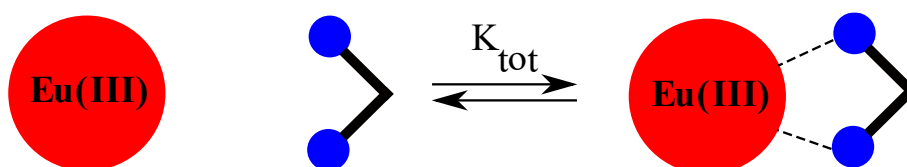
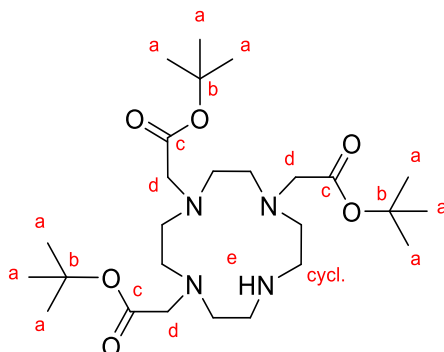


**Figure-7.4.** Pictographic presentation of the equilibrium detailed in termolecular 2:1 binding events.

## 7.6 Synthesis of ligands and complexes

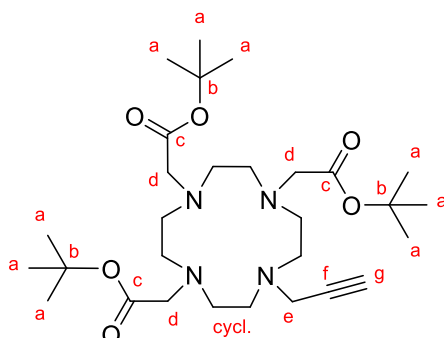
### tri-tert-butyl 2,2',2''-(1,4,7,10-tetraazacyclododecane-1,4,7-triyl)triacetate 2.1<sup>8,9</sup>



Cyclen (6.00 g, 34.8 mmol, 1.0 eq) was dissolved in acetonitrile (120 mL). NaHCO<sub>3</sub> (9.80 g, 116.7 mmol, 3.4 eq) was added and the suspension left to stir at 0 °C in an ice bath for 30 minutes. Tert-butyl bromoacetate (17.2 mL, 116.7 mmol, 3.4 eq) in acetonitrile (20 mL) was added dropwise over 30 minutes. The reaction was then left to stir at room temperature (RT) for 48 hours. The inorganic solids were then removed by filtration through filter paper, before the solvent was removed under reduced pressure to give an off-white solid. The solid was then washed and sonicated with toluene to remove other impurities before being filtered to yield the product as an off-white solid (8.84 g, 49%).

<sup>1</sup>H NMR (400 MHz, 298 K, CDCl<sub>3</sub>) δ<sub>H</sub> (ppm) = 9.98 (s, 1H, H<sup>e</sup>), 3.25 (s, 6H, H<sup>d</sup>), 3.04 (s, 4H, H<sup>cycl.</sup>), 2.85 (s, 12H, H<sup>cycl.</sup>), 1.45 (s, 27H, H<sup>a</sup>). <sup>13</sup>C NMR (101 MHz, CDCl<sub>3</sub>) δ<sub>C</sub> (ppm) = 170.5 (C<sup>c</sup>), 81.7 (C<sup>b</sup>), 56.8 (C<sup>d</sup>), 51.4-49.0 (C<sup>cycl.</sup>) 28.3 (C<sup>a</sup>). LRMS (ESI<sup>+</sup>) m/z 515 ([M+H]<sup>+</sup>, 100%), 537 ([M+Na]<sup>+</sup>, 57%), 1030 ([2M+H]<sup>+</sup>, 13%) HRMS m/z (ESI<sup>+</sup>) Found 515.3802, C<sub>26</sub>H<sub>50</sub>N<sub>4</sub>O<sub>6</sub> requires [M+H]<sup>+</sup> 515.3803. Spectroscopic data matches reported literature values.<sup>8</sup>

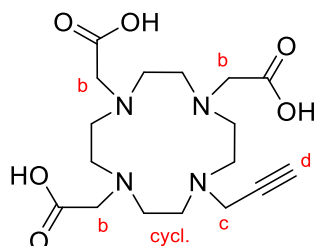
**tri-tert-butyl 2,2',2''-(10-(prop-2-yn-1-yl)-1,4,7,10-tetraazacyclododecane-1,4,7-triyl)triacetate 2.2<sup>10</sup>**



Compound-**2.1** (6.0 g, 11.7 mmol, 1 eq) was dissolved in acetonitrile (100 mL), potassium carbonate (4.0 g, 29.2 mmol, 2.5 eq) was added and the mixture stirred for 30 minutes at 0 °C in an ice bath. To this suspension propargyl bromide (1.63 mL, 15.2 mmol, 1.3 eq) was added dropwise, and the reaction was stirred overnight at RT. The resulting suspension was then filtered to remove the insoluble inorganic solids before the solvent was removed under reduced pressure to yield an orange oil. The crude product was then purified by silica gel (DCM:MeOH (95:5 to 90:10 in 1% increments)). This gave the final product as a pale yellow solid (5.51 g, 85%).

<sup>1</sup>H NMR (400 MHz, 298 K, CDCl<sub>3</sub>) δ<sub>H</sub> (ppm) = 3.24 (d, 2H, H<sup>e</sup>), 3.04 (s, 6H, H<sup>d</sup>), 2.83 (s, 16H, H<sup>cycl.</sup>), 2.08 (s, 1H, H<sup>g</sup>), 1.42 (s, 27H, H<sup>a</sup>). <sup>13</sup>C NMR (101 MHz, CDCl<sub>3</sub>) δ<sub>C</sub> (ppm) = 173.6 (C<sup>c</sup>), 172.9 (C<sup>b</sup>), 82.7 (C<sup>g</sup>), 79.2 (C<sup>f</sup>), 56.6 (C<sup>d</sup>), 57.8-54.2 (C<sup>cycl.</sup>), 43.0 (C<sup>e</sup>), 27.8 (C<sup>a</sup>). LRMS (ESI<sup>+</sup>) m/z 553 ([M+H]<sup>+</sup>, 100%), 575 ([M+Na]<sup>+</sup>, 79%). HRMS m/z (ESI<sup>+</sup>) Found 553.3960, C<sub>29</sub>H<sub>53</sub>N<sub>4</sub>O<sub>6</sub> requires [M+H]<sup>+</sup> 553.3960. Spectroscopic data matches reported literature values.<sup>10</sup>

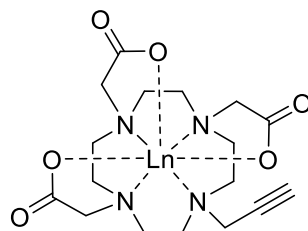
**2,2',2''-(10-(prop-2-yn-1-yl)-1,4,7,10-tetraazacyclododecane-1,4,7-triyl)triacetic acid 2.3**<sup>11,12</sup>



Compound-**2.2** (4.00 g, 7.24 mmol, 1.0 eq) was dissolved in DCM (12.0 mL) and left to stir for 30 minutes at 0 °C in an ice bath. An equal volume of TFA (12.0 mL) was added and the resulting solution was left to stir overnight at RT. The solution was then concentrated under reduced pressure before being co-evaporated with MeOH (5×20.0 mL). The resulting residue was then dissolved in MeOH (5.0 mL) before precipitation into diethyl ether (50 mL). The suspension was then centrifuged, the supernatant removed and the process repeated three times. This yielded the final product as a pale orange solid (2.03 g, 73%).

<sup>1</sup>H NMR (400 MHz, 298 K, MeOD-*d*<sub>4</sub>) δ<sub>H</sub> (ppm) = 3.83 (d, 2H, H<sup>c</sup>), 3.70 (s, 6H, H<sup>b</sup>), 3.27-3.22 (s, 8H, H<sup>cycl.</sup>), 3.25-3.05 (s, 8H, H<sup>cycl.</sup>), 2.80 (s, 1H, H<sup>d</sup>). LRMS (ESI<sup>+</sup>) m/z 385 ([M+H]<sup>+</sup>, 100%), 407 ([M+Na]<sup>+</sup>, 12%). HRMS m/z (ESI<sup>+</sup>) Found 385.2082, C<sub>17</sub>H<sub>29</sub>N<sub>4</sub>O<sub>6</sub> requires [M+H]<sup>+</sup> 385.2082. Spectroscopic data matches reported literature values.<sup>11,12</sup>

## General synthesis of Ln.p.DO3A complexes<sup>11</sup>



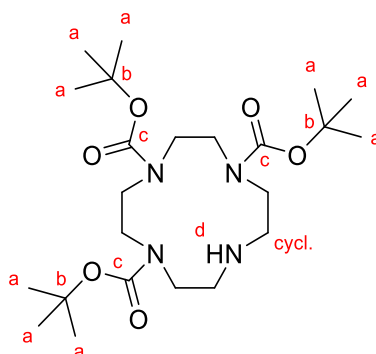
Compound-**2.3** (300 mg, 0.78 mmol, 1.0 eq) and lanthanide triflate (0.82 mmol, 1.05 eq) was dissolved in a solution of ethanol (EtOH)/H<sub>2</sub>O (1:1, 5 mL) and stirred for 24 hours at 60 °C. The pH of the solution was then adjusted to 4 by addition of aqueous NaOH (1.0 M), the solution was then left to stir for 48 hours at 60 °C. The solvent was then removed under reduced pressure, the resulting residue was then redissolved in water (5.00 mL) and the pH adjusted to 10 by addition of aqueous NaOH (1.0 M), to remove excess of the lanthanide as its insoluble hydroxide. The resulting suspension was then centrifuged and the supernatant removed and kept. The solvent of the supernatant was removed under reduced pressure and the residue redissolved in the minimum amount of MeOH (5.00 mL) before addition to diethyl ether (50.0 mL) to precipitate out the final product. The supernatant was disposed of and the solid kept as the final product.

**Eu2.4:** White powder. (250 mg, 0.47 mmol, 60%). <sup>1</sup>H NMR (500 MHz, 298 K, D<sub>2</sub>O) δ<sub>H</sub> (ppm) = 33.1, 27.9, 25.2, 23.6, 21.2, 19.1, 18.6, 17.1, 16.5, 16.2, 15.7, 15.2, 14.4, 13.7, 12.9, 12.0, 11.5, 11.2, 10.3, -0.98, -1.53, -1.9, -3.4, -3.7, -4.5, -4.7, -5.5, -6.3, -6.7, -7.0, -7.4, -8.2, -9.0, -10.2, -10.5, -11.2, -12.1, -13.1, -13.8, -14.0, -14.7, -15.7, -16.3, -16.5, -17.0, -17.8, -18.8, -19.4, -20.5, -21.2. HRMS m/z (ESI<sup>+</sup>) found 533.3559, C<sub>17</sub>H<sub>26</sub>EuN<sub>4</sub>O<sub>6</sub> requires [M+H]<sup>+</sup> 533.1045. HRMS m/z (ESI<sup>+</sup>) found 594.1584, C<sub>19</sub>H<sub>28</sub>EuN<sub>4</sub>O<sub>8</sub> requires [M+CH<sub>3</sub>CO<sub>2</sub>]<sup>+</sup> 594.1584.

**Tb2.4:** White powder. (150 mg, 0.27 mmol, 35%).  $^1\text{H}$  NMR (500 MHz, 298 K,  $\text{D}_2\text{O}$ )  $\delta_{\text{H}}$  = 493.6, 402.4, 244.4, 223.6, 190.7, -76.0, -94.9, -166.9, -179.8, -196.2, -354.1, -396.0. HRMS  $m/z$  ( $\text{ESI}^+$ ) found 541.1094,  $\text{C}_{17}\text{H}_{26}\text{TbN}_4\text{O}_6$  requires  $[\text{M}+\text{H}]^+$  541.1100.

Spectroscopic data matches reported literature values for both Eu(III) and Tb(III) complexes.<sup>4</sup>

**tri-*tert*-butyl 1,4,7,10-tetraazacyclododecane-1,4,7-tricarboxylate**  
**3.1<sup>13</sup>**

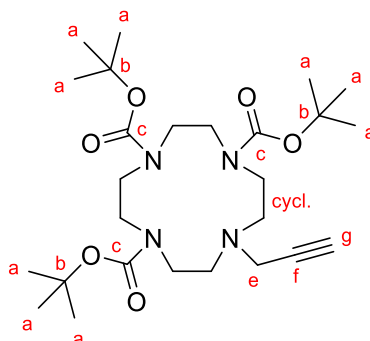


Cyclen (6.00 g, 34.9 mmol, 1.0 eq) and Et<sub>3</sub>N (15.0 mL, 105 mmol, 3.0 eq) were dissolved in CHCl<sub>3</sub> (170 mL) and stirred at 0 °C for 20 minutes. Di-*tert*-butyl-dicarbonate (23.0 g, 106 mmol, 3.0 eq) was dissolved in CHCl<sub>3</sub> (130 mL) and added dropwise to the solution over 2 hours at 0 °C, the solution was then allowed to warm to room temperature and stirred for 18 hours. The solution was then washed with distilled water (3×100 mL), the organic layer was collected and dried with MgSO<sub>4</sub>. The hydrated MgSO<sub>4</sub> was filtered off with filter paper and the solvent removed under reduced pressure. The crude product was purified by gradient column chromatography on silica (EtOAc:n-hexane:IPA (volume ratio, 25:75:0 to 50:50:0 to 50:45:5 in 5% increments)) to give the product as a white glassy solid (6.22 g, 38%).

<sup>1</sup>H NMR (400 MHz, 298 K, CDCl<sub>3</sub>) δ<sub>H</sub> (ppm) = 7.26 (s, 1H, H<sup>d</sup>), 3.56 (s, 4H, H<sup>cycl.</sup>), 3.26 (s, 8H, H<sup>cycl.</sup>), 2.87 – 2.68 (s, 4H, H<sup>cycl.</sup>), 1.39 (s, 27H, H<sup>a</sup>). <sup>13</sup>C NMR (101 MHz, CDCl<sub>3</sub>) δ<sub>C</sub> (ppm) = 171.0(C<sup>c</sup>), 79.4 (C<sup>b</sup>), 60.3 (C<sup>cycl.</sup>), 50.9-49.4 (C<sup>cycl.</sup>), 28.4 (C<sup>a</sup>). LRMS found *m/z* 473 ([M+H]<sup>+</sup>, 65%), 946 ([2M+H]<sup>+</sup>, 100%). HRMS *m/z* (ESI<sup>+</sup>) found 473.3331, C<sub>23</sub>H<sub>45</sub>N<sub>4</sub>O<sub>6</sub> requires [M+H]<sup>+</sup> 473.3334.

Spectroscopic data matches reported literature values.<sup>6</sup>

**tri-*tert*-butyl 10-(prop-2-yn-1-yl)-1,4,7,10-tetraazacyclododecane-1,4,7-tricarboxylate 3.2**<sup>14</sup>

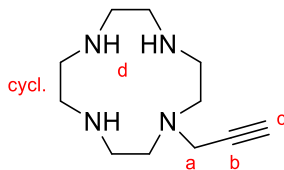


Compound-**3.1** (3.17 g, 6.71 mmol, 1.0 eq) was dissolved in anhydrous MeCN (200 mL), then sodium carbonate (2.85 g, 26.9 mmol, 4.0 eq) was added and the suspension left to stir for 20 minutes. Propargyl bromide (1.20 mL, 8.07 mmol, 1.2 eq) was added dropwise over 30 minutes and the suspension left to stir under reflux overnight. The insoluble salts were removed by filtration through filter paper and the solvent removed under reduced pressure. The residue was purified by column chromatography on silica (EtOAc:n-hexane (volume ratio, 1:1)) giving the product as a light brown solid (2.93 g, 86%).

<sup>1</sup>H NMR (400 MHz, 298 K, CDCl<sub>3</sub>) δ<sub>H</sub> (ppm) = 3.44 (s, 2H, H<sup>e</sup>), 3.38-3.10 (s, 16H, H<sup>cycl.</sup>), 2.72 (s, 1H, H<sup>g</sup>), 1.40 (s, 27H, H<sup>a</sup>). <sup>13</sup>C NMR (101 MHz, CDCl<sub>3</sub>) δ<sub>C</sub> (ppm) = 171.0 (C<sup>c</sup>), 79.4 (C<sup>b</sup>), 79.2 (C<sup>g</sup>), 60.3 (C<sup>f</sup>), 52.3-50.9 (C<sup>cycl.</sup>), 49.5 (C<sup>e</sup>), 28.6-28.4 (C<sup>a</sup>). LRMS found *m/z* 511 ([M+H]<sup>+</sup>, 100%), 1021 ([2M+H]<sup>+</sup>, 3%). HRMS *m/z* (ESI<sup>+</sup>) found 511.3489, C<sub>26</sub>H<sub>47</sub>N<sub>4</sub>O<sub>6</sub> requires [M+H]<sup>+</sup> 511.3490.

Spectroscopic data matches reported literature values.<sup>7</sup>

**1-(prop-2-yn-1-yl)-1,4,7,10-tetraazacyclododecane 3.3<sup>15</sup>**

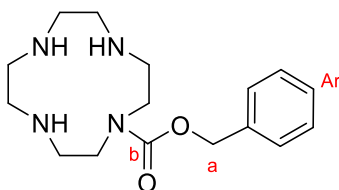


Compound-**3.2** (1.01 g, 1.98 mmol, 1.0 eq) was dissolved in dichloromethane (25 mL) and left to stir for 20 minutes. TFA (5.7 ml, 33.7 mmol, 17.0 eq) was added dropwise and the solution left to stir at room temperature for 18 hours. The solution was washed with distilled water (4×50 mL). The organic layer was collected, dried with MgSO<sub>4</sub> and the solvent removed under reduced pressure. The residue was dissolved and co-evaporated under reduced pressure with MeOH (3×10 mL). The resulting residue was then dissolved in minimum amount of MeOH and precipitated through the addition of diethyl ether (50 mL), the resulting suspension was centrifuged and the solid retained. This process was repeated 3 times to give a light orange solid (0.28 g, 68%).

<sup>1</sup>H NMR (400 MHz, 298 K, MeOD-*d*<sub>4</sub>) δ<sub>H</sub> (ppm) = 8.05 (s, 3H, H<sup>d</sup>), 3.47 (d, 2H, H<sup>a</sup>), 3.10 (s, 1H, H<sup>c</sup>), 3.05- 2.94 (m, 12H, H<sup>cycl.</sup>), 2.85 (d, 4H, H<sup>cycl.</sup>). <sup>13</sup>C NMR (101 MHz, MeOD-*d*<sub>4</sub>) δ<sub>C</sub> (ppm) = 76.0 (C<sup>b</sup>), 74.9 (C<sup>c</sup>), 44.6 (C<sup>a</sup>), 43.2-41.4 (C<sup>cycl.</sup>). LRMS found *m/z* 211 ([M+H]<sup>+</sup>, 100%). HRMS *m/z* (ESI<sup>+</sup>) found 211.1918, C<sub>11</sub>H<sub>23</sub>N<sub>4</sub> requires [M+H]<sup>+</sup> 211.1917.

Spectroscopic data matches reported literature values.<sup>8</sup>

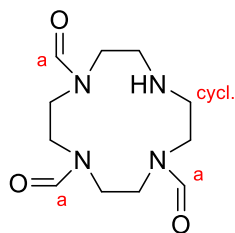
**Phenyl 1,4,7,10-tetraazacyclododecane-1-carboxylate 3.7<sup>16</sup>**



Cyclen (3.00 g, 17.4 mmol, 1.0 eq) was dissolved in  $\text{CHCl}_3$  (100 mL) and left to stir at RT for 20 minutes at 0 °C. A solution of benzyl chloroformate (2.97 g, 17.4 mmol, 1.0 eq) in  $\text{CHCl}_3$  (50 mL) was then added dropwise over 1 hour, the solution was then allowed to warm to RT and stirred overnight. The solvent was then removed under reduced pressure to yield the crude product as an off white solid, this was then purified by column chromatography on silica (DCM:MeOH: $\text{NH}_4\text{OH}$  (volume ratio, 50:50:0 to 50:45:5 in increments of 1%)) to give the product as an off white solid (2.71 g, 51%).

$^1\text{H}$  NMR (400 MHz, 298 K,  $\text{MeOD-}d_4$ )  $\delta_{\text{H}}$  (ppm) = 7.33 – 7.18 (m, 5H,  $\text{H}^{\text{Ar}}$ ), 5.08 (s, 2H,  $\text{H}^{\text{a}}$ ), 3.44-2.88 (m, 12H,  $\text{H}^{\text{cycl}}$ ), 2.74-2.64 (m, 4H,  $\text{H}^{\text{cycl}}$ ).  $^{13}\text{C}$  NMR (101 MHz,  $\text{MeOD-}d_4$ )  $\delta_{\text{C}}$  (ppm) = 170.3 ( $\text{C}^{\text{b}}$ ), 136.53 ( $\text{ArC}^{\text{quaternary}}$ ), 129.0 (ArC), 128.1 (ArC), 126.6 (ArC), 54.75 ( $\text{C}^{\text{a}}$ ), 49.2-44.6 ( $\text{C}^{\text{cycl}}$ ). LRMS found  $m/z$  307 ( $[\text{M}+\text{H}]^+$ , 43%), 651 ( $[\text{2M}+\text{K}]^+$ , 100%)

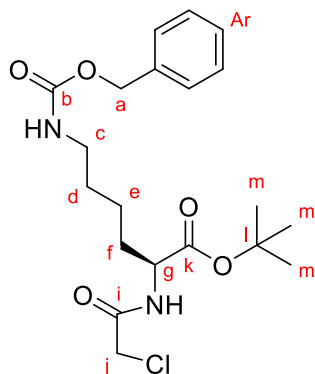
### 1,4,7,10-tetraazacyclododecane-1,4,7-tricarbaldehyde 3.7<sup>17</sup>



Cyclen (1.72 g, 10.0 mmol, 1.0 eq) was dissolved in EtOH (20.0 mL) and left to stir for 20 minutes before, chloral hydrate (9.92 g, 60.0 mmol, 6.0 eq) in EtOH (10.0 mL) was added dropwise and the solution heated to 60 °C and left to stir for 4 hours. The solvent was then removed under reduced pressure before, the crude product was purified by silica column chromatography (DCM:MeOH (volume ratio, 9:1)). This gave the product as a colourless oil (2.30 g, 90%).

<sup>1</sup>H NMR (400 MHz, 298 K, CDCl<sub>3</sub>) δ<sub>H</sub> (ppm) = 7.96 (s, 3H, H<sup>a</sup>), 3.38 (s, 12H, H<sup>cycl.</sup>), 2.91 – 2.76 (br t, 4H, H<sup>cycl.</sup>). <sup>13</sup>C NMR (101 MHz, CDCl<sub>3</sub>) δ<sub>C</sub> (ppm) = 163.70 (C<sup>a</sup>), 52.05 (C<sup>cycl.</sup>), 50.47 (C<sup>cycl.</sup>), 50.27 (C<sup>cycl.</sup>). LRMS found *m/z* 257 ([M+H]<sup>+</sup>, 2%), 513 ([2M+H]<sup>+</sup>, 100%).

***tert*-butyl *N*<sub>6</sub>-((benzyloxy)carbonyl)-*N*<sub>2</sub>-(2-chloroacetyl)-l-lysinate  
3.4a**

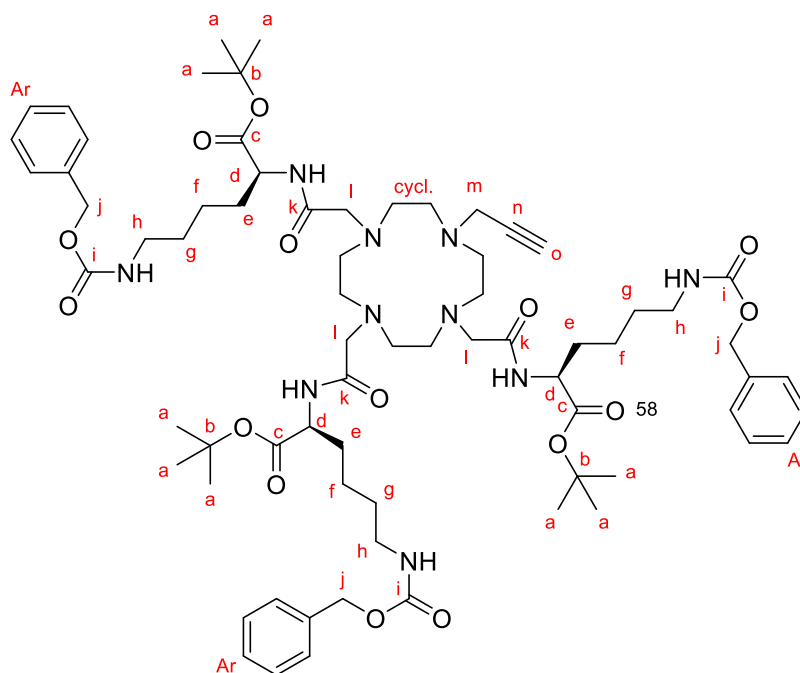


*N*'-Cbz-L-lysine *tert*-butyl ester hydrochloride (1.12 g, 3.00 mmol, 1.0 eq) and caesium carbonate (2.62 g, 8.04 mmol, 2.7 eq) in DCM (100 mL) cooled to 0 °C and stirred for 20 minutes. Then chloroacetyl chloride (1.12 mL, 3.49 mmol, 1.2 eq) was added dropwise and the solution allowed to warm to RT and stirred for 3 hours. The resulting solution was washed with distilled water (3×150 mL) and then with a saturated solution of NaHCO<sub>3</sub> (3×150 mL). The organic layer was collected and dried with MgSO<sub>4</sub>, the hydrated MgSO<sub>4</sub> was filtered off and the solvent removed under reduced pressure. The residue was then purified by silica column chromatography (DCM:MeOH (volume ratio, 100:0 to 95:5 in 1% increments)) to give the product as a white powder (1.16 g, 94%).

<sup>1</sup>H NMR (400 MHz, 298 K, MeOD-*d*<sub>4</sub>) δ<sub>H</sub> (ppm) = 7.51 – 6.98 (m, 5H, H<sup>Ar</sup>), 4.96 (s, 2H, H<sup>a</sup>), 4.16 (dd, 1H, H<sup>g</sup>), 3.96 (s, 2H, H<sup>j</sup>), 3.02 (t, 2H, H<sup>c</sup>), 1.79 – 1.55 (m, 2H, H<sup>f</sup>), 1.47 – 1.38 (m, 2H, H<sup>d</sup>), 1.36 (s, 9H, H<sup>m</sup>), 1.34 – 1.26 (m, 2H, H<sup>e</sup>). <sup>13</sup>C NMR (101 MHz, MeOD-*d*<sub>4</sub>) δ<sub>C</sub> (ppm) = 171.1 (C<sup>i</sup>), 167.9 (C<sup>h</sup>), 167.2 (C<sup>b</sup>), 136.0- 127.4 (C<sup>Ar</sup>), 81.7 (C<sup>l</sup>), 66.0 (C<sup>a</sup>), 53.4 (C<sup>j</sup>), 41.6 (C<sup>g</sup>), 40.0 (C<sup>c</sup>), 36.9 (C<sup>h</sup>), 30.8 (C<sup>f</sup>), 29.2 (C<sup>d</sup>), 26.8 (C<sup>m</sup>), 22.5 (C<sup>e</sup>). LRMS found *m/z* 413 ([M+H]<sup>+</sup>, 100%), 435 ([M+Na]<sup>+</sup>,

52%). HRMS  $m/z$  (ESI<sup>+</sup>) found 413.1841, C<sub>20</sub>H<sub>30</sub>N<sub>2</sub>O<sub>5</sub>Cl<sub>1</sub> requires [M+H]<sup>+</sup> 413.1838.

**tri-tert-butyl 2,2',2''-((2,2',2''-(10-(prop-2-yn-1-yl)-1,4,7,10-tetraazacyclododecane-1,4,7-triyl)tris(acetyl)tris(azanediy)))(2S,2'S,2''S)-tris(6-(((benzyloxy)carbonyl)amino)hexanoate) 3.5a<sup>18</sup>**

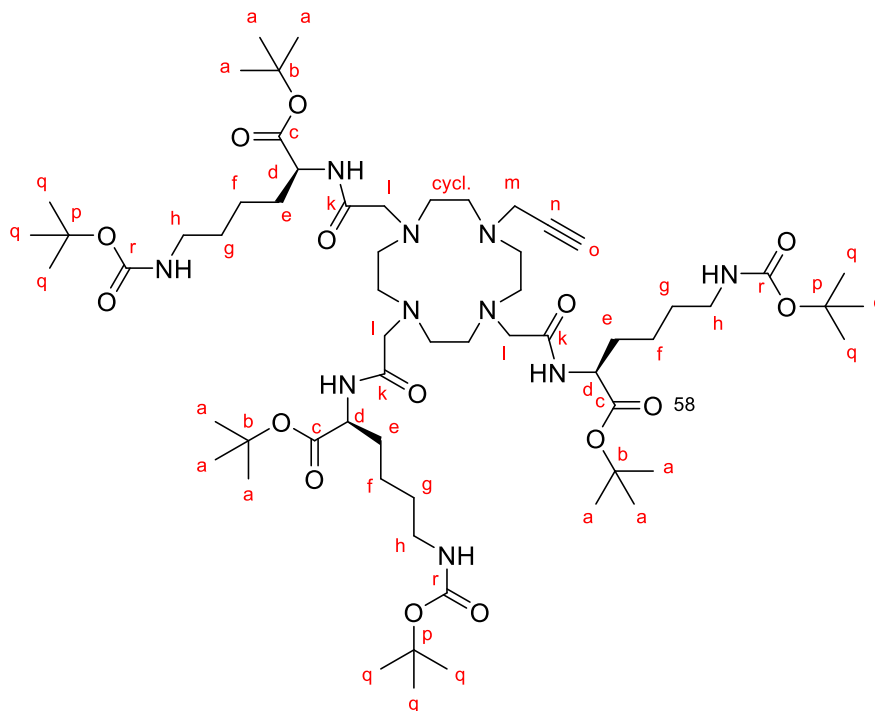


Compound-**2.3** (0.38 g, 1.00 mmol, 1.0 eq) was dissolved in MeCN (5.0 mL), to this solution HATU (2.28 g, 6.00 mmol, 6.0 eq), HOBt (0.81 g, 6.00 mmol, 6.0 eq) and DIPEA (1.74 mL, 10.00 mmol, 10.0 eq) was added and the mixture left to stir at RT for 30 minutes or until the solution turned golden brown. To this stirring solution, N'-Cbz-L-lysine tert-butyl ester hydrochloride (2.24 g, 6.00 mmol, 6.0 eq) in MeCN (5.0 mL) was added. The solution was then heated to 50 °C and left to stir overnight. The solvent was then removed under reduced pressure. The resulting residue was then redissolved in DCM (15 mL), this solution was then washed with MilliQ water (3×10 mL) and aqueous NaOH (0.1 M) solution (3×10 mL). The

organic layer was retained and dried using anhydrous  $\text{MgSO}_4$ , before the insoluble salts were removed by filtration. The solvent was then removed under reduced pressure to yield an oily residue. This was purified by silica column chromatography (DCM:MeOH: $\text{NH}_4\text{OH}$  (60:40:0 to 60:30:10 in 2% increments)). The resulting residue was then further purified by alumina column chromatography (MeCN: $\text{H}_2\text{O}$  (100:0 to 90:10 in 2% increments)) to yield the product as a yellow oil (0.62 g, 47%).

$^1\text{H}$  NMR (600 MHz, 298 K, MeOD)  $\delta_{\text{H}}$  (ppm) = 7.40-7.20 (m, 15H,  $\text{H}^{\text{Ar}}$ ), 5.03 (s, 6H,  $\text{H}^{\text{j}}$ ), 4.08 (br m, 3H,  $\text{H}^{\text{d}}$ ), 3.77 (br m, 2H,  $\text{H}^{\text{m}}$ ), 3.24 (br m, 1H,  $\text{H}^{\text{o}}$ ), 3.18-2.92 (br m, 16H,  $\text{H}^{\text{cycl.}}$ ), 2.88 (br m, 6H,  $\text{H}^{\text{l}}$ ), 2.77 (br m, 6H,  $\text{H}^{\text{h}}$ ), 1.94-1.28 (br m, 45H,  $\text{H}^{\text{a,e-g}}$ ).  $^{13}\text{C}$  NMR (151 MHz, MeOD)  $\delta_{\text{C}}$  = 174.6 ( $\text{C}^{\text{c}}$ ), 170.7 ( $\text{C}^{\text{k}}$ ), 162.1 ( $\text{C}^{\text{i}}$ ), 137.1 ( $\text{ArC}^{\text{quaternary}}$ ), 128.1 ( $\text{ArC}$ ), 127.6 ( $\text{ArC}$ ), 127.4 ( $\text{ArC}$ ), 82.8 ( $\text{C}^{\text{b}}$ ), 81.4 ( $\text{C}^{\text{n}}$ ), 80.8 ( $\text{C}^{\text{m}}$ ), 66.0 ( $\text{C}^{\text{o}}$ ), 65.9 ( $\text{C}^{\text{j}}$ ), 60.5 ( $\text{C}^{\text{l}}$ ), 57.9 ( $\text{C}^{\text{d}}$ ), 56.8 ( $\text{C}^{\text{cycl.}}$ ), 54.2 ( $\text{C}^{\text{m}}$ ), 40.1 ( $\text{C}^{\text{h}}$ ), 39.7 ( $\text{C}^{\text{e}}$ ), 39.0 ( $\text{C}^{\text{g}}$ ), 31.3 ( $\text{C}^{\text{a}}$ ), 22.5 ( $\text{C}^{\text{f}}$ ). LRMS found  $m/z$  670 ( $[\text{M}+2\text{H}]^+$ , 74%), 1340 ( $[\text{M}+\text{H}]^+$ , 100%)%. HRMS  $m/z$  (ESI $^+$ ) found 1361.7709,  $\text{C}_{71}\text{H}_{106}\text{N}_{10}\text{O}_{15}\text{Na}$  requires  $[\text{M}+\text{Na}]^+$  1361.7731.

**tri-tert-butyl 2,2',2''-((2,2',2''-(10-(prop-2-yn-1-yl)-1,4,7,10-tetraazacyclododecane-1,4,7-triyl)tris(acetyl)tris(azanediy)))(2S,2'S,2''S)-tris(6-((tert-butoxycarbonyl)amino)hexanoate) 3.5b<sup>18</sup>**

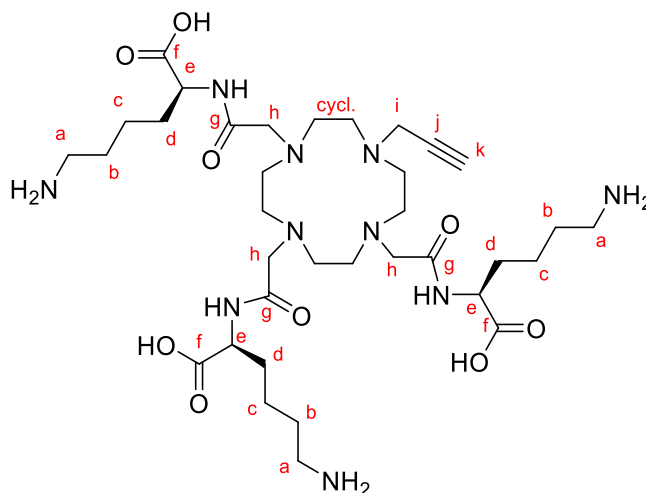


Compound-**2.3** (950 mg, 0.247 mmol, 1.0 eq) was dissolved in MeCN (5.0 mL), to this solution HATU (0.565 g, 3.71 mmol, 15.0 eq), HOBt (0.201 g, 1.49 mmol, 6.0 eq) and DIPEA (0.65 mL, 3.71 mmol, 15.0 eq) was added and the mixture left to stir at RT for 30 minutes or until the solution turned golden brown. To this stirring solution, N<sup>7</sup>-Boc-L-lysine tert-butyl ester hydrochloride (0.50 g, 1.49 mmol, 6.0 eq) in MeCN (5.0 mL) was added. The solution was then heated to 50 °C and left to stir overnight. The solvent was then removed under reduced pressure. The resulting residue was then redissolved in DCM (15 mL), this solution was then washed with MilliQ water (3×10 mL) and aqueous NaOH (0.1 M) solution (3×10 mL). The organic layer was retained and dried using anhydrous MgSO<sub>4</sub>, before the insoluble salts were removed by filtration. The solvent was then removed under reduced

pressure to yield an oily residue. This was purified by silica column chromatography (DCM:MeOH:NH<sub>4</sub>OH (60:40:0 to 60:30:10 in 2% increments)). The resulting residue was then further purified by alumina column chromatography (MeCN:H<sub>2</sub>O (100:0 to 90:10 in 2% increments)) to yield the product as a yellow oil (0.148 g, 54%).

<sup>1</sup>H NMR (600 MHz, 298 K, MeOD)  $\delta_{\text{H}}$  (ppm) = 4.40 (br m, 3H, H<sup>d</sup>), 4.35 (br m, 2H, H<sup>m</sup>), 3.96 (br m, 1H, H<sup>o</sup>), 3.72 (s, 6H, H<sup>l</sup>), 3.66-3.26 (br m, 16H, H<sup>cycl.</sup>) 3.09 (br m, 6H, H<sup>h</sup>), 1.97-1.65 (m, 6H, H<sup>e</sup>), 1.58 – 1.37 (m, 66H, H<sup>a,f,g,q</sup>). <sup>13</sup>C NMR (151 MHz, MeOD)  $\delta_{\text{C}}$  = 172.4 (C<sup>c</sup>), 163.5 (C<sup>k</sup>), 158.5 (C<sup>r</sup>), 86.0 (C<sup>n</sup>), 83.2 (C<sup>o</sup>), 83.0 (C<sup>b</sup>), 79.8 (C<sup>p</sup>), 55.9 (C<sup>l</sup>), 53.1 (C<sup>d</sup>), 43.9 (C<sup>cycl.</sup>), 41.0 (C<sup>m</sup>), 40.2 (C<sup>h</sup>), 32.5 (C<sup>e</sup>), 28.2 (C<sup>g</sup>), 28.3 (C<sup>q</sup>), 28.2 (C<sup>a</sup>), 18.8 (C<sup>f</sup>). LRMS found  $m/z$  619 ([M+2H]<sup>+</sup>, 4%), 1238 ([M+H]<sup>+</sup>, 100%),%. HRMS  $m/z$  (ESI<sup>+</sup>) found 1259.8218, C<sub>62</sub>H<sub>112</sub>N<sub>10</sub>O<sub>15</sub>Na requires [M+Na]<sup>+</sup> 1259.8201.

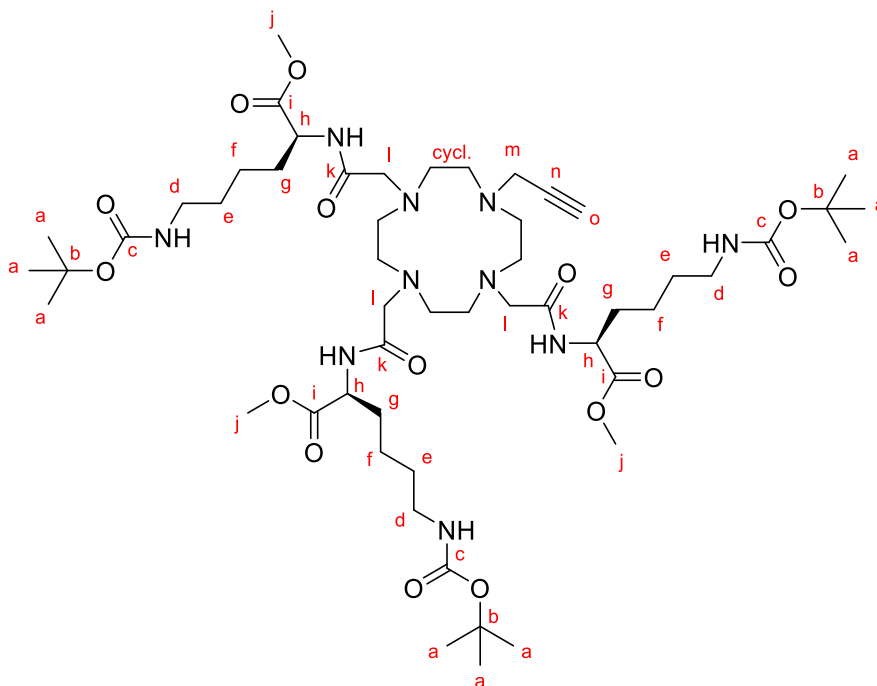
**(2S,2'S,2''S)-2,2',2''-((2,2',2''-(10-(prop-2-yn-1-yl)-1,4,7,10-tetraazacyclododecane-1,4,7-triyl)tris(acetyl)tris(azanediyl))tris(6-aminohexanoic acid) 3.6b**



Compound-**3.5b** (0.63 g, 0.51 mmol, 1.0 eq) was dissolved in dichloromethane (10 mL) and left to stir at RT for 20 minutes. TFA (10 ml, 59.1 mmol, 116 eq) was added dropwise and the solution left to stir at RT for 18 hours. The solution was concentrated *in vacuo* to leave an orange residue. The residue was then dissolved and co-evaporated with MeOH (3×10 mL). The resulting residue was then dissolved in the minimum amount of MeOH (5.0 mL) and precipitated with diethyl ether (50 mL), the suspension was centrifuged and the solid retained, this process was repeated 3 times to give an off-white solid (0.290 g, 75%).

<sup>1</sup>H NMR (600 MHz, 298 K, MeOD)  $\delta_{\text{H}}$  (ppm) = 4.47 – 4.44 (dd, 3H, H<sup>e</sup>), 3.88 – 3.66 (m, 2H, H<sup>i</sup>), 3.62 (s, 1H, H<sup>k</sup>), 3.25 (s, 1H), 3.06 – 2.84 (m, 22H, H<sup>cycl.,a</sup>), 1.50 (m, 24H, H<sup>b,c,d,h</sup>). <sup>13</sup>C NMR (151 MHz, MeOD)  $\delta_{\text{C}}$  174.5 (C<sup>f</sup>), 171.8 (C<sup>g</sup>), 77.2 (C<sup>j</sup>), 74.2 (C<sup>k</sup>), 54.2 (C<sup>h</sup>), 51.4 (C<sup>e</sup>), 39.2 (C<sup>i</sup>), 39.1 (C<sup>a</sup>), 31.3 (C<sup>d</sup>), 26.7 (C<sup>b</sup>), 22.2 (C<sup>c</sup>). HRMS *m/z* (ESI<sup>+</sup>) found 769.4931, C<sub>35</sub>H<sub>65</sub>N<sub>10</sub>O<sub>9</sub> requires [M+H]<sup>+</sup> 769.4930.

**trimethyl 2,2',2''-((2,2',2''-(10-(prop-2-yn-1-yl)-1,4,7,10-tetraazacyclododecane-1,4,7-triyl)tris(acetyl)tris(azanediy)))(2S,2'S,2''S)-tris(6-((tert-butoxycarbonyl)amino)hexanoate) 3.5c<sup>18</sup>**



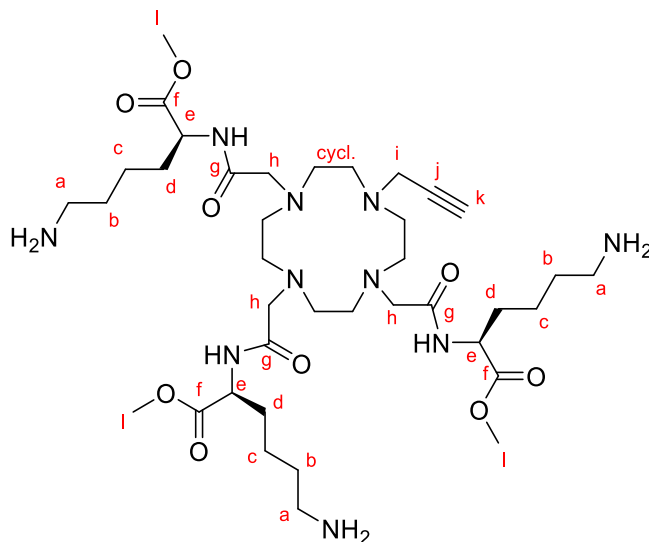
Compound-**2.3** (200 mg, 0.52 mmol, 1.0 eq) was dissolved in MeCN (5.0 mL), to this solution HATU (1.19 g, 3.12 mmol, 6.0 eq), HOBt (420 mg, 3.12 mmol, 6.0 eq) and DIPEA (1.36 mL, 7.81 mmol, 15.0 eq) was added and the mixture left to stir at RT for 30 minutes or until the solution turned golden brown. To this stirring solution, N'-Boc-L-lysine methyl ester hydrochloride (926 mg, 3.12 mmol, 6.0 eq) in MeCN (5.0 mL) was added. The solution was then heated to 50 °C and left to stir overnight. The solvent was then removed under reduced pressure. The resulting residue was then redissolved in DCM (15 mL), this solution was then washed with MilliQ water (3×10 mL) and aqueous NaOH (0.1 M) solution (3×10 mL). The organic layer was retained and dried using anhydrous MgSO<sub>4</sub>, before the insoluble salts were removed by filtration through filter paper. The solvent was then removed

under reduced pressure to yield an oily residue. This was then purified by silica column chromatography (DCM:MeOH:NH<sub>4</sub>OH (60:40:0 to 60:30:10 in 2% increments)). The resulting residue was then further purified by alumina column chromatography (MeCN:H<sub>2</sub>O (100:0 to 90:10 in 2% increments)) to yield the product as a yellow oil (0.283 g, 49%).

<sup>1</sup>H NMR (600 MHz, 298 K, MeOD)  $\delta_{\text{H}}$  (ppm) = 4.23 (br m, 3H, H<sup>h</sup>), 3.76 (br m, 1H, H<sup>o</sup>), 3.40 (s, 9H, H<sup>j</sup>), 3.37 (br m, 2H, H<sup>m</sup>), 3.22 – 3.02 (br m, 12H, H<sup>d,e</sup>), 3.02 – 2.95 (s, 6H, H<sup>l</sup>), 2.87 (t, 16H, H<sup>cycl.</sup>), 2.09 – 1.51 (m, 6H, H<sup>g</sup>), 1.49 (s, 33H, H<sup>a,f</sup>).

<sup>13</sup>C NMR (151 MHz, MeOD)  $\delta_{\text{C}}$  (ppm) = 174.4 (C<sup>i</sup>), 173.4 (C<sup>k</sup>), 158.6 (C<sup>c</sup>), 79.9 (C<sup>b</sup>), 78.9 (C<sup>n</sup>), 75.4 (C<sup>o</sup>), 58.6 (C<sup>l</sup>), 57.5 (C<sup>h</sup>), 54.2 (C<sup>cycl.</sup>), 52.3 (C<sup>j</sup>), 49.9 (C<sup>m</sup>), 41.0 (C<sup>d</sup>), 32.5 (C<sup>g</sup>), 31.7 (C<sup>e</sup>), 28.8 (C<sup>a</sup>), 24.3 (C<sup>f</sup>). LRMS found  $m/z$  556 ([M+2H]<sup>+</sup>, 62%), 1111 ([M+H]<sup>+</sup>, 100%), 1150 ([M+K]<sup>+</sup>, 22%). HRMS  $m/z$  (ESI<sup>+</sup>) found 1111.6927, C<sub>53</sub>H<sub>95</sub>N<sub>10</sub>O<sub>15</sub> requires [M+H]<sup>+</sup> 1111.6973.

**trimethyl 2,2',2''-((2,2',2''-(10-(prop-2-yn-1-yl)-1,4,7,10-tetraazacyclododecane-1,4,7-triyl)tris(acetyl)tris(azanediy)))(2S,2'S,2''S)-tris(6-aminohexanoate) 3.6c**

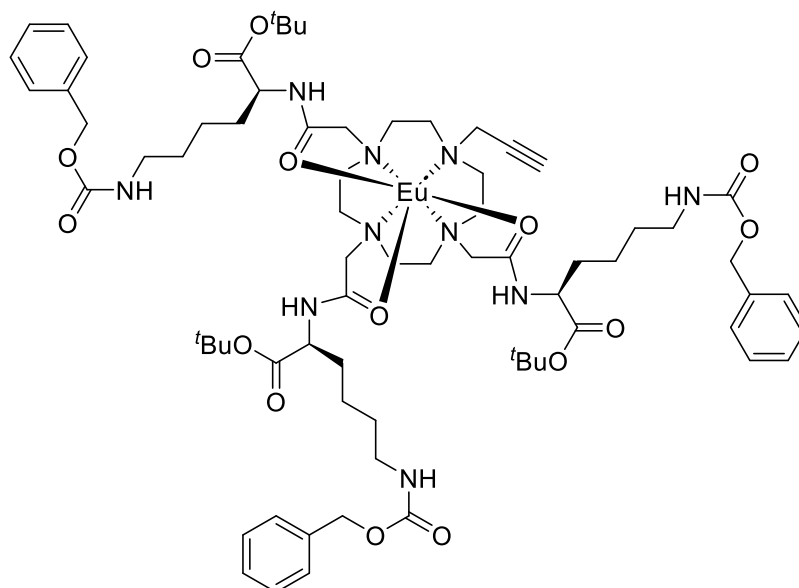


Compound-**3.5c** (100 mg, 0.09 mmol, 1.0 eq) was dissolved in dichloromethane (10 mL) and left to stir for 20 minutes. TFA (10 ml, 59.1 mmol, 116 eq) was added dropwise and the solution left to stir at RT for 18 hours. The solution was concentrated *in vacuo* to leave an orange residue. The residue was then dissolved and co-evaporated with MeOH (3×10 mL). The resulting residue was then dissolved in the minimum amount of MeOH (5.0 mL) and precipitated with diethyl ether (50 mL), the suspension was centrifuged and the solid retained, this process was repeated 3 times to give an off-white solid (60.1 mg, 82%).

$^1\text{H}$  NMR (600 MHz, 298 K, MeOD)  $\delta_{\text{H}}$  (ppm) = 4.40 (br m, 3H, H<sup>e</sup>), 3.97 – 3.84 (br m, 2H, H<sup>i</sup>), 3.72 (s, 9H, H<sup>l</sup>), 3.30 (s, 6H, H<sup>h</sup>), 2.92 (br m, 22H, H<sup>a</sup>, cycl.), 2.56 (br m, 1H, H<sup>k</sup>), 1.85 (m, 6H, H<sup>d</sup>), 1.65 (m, 6H, H<sup>b</sup>), 1.44 (m, 6H, H<sup>c</sup>).  $^{13}\text{C}$  NMR (151 MHz, MeOD)  $\delta_{\text{C}}$  (ppm) = 172.4 (C<sup>f</sup>), 171.8 (C<sup>g</sup>), 78.8 (C<sup>j</sup>), 74.0 (C<sup>k</sup>), 58.7 (C<sup>h</sup>), 55.3 (C<sup>e</sup>), 52.3 (C<sup>cycl.</sup>), 51.6 (C<sup>l</sup>), 50.9 (C<sup>i</sup>), 39.0 (C<sup>a</sup>), 35.2 (C<sup>d</sup>), 30.3 (C<sup>b</sup>), 26.7

(C<sup>e</sup>). LRMS found  $m/z$  406 ( $[M+2H]^+$ , 100%), 812 ( $[M+H]^+$ , 14%). HRMS  $m/z$  (ESI<sup>+</sup>) found 811.5412, C<sub>38</sub>H<sub>71</sub>N<sub>10</sub>O<sub>9</sub> requires  $[M+H]^+$  811.5400.

### Synthesis of Eu.p.DO3AM.Lys.O<sup>t</sup>Bu.CBz complex EuL<sup>3.5a</sup>

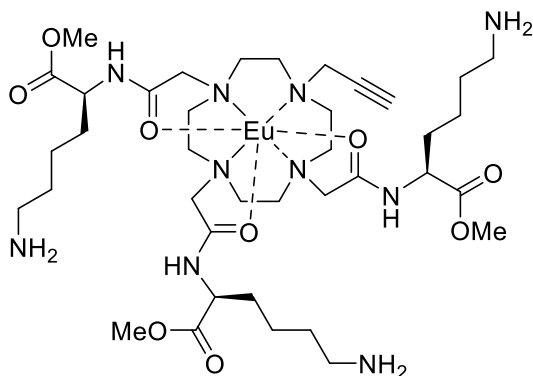


Compound-**3.5a** (100 mg, 0.075 mmol, 1.0 eq) and europium triflate (49 mg, 0.082 mmol, 1.1 eq) was dissolved in EtOH/H<sub>2</sub>O (1:1, 0.75 mL) and stirred for 24 hours at 60 °C. The pH of the solution was then adjusted to 4 by addition of aqueous NaOH (1 M), the solution was then left to stir for a further 24 hours at 60 °C. The solvent was then removed *in vacuo*. The remaining residue was then redissolved in the minimum amount of MeOH (5.0 mL) before being precipitated with diethyl ether (0°C) (50 mL) to yield the product as a white solid (53 mg, 47%).

<sup>1</sup>H NMR (500 MHz, 298 K, MeOD)  $\delta_H$  = 33.3, 24.9, 21.7, 19.0, 17.8, 16.9, 11.6, 10.3, -0.2, -0.9, -2.0, -3.0, -3.6, -5.3, -6.8, -7.5, -7.9, -10.0, -10.7, -11.6, -17.1, -20.9, -21.3, -22.0. Only resolved peaks outside the 0-10 ppm range are reported.

Luminescence lifetimes ( $\lambda_{\text{ex}} = 393 \text{ nm}$ ,  $\lambda_{\text{em}} = 616 \text{ nm}$ ): MeOH: 0.68 ms, MeOD: 1.21 ms,  $q = 0.7$ .

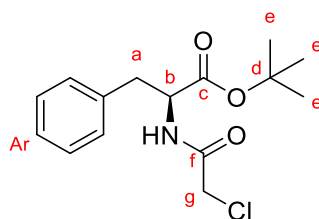
### Synthesis of Eu.p.DO3AM.Lys.OMe complex EuL<sup>3.6c</sup>



Compound-**3.6c** (100 mg, 0.123 mmol, 1.0 eq) and europium triflate (81 mg, 0.136 mmol, 1.1 eq) was dissolved in MeCN (1.2 mL) and stirred for 72 hours at 60 °C. The solvent was then removed in vacuo. The remaining residue was then redissolved in the minimum amount of MeOH (5.0 mL) before being precipitated with diethyl ether (0°C) (50 mL) to yield the product as a glassy yellow solid (76 mg, 65%).

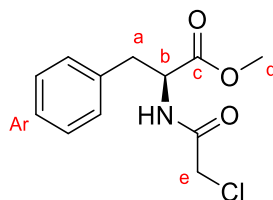
<sup>1</sup>H NMR (400 MHz, 298 K, D<sub>2</sub>O)  $\delta_{\text{H}} = 39.4, 31.5, 22.3, 16.1, 12.4, -0.2, -0.6, -2.9, -3.6, -4.5, -5.8, -7.3, -8.6, -9.1, -11.1, -14.4, -15.6, -16.1, -16.7, -18.0, -20.0, -22.5, -23.0, -33.7$ . Only resolved peaks outside the 0-10 ppm range are reported. <sup>1</sup>H NMR (500 MHz, CD<sub>3</sub>CN)  $\delta = 22.0, 20.4, 18.7, 17.4, 11.4, -0.6, -1.0, -1.3, -1.5, -1.8, -2.3, -2.4, -3.0, -5.2, -5.9, -6.6, -7.5, -8.8, -10.2, -10.6, -11.4, -12.1, -12.4, -18.6, -19.7$ . Only resolved peaks outside the 0-10 ppm range are reported. Luminescence lifetimes ( $\lambda_{\text{ex}} = 393 \text{ nm}$ ,  $\lambda_{\text{em}} = 616 \text{ nm}$ ): MeOH: 0.55 ms, MeOD: 2.26 ms,  $q = 2.5$ . H<sub>2</sub>O: 0.57 ms, D<sub>2</sub>O: 1.70 ms,  $q = 0.8$ .

**tert-butyl (2-chloroacetyl)-L-phenylalaninate 3.4a<sup>19</sup>**



Tert-butyl L-phenylalaninate (8.00 g, 31.1 mmol, 1.0 eq) was dissolved in DCM (30 mL), 2,6 di-tert-butylpyridine (13.5 mL, 64.1 mmol, 2.1 eq) was added and the solution was left to stir for 20 minutes at 0 °C. Chloroacetyl chloride (3.71 mL, 46.6 mmol, 1.5 eq) was added dropwise and the solution left to warm to RT and stir overnight. The solution was then washed with distilled water (3×100 mL) and brine (3×100 mL). The organic layers were collected and dried over anhydrous MgSO<sub>4</sub>, the hydrated MgSO<sub>4</sub> was filtered through filter paper and the solvent removed to give a yellow oil. The crude product was then purified by silica column chromatography (DCM:MeOH (volume ratio, 100:0 to 95:5 in increments of 1% MeOH)). This gave the final product as an off-white crystalline powder (5.97 g, 65%).

<sup>1</sup>H NMR (400 MHz, 298 K, MeOD) δ<sub>H</sub> (ppm) = 7.23 – 7.09 (m, 5H, H<sup>Ar</sup>), 4.46 (dd, <sup>3</sup>J<sub>HH</sub> = 7.9, 6.4 Hz, 1H, H<sup>b</sup>), 3.92 (s, 2H, H<sup>g</sup>), 3.02 (dd, <sup>3</sup>J<sub>HH</sub> = 13.9, 6.4 Hz, 2H, H<sup>a</sup>), 2.92 (dd, <sup>3</sup>J<sub>HH</sub> = 13.8, 8.0 Hz, 1H, H<sup>a</sup>), 1.30 (s, 9H, H<sup>e</sup>). <sup>13</sup>C NMR (101 MHz, MeOD) δ<sub>C</sub> 170.3 (C<sup>c</sup>), 167.5 (C<sup>f</sup>), 136.53 (ArC<sup>quaternary</sup>), 129.0 (ArC), 128.1 (ArC), 126.6 (ArC), 81.9 (C<sup>d</sup>), 54.75 (C<sup>b</sup>), 41.49 (C<sup>g</sup>), 36.97 (C<sup>a</sup>), 26.8 (C<sup>e</sup>). LRMS found *m/z* 320 ([M+Na]<sup>+</sup>, 100%), 617 ([2M+Na]<sup>+</sup>, 31%). HRMS *m/z* (ESI<sup>+</sup>) found 320.1025, C<sub>15</sub>H<sub>20</sub>N<sub>1</sub>O<sub>3</sub>Cl<sub>1</sub>Na<sub>1</sub> requires [M+Na]<sup>+</sup> 320.1024.

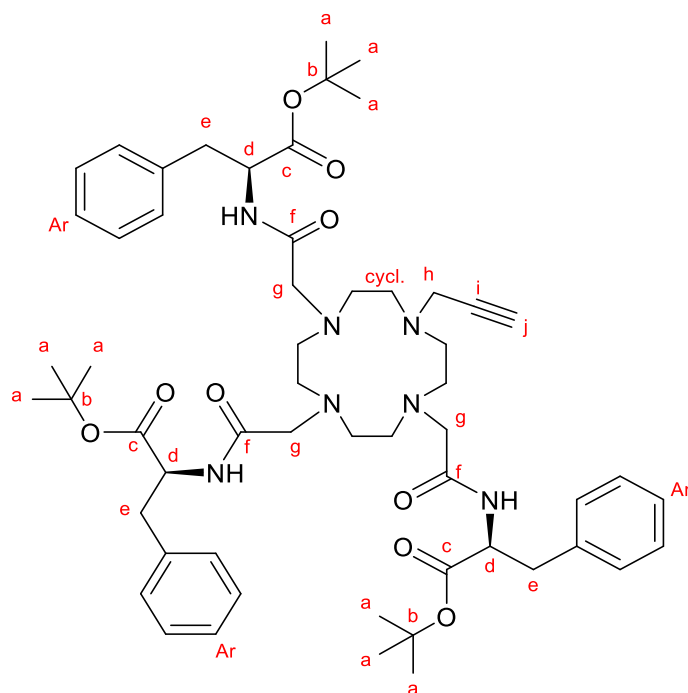
**Methyl (2-chloroacetyl)-L-phenylalaninate 3.4a1**<sup>19,20</sup>

Methyl L-phenylalaninate (1.05 g, 5.85 mmol, 1.0 eq) and caesium carbonate (5.54 g, 17.0 mmol, 2.9 eq) was added to EtOAc (100 mL) and stirred for 20 minutes at 0 °C. Chloroacetyl chloride (0.58 mL, 7.27 mmol, 1.3 eq) was added dropwise and the solution left to stir for 3 hours at RT. The solution was then washed with distilled water (3×150 mL) and a saturated NaHCO<sub>3</sub> solution (3×150 mL), the organic layer was collected and dried using anhydrous MgSO<sub>4</sub>. The hydrated MgSO<sub>4</sub> was then filtered off with filter paper, before the solvent was then removed under reduced pressure. The crude product was then purified by silica column chromatography (DCM:MeOH (volume ratio, 100:0 to 95:5 in 1% increments)) to give the product as a white solid (0.62 g, 44%).

<sup>1</sup>H NMR (400 MHz, 298 K, MeOD) δ<sub>H</sub> (ppm) = 7.35-7.17 (m, 5H, H<sup>Ar</sup>), 4.72 (dd, <sup>3</sup>J<sub>HH</sub> = 8.5, 5.6 Hz, 1H, H<sup>b</sup>), 4.17 (s, 2H, H<sup>c</sup>), 3.72 (s, 3H<sup>d</sup>), 3.20 (dd, <sup>3</sup>J<sub>HH</sub> = 13.8, 5.6 Hz, 1H, H<sup>a</sup>), 3.04 (dd, <sup>3</sup>J<sub>HH</sub> = 13.9, 8.5 Hz, 1H, H<sup>a</sup>). LRMS found *m/z* 256 ([M+H]<sup>+</sup>, 52%), 278 ([M+Na]<sup>+</sup>, 100%).

Spectroscopic data matches reported literature values.<sup>20</sup>

**tri-tert-butyl 2,2',2''-((2,2',2''-(10-(prop-2-yn-1-yl)-1,4,7,10-tetraazacyclododecane-1,4,7-triyl)tris(acetyl))tris(azanediy))tris(3-phenylpropanoate) 3.5d**<sup>18</sup>

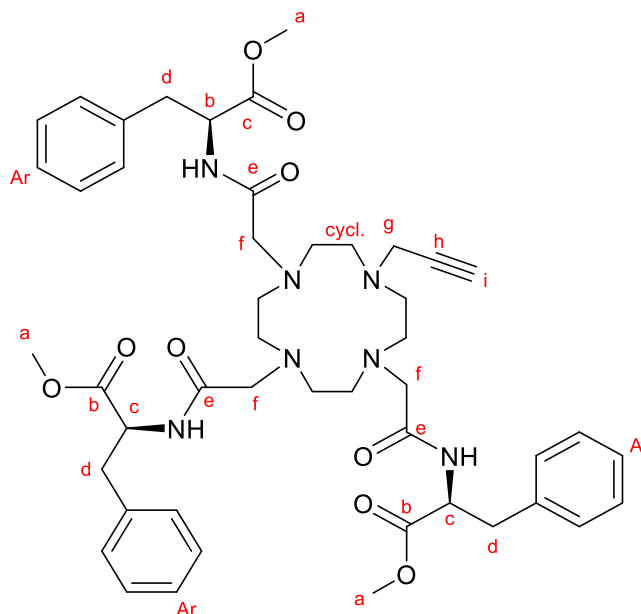


Compound-**2.3** (0.192 g, 0.50 mmol, 1.0 eq) was dissolved in MeCN (5.0 mL), to this solution HATU (1.14 g, 3.00 mmol, 6.0 eq), HOBT (0.405 g, 3.00 mmol, 6.0 eq) and DIPEA (1.31 mL, 7.50 mmol, 15.0 eq) was added and the mixture left to stir at RT for 30 minutes or until the solution turned golden brown. To this stirring solution, L-Phenylalanine tert-butyl ester hydrochloride (0.773 g, 3.00 mmol, 6.0 eq) in MeCN (5.0 mL) was added. The solution was then heated to 50 °C and left to stir overnight. The solvent was then removed under reduced pressure. The resulting residue was then redissolved in DCM (15 mL), this solution was then washed with MilliQ water (3×10 mL) and aqueous NaOH (0.1 M) solution (3×10 mL). The organic layer was retained and dried using anhydrous MgSO<sub>4</sub>, before the insoluble salts were removed by filtration through filter paper. The solvent was then removed under reduced pressure to yield an oily residue. This was then purified by silica column chromatography (DCM:MeOH:NH<sub>4</sub>OH (60:40:0 to 60:30:10 in 2% increments)). The resulting residue was then further purified by

alumina column chromatography (MeCN:H<sub>2</sub>O (100:0 to 90:10 in 2% increments)) to yield the product as a yellow oil (0.323 g, 65%).

<sup>1</sup>H NMR (400 MHz, 298 K, CD<sub>3</sub>CN) δ<sub>H</sub> (ppm) = 7.39 – 7.18 (m, 15H, H<sup>Ar</sup>), 4.78 – 4.43 (m, 3H, H<sup>d</sup>), 3.30 – 2.70 (m, 19H, H<sup>cycl.,h,j</sup>), 2.26 (s, 6H, H<sup>g</sup>), 2.13 (d, 6H, H<sup>e</sup>), 1.50 (s, 27H, H<sup>a</sup>). <sup>13</sup>C NMR (101 MHz, CD<sub>3</sub>CN) δ<sub>C</sub> = 173.4 (C<sup>c</sup>), 172.2 (C<sup>f</sup>), 138.3 (ArC<sup>quarternary</sup>), 130.5 (ArC), 129.4 (ArC), 127.8 (ArC), 82.7 (C<sup>b</sup>), 79.2 (C<sup>i</sup>), 74.9 (C<sup>j</sup>), 57.7 (C<sup>g</sup>), 55.5 (C<sup>d</sup>), 54.8 (C<sup>cycl.</sup>), 51.7 (C<sup>h</sup>), 38.6 (C<sup>e</sup>), 28.2 (C<sup>a</sup>). LRMS found *m/z* 498 ([M+2H]<sup>+</sup>, 11%), 994 ([M+H]<sup>+</sup>, 100%), 1016 ([M+Na]<sup>+</sup>, 67%). HRMS *m/z* (ESI<sup>+</sup>) found 994.6004, C<sub>56</sub>H<sub>80</sub>N<sub>7</sub>O<sub>9</sub> requires [M+H]<sup>+</sup> 994.6012.

**trimethyl 2,2',2''-((2,2',2''-(10-(prop-2-yn-1-yl)-1,4,7,10-tetraazacyclododecane-1,4,7-triyl)tris(acetyl))tris(azanediy))tris(3-phenylpropanoate) 3.5e<sup>18</sup>**

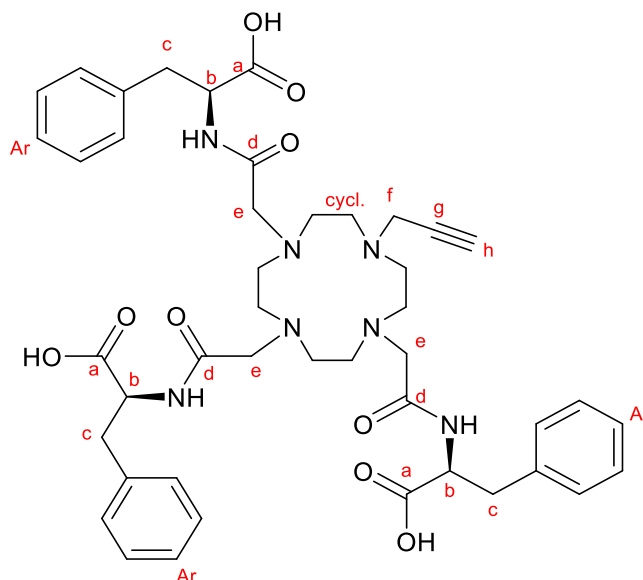


Compound-**2.3** (0.197 g, 0.51 mmol, 1.0 eq) was dissolved in MeCN (5.0 mL), to this solution HATU (1.17 g, 3.08 mmol, 6.0 eq), HOBt (0.412 g, 3.05 mmol, 6.0 eq) and DIPEA (1.31 mL, 7.50 mmol, 6.0 eq) was added and the mixture left to stir at RT for 30 minutes or until the solution turned golden brown. To this stirring solution, L-Phenylalanine tert-butyl ester hydrochloride (0.647 g, 3.00 mmol, 6.0 eq) in MeCN (5.0 mL) was added. The solution was then heated to 50 °C and left to stir overnight. The solvent was then removed under reduced pressure. The resulting residue was then redissolved in DCM (15 mL), this solution was then washed with MilliQ water (3×10 mL) and aqueous NaOH (0.1 M) solution (3×10 mL). The organic layer was retained and dried using anhydrous MgSO<sub>4</sub>, before the insoluble salts were removed by filtration through filter paper. The solvent was then removed under reduced pressure to yield an oily residue. This was purified by silica column chromatography (DCM:MeOH:NH<sub>4</sub>OH (60:40:0 to

60:30:10 in 2% increments)). The resulting residue was then further purified by alumina column chromatography (MeCN:H<sub>2</sub>O (100:0 to 90:10 in 2% increments)) to yield the product as a yellow oil (0.237 g, 54%).

<sup>1</sup>H NMR (600 MHz, 298 K, MeOD)  $\delta_{\text{H}}$  (ppm) = 7.45 – 7.21 (m, 15H, H<sup>Ar</sup>), 4.67 (t, 3H, H<sup>c</sup>), 3.84 (s, 9H, H<sup>a</sup>), 3.40 (s, 2H, H<sup>g</sup>), 3.12 (s, 1H, H<sup>i</sup>), 2.87 (m, 28H, H<sup>cycl.,d,f</sup>). <sup>13</sup>C NMR (151 MHz, MeOD)  $\delta_{\text{C}}$  (ppm) = 173.3 (C<sup>c</sup>), 172.7 (C<sup>e</sup>), 138.3 (ArC<sup>quaternary</sup>), 130.4 (ArC), 130.3 (ArC), 128.1 (ArC), 77.8 (C<sup>h</sup>), 76.4 (C<sup>i</sup>) 60.1 (C<sup>f</sup>), 55.9 (C<sup>c</sup>), 53.4 (C<sup>a</sup>), 53.0 (C<sup>cycl.</sup>), 43.8 (C<sup>g</sup>), 38.9 (C<sup>d</sup>). LRMS found  $m/z$  435 ([M+2H]<sup>2+</sup>, 1%), 868 ([M+H]<sup>+</sup>, 100%), 907 ([M+K]<sup>+</sup>, 3%),%. HRMS  $m/z$  (ESI<sup>+</sup>) found 868.4600, C<sub>47</sub>H<sub>62</sub>N<sub>7</sub>O<sub>9</sub> requires [M+H]<sup>+</sup> 868.4604.

**2,2',2''-((2,2',2''-(10-(prop-2-yn-1-yl)-1,4,7,10-tetraazacyclododecane-1,4,7-triyl)tris(acetyl)tris(azanediy))tris(3-phenylpropanoic acid) 3.6d**

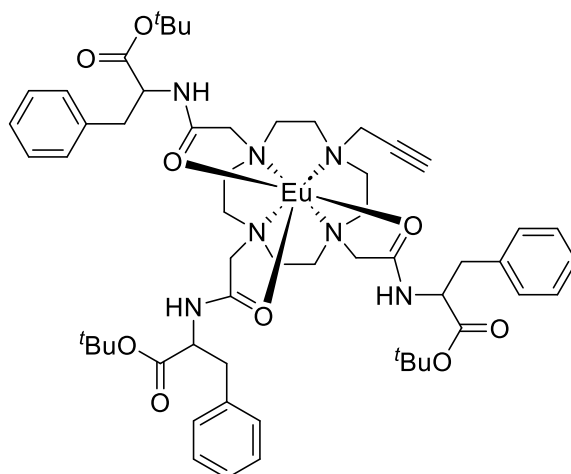


Compound-**3.5d** (0.320 g, 0.322 mmol, 1.0 eq) was dissolved in dichloromethane (5.0 mL) and left to stir for 20 minutes. TFA (5.0 ml, 29.6 mmol, 92.0 eq) was added dropwise and the solution left to stir at RT for 18 hours. The solution was concentrated *in vacuo* to leave an orange residue. The residue was then dissolved and co-evaporated with MeOH (3×10 mL). The resulting residue was then dissolved in the minimum amount of MeOH (5.0 mL) and precipitated with diethyl ether (50 mL), the suspension was centrifuged and the solid retained, this process was repeated 3 times to give an off-white solid (171 mg, 64%).

$^1\text{H}$  NMR (600 MHz, 298 K, MeOD)  $\delta_{\text{H}}$  (ppm) = 7.50 – 7.02 (m, 15H,  $\text{H}^{\text{Ar}}$ ), 4.69 (dd, 3H,  $\text{H}^{\text{b}}$ ), 3.61 (s, 2H,  $\text{H}^{\text{f}}$ ), 3.49 (s, 6H,  $\text{H}^{\text{e}}$ ), 3.28 (d, 1H,  $\text{H}^{\text{h}}$ ), 3.26 – 3.12 (m, 6H,  $\text{H}^{\text{c}}$ ), 2.66 (m, 16H,  $\text{H}^{\text{cycl}}$ ).  $^{13}\text{C}$  NMR (151 MHz, MeOD)  $\delta_{\text{C}}$  = 175.6 ( $\text{C}^{\text{a}}$ ), 173.7 ( $\text{C}^{\text{d}}$ ), 137.6 ( $\text{ArC}^{\text{quaternary}}$ ), 129.2 ( $\text{ArC}$ ), 128.9 ( $\text{ArC}$ ), 126.4 ( $\text{ArC}$ ), 65.5 ( $\text{C}^{\text{g}}$ ), 56.8

(C<sup>h</sup>), 56.0 (C<sup>e</sup>) 54.1 (C<sup>cycl</sup>), 44.1 (C<sup>f</sup>), 36.9 (C<sup>e</sup>). HRMS m/z (ESI<sup>+</sup>) found 826.4130,  
C<sub>44</sub>H<sub>56</sub>N<sub>7</sub>O<sub>9</sub> requires [M+H]<sup>+</sup> 826.4134.

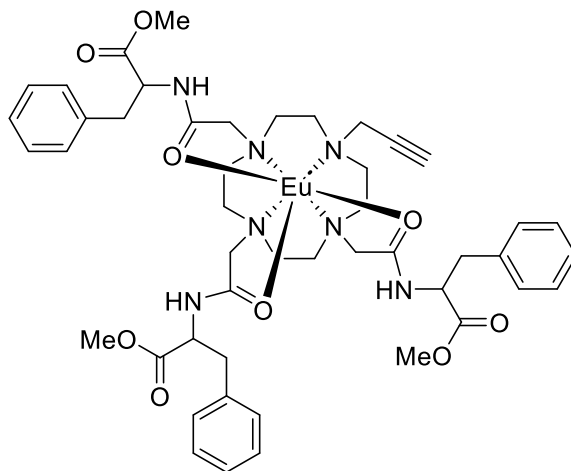
### Synthesis of Eu.p.DO3AM.Phen.O<sup>t</sup>Bu complex EuL<sup>3.5d</sup>



Compound-**3.5d** (99 mg, 0.107 mmol, 1.0 eq) and europium triflate (70 mg, 0.117 mmol, 1.1 eq) was dissolved in EtOH/H<sub>2</sub>O (1:1, 1.07 mL) and stirred for 24 hours at 60 °C. The pH of the solution was then adjusted to 4 by addition of aqueous NaOH (1 M), the solution was then left to stir for 48 hours at 60 °C. To yield the product as a white solid (54.6 mg, 45%).

<sup>1</sup>H NMR (500 MHz, 298 K, MeOD)  $\delta_{\text{H}}$  = 25.0, 21.7, 20.1, 18.6, 17.8, 16.8, 15.6, 12.5, -0.2, -0.5, -1.1, -3.2, -3.5, -3.9, -4.6, -6.0, -6.9, -8.8, -10.1, -10.6, -11.6, -12.3, -12.6, -13.5, -14.3, -14.7, -16.6, -16.9, -17.3, -18.3, -21.1, -22.1, -23.1. Only resolved peaks outside the 0-10 ppm range are reported. HRMS m/z (MALDI) found 1145.348, C<sub>56</sub>H<sub>80</sub>N<sub>7</sub>O<sub>9</sub>Eu requires [M+H]<sup>+</sup> 1145.515. Luminescence lifetimes ( $\lambda_{\text{ex}}$  = 393 nm,  $\lambda_{\text{em}}$  = 616 nm): MeOH: 0.45 ms, MeOD: 2.64 ms,  $q$  = 3.6.

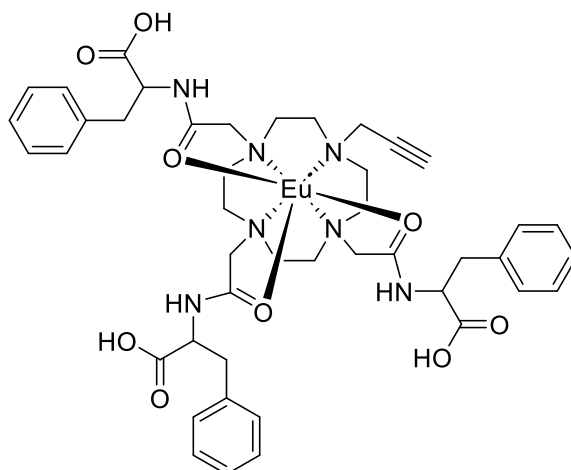
### Synthesis of Eu.p.DO3AM.Phen.OMe complex EuL<sup>3.5e</sup>



Compound-**3.5e** (100 mg, 0.115 mmol, 1.0 eq) and europium triflate (76 mg, 0.127 mmol, 1.1 eq) was dissolved in MeOH (1.15 mL) and stirred for 72 hours at 60 °C. The remaining residue was then redissolved in the minimum amount of MeOH (5.0 mL) before being precipitated with diethyl ether (0°C) (50 mL). To yield the product as a glassy light brown residue (67 mg, 57%).

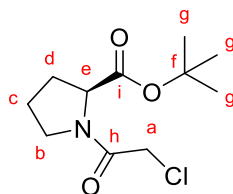
<sup>1</sup>H NMR (500 MHz, 298 K, MeOD)  $\delta_{\text{H}} = -0.2, -0.7, -1.2, -2.9, -3.8, -5.9, -6.7, -6.9, -7.2, -10.6, -10.9, -11.6, -12.1, -12.4, -13.7, -14.3, -16.8, -17.3$ . Only resolved peaks outside the 0-10 ppm range are reported. Luminescence lifetimes ( $\lambda_{\text{ex}} = 393$  nm,  $\lambda_{\text{em}} = 616$  nm): MeOH: 0.73 ms, MeOD: 1.52 ms,  $q = 0.9$ . H<sub>2</sub>O: 0.69 ms, D<sub>2</sub>O: 0.93,  $q = -0.1$ .

### Synthesis of Eu.p.DO3AM.Phen.OH complex EuL<sup>3.6d</sup>



Compound-**3.6d** (100 mg, 0.120 mmol, 1.0 eq) and europium triflate (83 mg, 0.139 mmol, 1.16 eq) was dissolved in a EtOH/H<sub>2</sub>O (1:1, 1.4 mL) and stirred for 24 hours at 60 °C. The pH of the solution was then adjusted to 4 by addition of aqueous 1 M NaOH, the solution was then left to stir for 48 hours at 60 °C. The solvent was then removed *in vacuo*. The remaining residue was then redissolved in the minimum amount of MeOH (5.0 mL) before being precipitated with diethyl ether (0°C) (50 mL) to give the product as an off-white residue (64 mg, 53%).

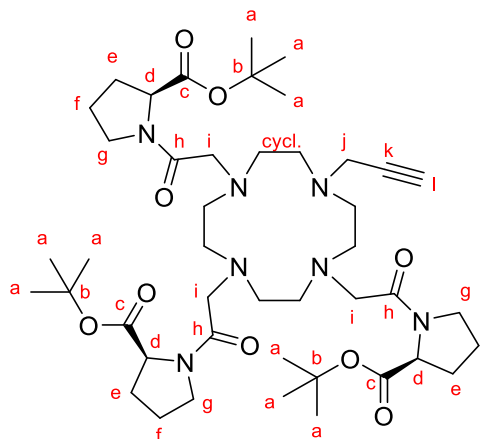
<sup>1</sup>H NMR (500 MHz, 298 K, MeOD)  $\delta_{\text{H}}$  = 8.6, 8.2, 7.9, 7.7, 7.4, 7.2, 6.9, 6.8, 6.5, 6.2, 4.9, 3.3, 2.8, 2.3, 2.2, 2.1, 1.8, 1.7, 1.3, 0.9, 0.6, 0.1, -0.5, -1.2, -1.8, -2.0, -2.9, -3.1, -3.9, -4.7, -5.9, -6.9, -7.2, -8.0, -10.6, -11.5, -12.1, -12.5, -13.7, -14.2, -16.8, -17.3. Luminescence lifetimes: MeOH: 0.71 ms, MeOD: 1.91 ms,  $q = 1.3$ .

**methyl (2-chloroacetyl)-L-prolinate 3.4c**<sup>21</sup>

Methyl L-prolinate (1.02 g, 7.92 mmol, 1.0 eq) was dissolved in DCM (150 mL) and caesium carbonate (7.56 g, 23.2 mmol, 2.9 eq) was added to this solution, this suspension was then left to stir for 20 minutes and cooled to 0 °C in an ice bath. Chloroacetyl chloride (0.80 mL, 10.1 mmol, 1.28 eq) was added dropwise over 1 hour and the solution left to stir at RT for 3 hours. The solution was then washed with distilled water (3×150 mL) and saturated NaHCO<sub>3</sub> solution (3×100 mL); the organic layer was then collected and anhydrous MgSO<sub>4</sub> was added, the hydrated MgSO<sub>4</sub> was then filtered off through filter paper and the solvent removed under reduced pressure to yield the product. The crude product was then purified by silica column chromatography (DCM:MeOH (volume ratio, 100:0 to 95:5 in increments of 1% MeOH)). Giving the product as a pale-yellow solid. (0.699 g, 68%).

<sup>1</sup>H NMR (400 MHz, 298 K, CDCl<sub>3</sub>) δ<sub>H</sub> (ppm) = 4.31 (dd, 1H, H<sup>e</sup>), 4.00 (s, 2H, H<sup>a</sup>), 3.65 – 3.50 (m, 2H, H<sup>b</sup>), 2.26 – 2.01 (m, 2H, H<sup>d</sup>), 2.01 – 1.81 (m, 2H, H<sup>c</sup>), 1.39 (s, 9H, H<sup>g</sup>). <sup>13</sup>C NMR (101 MHz, CDCl<sub>3</sub>) δ<sub>C</sub> (ppm) = 170.8 (C<sup>i</sup>), 164.8 (C<sup>h</sup>), 81.4 (C<sup>f</sup>), 60.1 (C<sup>e</sup>), 60.0 (C<sup>a</sup>), 47.1 (C<sup>b</sup>), 31.3 (C<sup>d</sup>), 27.9 (C<sup>g</sup>), 24.73 (C<sup>c</sup>). LRMS found *m/z* 206 ([M+H]<sup>+</sup>, 100%), 228 ([M+Na]<sup>+</sup>, 15%).

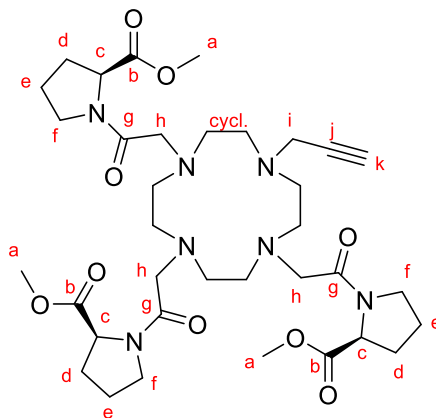
**tri-tert-butyl (2,2',2''-(10-(prop-2-yn-1-yl)-1,4,7,10-tetraazacyclododecane-1,4,7-triyl)tris(acetyl))(2'S,2''S)-tri-L-prolinate 3.5f<sup>18</sup>**



Compound-**2.3** (0.385 g, 1.00 mmol, 1.0 eq) was dissolved in MeCN (5.0 mL), to this solution HATU (2.28 g, 6.00 mmol, 6.0 eq), HOBt (0.811 g, 6.00 mmol, 6.0 eq) and DIPEA (2.61 mL, 10.0 mmol, 10.0 eq) was added and the mixture left to stir at RT for 30 minutes or until the solution turned golden brown. To this stirring solution, L-Proline tert-butyl ester hydrochloride (1.25 g, 6.00 mmol, 6.00eq) in MeCN (5.0 mL) was added. The solution was then heated to 50 °C and left to stir overnight. The solvent was then removed under reduced pressure. The resulting residue was then redissolved in DCM (15 mL), this solution was then washed with MilliQ water (3×10 mL) and aqueous NaOH (0.1 M) solution (3×10 mL). The organic layer was retained and dried using anhydrous MgSO<sub>4</sub>, before the insoluble salts were removed by filtration through filter paper. The solvent was then removed under reduced pressure to yield an oily residue. This was then purified by silica column chromatography (DCM:MeOH:NH<sub>4</sub>OH (60:40:0 to 60:30:10 in 2% increments)). The resulting residue was then further purified by alumina column chromatography (MeCN:H<sub>2</sub>O (100:0 to 90:10 in 2% increments)) to yield the product as a yellow oil (0.740 g, 88%).

$^1\text{H}$  NMR (600 MHz, 298 K, MeOD)  $\delta_{\text{H}} = 4.75$  (s, 2H, H<sup>j</sup>), 4.32 (m, 3H, H<sup>d</sup>), 3.51 (m, 6H, H<sup>g</sup>), 3.19 (s, 1H, H<sup>l</sup>), 2.86 (s, 6H, H<sup>i</sup>), 2.16 – 1.93 (m, 28H, H<sup>cycl.,e,f</sup>), 1.48 (s, 27H, H<sup>a</sup>).  $^{13}\text{C}$  NMR (151 MHz, MeOD)  $\delta_{\text{C}}$  (ppm) = 173.0 (C<sup>c</sup>), 172.0 (C<sup>h</sup>), 82.9 (C<sup>b</sup>), 79.4 (C<sup>k</sup>), 74.0 (C<sup>l</sup>), 62.6 (C<sup>d</sup>), 57.4 (C<sup>i</sup>), 56.2 (C<sup>cycl.</sup>), 51.6 (C<sup>g</sup>), 48.0 (C<sup>j</sup>), 32.3 (C<sup>e</sup>), 30.8 (C<sup>a</sup>), 26.0 (C<sup>f</sup>). LRMS found  $m/z$  435 ( $[\text{M}+2\text{H}]^+$ , 97%), 844 ( $[\text{M}+\text{H}]^+$ , 100%), 866 ( $[\text{M}+\text{Na}]^+$ , 31%). HRMS  $m/z$  (ESI<sup>+</sup>) found 844.5520,  $\text{C}_{44}\text{H}_{74}\text{N}_7\text{O}_9$  requires  $[\text{M}+\text{H}]^+$  844.5543.

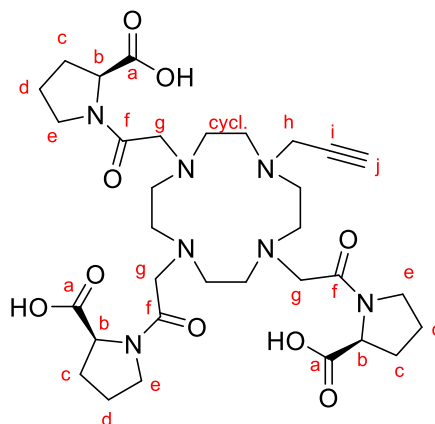
**trimethyl (2,2',2''-(10-(prop-2-yn-1-yl)-1,4,7,10-tetraazacyclododecane-1,4,7-triyl)tris(acetyl))(2'S,2''S)-tri-L-prolinate 3.5g<sup>18</sup>**



Compound-2.3 (0.192 g, 0.50 mmol, 1.0 eq) was dissolved in MeCN (5.0 mL), to this solution HATU (1.14 g, 3.00 mmol, 6.0 eq), HOBT (0.405 g, 3.00 mmol, 6.0 eq) and DIPEA (1.31 mL, 7.50 mmol, 15.0 eq) was added and the mixture left to stir at RT for 30 minutes or until the solution turned golden brown. To this stirring solution, L-Proline methyl ester hydrochloride (0.497 g, 3.00 mmol, 6.0 eq) in MeCN (5.0 mL) was added. The solution was then heated to 50 °C and left to stir overnight. The solvent was then removed under reduced pressure. The resulting residue was then redissolved in DCM (15 mL), this solution was then washed with MilliQ water (3×10 mL) and aqueous NaOH (0.1 M) solution (3×10 mL). The organic layer was retained and dried using anhydrous MgSO<sub>4</sub>, before the insoluble salts were removed by filtration through filter paper. The solvent was then removed under reduced pressure to yield an oily residue. This was then purified by silica column chromatography (DCM:MeOH:NH<sub>4</sub>OH (60:40:0 to 60:30:10 in 2% increments)). The resulting residue was then further purified by alumina column chromatography (MeCN:H<sub>2</sub>O (100:0 to 90:10 in 2% increments)) to yield the product as a yellow oil (0.401 g, 95%).

$^1\text{H}$  NMR (600 MHz, 298 K, MeOD)  $\delta_{\text{H}}$  (ppm) = 4.70 – 4.36 (m, 3H, H<sup>e</sup>), 3.84 (d, 2H, H<sup>i</sup>), 3.79 – 3.68 (s, 9H, H<sup>a</sup>), 3.67 – 3.46 (s, 6H, H<sup>h</sup>), 3.28 (dd, 1H, H<sup>k</sup>), 3.19 – 2.94 (m, 6H, H<sup>f</sup>), 2.88 (s, 16H, H<sup>cycl.</sup>), 2.06 (m, 12H, H<sup>d,e</sup>).  $^{13}\text{C}$  NMR (151 MHz, MeOD)  $\delta_{\text{C}}$  = 174.7 (C<sup>e</sup>), 172.0 (C<sup>g</sup>), 79.7 (C<sup>j</sup>), 74.5 (C<sup>k</sup>), 61.7 (C<sup>c</sup>), 57.7 (C<sup>h</sup>), 55.8 (C<sup>cycl.</sup>), 53.4 (C<sup>a</sup>), 52.6 (C<sup>f</sup>), 47.7 (C<sup>i</sup>), 29.9 (C<sup>d</sup>), 25.9 (C<sup>e</sup>). LRMS found  $m/z$  718 ([M+H]<sup>+</sup>, 100%), 740 ([M+Na]<sup>+</sup>, 56%), 360 ([M+2H]<sup>+</sup>, 37%). HRMS  $m/z$  (ESI<sup>+</sup>) found 718.4139, C<sub>35</sub>H<sub>56</sub>N<sub>7</sub>O<sub>9</sub> requires [M+H]<sup>+</sup> 718.4134.

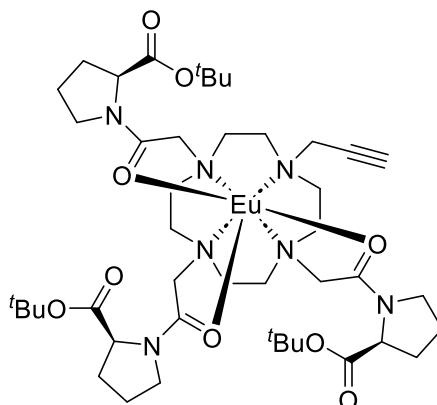
**(2'S,2''S)-(2,2',2''-(10-(prop-2-yn-1-yl)-1,4,7,10-tetraazacyclododecane-1,4,7-triyl)tris(acetyl))tri-L-proline 3.6f**



Compound-**3.5f** (0.390 g, 0.462 mmol, 1.0 eq) was dissolved in dichloromethane (5.0 mL) and left to stir for 20 minutes. TFA (5.0 mL, 29.6 mmol, 92.0 eq) was added dropwise and the solution left to stir at RT for 18 hours. The solution was concentrated *in vacuo* to leave an orange residue. The residue was then dissolved and co-evaporated with MeOH (3×10 mL). The resulting residue was then dissolved in the minimum amount of MeOH (5.0 mL) and precipitated with diethyl ether (50 mL), this process was repeated 3 times to give an off-white solid (0.244 g, 78%).

$^1\text{H}$  NMR (600 MHz, 298 K, MeOD)  $\delta_{\text{H}}$  (ppm) = 4.20 – 4.00 (m, 3H,  $\text{H}^{\text{b}}$ ), 3.64 – 3.43 (m, 12H,  $\text{H}^{\text{e,g}}$ ), 3.41 (d, 2H,  $\text{H}^{\text{h}}$ ), 3.23 (s, 1H,  $\text{H}^{\text{j}}$ ), 3.08 (s, 6H,  $\text{H}^{\text{c}}$ ), 2.31 (m, 6H,  $\text{H}^{\text{d}}$ ), 2.03 (s, 16H,  $\text{H}^{\text{cycl.}}$ ).  $^{13}\text{C}$  NMR (151 MHz, MeOD)  $\delta_{\text{C}}$  (ppm) = 174.5 ( $\text{C}^{\text{a}}$ ), 161.4 ( $\text{C}^{\text{f}}$ ), 65.5 ( $\text{C}^{\text{i}}$ ), 63.0 ( $\text{C}^{\text{j}}$ ), 59.5 ( $\text{C}^{\text{b}}$ ), 59.3 ( $\text{C}^{\text{g}}$ ), 48.5 ( $\text{C}^{\text{cycl.}}$ ), 46.6 ( $\text{C}^{\text{e}}$ ), 45.8 ( $\text{C}^{\text{h}}$ ), 28.8 ( $\text{C}^{\text{c}}$ ), 24.5 ( $\text{C}^{\text{d}}$ ). HRMS  $m/z$  (ESI $^{+}$ ) found 676.3664,  $\text{C}_{32}\text{H}_{50}\text{N}_7\text{O}_9$  requires  $[\text{M}+\text{H}]^{+}$  676.3665.

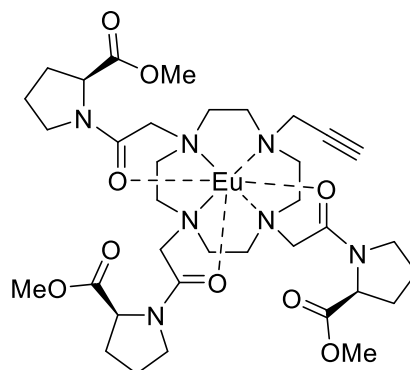
### Synthesis of Eu.p.DO3AM.Pro.O<sup>t</sup>Bu complex EuL<sup>3.5f</sup>



Compound-**3.5f** (100 mg, 0.118 mmol, 1.0 eq) and europium triflate (78.1 mg, 0.130 mmol, 1.1 eq) was dissolved in a EtOH/H<sub>2</sub>O (1:1, 1.18 mL) and stirred for 24 hours at 60 °C. The pH of the solution was then adjusted to 4 by addition of aqueous NaOH (1 M), the solution was then left to stir for 48 hours at 60 °C. The solvent was then removed in vacuo. The remaining residue was then redissolved in the minimum amount of MeOH (5.0 mL) before being precipitated by addition into diethyl ether (0°C) (50 mL). To yield the product as a white solid (52.3 mg, 45%).

<sup>1</sup>H NMR (500 MHz, 298 K, CD<sub>3</sub>CN) δ<sub>H</sub> (ppm) = 25.2, 24.2, 21.7, 19.7, -1.0, -2.2, -6.4, -7.9, -10.7, -11.3, -14.4, -15.3, -19.6, -21.3. Only resolved peaks outside the 0-10 ppm range are reported. Luminescence lifetimes (λ<sub>ex</sub> = 393 nm, λ<sub>em</sub> = 616 nm): MeOH: 0.55 ms, MeOD: 1.47 ms, *q* = 1.9.

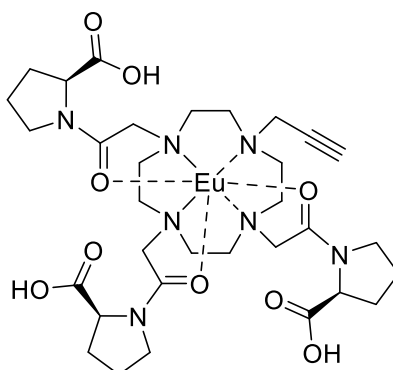
### Synthesis of Eu.p.DO3AM.Pro.OMe complex EuL<sup>3.5g</sup>



Compound-**3.5g** (100 mg, 0.139 mmol, 1.0 eq) and europium triflate (91.8 mg, 0.153 mmol, 1.1 eq) was dissolved in MeOH (1.39 mL) and stirred for 24 hours at 60 °C. The pH of the solution was then adjusted to 4 by addition of aqueous NaOH (1 M), the solution was then left to stir for 48 hours at 60 °C. The solvent was then removed *in vacuo*. The remaining residue was then redissolved in the minimum amount of MeOH (5.0 mL) before being precipitated with diethyl ether (0°C) (50 mL), to yield the product as a white solid (39 mg, 32%).

<sup>1</sup>H NMR (500 MHz, 298 K, D<sub>2</sub>O)  $\delta_{\text{H}}$  = 41.8, 34.9, 34.5, 32.3, 28.3, 26.3, 24.8, 23.7, 22.7, 21.4, 20.3, 19.1, 18.7, 16.9, 16.3, 15.2, 12.8, 12.4, 11.5, 11.1, 10.2, -0.3, -0.4, -0.9, -1.6, -2.3, -3.0, -3.3, -4.1, -5.0, -6.7, -7.4, -7.8, -8.3, -8.6, -10.2, -10.3, -10.5, -11.2, -12.9, -13.7, -14.0, -14.2, -14.4, -14.9, -15.6, -15.9, -16.2, -16.5, -17.5, -17.6, -18.2, -18.7, -20.0, -21.7, -22.8, -23.22, -32.9. Only resolved peaks outside the 0-10 ppm range are reported. Luminescence lifetimes ( $\lambda_{\text{ex}}$  = 393 nm,  $\lambda_{\text{em}}$  = 616 nm): MeOH: 0.67 ms, MeOD: 1.76 ms,  $q = 1.4$ . H<sub>2</sub>O: 0.49 ms, D<sub>2</sub>O: 1.37 ms,  $q = 1.0$ .

### Synthesis of Eu.p.DO3AM.Pro.OH complex EuL<sup>3.6f</sup>



Compound-**3.6f** (100 mg, 0.148 mmol, 1.0 eq) and europium triflate (97.5 mg, 0.163 mmol, 1.1 eq) was dissolved in a EtOH/H<sub>2</sub>O (1:1, 1.48 mL) and stirred for 24 hours at 60 °C. The pH of the solution was then adjusted to 4 by addition of aqueous NaOH (1 M), the solution was then left to stir for 48 hours at 60 °C. The solvent was then removed under reduced pressure. The remaining residue was then redissolved in the minimum amount of MeOH (5.0 mL) before being precipitated with diethyl ether (0°C) (50 mL), to yield the product as an off white solid (33 mg, 27%).

<sup>1</sup>H NMR (400 MHz, D<sub>2</sub>O) δ -1.3, -1.9, -8.6, -10.9, -11.2, -17.6, -18.2, -18.9, -20.1. Only resolved peaks outside the 0-10 ppm range are reported. Luminescence lifetimes ( $\lambda_{\text{ex}} = 393 \text{ nm}$ ,  $\lambda_{\text{em}} = 616 \text{ nm}$ ): MeOH: 0.41 ms, MeOD: 3.26 ms,  $q = 1.0$ . H<sub>2</sub>O: 0.33 ms, D<sub>2</sub>O: 2.68 ms,  $q = 1.1$ .

## 7.7 References

- 1 J. Leonard, B. Lygo and G. Procter, *Advanced Practical Organic Chemistry*, CRC Press, 2013.
- 2 G. R. Fulmer, A. J. M. Miller, N. H. Sherden, H. E. Gottlieb, A. Nudelman, B. M. Stoltz, J. E. Bercaw and K. I. Goldberg, *Organometallics*, 2010, **29**, 2176–2179.
- 3 S. J. Moench, T.-M. Shi and J. D. Satterlee, *Eur. J. Biochem.*, 1991, **197**, 631–641.
- 4 O. A. Blackburn, A. M. Kenwright, P. D. Beer and S. Faulkner, *Dalton Trans.*, 2015, **44**, 19509–19517.
- 5 E. Furet, K. Costuas, P. Rabiller and O. Maury, *J. Am. Chem. Soc.*, 2008, **130**, 2180–2183.
- 6 P. Kuzmič, *Anal. Biochem.*, 1996, **237**, 260–273.
- 7 T. B. Gasa, J. M. Spruell, W. R. Dichtel, T. J. Sørensen, D. Philp, J. F. Stoddart and P. Kuzmič, *Chem. Eur. J.*, 2009, **15**, 106–116.
- 8 D. Szücs, T. Csupász, J. P. Szabó, A. Kis, B. Gyuricza, V. Arató, V. Forgács, A. Vágner, G. Nagy, I. Garai, D. Szikra, I. Tóth, G. Trencsényi, G. Tircsó and A. Fekete, *Pharmaceuticals*, 2022, **15**, 666.
- 9 N. Raghunand, G. P. Guntle, V. Gokhale, G. S. Nichol, E. A. Mash and B. Jagadish, *J. Med. Chem.*, 2010, **53**, 6747–6757.
- 10 A. K. R. Junker, M. Tropiano, S. Faulkner and T. J. Sørensen, *Inorg. Chem.*, 2016, **55**, 12299–12308.
- 11 C. Allain, P. D. Beer, S. Faulkner, M. W. Jones, A. M. Kenwright, N. L. Kilah, R. C. Knighton, T. J. Sørensen and M. Tropiano, *Chem. Sci.*, 2013, **4**, 489–493.
- 12 N. George, S. Ofori, S. Parkin and S. G. Awuah, *RSC Adv.*, 2020, **10**, 24017–24026.
- 13 M. Woods, G. E. Kiefer, S. Bott, A. Castillo-Muzquiz, C. Eshelbrenner, L. Michaudet, K. McMillan, S. D. K. Mudigunda, D. Ogrin, G. Tircsó, S. Zhang, P. Zhao and A. D. Sherry, *J. Am. Chem. Soc.*, 2004, **126**, 9248–9256.
- 14 K. Jobe, C. H. Brennan, M. Motevalli, S. M. Goldup and M. Watkinson, *Chem. Commun.*, 2011, **47**, 6036–6038.
- 15 J. K. Molloy, O. Kotova, R. D. Peacock and T. Gunnlaugsson, *Org. Biomol. Chem.*, 2012, **10**, 314–322.
- 16 J. I. Bruce, P. J. O’Connell, P. G. Taylor, D. P. T. Smith, R. C. Adkin and V. K. Pearson, *Molecules*, 2020, **25**.
- 17 Z. Zeng, M. J. Belousoff, L. Spiccia, A. M. Bond and A. A. J. Torriero, *ChemPlusChem*, 2018, **83**, 728–738.
- 18 L. M. De León-Rodríguez, S. Viswanathan and A. D. Sherry, *Contrast Media Mol. Imaging*, 2010, **5**, 121–125.

- 19 I. Bonilla-Landa, J. L. Viveros-Ceballos and M. Ordóñez, *Tetrahedron: Asymmetry*, 2014, **25**, 485–487.
- 20 S. Y. Han and Y.-D. Gong, *Synth. Commun.*, 2019, **49**, 3426–3434.
- 21 G. Pandey, P. Das and Y. R. P., *Eur. J. Org. Chem.*, 2000, **2000**, 657–664.

## Appendix

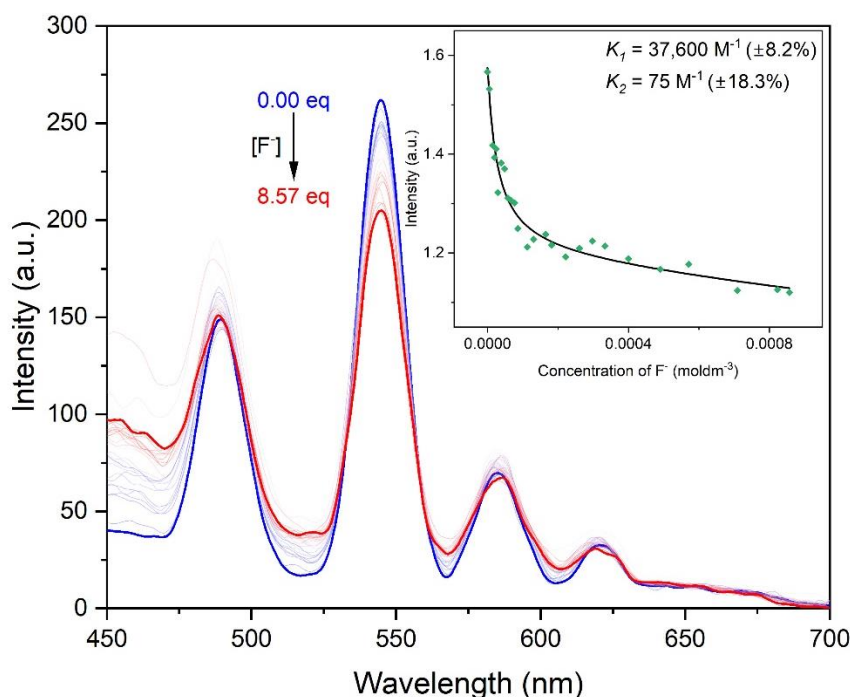


**Figure-A1.** Graph showing the change in luminescence spectrum of Tb.p.DO3A in 0.001 M Tris buffer, upon addition of increasing amounts of KF. With starting (blue) and end (red) concentrations highlighted,  $\lambda_{\text{ex}} = 226$  nm. *Inset:* binding isotherm from DynaFit®, plot of intensity ratio of the  $\Delta J=5/\Delta J=4$  (red-scatter=data points, line=binding isotherm) vs concentration of  $\text{F}^-$ .

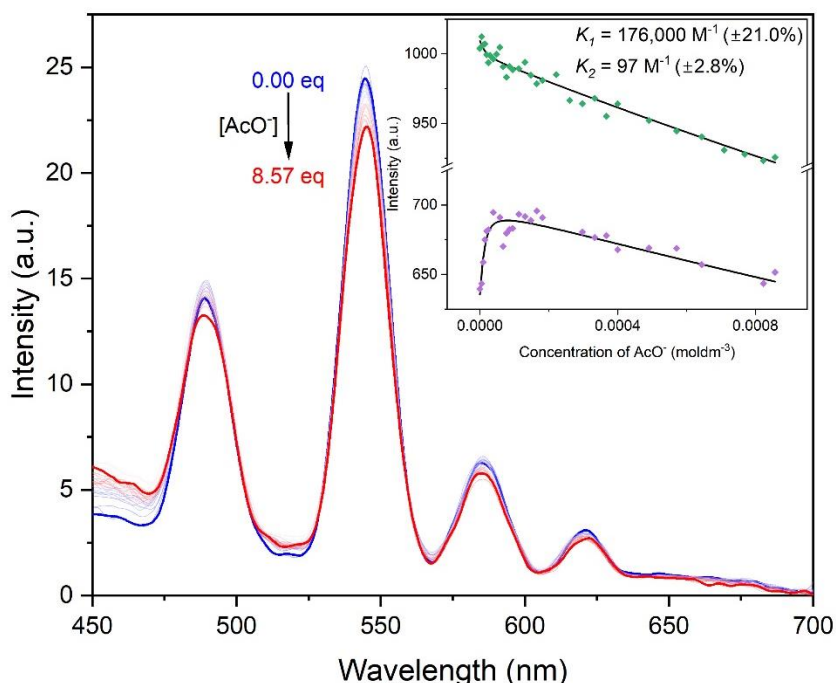


**Figure-A2.** Graph showing the change in luminescence spectrum of Tb.p.DO3A in 0.001 M Tris buffer, upon addition of increasing amounts of  $\text{AcO}^-$ . With starting (blue) and end (red) concentrations highlighted,  $\lambda_{\text{ex}} = 226$  nm. *Inset:* binding isotherm from DynaFit®, plot of the integrated intensity of  $\Delta J=6$  (red-scatter=data points, line=binding isotherm) and  $\Delta J=5$  (blue-scatter=data points, line=binding isotherm) vs concentration of  $\text{F}^-$ .

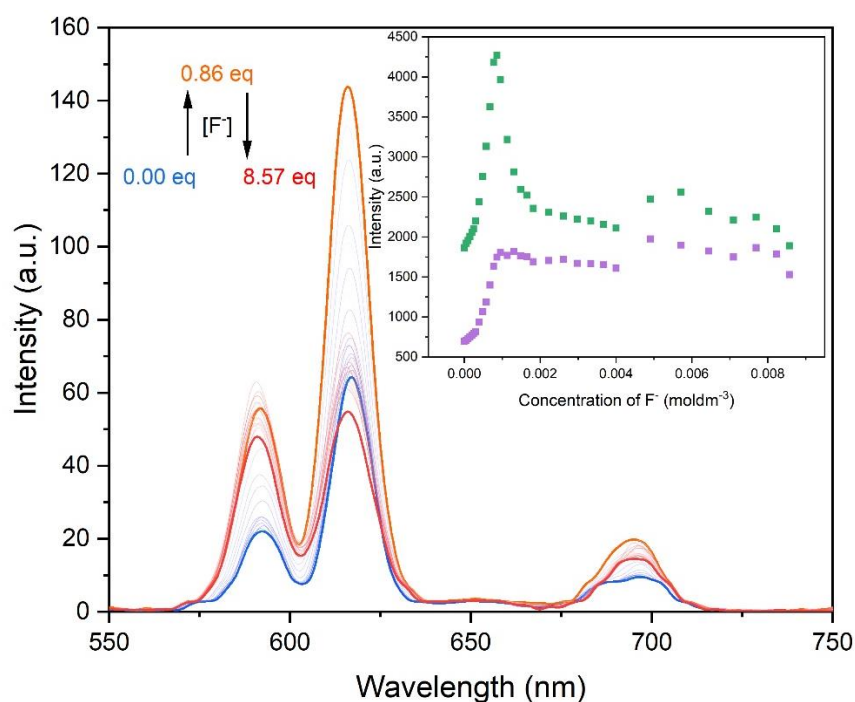


**Figure-A3.** Graph showing the change in luminescence spectrum of Eu.p.DO3AM.Phen.OMe ( $1 \times 10^{-3}$  mol dm $^{-3}$ ) in MeOH, upon addition of increasing amounts of TBAF ( $0.02$  mol dm $^{-3}$ ). With starting (blue), maximum intensity (orange) and end (red) concentrations highlighted,  $\lambda_{\text{ex}} = 393$  nm. *Inset:* plot of change in intensity of area  $\Delta J=2$  (dark green) and area  $\Delta J=1$  (purple) vs concentration of  $F^-$ .

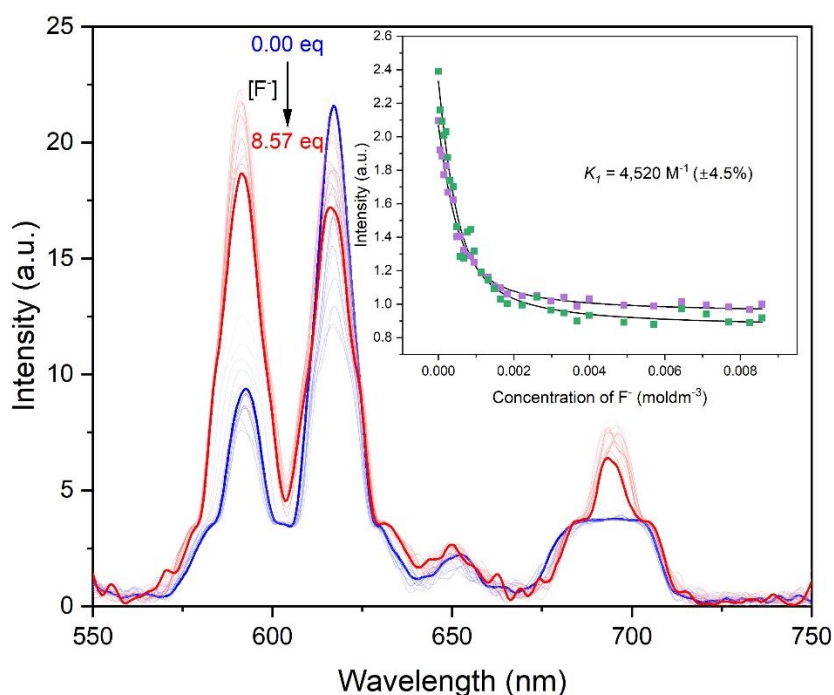


**Figure-A4.** Graph showing the change in luminescence spectrum of Eu.p.DO3AM.Phen.OMe ( $1 \times 10^{-3}$  mol dm $^{-3}$ ) in MilliQ water, upon addition of increasing amounts of TBAF ( $0.02$  mol dm $^{-3}$ ). With starting (blue) and end (red) concentrations highlighted,  $\lambda_{\text{ex}} = 393$  nm. *Inset:* binding isotherm from DynaFit®, plot of change in intensity ratio of  $617$  nm/ $591$  nm (dark green) and  $\Delta J=2/\Delta J=1$  (purple) vs concentration of  $F^-$ .

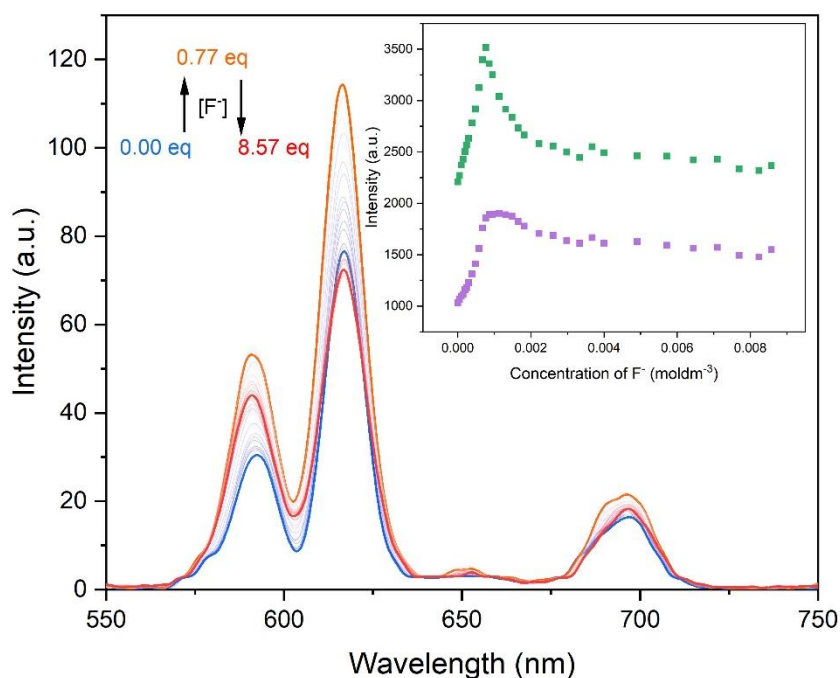


**Figure-A5.** Graph showing the change in luminescence spectrum of Eu.p.DO3AM.Pro.OMe ( $1 \times 10^{-3} \text{ mol dm}^{-3}$ ) in MeOH, upon addition of increasing amounts of TBAF ( $0.02 \text{ mol dm}^{-3}$ ). With starting (blue), maximum intensity (orange) and end (red) concentrations highlighted,  $\lambda_{\text{ex}} = 393 \text{ nm}$ . *Inset:* plot of change in intensity of area  $\Delta J=2$  (dark green) and area  $\Delta J=1$  (purple) vs concentration of  $\text{F}^-$ .

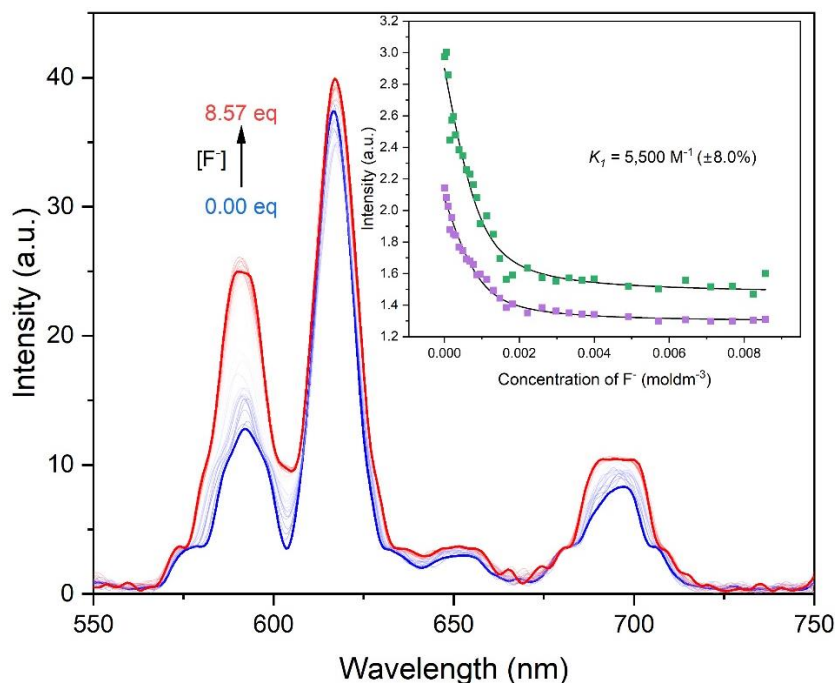


**Figure-A6.** Graph showing the change in luminescence spectrum of Eu.p.DO3AM.Pro.OMe ( $1 \times 10^{-3} \text{ mol dm}^{-3}$ ) in MilliQ water, upon addition of increasing amounts of TBAF ( $0.02 \text{ mol dm}^{-3}$ ). With starting (blue) and end (red) concentrations highlighted,  $\lambda_{\text{ex}} = 393 \text{ nm}$ . *Inset:* binding isotherm from DynaFit<sup>®</sup>, plot of intensity of  $617 \text{ nm}/591 \text{ nm}$  (dark green) and  $\Delta J=2/\Delta J=1$  (purple) vs concentration of  $\text{F}^-$ .

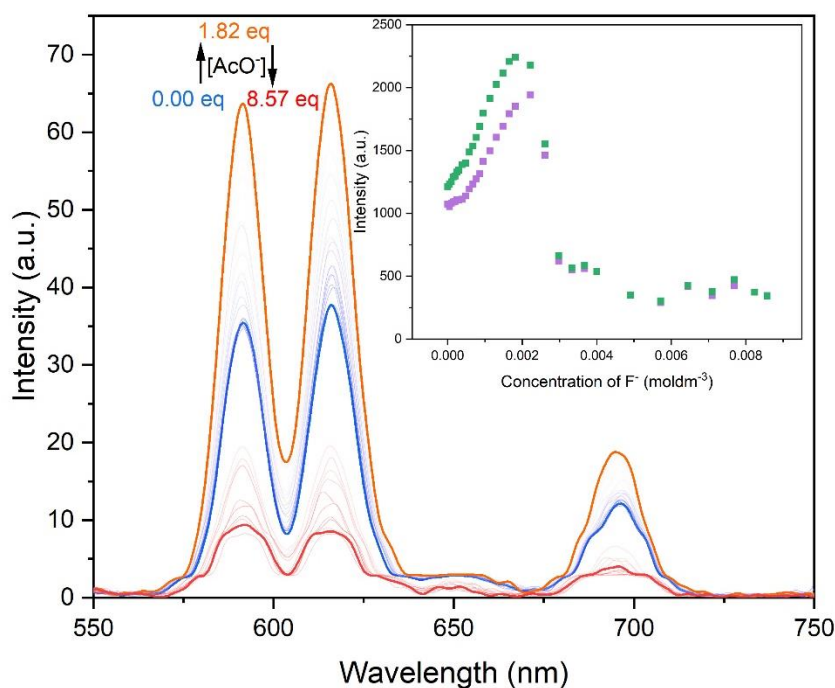


**Figure-A7.** Graph showing the change in luminescence spectrum of Eu.p.DO3AM.Pro.OH ( $1 \times 10^{-3}$  mol dm $^{-3}$ ) in MeOH, upon addition of increasing amounts of TBAF (0.02 mol dm $^{-3}$ ). With starting (blue), maximum intensity (orange) and end (red) concentrations highlighted,  $\lambda_{\text{ex}} = 393$  nm. Inset: plot of change in intensity of area  $\Delta J=2$  (dark green) and area  $\Delta J=1$  (purple) vs concentration of F $^{-}$ .

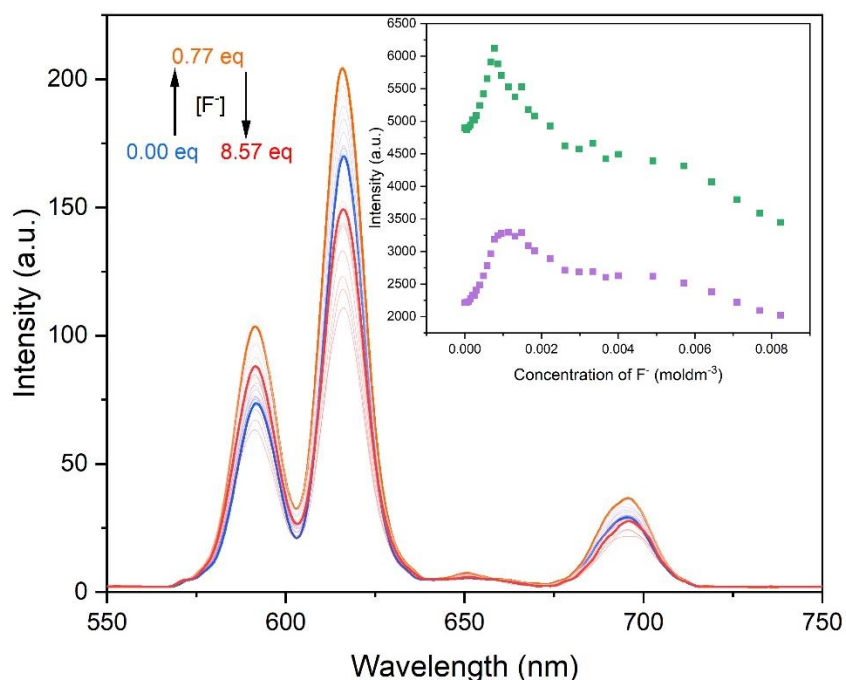


**Figure-A8.** Graph showing the change in luminescence spectrum of Eu.p.DO3AM.Lys.O'Bu.CBz in MilliQ water, upon addition of increasing amounts of KF. With starting (blue), maximum intensity (orange) and end (red) concentrations highlighted,  $\lambda_{\text{ex}} = 393$  nm. Inset: plot of change in intensity of area  $\Delta J=2$  (dark green) and area  $\Delta J=1$  (purple) vs concentration of F $^{-}$ .

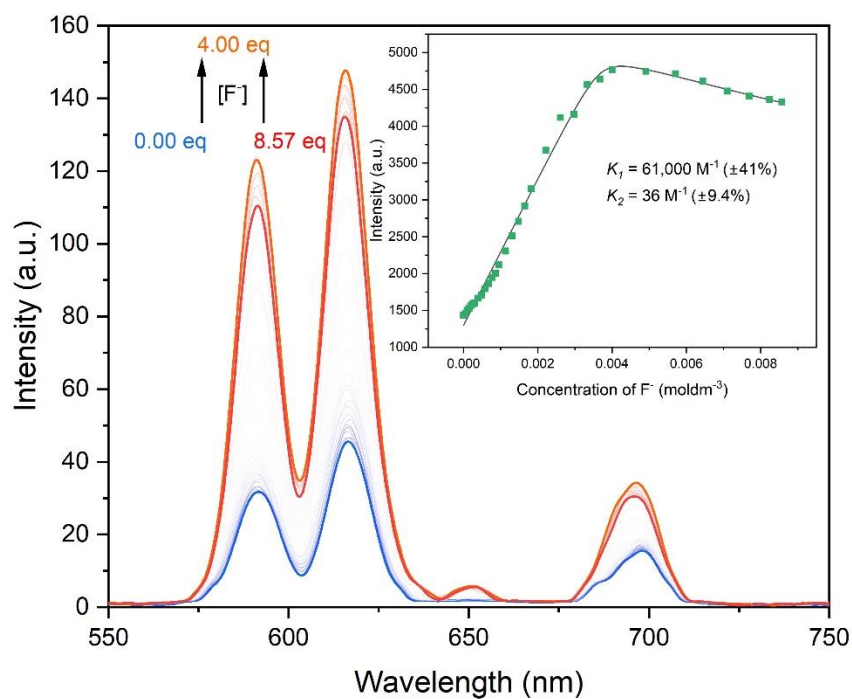


**Figure-A9.** Graph showing the change in luminescence spectrum of Eu.p.DO3AM.Lys.OMe in MeOH, upon addition of increasing amounts of TBAF. With starting (blue), maximum intensity (orange) and end (red) concentrations highlighted,  $\lambda_{\text{ex}} = 393$  nm. Inset: binding isotherm from DynaFit<sup>®</sup>, plot of intensity of area  $\Delta J=2$  (dark green) vs concentration of  $\text{F}^-$ .

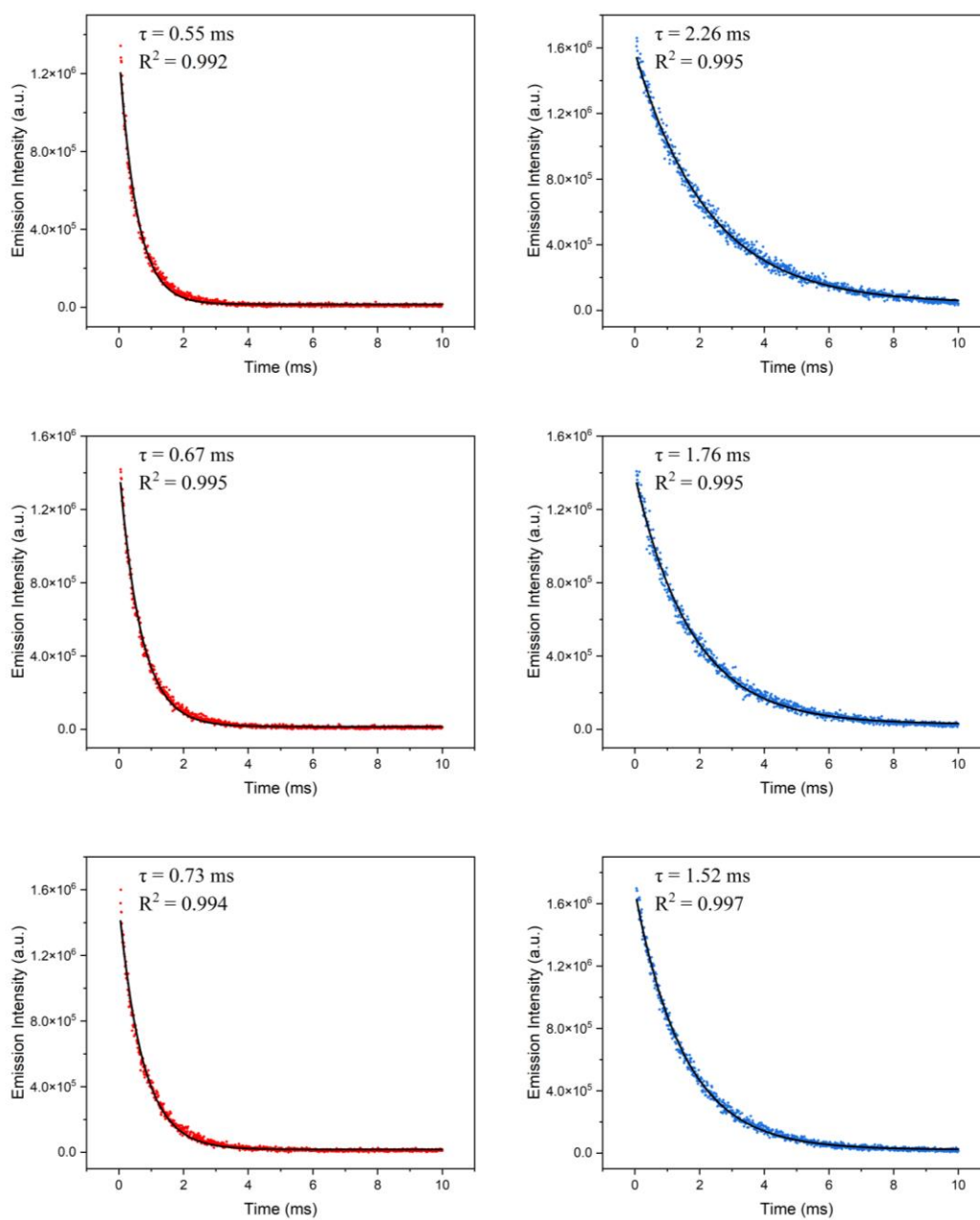


**Figure-A10.** Fitted luminescence lifetimes spectra of Eu.p.DO3AM.Lys.OMe (*top*), Eu.p.DO3AM.Phen.OMe (*middle*) and Eu.p.DO3AM.Pro.OMe (*bottom*) dissolved in MeOH (*left, red*) and MeOD (*right, blue*).  $\lambda_{\text{ex}} = 393 \text{ nm}$ ,  $\lambda_{\text{em}} = 616 \text{ nm}$ , concentration of all complexes  $1 \times 10^{-3} \text{ mol dm}^{-3}$ .